The Importance of Baryonic Effects in Galaxy Groups for Precision Cosmology

---

Dissertation

zur

Erlangung der naturwissenschaftlichen Doktorwürde
(Dr. sc. nat.)

vorgelegt der

Mathematisch-naturwissenschaftlichen Fakultät

der

Universität Zürich

von

Manuel Hermann Rabold

aus

Deutschland

Promotionskommission

Prof. Dr. Ben Moore (Vorsitz)

Prof. Dr. Romain Teyssier

Prof. Dr. Oliver Hahn

Zürich, 2017

"Doubt is the basis of all scientific progress."

T'Pol of Vulcan

[CBB04]

Zusammenfassung

Die Arbeit dieser Dissertation ist ein Beitrag zu den Bemühungen, der präzisen Bestimmung der kosmologischen Parameter, welche unser Universum beschreiben; speziell des Letzteren zeitliche Entwicklung und Komposition. Zukünftige Himmelsvermessungen wie Euclid, oder das Large Synoptic Survey Telescope, werden die relevanten kosmologischen Spektren mit bisher unerreichter Präzision messen. Diese Spektren, welche statistische Quantifizierungen des Anhäufens von Materie auf verschiedenen Skalen sind, hängen direkt von diesen kosmologischen Parametern ab. Eine höhere Präzision bei der Messung der Spektren, bedeutet daher kleinere Unsicherheiten bei den Werten der Parameter.
Die Informationen von diesen präzisen Messungen können nur dann voll ausgenutzt werden, wenn es auf der theoretischen Seite gelingt diese Spektren mit der gleichen hohen Genauigkeit zu berechnen. Die Arbeit dieser Studie liegt hier. Durch die Nutzung von Computer Simulationen, kann die Evolution der grossskaligen Strukturen im Universum, für ein gegebenes Set von Parametern, berechnet werden. Die Spektren können dann vom Resultat der Simulationen extrahiert, und mit den experimentellen Gegenstücken verglichen werden.
Es ist deshalb von grosser Bedeutung, dass jegliche Unsicherheiten welche durch numerische Effekte in den Simulationen entstehen, genau quantifiziert werden. Darüber hinaus ist es nützlich für das physikalische Verständnis, den Einfluss der verschiedenen physikalischen Prozesse, welche in den Simulationen mit eingeschlossen sind, zu quantifizieren.
Der Fokus dieser Arbeit liegt auf der Materieverteilung innerhalb von Massenansammlungen in der Grösse von Galaxiengruppen, da diese den stärksten Beitrag zu den zuvor erwähnten Spektren liefern. Sechzehn Halos dieser Grösse wurden simuliert und schichtweise wurden zusätzliche physikalische Effekte mit einbezogen. Der Startpunkt waren Simulation die nur dunkle Materie enthielten. In einem zweiten Schritt wurde die baryonische Komponente, als nicht durch Strahlung wechselwirkendes Fluid, mit eingeschlossen. In darauf folgenden Schritten wurde der Baryonen Komponente die Fähigkeit zu kühlen und Sterne zu bilden hinzugefügt, so wie ein etabliertes Modell stellaren Feedbacks.
Darüber hinaus wurde ein experimentelles Modell von Aktiven Galaktischen Kern Feedback getestet. Dieser physikalische Prozess ist von besonderer Bedeutung, da mit ihm die Erwartung verbunden wird, dass er die existierende Diskrepanz, zwischen Theorie und Beobachtung, des Baryonen Gehalts von Galaxiengruppen und -haufen, auflösen wird.
Die Dissertation beinhaltet ebenfalls einen Bericht darüber, wie numerische Parameter die Massenverteilung in Galaxiengruppen beeinflussen, im Vergleich zu dem Einfluss den physikalische Ursachen haben.

Summary

This thesis work is a contribution to the quest of the precise determination of the cosmological parameters which describe our universe, in particular its time evolution and its composition. Future sky surveys like Euclid or the Large Synoptic Survey Telescope will measure the relevant cosmological spectra with unprecedented precision. These spectra, which are statistical quantifications of the clumping of matter on different scales, depend directly on the cosmological parameters. A higher observational precision on the spectra, means therefore smaller uncertainties onto the values of the parameters.
The information from these precise measurements can be fully exploited only, if on the theoretical side, the spectra are calculated with the same high accuracy. The work of this study is situated here. Through the utilization of computer simulations, the evolution of the large scale structure in the universe can be computed, for a given set of cosmological parameters. The spectra can then be extracted from the simulation results and compared with the observational counterpart.
It is therefore of crucial importance that any uncertainties arising from numerical effects in the simulations are precisely quantified. Beyond this it is useful for the physical understanding, to quantify the influence of different physical processes, which are included in the simulations.
The focus of this work lies on the matter distribution within galaxy groups sized mass accumulations, since they give the strongest contribution to the aforementioned spectra. Sixteen halos of this size have been simulated with various layers of included physics. The starting point are pure dark matter only simulations. Then in a second step the baryonic component is included as a non-radiative fluid. In subsequent steps the ability to cool and form stars was added to the baryon component, as well as an established model of stellar feedback.
Beyond these an experimental implementation of Active Galactic Nucleus feedback was tested. This physical process is of particular importance, as it is expected to resolve existing mismatches between theory and observation in the baryon content of galaxy groups and clusters.
The thesis also contains a report, on how the numerical parameters affect the mass distributions within the galaxy group halos, as compared to impacts from physical causes.

Contents

1 Introduction

1.1 The scientific Background of modern Cosmology

Cosmology is the branch of physics which aims to describe the universe as a whole; its origin and evolution, but also its constituents and the structures which they form. Thereby it addresses some of the most fundamental questions, which scientific curiosity has raised throughout the millennia:

- How old is the universe ?
- What is the universe made of ?
- What are our origins ?
- Is the universe finite or infinite?

A wide range of physical principals and methods are therefore needed, to understand the various aspects that nature reveals on different scales. From quantum mechanics and quantum field theory, for the description of the properties of elementary particles as the basic constituents of the universe, over astrophysics which describes the dynamics of galaxies, up to the general theory of relativity which describes the physical processes on the largest scales, where gravitation is the only interaction of relevance.

The dawn of cosmology in the modern sense was at the beginning of the 20th century, when a series world view changing discoveries took place:

- The general theory of relativity, which describes gravitation without referring to an absolute space, like in the Newtonian theory.
- The realization that other galaxies exist aside from our own (the Milky Way), after it was discovered, that what was previously called extragalactic nebula are actually other galaxies.
- Perhaps most important: The discovery by Edwin Hubble, that the universe is expanding which he inferred from his observation, that galaxies are receding from each other.

The expansion of the universe is mathematically described by the general theory of relativity, so that our knowledge of the universe has established itself in a concrete physical description. A very important assumption in this description is that the universe, on its largest scales, is homogeneous and isotropic. A direct consequence of this assumption is, that there should be neither a preferred location nor direction in the universe, which is nothing else but a mathematical formulation of the Copernican principle. How can the universe be homogeneous and isotropic, when we observe islands of stars called galaxies in the vastness of empty space? The answer is, that homogeneity and isotropy only apply to the largest scales, meaning to the accumulations of galaxies in a cosmic web.

The metric of an expanding, homogeneous and isotropic universe is called Friedman-Robertson-Walker metric (FRW metric) [Ryd03] [Dod03]

$$ds^2 = -c^2dt^2 + a^2_{(t)} \cdot [d\chi^2 + \chi^2 \cdot (d\theta^2 + \sin^2(\theta) \cdot d\phi^2)] \tag{1.1}$$

The time coordinate is t, spacial coordinates (expressed in spherical symmetry) are χ, θ and ϕ. $a_{(t)}$ is called the scale factor and describes the actual expansion of the universe

as a function of time. Here we have assumed, that the total curvature of the universe is zero. This is justified, since no observational evidence so far has indicated anything else. Throughout the underlying work, we assume therefore the total curvature of the universe to be zero. This metric solves the Einstein equations,

$$R_{\mu\nu} - \frac{1}{2} R \cdot g_{\mu\nu} = \frac{8\pi G}{c^4} \cdot T_{\mu\nu} \tag{1.2}$$

where the energy-momentum tensor on the right hand side is given by the known species of energy density in the universe $\epsilon_{(t)}$. The 0-0-component of the Einstein equations in the underlying case is [Ryd03] [Dod03]:

$$\left(\frac{\dot{a}_{(t)}}{a_{(t)}} \right)^2 = \frac{8\pi G}{3c^2} \cdot \epsilon_{(t)} \tag{1.3}$$

Since the universe is expanding at present the assumption lies close, that it was also expanding in its past. A direct consequence of this would be that the energy content of the universe (e.g. matter and radiation) must have been in a more dens and hot state at early times. In contrast to the observable universe of today, where massive structures of matter, are emitting light that can propagate to us more or less unhindered, at those early times matter and radiation were not two separate things, but rather coupled to each other in the form of a cosmic plasma. This plasma, consisting partly of electrons, protons and photons, was in such a dens state that photons could not travel freely, instead they scattered off electrons continuously. While the electrons likewise scattered off the protons continuously. Temperature and photon abundance were high enough that any hydrogen atom that had formed, was immediately ionized again, by a photon. Three of the major components of the cosmic plasma were therefore in thermal equilibrium. It is not difficult to imagine that this cosmic plasma also possessed overall homogeneity and isotropy, with small perturbations to them.

Through the expansion of the universe, temperature and scattering rates fell so that at a certain instant hydrogen atoms could become stable. This process is called recombination. Ones the electrons were bound within the atoms, the scattering rate of electrons and photons dropped even further, marking the era of photon decoupling, which is followed further by the era of last scattering. As the name implies, after it the photons could travel freely through the now no longer opaque universe, keeping their black body spectrum as a remnant of the thermal equilibrium of the cosmic plasma. These free streaming photons must be observable at any point in the universe. And they are, in what is called the cosmic microwave background (CMB), an isotropic radiation with a black body spectrum corresponding to a temperature of 2.725 K. This low temperature value is due to the loss of energy the photons experience during their propagation through the expanding universe. Calculations, making use of the dynamics of the universe, allow to date the events from which the CMB emerged to 13 Gyr ago. At these early times, the decoupled photons had a temperature of 3000 K.

The CMB was predicted 1948 by Ralph Alpher and Robert Herman. When it was discovered later in 1964 by Arno Penzias and Robert Wilson [PW65] it was the ultimate proof of what theorists previously suggested as the Hot Big Bang model. In other words: confirmation that we live in an expanding universe, whose components were initially in a hot, dens state, only to cool and form structures during the expansion, such as galaxies, stars and planets.

The CMB radiation is therefore not only severe evidence that the universe was expanding in its past, but also that it was homogeneous and isotropic, on its largest scales, at

this era, too. Through precise measurements however anisotropies can be found within the CMB. Their highest deviation from the average temperature of 2.725 K is 10^{-5} K. These anisotropies are the origins of the inhomogeneous and anisotropic structures, formed by matter, that exist today.

A big surprise for physicist in this context was the discovery of the accelerated expansion of the universe at the end of the 20th century, through Nobel Prize winning results from super novae observations [RFC+98] [PAG+99]. The physical cause of this acceleration is parametrised with an additional term in the field equations, which describe the expansion. This term is denoted with Λ and in the most general sense referred to as dark energy. It is from its very nature of gravitational interaction different from the baryonic component (which makes up stars, planets and everything on them). While the ordinary baryonic matter is gravitationally attractive and therefore causes the expansion of the universe to decelerate, dark energy does the opposite.

A further key component of the cosmological composition is, what is called dark matter. It was predicted early in the 20th century by the visionary Swiss astrophysicist Fritz Zwicky, to explain the dynamics of an observed galaxy cluster [Zwi33]. Dark matter is in its gravitational interaction similar to ordinary baryonic matter (attractive, causing the cosmic expansion to decelerate), but does not interact through radiation, and hence has, to this date, not been observed directly.

Given this observational evidence and successful theoretical description, the aim of cosmologist in the second half of the 20th century had become the determination of the precise time evolution history of the cosmic expansion and the evolution of structures within the universe. These two issues are closely entangled with each other, since the components of the universe which form the structures are also determining the rate of expansion. The rate of expansion in turn influences the growth of structure. These two statements are mathematically formulated through the following physical description:

How are the energy densities of the individual components influenced by the expansion:

Starting from the general relativistic equation of energy conservation

$$T^{0\mu}{}_{;\mu} = \frac{\partial}{\partial x^\mu} T^{0\mu} + \Gamma^0_{\nu\mu} T^{\nu\mu} + \Gamma^\mu_{\nu\mu} T^{0\nu} = 0 \tag{1.4}$$

which for the FRW metric takes the form:

$$\frac{\partial \epsilon}{\partial t} + \frac{\dot{a}}{a} \cdot 3 \cdot (\epsilon + P) = 0 \tag{1.5}$$

In addition it is assumed that the relation between pressure P and energy density ϵ (equation of state) is linear for each of the components:

$$P = w \cdot \epsilon \tag{1.6}$$

So that finally one finds

$$\epsilon \propto \left(\frac{1}{a}\right)^{3\cdot(1+w)} \tag{1.7}$$

The constituents of the universe can be sorted into the following three categories:

1. Matter: $w = 0$

$$\epsilon_{m\,(t)} = \epsilon_{m,0} \cdot \left(\frac{a_0}{a}\right)^3 \Longrightarrow \epsilon_m \sim \frac{1}{a^3} \tag{1.8}$$

The interpretation for matter is simple. The energy density drops with the number density of particles during the expansion, since their rest mass is the only contribution to it. With this it follows $\epsilon_m = \rho \cdot c^2$, where ρ is the mass density. Both dark matter and baryonic matter exert this kind of behaviour.

2. Radiation: $w = \frac{1}{3}$

$$\epsilon_{rad\,(t)} = \epsilon_{rad,0} \cdot \left(\frac{a_0}{a}\right)^4 \Longrightarrow \epsilon_{rad} \sim \frac{1}{a^4} \tag{1.9}$$

Because of its nonzero pressure, the radiation content within a volume element carries out work on the surrounding surfaces of other volume elements [Wal97]. Therefore the energy density of radiation is decreasing more rapidly, than the one of matter, with the expansion. The radiation content of the universe is contributed for the most part by photons (of the CMB).

3. Dark Energy: $w < -\frac{1}{3}$

$$\epsilon_{\Lambda\,(t)} = \epsilon_{\Lambda,0} \cdot \left(\frac{a_0}{a}\right)^0 \Longrightarrow \epsilon_{\Lambda} \sim const. \tag{1.10}$$

Assuming the equation of state parameter to be -1, the energy density of dark energy would remain constant throughout the expansion. Therefore dark energy with $w = -1$ is named cosmological constant, whereas for any other value of w it is usually called quintessence.

How is the expansion influenced by the energy densities of the individual components:

Starting point is the i-i-component of the Einstein equations

$$\frac{\ddot{a}_{(t)}}{a_{(t)}} + \frac{1}{2} \cdot \left(\frac{\dot{a}_{(t)}}{a_{(t)}}\right)^2 = -\frac{4\pi G}{c^2} \cdot p_{(t)} \tag{1.11}$$

This, together with the 0-0-component of the Einstein equations, gives the acceleration equation, named that way because it describes how energy density and pressure accelerate or decelerate the expansion of the universe, depending on their sign and ratio:

$$\frac{\ddot{a}_{(t)}}{a_{(t)}} = -\frac{4\pi G}{3c^2} \cdot (\epsilon_{(t)} + 3 \cdot p_{(t)}) \tag{1.12}$$

All off-diagonal components ($0i$- and ij-components) of the Einstein equations are identical to zero. Again it is assumed that the equation of state for each of the components is linear: $p = w \cdot \epsilon$, so that

$$\frac{\ddot{a}_{(t)}}{a_{(t)}} = -\frac{4\pi G}{3c^2} \cdot (1 + 3\,w) \cdot \epsilon_{(t)} \tag{1.13}$$

It is interesting to see, that while the energy densities determine the expansion rate of the universe $\dot{a}_{(t)}$, the change in the rate of expansion $\ddot{a}_{(t)}$ is determined by energy density and pressure.

The key equation in cosmology, the Friedmann equation, can be expressed in a slightly different way, after the dependence of the individual energy densities on the scale factor is substituted and a_0, the value of the scale factor at the present, is set to one:

$$H^2_{(t)} = \left(\frac{\dot{a}_{(t)}}{a_{(t)}}\right)^2 = \frac{8\pi G}{3c^2} \cdot \left(\frac{\epsilon_{m,0}}{a^3_{(t)}} + \frac{\epsilon_{rad,0}}{a^4_{(t)}} + \epsilon_{\Lambda,0}\right) \tag{1.14}$$

Here we have defined the Hubble rate $H_{(t)}$. With that we define the critical energy density as

$$\epsilon_{cr\,(t)} = \frac{3c^2 \cdot H_{(t)}^2}{8\pi G} \quad \text{and evaluating it at the present} \quad \epsilon_{cr,0} = \frac{3c^2 \cdot H_0^2}{8\pi G} \tag{1.15}$$

allows to express the Friedmann equation as

$$\left(\frac{H_{(t)}}{H_0}\right)^2 = \left(\frac{\epsilon_{m,0}}{\epsilon_{cr,0} \cdot a_{(t)}^3} + \frac{\epsilon_{rad,0}}{\epsilon_{cr,0} \cdot a_{(t)}^4} + \frac{\epsilon_{\Lambda,0}}{\epsilon_{cr,0}}\right) \tag{1.16}$$

Further, the energy density parameter is defined as

$$\Omega_{i(t)} = \frac{\epsilon_{i(t)}}{\epsilon_{cr(t)}} \quad \text{and respectively} \quad \Omega_{i,0} = \frac{\epsilon_{i,0}}{\epsilon_{cr,0}} \tag{1.17}$$

which gives

$$\left(\frac{H_{(t)}}{H_0}\right)^2 = \left(\frac{\Omega_{m,0}}{a_{(t)}^3} + \frac{\Omega_{rad,0}}{a_{(t)}^4} + \Omega_{\Lambda,0}\right) \tag{1.18}$$

or

$$\left(\frac{H_{(t)}}{H_0}\right)^2 = \left(\frac{H_{(t)}}{H_0}\right)^2 \cdot \left(\Omega_{m(t)} + \Omega_{rad(t)} + \Omega_{\Lambda(t)}\right) \tag{1.19}$$

One can see from this expression, that at any time the energy density parameters of all components need to add up to one for a universe with zero total curvature. Or in other words, the sum of the energy densities of all components ϵ matches the critical energy density. This explains why the latter is called that way.

By knowing the current values of the energy densities of the different components through observations, it is possible to calculate the values of the scale factor at which the individual contributions of two components to the total energy density were equal. The default values for the present density parameters are [Ryd03]:

$$\begin{aligned} \Omega_{rad,0} &\approx 8.3 \cdot 10^{-5} \\ \Omega_{m,0} &\approx 0.3 \\ \Omega_{\Lambda,0} &\approx 0.7 \end{aligned}$$

Hence The content of the universe is in rough numbers: dark energy 70%, dark matter 25% ($\Omega_{dm,0} \approx 0.25$) and ordinary baryonic matter 5% ($\Omega_{b,0} \approx 0.05$). The questions about the nature of dark matter and dark energy are therefore among the key issues of fundamental physics in the 21st century.

Prior to each moment of equality, the component whose energy density increases more rapidly with decreasing scale factor, was the dominant form of energy in the universe.

$$\frac{\epsilon_{i\,(t_{eq})}}{\epsilon_{j\,(t_{eq})}} = 1 \quad \text{with} \quad n_i = 3 \cdot (1 + w_i) \tag{1.20}$$

$$\frac{\epsilon_{i,0}}{(a_{(t_{eq})})^{n_i}} = \frac{\epsilon_{j,0}}{(a_{(t_{eq})})^{n_j}} \tag{1.21}$$

$$\frac{\epsilon_{i,0}}{\epsilon_{j,0}} = (a_{(t_{eq})})^{n_i - n_j} \tag{1.22}$$

$$\Longrightarrow a_{eq} = a_{(t_{eq})} = \left(\frac{\epsilon_{i,0}}{\epsilon_{j,0}}\right)^{\frac{1}{n_i - n_j}} \tag{1.23}$$

This allows one to divide the history of the universe into three epochs, denominated by their dominant form of energy and bounded by the instants of equality between the two components of interest. Each epoch has a simplified time dependence of the scale factor, since the energy densities of the non-dominant components can be neglected within the Friedmann equation, and the remaining differential equation for the scale factor can be solved analytically. In Table 1.1, the relevant events and epochs are listed. It is useful to define the redshift z of a source galaxy as

$$z = \frac{\lambda_{obs} - \lambda_{em}}{\lambda_{em}} \tag{1.24}$$

Here λ_{em} stands for the wavelength of light emitted by a source that is moving away from an observer. It is measured in the reference frame of the emitter. The observer measures the wavelength of the light in his reference frame as λ_{obs}. For a source moving towards the observer the light would be blue shifted. Because the relation of redshift z to scale factor a is bijective $a = 1/(1+z)$, as are the relations of both of them to time t, the three quantities t, a and z can be used interchangeably.

By the end of the 20th century cosmologists had a coherent picture of the cosmos: the universe is expanding at present and was also expanding in its past. Homogeneity and isotropy apply only to its largest scales. The information about the cosmological parameters was thereby extracted mainly from direct observables e.g. the rate of expansion from the spectra of galaxies, or the dark energy density from observations of supernova. But also statistical quantities such as the CMB power spectrum, played an important role already. With this kind of knowledge the cosmological parameters were determined well enough to compute the beginnings and endings of the cosmic eras, of domination by the individual species. Beyond these, the era of decoupling and the origin of the CMB radiation, were determined to have taken place roughly 13 billion years ago. Finally, the Big Bang itself is assumed to lie back another 300,000 years from this era. This picture of the universe is therefore called the Hot Big Bang model or ΛCDM model after its main components: dark energy (Λ) and cold dark matter (CDM). The word cold hereby denotes the non-relativistic nature of the latter.

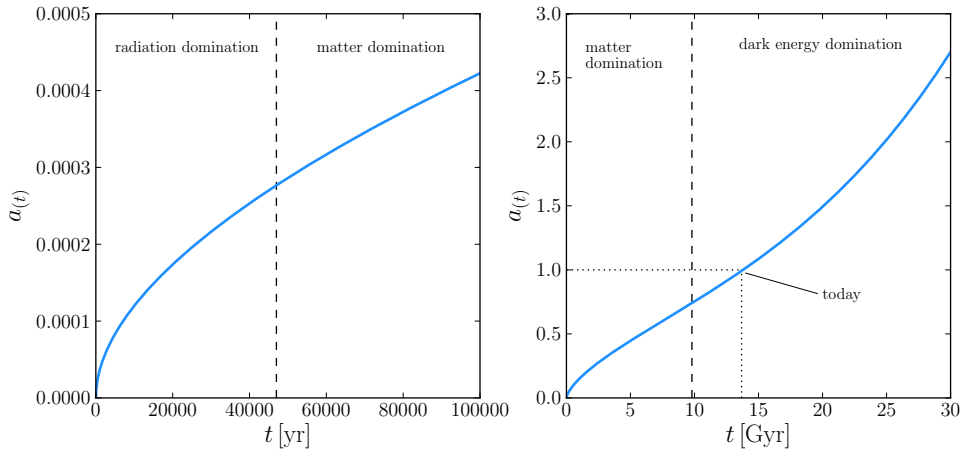

Figure 1.1: **The expansion of the universe and the cosmological eras.**

Table 1.1: **Timetable of cosmological events and eras.**

Event/**Era**	Time t	Scale factor a	Redshift z
Big bang (postulated, not observed so far)	0	0	∞
Era of radiation domination $\mathbf{a \sim t^{1/2}}$	? - 47000 yr	? - 0.00028	? - 3570
Big bang nucleosynthesis	3 min - 20 min		
Era of matter domination $\mathbf{a \sim t^{2/3}}$	47000 yr - 9.8 Gyr	0.00028 - 0.75	3570 - $\frac{1}{3}$
Recombination	240000 yr	0.00073	1370
Photon decoupling	350000 yr	0.0009	1100
Last scattering of electrons and photons	350000 yr	0.0009	1100
Era of dark energy domination $\mathbf{a \sim e^{C \cdot t}}$	9.8 Gyr - 13.8 Gyr	0.75 - 1	$\frac{1}{3}$ - 0
Today	13.8 Gyr	1	0

1.2 The contemporary Research: Precision Cosmology as Utilisation of Information from cosmic Structures

Currently the scientific community witnesses the era of precision cosmology. With the overall time evolution of the universe being determined qualitatively well, by the beginning of the 21st century, the goal of cosmology had become to develop also a precise quantitative understanding. In other words the desire is to know the cosmological parameters with sub percent uncertainty. For this task either new sources of information are required, or the precision on already utilized ones needs to be increased. For the latter option, the first endeavour towards this goal was the Planck space probe, launched in 2009, and taking data from 2009 to 2013 [PAA+16]. It has determined the anisotropy map of the CMB with much higher accuracy than its predecessor WMAP, which was in operation from 2001 till 2010 [BLW+13] [HLK+13].

Regarding the first option, a brand new source to retrieve information about the cosmos, which has not been explored before, is the gravitational distortion of light. For the cosmological application of this effect the observed light is the one, which is emitted from galaxies [Dod03]. This light becomes deflected continuously by the gravitational influence of the mass distribution between the source galaxy and the observer. This effect is called cosmological weak gravitational lensing (WL) and can be utilized to obtain the statistical information about the large scale structure, which is imprinted onto the distortion patterns of the deflected light. The term weak hereby refers to the fact that the distortions induced in the observed images of source galaxies are of order of only 1-2%, as opposed to strong gravitational lensing, where the distortion is so strong, that the disk like or elliptical shapes of the source galaxies are distorted into arcs, or even multiple images. The difference between the two categories can also be quantified in terms of the lenses: in strong lensing the lenses are systems of high density, as opposed to weak lensing. The effect of strong lensing is therefore applied to the mass determination of individual systems, like galaxy clusters or galaxy groups. This method was suggested first, also by Fritz Zwicky [Zwi37].
Weak lensing on the other hand is predestined to provide us with information about the large scale structure of the universe, since the density contrast of the latter is small. A particular advantage is that it is also sensitive to the dark matter component, which otherwise cannot be observed directly, but has the same deflecting influence onto the propagation of light through its gravitating nature, as the luminous baryonic component has. The key question is now: how can the effect of the 1-2% distortion of source images, which is in the form of induced ellipticity, be distinguished from the intrinsic ellipticity of the source galaxies ? The answer lies in the statistical nature of the effect: a whole number of background galaxies needs to be taken into account as potentially lensed images, instead of only one. In an image of a galaxy accumulation, which is completely unlensed, there should be no preferred direction, along which the ellipticities of the individual galaxy images are aligned. But if a lens is positioned in the foreground, a preferred direction must be found. The principle is illustrated in Figure 1.2.

The observational requirement to utilize the WL effect is therefore, to be able to take highly accurate images of galaxies (at various redshifts) and to construct a distortion map from them. Severe experimental efforts are planned for a precise determination of the WL spectrum: The Large Synoptic Survey Telescope (LSST) [LSS12], currently under construction and scheduled for full operation in 2022, will undertake a wide survey to measure and map the ellipticities of distant galaxies, from which the weak lensing spectrum can be obtained. The term wide hereby denotes a survey, whose focus lies on the maximization of the sky fragment that is covered by the survey. In contrast to a deep survey which is designed for

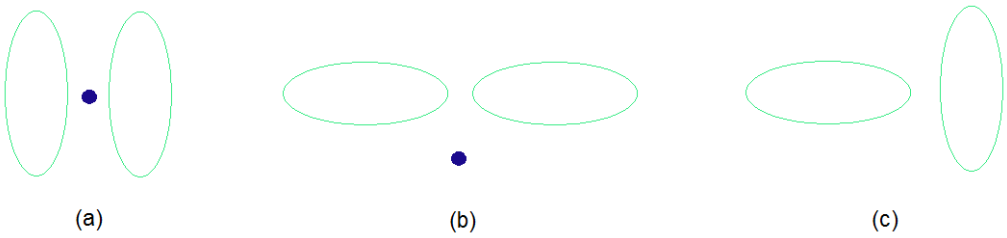

Figure 1.2: **Distinguishing between weakly lensed and unlensed background images. The ellipticities of the images (teal) in (a) and (b) could be induced through lensing, since they show a preferred direction from which the position of the questionable lensing mass (blue) could be inferred. The images in (c) however show no such preferred direction, so that it can be excluded, that their ellipticities are induced through gravitational lensing.**

the observation of galaxies at high redshifts, or equivalently large radial distances. In the near future the Euclid space probe [LAA+11] [AAA+16], which is a project by the European Space Agency (ESA) and scheduled to be launched in 2020, will pursue a task mainly similar to the wide survey of the LSST, with the advantage of not underlying any atmospheric influences. For its observation it will be placed at the Sun-Earth Lagrange point L2, which is located $1.5 \cdot 10^6$ km above the point of the Earth which is the farthest away from the sun. A part of its time will also be devoted to a deep survey.

The important point about the two mentioned information sources CMB anisotropies and WL is that they are measures of the inhomogeneities in the universe, namely the large scale structure. This means that we explicitly utilize the information contained in these inhomogeneities, to infer the cosmological parameters. This is possible since the characteristics of the inhomogeneities are predicted by the underlying cosmological model. For example do the values of cosmological parameters determine the expansion rate of the universe, which in turn determines how fast structures grow on different scales. This stands in contrast to the methods mentioned in the previous chapter (e.g. super nova observations, or galaxy spectroscopy, to determine the expansion rate), where the inhomogeneities are a perturbing factor, which needs to be alleviated through increasing the number of observations, for example.
The key difference between these, and methods which make use of the inhomogeneities, is that in the latter case an additional layer of uncertainty is present because of the statistical nature of the inhomogeneities, as will be explained in the following. Since the universe is overall homogeneous and isotropic there is no information contained in the value of cosmic structure at a certain point, since there should be no preferred location. Further, the ensemble average, which is the average over all possible realization of the underlying model universe should always give the same result. This is also formulated mathematically and will be illustrated now, on the central quantity of the cosmological large scale structure, the density contrast of the mass density (of the matter component):

$$\delta_{(\vec{x})} = \frac{\rho_{(\vec{x})} - \bar{\rho}}{\bar{\rho}} \tag{1.25}$$

Here $\rho_{(\vec{x})}$ is the matter density field of the universe and $\bar{\rho} = \langle \rho_{(\vec{x})} \rangle$ denotes the average mass density in the universe. It follows

$$\langle \delta_{(\vec{x})} \rangle = 0 \tag{1.26}$$

Statistical information can be found by looking at the two-point correlation function (also called the autocorrelation function) of the density contrast.

$$\langle \delta_{(\vec{x})} \delta_{(\vec{x}+\vec{r})} \rangle = \xi_{(r)} \tag{1.27}$$

Because of homogeneity and isotropy this quantity can only be a function of the absolute of the distance r between the two points under consideration $\vec{x}$ and $\vec{x}+\vec{r}$ [Dod03]. Instead of the cosmic density contrast field itself, one can also work with its Fourier transform

$$\tilde{\delta}_{(\vec{k})} = \int_{-\infty}^{\infty} d^3x \, e^{-i\vec{k}\vec{x}} \, \delta_{(\vec{x})} \quad \Longrightarrow \quad \delta_{(\vec{x})} = \frac{1}{(2\pi)^3} \int_{-\infty}^{\infty} d^3k \, e^{i\vec{k}\vec{x}} \, \tilde{\delta}_{(\vec{k})} \tag{1.28}$$

It follows directly

$$\langle \tilde{\delta}_{(\vec{k})} \rangle = 0 \quad \Longleftrightarrow \quad \langle \delta_{(\vec{x})} \rangle = 0 \tag{1.29}$$

and further it can be shown, that the assumption of homogeneity and isotropy translates into

$$\langle \tilde{\delta}_{(\vec{k})} \tilde{\delta}^*_{(\vec{k'})} \rangle = (2\pi)^3 \, P_{(k)} \, \delta^D_{(\vec{k'}-\vec{k})} \quad \Longleftrightarrow \quad \langle \delta_{(\vec{x})} \delta_{(\vec{x}+\vec{r})} \rangle = \xi_{(r)} \tag{1.30}$$

[Dod03]. $P(k)$ is called the matter power spectrum (MPS) ($\delta^D_{(\vec{k'}-\vec{k})}$ is the Dirac-Delta function in three dimensions). The MPS is the most important quantity for the description of the large scale structure of the universe, as it describes how mass clumps on different scales of size $2\pi/k$, in a statistical sense. What does that mean? It means, that only the ensemble averaged quantities $\langle \tilde{\delta}_{(\vec{k})} \tilde{\delta}^*_{(\vec{k'})} \rangle$, $\langle \delta_{(\vec{x})} \delta_{(\vec{y})} \rangle$, $\langle \tilde{\delta}_{(\vec{k})} \rangle$ and $\langle \delta_{(\vec{x})} \rangle$ are predicted by the underlying cosmological model and the cosmological parameters. The quantities $\tilde{\delta}_{(\vec{k})} \tilde{\delta}^*_{(\vec{k'})}$, $\delta_{(\vec{x})} \delta_{(\vec{y})}$, $\tilde{\delta}_{(\vec{k})}$ and $\delta_{(\vec{x})}$ can take any value for a given cosmology. In words: The value of one of the mentioned observables at a specific location, does not tell anything about the cosmology. One also finds that

$$\xi_{(r)} = \frac{1}{(2\pi)^3} \int_{-\infty}^{\infty} d^3k \, e^{-i\vec{k}\vec{r}} \, P_{(k)} \tag{1.31}$$

and further

$$\sigma = \xi_{(0)} = \langle \delta_{(\vec{x})} \delta_{(\vec{x}+\vec{0})} \rangle = \langle \delta^2_{(\vec{x})} \rangle = \frac{1}{(2\pi)^3} \int_{-\infty}^{\infty} d^3k \, P_{(k)} \tag{1.32}$$

For the CMB and cosmological WL, power spectra can be defined as well. These are closely connected to the MPS. So is the CMB power spectrum a two-dimensional angular quantity, a slice of the MPS at the radial coordinate which corresponds to $z = 1100$. Since the CMB anisotropies can be described on the surface of a sphere and expanded in spherical harmonics the CMB power spectrum is given by the coefficients C_l of the Legendre polynomials, which describe the CMB two-point correlation function. The relation corresponding to (1.30), is therefore

$$\langle a_{lm} a^*_{l'm'} \rangle = C_l \, \delta_{ll'} \, \delta_{mm'} \tag{1.33}$$

[Dod03]. For WL the situation is similar, however the radial coordinate is not reduced to just one redshift z, since source galaxies whose images undergo the weak lensing effect are located at various redshifts. This means one can retrieve information about the third (radial) dimension, but not to the point where the WL power spectrum could be determined as a function of z. Instead the possibilities are reduced, to sorting the source galaxies into redshift bins. Redshifts of galaxies are determined either by spectroscopy or photometry. The result are angular power spectra for each of the redshift bins, so that they can be auto- and cross correlated. Another interesting feature about WL is that the information about the matter distribution between the source image and the observer, which is responsible for

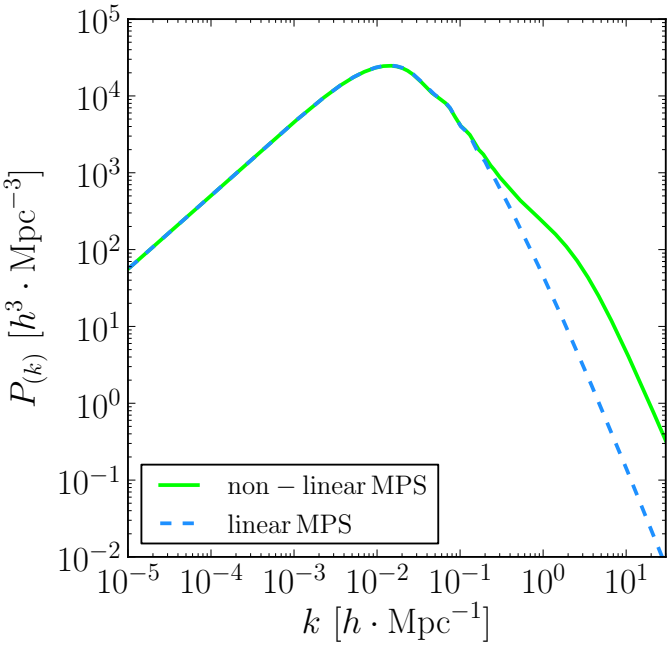

Figure 1.3: **The matter power spectrum at $z = 0$ for a ΛCDM cosmology. When non-linearities are taken into account, its shape changes dramatically above a certain k-value. This point at which non-linearities become important depends on the redshift.**

the distortion of the light, is not retained. Only the averaged effect over the radial distance covered, is accessible so that the information content is projected onto the redshift of the considered source galaxies.

Back to the matter power spectrum: after combining all information from sources like the CMB or abundance of galaxy clusters the result, which is depicted in Figure 1.3, is obtained. One can see three distinct features in it: first the linear increase $\propto k$ up to $k = 0.01\,h/\mathrm{Mpc}$ ($1\ \mathrm{Mpc} = 3 \cdot 10^{22}$ m), second the kink around $k = 0.01\,h/\mathrm{Mpc}$, and third the decrease $\propto k^{-3}$ for $k > 0.01\,h/\mathrm{Mpc}$. In addition to k the MPS also depends on time (or equivalently the scale factor). The $\propto k$ dependence for large scales is interpreted by physicists as a remnant of the primordial MPS, as it was during a postulated era, even before radiation domination [Dod03] [BT08]. It is assumed that during this epoch the power spectrum of gravitational potentials $P_{\Phi\,(k)}$ was scale free, which means it must be proportional to k^{-3}. During the era of radiation domination first the small perturbation modes in the gravitational potential enter the horizon and then subsequently larger ones, as the horizon size grows. Modes within the horizon undergo suppression since the gravitational potentials are decaying in this epoch. Consequently, density fluctuations in the matter distribution indeed grow during this era, but not considerably. This leaves a distinct k-dependence on the perturbation spectrum, since the smaller the perturbation, the earlier it entered the horizon and the more time it was exposed to the decaying potentials. At the end of the radiation dominated era the largest mode to enter the horizon was $k = 0.01\,h/\mathrm{Mpc}$. On larger scales of $k < 0.01\,h/\mathrm{Mpc}$ the perturbations enter at times, at which the universe is matter dominated, already. In this era the gravitational potentials are constant, and the density perturbations keep their initial k-dependence as they grow independent of their magnitude. During matter domina-

tion the power spectrum of the gravitational potential perturbations can be related to the MPS through the Poisson equation $\delta \propto k^2 \delta\Phi$, which is a linear combination of the Einstein equations valid during this epoch [Dod03]. With this one finds the $\propto k$ increase in the MPS which is the case for modes that stayed outside of the horizon during radiation domination. According to this theoretical interpretation, the characteristic kink in the MPS is a direct probe of the horizon size at matter-radiation equality, and therefore for the moment of matter-radiation equality itself. This instant in turn is determined by the abundances of radiation and matter in the universe, so that the shape of the MPS gives a direct indication for the parameters $\Omega_{rad,0}$ and $\Omega_{m,0}$. During the epochs of matter and dark energy domination the density perturbations grow independent of k, so that the MPS changes only its amplitude, but not its shape [Dod03]. Mathematically this is described by the growth factor $G_{(a)}$

$$\tilde{\delta}_{(a,\vec{k})} = \tilde{\delta}^{ini}_{(\vec{k})} \cdot G_{(a)} \Longrightarrow P_{(a,\vec{k})} = P^{ini}_{(k)} \cdot G^2_{(a)} \tag{1.34}$$

While $G_{(a)} = a$ would be the case for a universe which contains only matter, it will be a more complicated relation, if there is also a presence of dark energy, which slows down the growth of matter accumulations, since the expansion rate will be higher [Dod03].

A very important caveat about the scale free evolution is, that it is only true in the linear regime, which is defined as all situations in which

$$\left|\tilde{\delta}_{(\vec{k})}\right| << 1 \Longleftrightarrow \left|\delta_{(\vec{x})}\right| << 1 \tag{1.35}$$

holds. This is true for the early universe evolution which was describe above, but not for the late time. In the latter case, the perturbations in the matter content of the universe evolve into cosmic structures as they contract under their own gravitation. This gravitational collapse is not describable through linear theory and non-linearities need to be taken into account (see Figure 1.3). Non-linearity means that different k-modes and hence different scales are coupled now, in the differential equations which describe the time evolution of $\tilde{\delta}_{(\vec{k})}$. Structures grow from the bottom up. This means that first the smallest scales (large k-modes) gain power and subsequently larger ones. Another way of plotting the MPS and visualizing the effect of non-linearities is to define the function $\Delta_{(k)} = k^3 P_{(k)}/2\pi^2$ (Figure 1.4). This quantity has the advantage of being dimensionless. The k-modes for which non-linearities can no longer be neglected are marked by the point where $\Delta_{(k)}$ becomes larger than one. This point depends on the redshift. In the linear regime the evolution of density perturbations can be described through the Einstein-Boltzmann equations, which correspond to the Eulerian description of the dynamics of fluids.
A different approach not directly associated with one of the fluid dynamics perspective is the one of spherical collapse. Here the assumption is, that during the expansion of the universe specific regions of the matter field, which are assumed to be spherical, discontinue to participate in the expansion, and instead collapse under their self-gravitation [Zen07] [MvW10] [BT08]. This turnover happens when a certain threshold of the density perturbations $\delta_{(\vec{x})}$ is crossed. For the underlying cosmology of ΛCDM, this value is $\delta_c = 1.69$. This value is derived from the assumption of spherical collapse. For a derivation see [MvW10]. If one assumes that the amplitude of the density perturbation is a Gaussian random field in each point in space, or equivalently for each k-mode in Fourier space, then the probability density of finding a certain value of δ in a point of space, or for a k-mode in Fourier space is given by:

$$p_{(\delta_{(\vec{x})})} = \frac{1}{\sqrt{2\pi\sigma}} \cdot e^{-\frac{\delta^2_{(\vec{x})}}{2\sigma^2}} \tag{1.36}$$

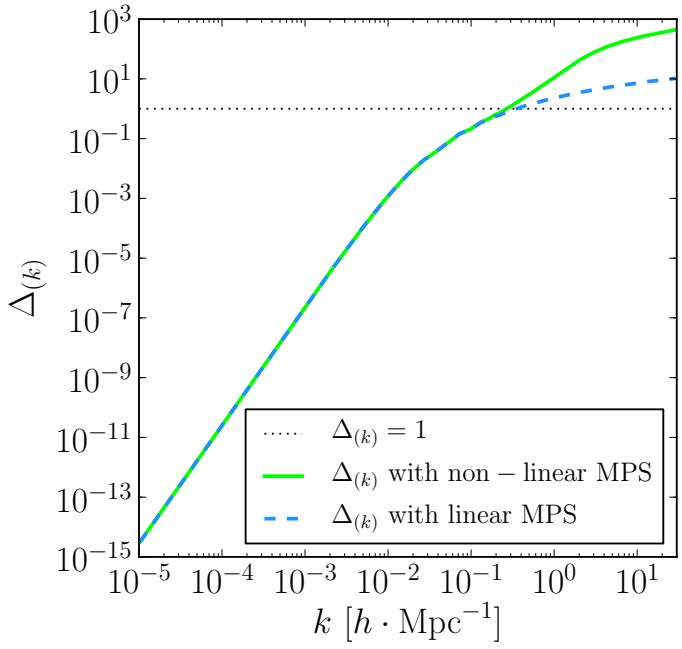

Figure 1.4: **Another way of plotting the matter power spectrum. Here the k-value above which non-linearities need to be taken into account, is marked by the point where $\Delta_{(k)} = 1$. This point depends on the redshift. In this plot the underlying MPS is the same as the one plotted in Figure 1.3, hence $z = 0$.**

From this it follows that the probability to find a collapsed object is

$$F = \int_{\delta_c}^{\infty} d\delta \, p_{(\delta_{(\vec{x})})} = \int_{\delta_c}^{\infty} d\delta \, \frac{1}{\sqrt{2\pi}\sigma} \cdot e^{-\frac{\delta^2(\vec{x})}{2\sigma^2}} \tag{1.37}$$

The first objects to collapse in this picture are the highest peaks in the density field, which are associated with the smallest scales R or conversely the smallest masses m. As the density contrast increases with time according to $\tilde{\delta}_{(a,\vec{k})} = \tilde{\delta}^{ini}_{(\vec{k})} \cdot G_{(a)}$ larger structures around these peaks will also cross the critical threshold and collapse with them. Hence, if one is interest in the question of how many structures below a fixed mass m, or correspondingly smaller than a fixed radius R, are collapsed at a certain time, one answer would be to adjust the characteristic density threshold δ_c. The second and more commonly used option, is to keep the critical value δ_c fixed to $\delta_c = 1.69$ and instead manipulate the underlying density contrast field $\delta_{(\vec{x})}$, such that all peaks (and troughs), which are thinner than the scale R of interest, which correspond to a mass m via $m = 4\pi\bar{\rho}R^3/3$ are erased. The labels R and m can hence be used interchangeably. This manipulation is done by smoothing $\delta_{(\vec{x})}$ with a top-hat window function $W_{R\,(\vec{x})} = \Theta_{(R-x)} \cdot 3/(4\pi R^3)$.

$$\delta_{m\,(\vec{x})} = \int_{-\infty}^{\infty} d^3x' \, \delta_{(\vec{x'})} \, W_{R\,(\vec{x'}-\vec{x})} \quad \Longleftrightarrow \quad \tilde{\delta}_{m\,(\vec{k})} = \tilde{\delta}_{(\vec{k})} \cdot \tilde{W}_{R\,(\vec{k})} \tag{1.38}$$

One arrives at the corresponding relation for the smoothed density contrast variance

$$\sigma_m = \xi_{m\,(0)} = \langle \delta_{m\,(\vec{x})} \delta_{m\,(\vec{x}+\vec{0})} \rangle = \langle \delta^2_{m\,(\vec{x})} \rangle = \frac{1}{(2\pi)^3} \int_{-\infty}^{\infty} d^3k \, P_{(k)} \cdot \tilde{W}^2_{R\,(\vec{k})} \tag{1.39}$$

With these quantities one can define the probability density of finding a certain value of δ_m in a point of space in analogy to (1.36)

$$F_{(m)} = p_{(\delta_{m\,(\vec{x})})} = \frac{1}{\sqrt{2\pi}\sigma} \cdot e^{-\frac{\delta^2_{m\,(\vec{x})}}{2\sigma^2_m}} \tag{1.40}$$

From this it follows that the probability of finding an object that is discontinuing to participate in the expansion of the universe and collapsing is

$$\int_{\delta_c}^{\infty} d\delta_m \, p_{(\delta_{m\,(\vec{x})})} = \int_{\delta_c}^{\infty} d\delta_m \, \frac{1}{\sqrt{2\pi}\sigma_m} \cdot e^{-\frac{\delta^2_{m\,(\vec{x})}}{2\sigma^2_m}} \tag{1.41}$$

This expression can be converted into a quantity which is directly accessible through observations the halo mass function $n_{(m)}$. It is the number density of halos with mass m, divided by the mass. Hence its units are $\mathrm{m}^{-3}\mathrm{kg}^{-1}$. With $F_{(m)}$ we have the probability of finding a halo with mass smaller than m, when multiplied with the total mass of the universe $(m_{tot} \cdot F_{(m)})$, this is nothing else but the mass, which is residing in halos of these masses. Hence first we need to subtract $F_{(m)}$ from $F_{(m+dm)}$, the probability of finding a halo with mass smaller than $m + dm$. Now we have with $F_{(m+dm)} - F_{(m)}$ the probability of finding a halo with mass m, or with $m_{tot} \cdot (F_{(m+dm)} - F_{(m)})$ the fraction of mass of the total mass of the universe which is residing in halos with mass in the interval $[m; m + dm]$. The same quantity, the fraction of mass of the total mass of the universe which is residing in halos with mass in the interval $[m; m + dm]$, is also given by $m \cdot (N_{(m+dm)} - (N_{(m)})$, where $N_{(m)}$ is the number of halos with mass smaller than m, in the universe. Hence

$$\begin{aligned} m \cdot (N_{(m+dm)} - N_{(m)}) &= m_{tot} \cdot (F_{(m+dm)} - F_{(m)}) \\ \iff N_{(m+dm)} - N_{(m)} &= \frac{m_{tot}}{m} \cdot (F_{(m+dm)} - F_{(m)}) \end{aligned} \tag{1.42}$$

It follows further with $\tilde{n}_{(m)} = \frac{N_{(m)}}{V}$

$$\tilde{n}_{(m+dm)} - \tilde{n}_{(m)} = \frac{m_{tot}}{V} \cdot \frac{1}{m} \cdot (F_{(m+dm)} - F_{(m)}) = \frac{\bar{\rho}}{m} \cdot (F_{(m+dm)} - F_{(m)}) \tag{1.43}$$

$$\begin{aligned} &= \frac{\bar{\rho}}{m} \cdot \frac{(F_{(m+dm)} - F_{(m)})}{dm} \, dm \\ \iff \frac{d\tilde{n}_{(m)}}{dm} &= \frac{\bar{\rho}}{m} \cdot \frac{dF_{(m)}}{dm} \\ &= n_{(m)} \end{aligned} \tag{1.44}$$

The number density halos of a certain mass is already a quantity which can be compared to observation, directly. However, it would be preferable to be able to compute the MPS itself. A model to achieve this by taking the halo mass function $n_{(m)}$ as one ingredient and as a second one the matter distribution within the halos, is the following, which is heavily used in current cosmological research [CS02]. The key assumption of the model is, that the two-point correlation function and hence MPS can be decomposed into a part, which describes the correlation of mass within one and the same halo $\xi_{1\,(r)}$ $(P_{1\,(k)})$ and a second part, which corresponds to correlations of masses between two different halos $\xi_{2\,(r)}$ $(P_{2\,(k)})$.

$$\xi_{(r)} = \xi_{1\,(r)} + \xi_{2\,(r)} \iff P_{(k)} = P_{1\,(k)} + P_{2\,(k)} \tag{1.45}$$

$\xi_{1\,(r)}$ $(P_{1\,(k)})$ is called 1-halo term and should dominate on small scales (large k). $\xi_{2\,(r)}$ $(P_{2\,(k)})$ is the 2-halo term accordingly and is expected to dominate on large scales (small k). Both are convolutions of the halo mass function with the halo density profiles $\rho_{m\,(r)}$. The

latter is the mass density within a halo as a function of radius. The assumption of spherical symmetry is hereby implicit, as is the premise, that the halo mass is the only parameter on which the halo profile depends on. The individual terms have the form

$$\xi_{1\,(\vec{x}-\vec{x'})} = \int_0^\infty dm\,\frac{n_{(m)}}{\bar{\rho}^2}\int_{-\infty}^\infty d^3y\,\rho_{m\,(\vec{y})}\cdot\rho_{m\,(\vec{y}+\vec{x}-\vec{x'})} \tag{1.46}$$

$$\begin{aligned}\xi_{2\,(\vec{x}-\vec{x'})} &= \int_0^\infty dm_1\,\frac{n_{(m_1)}}{\bar{\rho}}\int_0^\infty dm_2\,\frac{n_{(m_2)}}{\bar{\rho}}\cdot\\ &\quad\cdot\int_{-\infty}^\infty d^3y_1\,\rho_{m_1(\vec{x}-\vec{y_1})}\int_{-\infty}^\infty d^3y_2\,\rho_{m_2(\vec{x'}-\vec{y_2})}\,\xi_{12\,m_1,m_2\,(\vec{y_1}-\vec{y_2})}\end{aligned} \tag{1.47}$$

[MVV14] [CS02]. Correspondingly in Fourier space one has multiplications instead of convolutions

$$P_{1\,(k)} = \int_0^\infty dm\,\frac{n_{(m)}}{\bar{\rho}^2}\left|\tilde{\rho}_{m\,(k)}\right|^2 \tag{1.48}$$

$$P_{2\,(k)} = \int_0^\infty dm_1\,\frac{n_{(m_1)}}{\bar{\rho}}\int_0^\infty dm_2\,\frac{n_{(m_2)}}{\bar{\rho}}\cdot\tilde{\rho}_{m_1\,(k)}\,\tilde{\rho}_{m_2\,(k)}\,P_{12\,m_1,m_2\,(k)} \tag{1.49}$$

Here $\rho_{m\,(k)}$ is the Fourier transform of the halo density profiles

$$\begin{aligned}\tilde{\rho}_{m\,(k)} &= \int_{-\infty}^\infty d^3\vec{x}\,e^{-i\vec{k}\vec{x}}\,\rho_{m\,(\vec{y})}\\ &= 4\pi\int_0^R dx\,\frac{\sin(kr)}{kr}\,\rho_{m\,(x)}\end{aligned} \tag{1.50}$$

and $\xi_{12\,m_1,m_2\,(\vec{y_1}-\vec{y_2})}$ or correspondingly $P_{12\,m_1,m_2\,(k)}$ describe the correlation between two different halos of masses m_1 and m_2. This formalism is completely general, there are no approximations or assumptions made so far. With this mathematical description of the statistical properties of the large scale structure of the universe, theoretical predictions can be compared to observations at different levels. Either at the level of the MPS itself or, at the level of the halo mass function and halo mass profiles. For the theoretical computation of these quantities both analytical and numerical techniques have been developed as well as combinations of both. For example could the numerical result for the halo mass function be combined with an analytical prediction for the halo mass profiles.

The goal of this thesis work is the quantification of baryonic effects onto halo profiles. The latter are extracted from numerical simulations. A potential application of this is the development of a analytical model which describes how these effects change the halo profiles of pure dark matter simulations, as suggested by [ST15]. Together with a model for the mass function, this can be used to quantify how the baryonic physics affects the MPS itself. Since computational resources are limited we cannot simulate sufficient amounts of halos, such that their numbers would be representative for all mass intervals. We have therefore concentrated our computational effort onto the mass interval from which the strongest contribution is expected, to the scales of the MPS where the baryonic effects are the most important: $1\,h\,\mathrm{Mpc}^{-1} < k < 10\,h\,\mathrm{Mpc}^{-1}$ [vSBD11].
As suggested by the work of [Sel00], which is based on the halo model introduced above, the strongest contribution to the dark matter MPS in the range $k \sim 10\,h\,\mathrm{Mpc}^{-1}$ should come from halos of mass $10^{14}M_\odot h^{-1} < M < 10^{13}M_\odot h^{-1}$, and to the range $k \sim 100\,h\,\mathrm{Mpc}^{-1}$ from halos of mass $10^{12}M_\odot h^{-1} < M < 10^{13}M_\odot h^{-1}$. We have taken this result as indication and chosen to simulate halos of masses $5\times10^{12}M_\odot h^{-1} < M < 5\times10^{13}M_\odot h^{-1}$ in our study. This mass interval corresponds to halos of larger galaxy groups or the smallest

galaxy clusters, depending on the definition. The focus of this work is therefore the numerical determination of the halo mass density profiles of galaxy group halos. To achieve this we have simulated a statistically representative sample of halos in the mentioned mass range.

The MPS as well as its special cases, the power spectra of WL and CMB, are quantities which describe the clustering of matter in the universe in a statistical sense, so that our theoretical prediction about the formation of structure can be compared with them. In addition these spectra depend on the cosmological parameters which describe the composition of the universe, e.g. the energy density of baryons, dark matter and dark energy, the parameter w which describes the time evolution of the dark energy density, the number of neutrino species and their respective masses. These parameters are the numbers which quantify the composition of our cosmos and therefore influence its evolution. Determining them with sub percent uncertainties is the ultimate goal of precision cosmology.

The requirements on researchers are hereby twofold: on the instrumental side, for the experiment designers, observers and data reductionists to determine the spectra with the desired precision, and on the other side for the theoreticians to computed the spectra from the respective theories, for any given set cosmological parameters with accuracy as equally high, as reached in the observations. The basic idea is to compare the spectra calculated for given sets of parameters with the observed one, and thereby determine which parameter set gives the best fit. The key issue thereby is, that any such attempt is inconclusive, unless it is proven, that the theoretical computation of the considered spectra achieves the same sub-percent accuracy as the observations.
This thesis work is located precisely here, at this computational challenge, since we attempt to reach the same amount of accuracy in our predictions, as is achieved by the observers.

1.3 The Large Scale Structure and the Meaning of Galaxy Groups for Precision Cosmology

Our information about the large scale structure of the universe comes form observations of galaxies. Their angular positions on the sky together with their redshifts (radial positions) enabled astronomers to create three dimensional maps. The first feature of these maps which meets the eye, is that galaxies form a web like structure of filaments with large accumulations of galaxies at the nodes, where these filaments intersect and voids between them. Though on first sight galaxies appear to be isolated and spatially well separated system, their evolution is in fact influenced by their environment, which means by other neighbouring galaxies. In the regions of the cosmic web, where the galaxies accumulate they form gravitationally bound systems, which are called galaxy groups or galaxy clusters depending on the number of their member galaxies. Accumulations with less than 50 galaxies are typically called groups, the ones with more than 50 clusters. However, this definition is quite arbitrary and other categorizations by member number are common. The galaxies which are not, or not yet part of groups or clusters are called field galaxies. The accepted scenario for the evolution of the large scale structure is, that with passing time galaxies fall towards the neighbouring groups and clusters which attract them gravitationally. So that these structures grow further in number of galaxies and hence mass. This is called the hierarchical clustering scenario, or the bottom-up formation of structure. Galaxies come as different types, which are dependent on their age and interaction history with other galaxies. Typical appearances are spiral galaxies and elliptical galaxies, just to mention the two most common categories. Spiral galaxies, like the Milky Way, are younger objects which have not yet merged with other galaxies, so that their initial spiral shape is still preserved. Ellipticals on the other hand are older systems and the result of various galaxy mergers. They are the most massive types and typically found at the centres of groups and clusters. Aside from the categorization of galaxies according to their visual appearance they are also distinguished by their size. In this respect dwarf galaxies are separated, from regular sized galaxies, as systems which contain between 10^8 and 10^{11} stars. The different galaxy types also have different kinds of stars, since the star formation history depends on the diversity of the available chemical elements and with that on the age of the galaxy. The stellar composition of galaxies is however neither part of this thesis, nor is it relevant for the underlying study. Also the categorization of galaxy types is of no direct consequence for this study, references to it within this thesis are mostly for illustration purposes.

Galaxies are objects which are directly observable because the stars of which they are composed emit light. However fascinatingly, stars and hence galaxies make up only a tiny fraction of the total mass of the large scale structure. The two main contributions to the latter are actually baryonic gas with 15% and dark matter with 85%. The first one is mainly composed of hydrogen and is in its microscopic nature closely related to the stellar component, since stars form from baryons. However, in its macroscopic behaviour on astrophysical scales the baryonic gas resembles more the one of the main component dark matter. Since both of them do not form the characteristic contracted shapes of galaxies, but rather stay in a broad spherical distribution. The general picture is that both baryonic gas and dark matter form spherical structures, called halos, around the galaxies or galaxy accumulations. These halos vary in size and mass just like the amount of galaxies and stars within them. The result is a hierarchy of characteristic halo masses ranging from the halos of dwarf galaxies to the ones of the largest galaxy clusters (see Table 1.2). These structures are not exclusive, in the sense that for example a dwarf galaxy halo can be a part of a galaxy halo, or galaxy halos can be part of galaxy group or cluster halos. If that is the case one refers to these substructures as subhalos. In the context of this thesis the term halo (or subhalo) is used

to describe the entire mass accumulation under consideration, with all its components (dark matter, baryons, stars).

Table 1.2: **List of astrophysical structures relevant for cosmology and their typical halo masses. It should be noted that these categories are not defined by their masses. The listed intervals are therefore only an approximate guideline. So can for example the halo of a large elliptical galaxy be more massive, than the one of a small galaxy group.**

Object Type	Halo Mass $[M_\odot]$
Dwarf Galaxy	$< 10^{11}$
Galaxy	$10^{11} - 5 \cdot 10^{12}$
Galaxy Group	$5 \cdot 10^{12} - 5 \cdot 10^{13}$
Galaxy Cluster	$> 5 \cdot 10^{13}$

Like stars the baryonic gas also emits radiation, but only if specific conditions about the environment and the intrinsic properties of the gas are met. For example within galaxy clusters and groups the gas is hot enough ($T_{gas} \approx 10^8$K) to emit X-ray radiation, which can be observed with X-ray telescopes. This X-rays are bremsstrahlung originating in the electro-magnetic interaction of the electrons with the ions. The electrons are thereby not captured by the ions, but remain free after this scattering process. The main component dark matter can ironically only be inferred through its gravitational effect onto the luminous components, e.g. through the additional gravitational attraction that it exerts on the latter, or through the gravitational lensing effect. By applying the virial theorem to the kinematics of the galaxies within a cluster, Fritz Zwicky was able to predict the existence of dark matter first in 1933 [Zwi33]. Later in 1937 he derived methods to determine the masses of such systems, through this method and through the effect of gravitational lensing [Zwi37]. The picture which emerges from this knowledge is an infinite cosmic web of mostly dark matter which contains galaxies as biased tracers of the overall structure. The largest bound objects, galaxy groups and cluster halos, are located in the regions, where the filaments form nodes.

The cosmic web of the large scale structure may be very irregular in appearance. Nevertheless the assumption that its substructures like galaxy group and cluster halos can be treated as spherical systems, which also underlie the theory of spherical collapse introduced above, is a useful one. The information which could be added, by taking into account the general ellipsoidal nature of these structures is limited, for the statistical treatment of precision cosmology. The aim is to describe the dynamical and thermodynamical properties of the halos, like mass density or gas temperature, as functions of the distance r to the halo's centre of mass.

The most successful attempt to describe the total mass distribution within a halo was found in 1996 by Navarro, Frenk and White [NFW96], it is therefore called the NFW-model of halo mass density profiles. It is valid over a wide range of halo masses. The key assumption

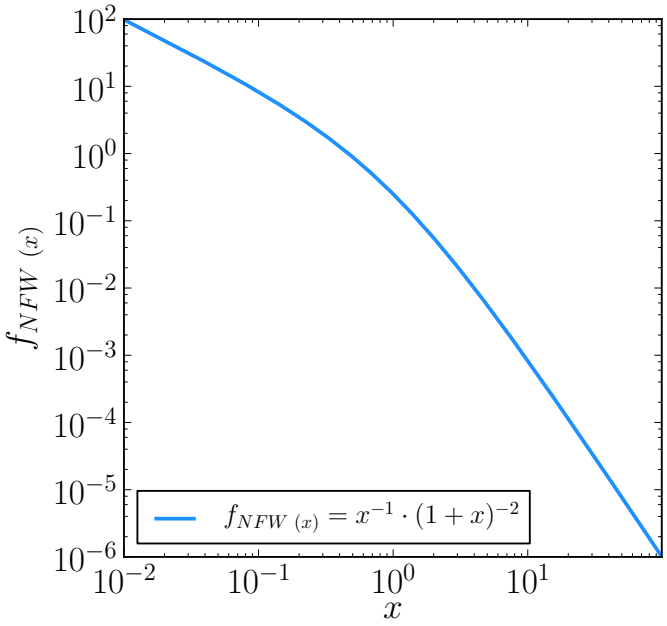

Figure 1.5: **The function of the NFW density profile.**

is that the total mass density within a halo is described by the following relation:

$$\rho_{tot\,(r)} = \frac{\rho_s}{\frac{r}{r_s}\left(1+\frac{r}{r_s}\right)^2} \tag{1.51}$$

Hence the density falls of proportional to r^{-1} near the centre and proportional to r^{-3} in the outer parts. The two crucial ingredients are the y-normalization ρ_s and the x-normalization r_s, also called the scale radius. Since the most part of the total mass of a halo is composed of dark matter, this relation is not directly comparable with observation. It was actually found by fitting profiles to results from computer simulations of halos. However the observational implications of the model, which are described below, have been confirmed countless times. For the mass of the halo it follows from the integration over the density give by the NFW-model

$$M_{tot\,(r)} = 4\pi \int_0^r dr'\, \rho_{tot\,(r')}\, r'^2 = 4\pi\, \rho_s\, r_s^3 \cdot \left[\ln\left(1+\frac{r}{r_s}\right) - \frac{r/r_s}{1+r/r_s}\right] \tag{1.52}$$

As can be seen this relation is divergent for $r \to \infty$. An additional ingredient of this model is therefore an outer radius, which defines the boundary of the halo, so that the expression for the halo mass is finite. This characteristic halo property needs therefore to be chosen by physical motivation. For matter only universes without curvature, it has been found that the radius, where the mass within the enclosed sphere equals the mass corresponding to 200 time the density of the universe is a good estimate for the virial radius of a halo.

$$\begin{aligned} M_{tot\,(r)} &= \frac{4\pi}{3} \cdot \Delta \cdot \rho \cdot r^3 \quad \text{with} \quad \Delta = 200 \\ \Longrightarrow \frac{M_{tot\,(r_{200})}}{r_{200}^3} &= \frac{3}{4\pi} \cdot \frac{1}{\Delta \cdot \rho} \end{aligned} \tag{1.53}$$

Hence inside this radius the halo can be considered as a structure in virial equilibrium. If one wants to generalize this to universes with no total curvature, which do not only contain matter one needs to choose whether to use the critical density $\rho_{cr\,(t)}$ or the average matter density $\rho_{m\,(t)}$ for the virial radius definition. Throughout this thesis the definition with the average matter density is used and the corresponding virial radius and mass of the halo are denoted with r_{200} and M_{200}, respectively. When comparison with other studies, which use different definitions, is required the corresponding Δ and density are stated. The virial mass of a halo in the NFW-model is then given by

$$M_{200} = M_{(r_{200})} = 4\pi\,\rho_s\,r_s^3 \cdot \left[\ln(1+c) - \frac{c}{1+c}\right] \quad \text{with} \quad c = \frac{r_{200}}{r_s} \tag{1.54}$$

c is called the halo concentration parameter or simply the halo concentration. Instead of r_s and ρ_s one could also use c and M_{200} to characterize a halo. The usefulness of the chosen parameters depends on the application. However, two parameters are necessary for the NFW-description. Additional models have been developed, which link the two parameters with each other, so that only one free parameter remains, which is commonly the halo mass. With only the halo mass as a remaining parameter, the NFW model can be used as mass density profile $\rho_{m\,(k)}$ in the halo model formalism introduced in Section 1.2.

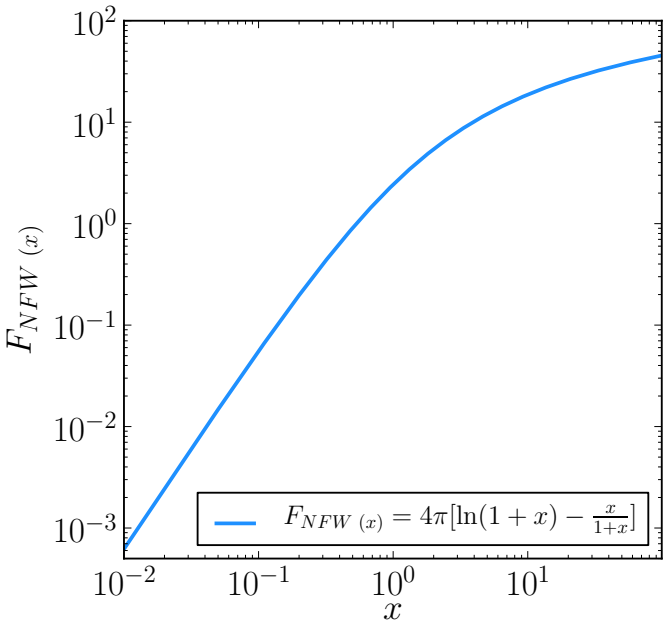

Figure 1.6: **The function of the NFW mass profile.**

To compare such a model with observations one needs to connect the analytical predictions to observable properties, e.g. the ones of the baryonic gas component within the halos. This component is called intragroup or intracluster medium (IGM or ICM), respectively. For galaxy groups and clusters its distribution can be inferred from the X-ray emissivity of the gas. This quantity is closely related to the entropy of the gas component, which in turn is given by the gas density and temperature. The key assumption which connects the total mass distribution with the mass distribution of the gas component only and also with

the thermodynamics of the gas, is the assumption of hydrostatic equilibrium. Within the constraint of spherical symmetry this condition reads

$$\frac{1}{\rho_{gas\,(r)}} \cdot \frac{dP_{gas\,(r)}}{dr} = -\frac{GM_{tot\,(r)}}{r^2} \tag{1.55}$$

In words, this equation connects the gravitational force which is felt by dark matter and baryons alike, to the gas pressure of the baryonic gas. The gas pressure originates in the random thermal motion of the gas atoms, which collide with each other, as opposed to the particles of which the dark matter consists. The picture which underlies this description is that the baryonic gas is situated in a static configuration, balancing the gravitational force, which is directed radially inward, with the gas pressure. The gravitation is caused by the dark matter as well as by the baryonic component itself. The dark matter particles cannot balance the gravitational force by pressure since they are collisionless. However because of this fact the dark matter particles do not dissipate their kinetic energy and hence have enough of their initial velocity to stay on orbits around the halos' centre (centrifugal equilibrium). For the gas however the bulk velocity with respect to the halo's centre of mass velocity can be neglected completely. The expression for the HSE, Equation (1.55), can be derived from the general equation of motion of an ideal fluid with non-zero pressure, but zero viscosity, experiencing an additional force. In the underlying case the ideal fluid is the baryonic gas and the additional force is gravitation. This equation is the momentum conservation equation of the Euler equations of hydrodynamics, which correspond to Newton's second law $F = ma$, for the case of a point mass. In its most general form it can be written as

$$\frac{\partial}{\partial t}(\rho_{(r)} \cdot v_{i\,(r)}) + \nabla_j(\rho_{(r)} \cdot v_{j\,(r)} \cdot v_{i\,(r)}) + \nabla_i P_{(r)} = -\nabla_i \Phi_{(r)} \cdot \rho_{(r)} \tag{1.56}$$

which reads for the r-component in spherical coordinates

$$\frac{\partial \dot{r}}{\partial t} - \frac{(r\,\dot{\theta})^2}{r} - \frac{(\sin\theta\, r\,\dot{\phi})^2}{r} + \vec{v} \cdot \nabla \dot{r} + \frac{1}{\rho_{(r)}} \cdot \frac{dP_{(r)}}{dr} = -\frac{GM_{(r)}}{r^2} \tag{1.57}$$

Expression (1.55) follows after setting all terms which involve time derivatives to zero, so that the static special case is found.

To compare theory with observation, the next step is to find a solution for the gas pressure and density as a function of radius, in Equation (1.55), where the total mass is given by the NFW-model. For hydrogen the assumption of an ideal gas with no additional degrees of freedom is valid. Here the thermodynamic quantities of interest, density, pressure and temperature are related via the ideal gas equation:

$$P = \frac{k_B}{m_H} \cdot \rho \cdot T \tag{1.58}$$

Having a solution for two of them hence fixes the third one. The ideal gas relation alone however cannot help to solve the HSE equation (Equation (1.55)). A physically well motivated assumption is hence

$$P_{gas\,(r)} \propto \rho^{\Gamma}_{gas\,(r)} \tag{1.59}$$

[KS01]. The following parametrisation with $f_{(0)} = 1$ fulfils this requirement

$$T_{gas\,(r)} = T_0 \cdot f_{(r)} \tag{1.60}$$

$$\rho_{gas\,(r)} = \rho_0 \cdot f_{(r)}^{\frac{1}{\Gamma-1}} \tag{1.61}$$

$$P_{gas\,(r)} = P_0 \cdot f_{(r)}^{\frac{\Gamma}{\Gamma-1}} \tag{1.62}$$

as can easily be verified by substituting these expression into Equation (1.58). Inserting Equations (1.61) to (1.62) into Equation (1.58) gives, the relation between the constants

$$P_0 = \frac{k_B}{m_H} \cdot \rho_0 \cdot T_0 \tag{1.63}$$

Substituting Equations (1.61) and (1.62) into the HSE equation gives after taking the derivative

$$\frac{P_0}{\rho_0} \cdot \frac{\Gamma}{\Gamma - 1} \cdot \frac{df_{(r)}}{dr} = -\frac{GM_{tot\,(r)}}{r^2} \tag{1.64}$$

Separating the variables f and r and integrating leads to

$$\frac{P_0}{\rho_0} \cdot \frac{\Gamma}{\Gamma - 1} \int_{f_{(0)}}^{f_{(r)}} df = -\int_0^r dr' \, \frac{GM_{tot\,(r')}}{r'^2} \tag{1.65}$$

The integral on the right hand side is found after inserting the NFW mass

$$\int_0^r dr' \, \frac{GM_{tot\,(r')}}{r'^2} = 4\pi \cdot G \cdot \rho_s \cdot r_s^2 \left[\frac{\ln(1 + r'/r_s)}{r'/r_s} \right]_0^r \tag{1.66}$$

Together with the left hand side one finds

$$\frac{k_B}{m_H} \cdot T_0 \cdot \frac{\Gamma}{\Gamma - 1} \cdot (f_{(r)} - \underbrace{f_{(0)}}_{=1}) = 4\pi \cdot G \cdot \rho_s \cdot r_s^2 \cdot \left(\frac{\ln(1 + r/r_s)}{r/r_s} - \frac{\ln(1 + 0/r_s)}{0/r_s} \right) \tag{1.67}$$

It can be shown with l'Hopital's rule that the second term in the brackets on the right hand side equals one. With the same rule follows that the first term in the brackets on the right hand side goes to zero at infinity. With the assumption that $f_{(r)}$ also goes to zero at infinity, the equation would be fulfilled for $r \to \infty$, when

$$-\frac{k_B}{m_H} \cdot T_0 \cdot \frac{\Gamma}{\Gamma - 1} = -4\pi \cdot G \cdot \rho_s \cdot r_s^2 \tag{1.68}$$

inserting this into Equation (1.67) directly gives

$$f_{(r)} = \frac{\ln(1 + r/r_s)}{r/r_s} \tag{1.69}$$

which is indeed zero at $r = \infty$.

To summarize, we have found the functional dependence of gas temperature, density and pressure of r, for the assumption (1.59)

$$T_{(r)} = T_0 \, \frac{\ln(1 + r/r_s)}{r/r_s} \tag{1.70}$$

$$\rho_{(r)} = \rho_0 \, \frac{\ln(1 + r/r_s)^{\frac{1}{\Gamma - 1}}}{r/r_s} \tag{1.71}$$

$$P_{(r)} = P_0 \, \frac{\ln(1 + r/r_s)^{\frac{\Gamma}{\Gamma - 1}}}{r/r_s} \tag{1.72}$$

the temperature normalization is also determined already by the HSE, the NFW mass profile and the behaviour at infinity

$$T_0 = \frac{4\pi \cdot G \cdot \rho_s \cdot r_s^2 \cdot m_H}{k_B} \cdot \frac{\Gamma - 1}{\Gamma} \tag{1.73}$$

An additional constraint is still required to determine the normalization of either the gas density or the gas pressure profile. After one of them is fixed the other one follows from Equation (1.63). Two possible normalization for the gas density are

$$M_{gas}(r_{200}) = \frac{\Omega_b}{\Omega_m} \cdot M_{tot}(r_{200}) \quad \text{or} \quad \rho_{gas}(r_{200}) = \frac{\Omega_b}{\Omega_m} \cdot \rho_{tot}(r_{200}) \tag{1.74}$$

Also the polytropic index Γ is not yet determined by the underlying assumptions. The here introduced model is used to compare the numerical results of this thesis work to an analytical prediction.

The focus of this work is the distribution of mass within galaxy group size halos. It is therefore elementary to take a closer look onto the physical properties of this specific category of the cosmological structures and onto the properties of the galaxies which it comprises. To illustrate the typical distances in cosmology and astrophysics of galaxy accumulations it is best to start in the environment of the Milky Way.

As already mentioned above, galaxy groups are distinguished from galaxy clusters by the number of member galaxies, which is less than 50. From below, there is also the requirement that an accumulation must contain more than two galaxies, to be a group. Most of the observable galaxies in the local universe are members of galaxy groups. The typical diameter of such an accumulation lies between 0.2 Mpc and 2 Mpc. Velocities of galaxies with respect to the groups' centres of masses are typically of the order of a few hundred km/s.

The Milky Way, whose diameter is estimated to be between 31 and 55 kpc. is also a member of a group of galaxies, called the Local Group. This group, has a diameter of roughly 2 Mpc and consist of 3 galaxies and more than 50 dwarf galaxies. The most prominent members, aside from the Milky Way itself, are the neighbouring Andromeda Galaxy (also known as M31) and the Triangulum Galaxy (also known as M33). Both of them are spiral galaxies, like the Milky Way. Andromeda, the largest galaxy of the local group, is located 780 kpc away from the Milky and the Triangulum Galaxy, the third largest in the group, is situated 940 kpc away from the Milky way. Andromeda has 10^{12} stars and the Triangulum Galaxy has $4 \cdot 10^{10}$, while for the Milky the estimates lie between 10^{10} and $4 \cdot 10^{11}$ stars. Andromeda and the Milky Way currently move towards each other with 120 km/s relative velocity and are expected to merge in 4.5 billion years. The Milky way itself is the second largest member and accompanied by two larger satellite dwarf galaxies, the Large and Small Magellanic Clouds, in orbits at 50 kpc and 60 kpc distance, respectively. They are the fourth and fifth largest group members. All the five mentioned galaxies have roughly the same distance to the groups centre of mass, around 0.5 Mpc. The total mass of the local group is estimated to be $5 \cdot 10^{12} M_\odot$ (see [BT08] p.762).

Next to the local group are a few neighbouring galaxy groups within a radius of around 10 Mpc:
- the sculptor group at 3.9 Mpc distance with 11 member galaxies and an estimated total mass of $2 - 3 \cdot 10^{10}\, M_\odot$ [Kar05]
- the Centaurus A group at 3.66 Mpc with 28 galaxies and an estimated total mass of $3 - 5 \cdot 10^{10}\, M_\odot$ [Kar05]
- the M81 group at 3.6 Mpc with 29 galaxies and an estimated total mass of $10^{12}\, M_\odot$ [Kar05]

One loosely distinguishes between open and closed galaxy groups, to describe how virialised they are. Closed groups are well virialised systems, which are already decoupled from the cosmic expansion, so that the dynamics of their member galaxies and dark matter halo

is mainly determined by their self-gravity. These systems are hence very spherical and can mostly be found at the nodes of the cosmic web. Open groups on the other hand are at the initial stages of the gravitational collapse and currently decoupling from the cosmic expansion. They are therefore far from virialised and their shape is not spherical but rather elongated or ellipsoidal. These open groups are most likely found in the filaments of the cosmic web, or an individual open group itself is considered a filament. One such example is the above mentioned sculptor group, which is a filament, that is stretched along the line-of-sight, as seen from Earth.
Two special categories of galaxy groups are: compact groups and fossil groups. Compact groups are accumulations of a small number of galaxies, around five for example. An example is Stephan's Quintet at a distance of 100 Mpc (see Figure 1.7). Fossil groups are groups which have already form very early and are now in final state of group evolution, where all the galaxies have merged into a giant elliptical galaxy at the groups' centre. Eventually a few dwarf galaxies might still be in satellite orbits.

Figure 1.7: **The compact galaxy group Stephan's Quintet at roughly 100 Mpc distance from the Milky Way. It actually consists of only four galaxies since NGC 7320 (upper left), turned out to be a foreground galaxy at 12 Mpc distance from the Milky Way. The member galaxies are the barred spiral NGC 7319 (top right), next to it the two colliding galaxies NGC 7318A and NGC 7318B (image centre) and the elliptical galaxy NGC 7317 (lower left). The picture is taken in the visible and near-infrared light, with the Wide Field Camera 3 of the Hubble Space Telescope (HST). Image Credit: NASA/Hubble Space Telescope.**

The galaxy cluster which is located closest to the Milky Way is the Virgo Cluster at 16.5 Mpc distance. It is estimated to have a total mass of $1.2 \cdot 10^{15}\, M_\odot$ and to comprise around 1500 galaxies. Another galaxy cluster, even larger than the Virgo Cluster, is the Coma Cluster at roughly 100 Mpc distance. It contains more than 1000 galaxies and its total mass

is estimated to be $7 \cdot 10^{14}\, M_{\odot}$. It is the cluster whose galaxy kinematics led Fritz Zwicky to predict the existence of the dark matter component [Zwi33].

Clusters and groups themselves are gravitationally bound in superclusters. So is the Local Group together with the other above mentioned galaxy groups, the Virgo Cluster and several other galaxy clusters and groups, part of the Virgo Supercluster. The supercluster closest to the Virgo Supercluster is the Coma Supercluster at 92 Mpc distance, which contains the Coma Cluster and other galaxy accumulations. The information about the cosmological environment of the Earth is from [CO07] and wikipedia.org.

The masses of cluster and groups can be determined through the following methods:

1. The kinematics of the galaxies: When the velocity of a galaxy within a cluster can be determined, the gravitating mass corresponding to this velocity can be inferred.
2. X-ray emissions from the intragroup or intracluster medium: since the IGM/ICM is emitting X-ray radiation, its distribution within the group or cluster can be determined. Through the HSE equation (Equation 1.55), which can be rearranged to

$$M_{tot\,(r)} = -\frac{k_B\, T_{gas\,(r)}\, r}{G\, m_H} \cdot \left(\frac{d \ln \rho_{gas\,(r)}}{d \ln r} + \frac{d \ln T_{gas\,(r)}}{d \ln r} \right) \tag{1.75}$$

the total mass within the radius r can be calculated for different radii. This method has the potential flaw, that the group or cluster under consideration might not be in hydrostatic equilibrium. This would mean that a part of the pressure support to balance the gravitation is of non-thermal origin, arising from macroscopic random motion.
3. Gravitational lensing: The mass within a group or a cluster causes a deflection of the light emitted from galaxies behind the considered system. These source galaxies are hence located further away, than the considered group or cluster and may belong to different groups and clusters.
4. Sunyaev-Zel'dovich effect: The electrons of the intragroup or intracluster medium can interact electro-megnetically with the photons of the CMB through the inverse Compton scattering effect. In this inelastic scattering process an electron transfers energy to a photon, as opposed to the Compton effect itself, where the photon transfers energy to the electron in the collision. The modified energy of the CMB photons results in a small deviation from the CMB's black body spectrum in the direction of the galaxy cluster. This deviation is detectable, so that position and size of galaxy clusters can be inferred.

Because in the bottom-up scenario of structure formation smaller structures assemble earlier than larger ones. Galaxy groups should have had more time to collapse than clusters, which have begun their collapse later. Hence, galaxy groups are expected to be more concentrated than clusters. Subtle difference like these show that groups are not exactly scaled down versions of clusters.

2 Numerical Techniques and the Importance of Simulations on High Performance Computers

2.1 Overview

As described above the theoretical prediction in cosmology is done by solving the equations of the underlying theory, for a given set of cosmological parameters. In this context the application of numerical techniques is inevitable.
In the early universe the perturbations in the cosmic matter density were still small, and their evolution can be described with linear methods. This allows to solve the equations with relatively modest numerical effort, e.g. to carry out the computations on a desktop computer, or even invoke semi-analytical techniques. At later times of redshifts around $z = 100$ or $z = 50$ however, when the universe had reached 1-2% of its current size, non-linearities can no longer be neglected as the cosmic matter perturbations grew into structures through their self-gravity. Since the non-linear terms have to be kept in the differential equations relevant for the evolution of the statistical quantities, like the MPS, solving these equations analytically or numerically becomes impossible. It is at this point ($z = 100$ or $z = 50$) easier to sample the phase space of the matter field (dark matter and baryons) in the universe with particles or fluids in real space, and evolve them forward in time, according to the equations of motion, by which they are characterized. The numerical description of the evolution of these structures requires simulations on high performance computer clusters, where the computations are performed on several hundred or thousand processors in parallel. The essential methods of the numerical technique are described in the following.

Linear theory provides the initial conditions for the simulations, since as mentioned above it is valid in the early universe. The actual simulation starts hence at a cosmic time, when the universe had 1-2% of its current size. The initial matter density and velocity field are transformed into positions and velocities of particles in a cubic simulation volume representing the cosmological matter content. For simulations, as required for our project, typical values for simulation volume side length and particle number are: 100 Mpc and 20 million particles. The equations of motion of this N-body system are solved, and hence the particle configuration advanced forward in time in a number of discrete time steps. When the simulation reaches the cosmic epoch of the present it is terminated and its final state is analysed and quantified, in order to be compared with observation.

The crucial ingredient in such endeavours is what was called equations of motion (EOM). In other words it is the amount of physical principles which enters into the simulation project and hence a measure for how good the simulation mimics the real universe.
The simplest approach is to describe all particles as interacting with each other only through the gravitational force, hence their EOM being the laws Newtonian gravity. This gives a satisfactory description of the dark matter component, but not of the baryonic one, since baryons interact with each other also through the electro-magnetic force. Nevertheless, since dark matter makes up 80% of the total matter budget, this numerical approximation still gives a good description, and has been an important tool for physicist in the understanding of the cosmological structure formation, over the past decades.
The next step is to implement a realistic description of the baryonic component which takes into account its electro-magnetic interaction and not only the gravitational part. Therefore baryons are modelled as a fluid with non-zero pressure. Hence their equations of motions are the ones of hydrodynamics, which is a concept found in many branches of physics. Describing the more complex baryonic component in this way introduces the necessity to implement further physical processes which are not accounted for by hydrodynamics, such as cooling

and heating via radiation transfer, star formation, supernovae, galaxy physics and black holes. While hydrodynamics in its simplest form was successfully implemented into cosmological simulations already in the last decade of the previous century, the complex baryonic processes mentioned above are pioneering works of physicist in the 21st century.
In contemporary research of astrophysics and cosmology, the numerical modelling of feedback processes in galaxies with black holes at their centre, known as Active Galactic Nuclei (AGN), is among the most important open issues.

This process is expected to resolve the mismatch, between observations and simulations of galaxy groups and galaxy clusters. In both types the galaxies (which consist of stars) make up only 1% of the total mass. Another 9-10% is contributed by baryons and distributed close to spherically symmetric in the system. This component is the aforementioned intracluster or intragroup medium, respectively, and consist mostly of ionized hydrogen gas. The main contribution (90%) however is dark matter, which is also distributed spherically symmetric. Observers have detected, via galaxy and X-ray astronomy, much fewer stars and much less hydrogen gas in these systems, as numerical simulations predict. The assumption is that the problem can be solved, if feedback processes are implemented in the simulations because these are believed to be responsible for quenching the formation of stars and to push baryons out of groups and clusters, so that observations are met. Implementations of supernova feedback (gas pressure arising from star explosions) have been successful in this attempt for systems with less than 10^{12} solar masses. For larger accumulations, namely galaxy groups and clusters, the power from this kind of feedback process is not sufficient, however and a different feedback mechanism is proposed, namely Active Galactic Nucleus feedback. This is in essence radiation and gas pressure arising from accretion disks around super massive black holes in the centres of galaxies.

Time and computational resources of many research groups around the world are devoted to this topic specifically, at the time of writing. This thesis project is among them.

2.2 Initial conditions

As was already mentioned above the starting point for doing inhomogeneous cosmology, is the initial MPS which is proportional to k. From there the cosmological perturbations can be evolved in time numerically, with a modest computational effort, to a time of around $z = 50$ or $z = 100$. At this time the necessity for the application of the linear theory, $\left|\delta_{(\vec{x})}\right| << 1$, brakes down. The linearised Boltzmann equations describe the time evolution of the cosmological perturbations in k-space during the mentioned time interval. They are for the collisionless dark matter component

$$\frac{\partial \delta_{c\,(\vec{k},t)}}{\partial t} - ik \cdot \frac{1}{a} v^i_{c\,(\vec{k},t)} + 3 \cdot \frac{1}{c^2} \frac{\partial \Phi}{\partial t} = 0 \tag{2.1}$$

$$\frac{\partial v^i_{c\,(\vec{k},t)}}{\partial t} + H \cdot v^i_{c\,(\vec{k},t)} - \frac{1}{a} ik \cdot \Psi = 0 \tag{2.2}$$

and for the collisional baryonic component

$$\frac{\partial \delta_{b\,(\vec{k},t)}}{\partial t} + ik \cdot \frac{1}{a} v^i_{b\,(\vec{k},t)} + 3 \cdot \frac{1}{c^2} \frac{\partial \Phi}{\partial t} = 0 \tag{2.3}$$

$$\frac{\partial v^i_{b\,(\vec{k},t)}}{\partial t} + H \cdot v^i_{b\,(\vec{k},t)} + ik \cdot \frac{1}{a} \Psi = \frac{4}{3} \frac{\rho_\gamma}{\rho_b} \cdot n_e \cdot \sigma_T \cdot (v^i_{\gamma\,(\vec{k},t)} - v^i_{b\,(\vec{k},t)}) \cdot c \tag{2.4}$$

[MB95] [Dod03] (n_e = particle density of the electrons, σ_T = Thomson cross section, ρ_γ and v_γ = photon energy density and photon velocity).
Because of the linearity of the equations they do not mix different k modes and can be integrated, for one k value at a time [MB95]. The Gaussian nature of the density perturbation is kept throughout the linear time evolution. This method was developed by Ma and Bertschinger in 1995 (see the previous reference). Subsequently codes with refined methods to solve the Boltzmann equations have been developed: CMBFAST in 1996 by Seljak and Zaldarriaga [SZ96] and its successor CAMB by Lewis and Challinor [LC11]. The result of these codes is the transfer function $\tilde{T}_{(k)}$ or likewise the MPS at the desired redshift. This quantity contains all the information about the inhomogeneities arising from the chosen set of cosmological parameters. There is also the possibility to analytically fit the transfer function $\tilde{T}_{(k)}$, as suggested by Bardeen, Bond, Kaiser and Szalay (BBKS) in 1986 [BBKS86] or Eisenstein and Hu in 1998 [EH98a]. To begin the simulations of the non-linear evolution, this statistical quantity needs to be transformed into the density contrast field $\delta_{(\vec{x})}$ of the cosmological volume which is to be simulated.
At this point the actual work of the initial condition generating code begins. To draw a concrete realization of the universe from the underlying cosmological model, white noise needs to be added to the MPS either by multiplying in Fourier space or by a convolution in real space [PPA$^+$08] [HA11]:

$$\tilde{\delta}_{(\vec{k})} = \sqrt{\tilde{T}_{(k)}} \cdot \tilde{\mu}_{(k)} \quad \text{or} \quad \delta_{(\vec{x})} = \sqrt{T_{(x)}} * \mu_{(x)} \tag{2.5}$$

The requirement is thereby that the average over all $\vec{k}$-modes, for given absolute value of k, gives back the original MPS. In the first case the Fourier transform of the obtained $\vec{k}$-modes to real space has to be done, to arrive at the density contrast field for the simulation volume. In the second case, the Fourier transform of the transfer function to real space needs to be done. The latter option is applied in the MUSIC (MUlti Scale Initial Conditions) [HA11] code for initial conditions of cosmological simulations developed by Oliver Hahn and Tom Abel. All the simulation initial conditions used in this thesis were generated and computed

with this code. For the transfer function the underlying version of MUSIC allowed for selecting the CAMB code for its computation, or to use the analytical transfer function fit by either BBKS or Eisenstein and Hu. For this thesis work the fit from Eisenstein and Hu was chosen.
For the resulting density contrast field $\delta_{(\vec{x})}$ the argument $\vec{x}$ covers the entirety of the volume, that is to be simulated. For cosmological simulations this volume is typically cubical, and has a side length of the order of 100 Mpc (comoving), in the case of this thesis $V = 100\,\mathrm{Mpc}\ h^{-1} = 147\,\mathrm{Mpc}$. If the simulations work with the Eulerian perspective, then the density contrast field can already be used as the initial conditions for the simulation. If however the Lagrangian perspective is applied then the density contrast $\delta_{(\vec{x})}$ needs to be converted into particle positions and velocities, which are then the initial conditions of the simulation. For this purpose the Lagrangian perturbation theory is applied [Bou96] [BCGS02] [HA11].
The idea of this approach is that the simulation volume is probed with equidistantly placed particles with zero velocity, which hence form a grid. These particles are then displaced and given a velocity, which reflect the initial perturbation field $\delta_{(\vec{x})}$. This is achieved in the following way:
Consider a particle at initial grid position $\vec{x}$. Its time evolution can be described through the displacement field $\vec{L}_{(\vec{x},t)}$, which depends on the initial density perturbation field $\delta_{(\vec{x})}$, such that

$$\vec{x}'_{(t)} = \vec{x} + \vec{L}_{(\vec{x},t)} \quad \text{and} \quad \dot{\vec{x}}'_{(t)} = \frac{d}{dt}\vec{L}_{(\vec{x},t)} \tag{2.6}$$

where in first order the displacement field is given by the growth factor and the gradient of the initial gravitational potential $\phi_{(\vec{x})}$ generated by the density perturbation field [Bou96] [BCGS02] [HA11]

$$\vec{L}_{(\vec{x},t)} = \frac{G_{(t)}}{4\pi\, G\, \rho_{m\,(t)}\, a^2_{(t)}} \cdot \nabla\phi_{(\vec{x})} \tag{2.7}$$

$\phi_{(\vec{x})}$ and $\delta_{(\vec{x})}$ are related by the Poisson equation [Bou96] [BCGS02] [HA11] [Dod03]

$$\Delta\phi_{(\vec{x})} = -4\pi\, G\, \rho_{m\,(t)}\, a^2_{(t)}\, \delta_{(\vec{x})} \tag{2.8}$$

The particles are hence displaced parallel to the gradient of the gravitational potential, and also their velocities point in this direction. At this step non-Gaussianities have been introduced to the particle positions and velocities.
In second order the displacement field in Equation (2.6) is given by

$$\begin{aligned} \vec{L}_{(\vec{x},t)} \quad = \quad & \frac{G_{(t)}}{4\pi\, G\, \rho_{m\,(t)}\, a^2_{(t)}} \cdot \nabla\phi_{(\vec{x})} + \\ & + \frac{G_{2\,(t)}}{4\pi\, G\, \rho_{m\,(t)}\, a^2_{(t)}} \cdot \sum_{i,j} \left[\left(\frac{\partial^2}{\partial q_i^2}\phi_{(\vec{x})} \right) \cdot \left(\frac{\partial^2}{\partial q_j^2}\phi_{(\vec{x})} \right) - \left(\frac{\partial}{\partial q_i}\frac{\partial}{\partial q_j}\phi_{(\vec{x})} \right)^2 \right] \end{aligned} \tag{2.9}$$

here $G_{2\,(t)} \simeq 3/7 \cdot G^2_{(t)}$ [Bou96] [BCGS02] [HA11].
The displacement field in this second order approach contains second order derivatives of the gravitational potential. The particle displacements and velocities are now parabolic.
To summarize, the input for the Lagrangian perturbation theory is the density contrast field $\delta_{(\vec{x})}$ within the cubical simulations volume. In both cases of first and second order Lagrangian perturbation theory, the results are the values of the particles' positions and velocities within the simulations volume, which are then used as the initial conditions for the simulations. These perturbations no longer inherit their primordial Gaussian nature which was kept throughout the linear evolution of the Boltzmann equations.

So far the description of the computation of the initial conditions held for a single fluid, which in the case of a ΛCDM-model is the dominant dark matter. For a simulation which only contains the collisionless dark matter component, this information is already adequate. Even for simulation, where both dark matter and baryons are modelled separately the dark matter only initial conditions can be used to initialize both species in the simulation. For the baryonic component which is modelled in the Eulerian perspective the density contrast field $\delta_{(\vec{x})}$ which comes out of the transfer function is therefore used. In principle however baryons and dark matter have differing perturbation spectra. The difference becomes apparent particularly at high redshift, where the baryon perturbations do not yet follow the dark matter ones exactly. It is therefore desirable to compute the transfer function for a two-component fluid (dark matter + baryons), which then gives separate density contrast field for both species. In this case the perturbations in the baryon and dark matter velocities also need to be computed from the Boltzmann equations, so that a corresponding transfer function can be found for each species' velocity perturbations. The result of the inclusion of baryons at the linear level is hence the density perturbation field for baryons in addition to the one for the dark matter, and velocity perturbation fields for the three components of the baryon velocity. To the latter the Lagrangian perturbation theory formalism introduced above can be applied to introduce non-Gaussianities.

Dark matter positions and velocities, as well as the baryon velocity perturbation fields, contain the non-Gaussian information of non-linear evolution through the application of the Lagrangian perturbation theory (likewise first or second order). The baryonic density perturbation field however is untouched by this process and still in the Gaussian state, in which it came out of the linear Boltzmann equations evolution. This is a principle inconsistency even though a small one. The solution is to mimic the effect of the Lagrangian perturbation theory for the grid of the baryon density perturbation field. By making use of mass conservation one finds the following identity between a mass element in the initial grid and the corresponding one in the displaced particle field

$$\begin{aligned} \rho_{(\vec{x}',t)} d^3x' &= \rho_{(\vec{x})} d^3x \\ &= \bar{\rho}\, d^3x \end{aligned} \tag{2.10}$$

since the coordinates are related through the Jacobian matrix

$$\begin{aligned} d^3x' &= \left|\frac{\partial x_i'}{\partial x_j}\right| d^3x \\ \Longrightarrow \rho_{(\vec{x}',t)} \left|\frac{\partial x_i'}{\partial x_j}\right| d^3x &= \bar{\rho}\, d^3x \end{aligned} \tag{2.11}$$

it follows for the denity at $\vec{x}'$

$$\rho_{(\vec{x}',t)} = \frac{\bar{\rho}}{\det\left(\delta_{ij} + \frac{\partial L_i}{\partial x_j}\right)} \tag{2.12}$$

This is called the local Lagrangian approximation (LLA) [HA11]. The most precise and consistent procedure is hence to compute the initial condition with second order Lagrangian perturbation theory and LLA. The latter one can however be neglected, as it does not change the initial density field considerably. And neither does including the baryons into the computation of the transfer function. For the default model of this work, both have therefore been omitted. We show in Section 3 that this choice is justified.

2.3 Numerically modelling the dark matter component

2.3.1 Overview

Dark matter is the most important component in cosmological simulations, as it dominates the matter content of the universe with 85%. Fortunately its physical nature is also the simplest one to model, since dark matter is only interacting through gravitation, with itself and with the other species. In particular it is collisionless and hence pressureless. Further it does not participate in the electro-magnetic interaction. A possible participation in the weak interaction or another unknown force can neither be ruled out nor confirmed with current astrophysical observations. Beyond these aspects, dark matter can also be considered non-relativistic, since the average peculiar velocities, which the dark matter particles inherit from the initial cosmic plasma, are much smaller than the speed of light. No elementary particle interaction through which dark matter particles could annihilated or decay into other particles, has been observed to this date.
Numerically it is therefore straight forward to model the dark matter in a simulation as a fixed number of particles (denoted by n) which is given by the cosmic dark matter density, the simulation volume and the resolution. Hence, if a simulation is run which contains only the dark matter component, which is justified approximation as mentioned above, one is confronted with the classical n-body problem: the gravitational acceleration of the i-th particle is determined by the positions and masses of all the other $n-1$ particles in the simulation.

$$\begin{aligned} \frac{d^2\vec{x}_i}{dt^2} &= -\nabla\Phi_{(\vec{x},t)} \\ \Longleftrightarrow \vec{g}_i &= -\sum_j Gm_j \frac{\vec{x_j} - \vec{r}_i}{|\vec{x_j} - \vec{x}_i|^3} \end{aligned} \tag{2.13}$$

This second order differential equation in time, needs to be integrated twice in order to obtain the desired quantity $x_{i\,(t)}$, the trajectory of the i-th particle. To tackle this problem numerically the first step is to write this second order differential equation as two first order differential equations:

$$\frac{d\vec{x}_i}{dt} = \vec{v}_i \quad \text{and} \quad \frac{d\vec{v}_i}{dt} = -\nabla\Phi_{(\vec{x}_i,t)} \tag{2.14}$$

These can be integrated numerically by choosing a time step Δt, as will be described below. The most direct approach to calculate the acceleration $\vec{g}_i$ of the i-th particle would be to carry out the sum over the $n-1$ other particles in (2.13) to obtain the gravitational potential. This has to be done for all n particles, so that $1/2 \cdot n \cdot (n-1) \simeq n^2$ operations are necessary. For a typical particle numbers like $n = 10^7$ as they are required for most astrophysical and cosmological situations, the number of operations ($n^2 = 10^{14}$) is therefore to large for the computational resources.
For this reason algorithms have been developed by astrophysicists which approximate the computation of the gravitational potential and with that reduce the number of required operations. The two main ones are described in the following.

2.3.2 Tree Codes

The basic idea is to compute the gravitational potential, which is experienced by the i-th of all the n particles, not as the sum over all $n-1$ other particles, but instead to group together particles which are further away from the i-th one and calculate the contribution to the gravitational potential of these groups. In the simplest case this can be done by using the centre of mass of such a particle group as the group position and the sum of the particle masses as the total mass. In a more sophisticated version of the method, the

information about the mass distribution within a group can be retained by treating it as a low order multipole expansion and then calculate the group's contribution to the gravitational potential from it.
The question is now: how can the particles be grouped together. This is done by dividing the simulation volume into eight equal sub-cubes with half its side length, some containing particle others eventually not. If one of these eight sub-cubes contains more than one particle, it is subdivided again into eight equal sub-cubes with side length of 1/4 of the simulation volume. This process is continued till each of these sub-cubes contains only one particle. The result is a hierarchy of sub-cube levels, which is called a tree. The entire simulation volume itself is the root or trunk and the subsequent levels are branches or twigs, till finally the sub-cubes which contain only one particle are called leaves.
Once this tree is constructed, one can go through the different levels starting from the eight sub-cubes of the total volume. The size of a sub-cube divided by the distance of the sub-cube from the i-th particle, is roughly the opening angle which the sub-cube subtends as seen from the i-th particle's positions. This opening angle serves as an accuracy criterion. At each tree level in the hierarchy, starting from the eight sub-cubes of the total volume, the opening angle of each of these sub-cubes can be checked. If it is smaller than the applied accuracy criterion, then the contribution to the gravitational potential is calculated for the entire sub-cube, by making use of the information of the group of particles in this sub-cube in the way described above. The information about subsequent sub-cubes contained in this one is no longer required. If however the opening angle is larger than the applied accuracy criterion, then the eight sub-cubes of the considered sub-cube will be checked likewise in the next level. This process goes on till all particles are accounted for in the calculation of the gravitational potential for the i-th particle, either as members of sub-cubes which have fulfilled the accuracy criterion at some level in the hierarchy, or as individual particle in a leave cell. In the latter case the contribution of the particle to the potential is the same as in the direct summation. To obtain the gravitational acceleration for each of the n particles only $n \cdot \ln(n)$ operations are necessary.
Important references on the numerical method of tree codes are [BH86], [BH88] and [Yep97].

2.3.3 Particle-Mesh (PM) Codes

The idea of a particle mesh code is that the masses of all particles in the simulation are assigned to the cells of a Cartesian grid which covers the simulation volume. The result is a discrete mass density map, from which the gravitational potential at each cell can be calculated through the Poisson equation.
The grid itself can be regular, or adaptively refined in high density regions. For the assignment of the particle masses to the grid cells several opportunities exist. E.g. could a particle's mass simply be associated with its nearest grid cell. This is called the nearest grid point method (NGP). Or it can be projected onto a cubical volume with homogeneous density which is centred at the particle's position and has the side length of a grid cell. That way the particle's mass is distributed over eight grid cells, in the general case. This method is called cloud in cell (CIC). Mass assignment schemes with more complicated spacial dependence are possible, such that a whole hierarchy of possibilities exist.
Once the particle masses are assigned to the grid, the Poisson equation for the resulting discrete density field can be solved with the discrete Fourier transform.

$$\Delta\Phi_{(\vec{x},t)} = 4\pi G\,\rho_{(\vec{x},t)} \Longrightarrow \Phi_{\vec{k}\,(t)} = \frac{4\pi G}{k^2}\,\rho_{\vec{k}\,(t)} \tag{2.15}$$

The gravitational forces are then computed by taking the gradient of the potential, e.g. with a finite difference approximation. Next the gravitational forces need to interpolated back from the mesh cells to the particle positions in order to obtain the particle acceleration.

With this information the particles can be advanced in time with the relations (2.14). To compute the gravitational acceleration for n particles with this method, a number of operations of the order $n_g \cdot \ln(n_g)$ is required, where n_g is the number grid cells, which usually equals the number of particles n. The maximum spacial resolution which can be achieved with this method, is given by the size of the mesh cells.
The Ramses code applies the PM method to evolve the collisionless dark matter particles, with the CIC scheme to assign particle masses to the grid cells. From the resulting discrete density field the gravitational potential is computed through the discrete Fourier transform method. The gradient is taken first on the mesh through the use of a 5-point finite difference approximation scheme and then the resulting force is interpolated back to the particle positions using an inverse CIC scheme.
The resulting accelerations at the particle positions are then used to integrate the differential equations (2.14), describing the n particles, with a discrete time step Δt. Here Ramses uses a second-order midpoint scheme. For the case of a constant time step, this reduces to a kick-drift-kick leap-frog scheme.

$$\vec{v}^{\,n+1/2} = \vec{v}^{\,n+1} - \nabla\Phi^n \cdot \frac{\Delta t}{2} \tag{2.16}$$

$$\vec{x}^{\,n+1} = \vec{x}^{\,n+1} + \vec{v}^{\,n+1/2} \cdot \Delta t \tag{2.17}$$

$$\vec{v}^{\,n+1} = \vec{v}^{\,n+1/2} - \nabla\Phi^{n+1} \cdot \frac{\Delta t}{2} \tag{2.18}$$

$$\text{where} \quad \Phi^n = \Phi_{(\vec{x}^{\,n}, t^n)} \quad \text{and} \quad \Phi^{n+1} = \Phi_{(\vec{x}^{\,n+1}, t^{n+1})} \tag{2.19}$$

Important references on the particle mesh method are [HE88], [Yep97] and [Tey02].

2.4 Numerically modelling the baryonic matter component

2.4.1 Overview

Although baryons make up only 15% of the total mass budget of the universe, their influence onto the processes of mass accumulation become apparent when high precision is required on small scales. Baryons are not fundamentally different from dark matter in the sense, that they also interact with themselves and with the other species through gravitation. However, unlike dark matter they also interact through the electro-magnetic force. First, this fact makes them a collisional fluid, which interacts with itself also through its non-zero pressure. And second, it allows the baryons to emit and absorb electro-magnetic radiation, such that energy can be exchanged with the environment. The latter property manifests itself in particular in the processes of radiative cooling and heating of baryons. The most basic step is to include the baryons as non-radiative fluid into the simulations, so that no exchange of internal energy with the environment, through radiation, is possible. The baryonic fluid then follows the description of a perfect fluid with a pressure, which is described by the Euler equations of fluid dynamics (for details see Appendix A):

Mass conservation / Continuity equation:

$$\frac{d\rho_{(\vec{x},t)}}{dt} = -\rho_{(\vec{x},t)} \cdot \nabla \vec{v}_{(\vec{x},t)} \quad \Longleftrightarrow \tag{2.20}$$

$$\frac{\partial \rho_{(\vec{x},t)}}{\partial t} + \nabla(\rho_{(\vec{x},t)} \cdot \vec{v}_{(\vec{x},t)}) = 0 \tag{2.21}$$

Momentum conservation equation:

$$\frac{dv_{i\,(\vec{x},t)}}{dt} = -\frac{1}{\rho_{(\vec{x},t)}} \cdot \nabla P_{(\vec{x},t)} - \nabla \Phi_{(\vec{x},t)} \quad \Longleftrightarrow \tag{2.22}$$

$$\frac{\partial(\rho_{(\vec{x},t)} \cdot v_{i\,(\vec{x},t)})}{\partial t} + \nabla_j(\rho_{(\vec{x},t)} \cdot v_{j\,(\vec{x},t)} \cdot v_{i\,(\vec{x},t)}) = -\nabla_i P_{(\vec{x},t)} - \rho_{(\vec{x},t)} \cdot \nabla_i \Phi_{(\vec{x},t)} \tag{2.23}$$

Energy conservation equation:

$$\frac{dE_{(\vec{x},t)}}{dt} = -\frac{P_{(\vec{x},t)}}{\rho_{(\vec{x},t)}} \cdot \nabla \vec{v}_{(\vec{x},t)} \quad \Longleftrightarrow \tag{2.24}$$

$$\frac{\partial(\rho_{(\vec{x},t)} \cdot e_{(\vec{x},t)})}{\partial t} + \nabla(\rho_{(\vec{x},t)} \cdot \vec{v}_{(\vec{x},t)} \cdot e_{(\vec{x},t)}) = -\nabla(\vec{v}_{(\vec{x},t)} \cdot P_{(\vec{x},t)}) - \rho_{(\vec{x},t)} \cdot \nabla \Phi_{(\vec{x},t)} \cdot \vec{v}_{(\vec{x},t)} \tag{2.25}$$

Here $E_{(\vec{x},t)}$ is the internal energy per volume and mass, so that the total energy per volume and mass $e_{(\vec{x},t)}$, which includes the kinetic energy of the bulk motion of the fluid is given by

$$e_{(\vec{x},t)} = E_{(\vec{x},t)} + \frac{1}{2} \cdot v^2_{(\vec{x},t)} \tag{2.26}$$

The fluid equations plus the Poisson equation are four equations, the number of variables is however five: mass density $\rho_{(\vec{x},t)}$, bulk velocity $\vec{v}_{(\vec{x},t)}$, pressure $P_{(\vec{x},t)}$, internal energy density per mass $E_{(\vec{x},t)}$ and gravitational potential $\Phi_{(\vec{x},t)}$. A fifth equation is therefore needed to solve the system, the equation of state, which relates the pressure to the internal energy density per mass and volume.

$$P_{(\vec{x},t)} = \frac{2}{f} \cdot \rho_{(\vec{x},t)} \cdot E_{(\vec{x},t)} \tag{2.27}$$

Here f is the number of the degrees of freedom, which the molecules or atoms of the modelled gas are supposed to have. The baryonic gas relevant for the underlying project, consist mostly of ionized hydrogen, hence it has only the three translational degrees of freedom ($f = 3$) and no additional ones. f is also related to the adiabatic exponent of the gas γ via

$$\gamma = \frac{2}{f} + 1 \tag{2.28}$$

The adiabatic exponent γ in turn is related to the polytropic index Γ introduced in Section 1.3, since for any ideal gas, which interacts with the environment only adiabatically, it holds that

$$P \propto \rho^{\gamma} \tag{2.29}$$

This relation can be derived from first principles. The polytropic index introduced in relation (1.59) on the other hand is an assumption, that a gas which is interacting also with its environment through non-adiabatic means, can be described effectively by $P \propto \rho^{\Gamma}$, with Γ being different from γ in general. For the baryonic gas the interaction with the gravitational field can induce non-adiabatic behaviour into the gas in the form of shocks. The equation of state is actually another way to express the ideal gas law $P = k_B/m_H \cdot \rho \cdot T$ since temperature is nothing but twice the mean kinetic energy per particle and degree of freedom.

$$E = \frac{f}{2} \cdot \frac{k_B}{m_H} \cdot T \tag{2.30}$$

After inserting Equation (2.30) into Equation (2.27) one recovers Equation (1.58).

Just as for the dark matter, also for the description of the baryonic component, two main branches of numerical modelling have been established. Each one is connected to one of the dark matter modelling approaches:

2.4.2 Smoothed Particle Hydrodynamics (SPH) Codes

This hydro scheme comes in combination with the Tree approach for the dark matter. Smoothed Particle Hydrodynamics codes sample the phase space of the baryonic fluid with particles like it is done for dark matter component. This corresponds to the first expressions of the Euler equations (2.21), (2.23) and (2.25). In other words the time step used by the code to evolve the differential equation system, is the total time derivative. From integrating the momentum conservation equation the particle velocity $\vec{v}_i$ follows. And with that in turn the particle position can be obtained by integrating

$$\frac{d\vec{x}_i}{dt} = \vec{v}_i \tag{2.31}$$

such that the particle trajectory $x_{i\,(t)}$ follows. The relevant fluid quantities which enter into Euler equations at the position of the i-th particle, density, pressure, internal energy per mass and volume, are computed by the following method. The properties of all n particles are summed and assigned to the position of the i-th particle through the use of a smoothing function. For the density one has

$$\rho_{(\vec{x}_i)} = \sum_{j=1}^{N} m_j W_{(\vec{x}_i - \vec{x}_j,\, h)} \tag{2.32}$$

where $W_{(\vec{x}_i - \vec{x}_j,\, h)}$ is the smoothing function of radius h. For the other fluid variables the assignment is

$$A_{(\vec{x}_i)} = \sum_{j=1}^{N} m_j \frac{A_j}{\rho_j} W_{(\vec{x}_i - \vec{x}_j,\, h)} \tag{2.33}$$

References on the numerical method of SPH are [Yep97] and [MvW10].

2.4.3 Grid Based Hydro Solvers / Godunov Schemes

In this technique the Euler equations of fluid dynamics are solved on a grid in normal space, which can be regular or adaptive. Meaning the time step used by the code to evolve the differential equation system, is the partial time derivative. The grid approach makes this technique the perfect combination with particle mesh codes. Hence, unlike in the SPH case no particle trajectories are calculated. Instead the fluid entities, density, pressure, etc., are calculated at the fixed cell positions. In the most basic approach of this technique the fluid quantities are constant over each cell and this constant value is updated at each time step. This scheme is therefore is called piecewise constant. Piecewise because at the cell boundaries the quantities are necessarily discontinuous. A more sophisticated version of the method is to retain also the information about the change of the hydro variables within the cells. This is done in the piecewise linear approach, where not just the absolute value of the hydro variable within the cell is used in the computation process, but also the slope. The starting point are the second expressions of the Euler equations (2.21), (2.23) and (2.25), which can be written in the following way (I and J are spatial indices, capital letters are used to distinguish them from the small letters used further down for the grid cell numbers):

$$\frac{\partial \vec{U}_{(\vec{x},t)}}{\partial t} + \nabla_J \vec{F}_{J\,(\vec{x},t)} = \vec{S}_{(\vec{x},t)} \quad \text{where} \tag{2.34}$$

$$\vec{U} = \begin{pmatrix} \rho \\ \rho \cdot v_I \\ \rho e \end{pmatrix} \;,\; \vec{F}_J = \begin{pmatrix} \rho \cdot v_J \\ \rho \cdot v_I \cdot v_J + P \cdot \delta_{IJ} \\ \rho \cdot e \cdot v_J + P \cdot v_J \end{pmatrix} \;,\; \vec{S} = \begin{pmatrix} 0 \\ \rho \cdot (\nabla_I \Phi) \\ \rho \cdot (\nabla_I \Phi) \cdot v_I \end{pmatrix} \tag{2.35}$$

S hereby designates the source terms, which represent gravity. U are called the conservative hydro variables since the Euler equations are conservation laws for these variables for the case that the source terms are zero. The regular hydro variables ρ, $\vec{v}$, e, etc. are commonly called primitive hydro variables. F_J are called fluxes, which are functions of the hydro variables. The Godunov method is the discretisation of the hydro variables in time and space by the averaging over a control volume in both time and space, which corresponds to the cell size and the time step. In one dimension this would read

$$\begin{aligned} &\frac{1}{\Delta t \Delta x} \int_{t^n}^{t^{n+1}} \int_{x_{i-\frac{1}{2}}}^{x_{i+\frac{1}{2}}} dx\, dt\, \frac{\partial \vec{U}}{\partial t} + \frac{1}{\Delta t \Delta x} \int_{t^n}^{t^{n+1}} \int_{x_{i-\frac{1}{2}}}^{x_{i+\frac{1}{2}}} dx\, dt\, \frac{\partial \vec{F}}{\partial x} \\ &= \frac{1}{\Delta t \Delta x} \int_{t^n}^{t^{n+1}} \int_{x_{i-\frac{1}{2}}}^{x_{i+\frac{1}{2}}} dx\, dt\, \vec{S} \end{aligned} \tag{2.36}$$

After applying the fundamental theorem of calculus and defining the average quantities

$$\bar{U}_i^n = \frac{1}{\Delta x} \int_{x_{i-\frac{1}{2}}}^{x_{i+\frac{1}{2}}} dx\, U_{(x,t^n)} \quad \text{and} \quad \bar{F}_{i+\frac{1}{2}}^{n+\frac{1}{2}} = \frac{1}{\Delta t} \int_{t^n}^{t^{n+1}} dt\, F_{(t,x_{i+\frac{1}{2}})} \tag{2.37}$$

one arrives at the following compact form of the fluid dynamical equations

$$\bar{U}_i^{n+1} = \bar{U}_i^n - (\bar{F}_{i+\frac{1}{2}}^{n+\frac{1}{2}} - \bar{F}_{i-\frac{1}{2}}^{n+\frac{1}{2}}) \cdot \frac{\Delta t}{\Delta x} = \bar{S}_i^{n+\frac{1}{2}} \cdot \Delta t \tag{2.38}$$

For the case of the source term being zero, the update of the hydro variable in a cell from one time step to another would simply be given by the time centred fluxes across the cell

interfaces $\bar{F}^{n+\frac{1}{2}}_{i+\frac{1}{2}}$ and $\bar{F}^{n+\frac{1}{2}}_{i-\frac{1}{2}}$. The fluxes are functions of the hydro variables, which are defined within the cells. At the cell boundary, where a discontinuity in the hydro variables exists, it is therefore unclear which functional value could be assigned to the hydro variables and the fluxes. The fluxes must therefore be defined as functions of the hydro variable values of the cells left and right of the cell boundary under consideration:

$$\bar{F}^{n+\frac{1}{2}}_{i-\frac{1}{2}} = F_{(U^{n+\frac{1}{2}}_{i-1}, U^{n+\frac{1}{2}}_{i})} \quad \text{and} \quad \bar{F}^{n+\frac{1}{2}}_{i+\frac{1}{2}} = F_{(U^{n+\frac{1}{2}}_{i}, U^{n+\frac{1}{2}}_{i+1})} \tag{2.39}$$

For the piecewise constant case the only option is therefore

$$\bar{F}^{n+\frac{1}{2}}_{i-\frac{1}{2}} = F_{(\bar{U}^{n+\frac{1}{2}}_{i-1}, \bar{U}^{n+\frac{1}{2}}_{i})} \quad \text{and} \quad \bar{F}^{n+\frac{1}{2}}_{i+\frac{1}{2}} = F_{(\bar{U}^{n+\frac{1}{2}}_{i}, \bar{U}^{n+\frac{1}{2}}_{i+1})} \tag{2.40}$$

unless cells further away, than the ones which are sharing the boundary, are also considered for the computation of the flux.

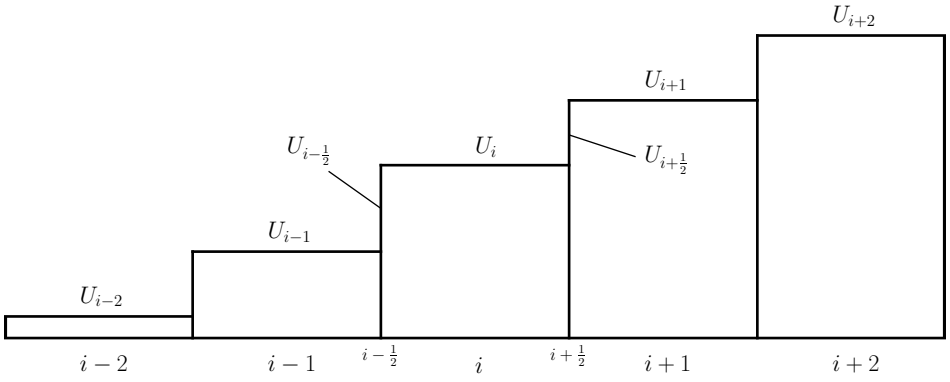

Figure 2.1: **Illustration of the piecewise constant method. The superscript for the time step is dropped for simplicity.**

The sophistication of this method is the piecewise linear approach: After each time step when the average of the hydro variable is updated in a certain cell, also a slope is assigned to this cell's hydro variables. This is done in what is called linear reconstruction, through the use of the average values from the two neighbouring cells. This step is described in more detail below. For the discussion of how fluxes at the cell boundaries are to be calculated the important point is that one can now work with values of the hydro variables which contain the additional information obtained through the linear reconstruction.

$$\bar{F}^{n+\frac{1}{2}}_{i-\frac{1}{2}} = F_{(U^{n+\frac{1}{2}}_{i-\frac{1}{2},\,L}, U^{n+\frac{1}{2}}_{i-\frac{1}{2},\,R})} \quad \text{and} \quad \bar{F}^{n+\frac{1}{2}}_{i+\frac{1}{2}} = F_{(U^{n+\frac{1}{2}}_{i+\frac{1}{2},\,L}, U^{n+\frac{1}{2}}_{i+\frac{1}{2},\,R})} \tag{2.41}$$

Here $U^{n+\frac{1}{2}}_{i+\frac{1}{2},\,L}$ and $U^{n+\frac{1}{2}}_{i+\frac{1}{2},\,R}$ denote the values of $U^{n+\frac{1}{2}}_{i\,(x)}$ and $U^{n+\frac{1}{2}}_{i+1\,(x)}$ respectively, at the boundary between the i-th and $(i-1)$-th cell after the linear reconstruction. Whereas $U^{n+\frac{1}{2}}_{i-\frac{1}{2},\,L}$ and $U^{n+\frac{1}{2}}_{i-\frac{1}{2},\,R}$ are the values of $U^{n+\frac{1}{2}}_{i-1\,(x)}$ and $U^{n+\frac{1}{2}}_{i\,(x)}$ respectively, at the boundary between the i-th

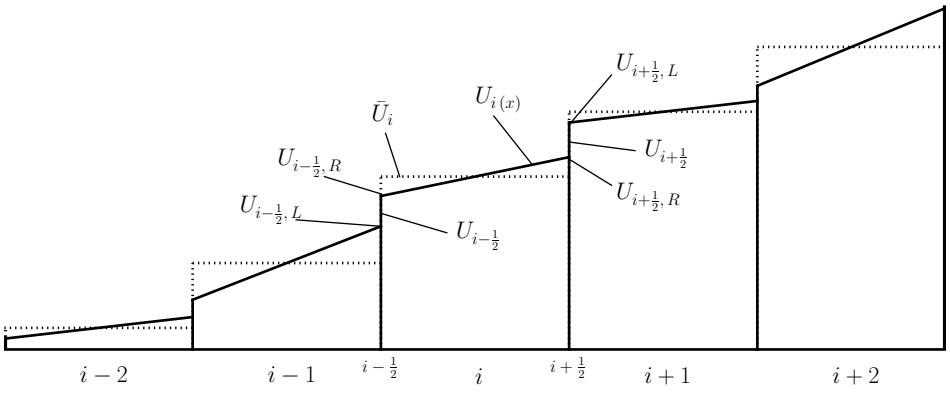

Figure 2.2: **Illustration of the piecewise linear method. The superscript for the time step is dropped for simplicity.**

and $(i+1)$-th cell.

The linear reconstruction itself introduces numerical subtleties, whose investigation is part of this thesis work. The method is illustrated in the following. The most intuitive way to define the slope of U in the i-cell is by the central finite difference approximation

$$m_{i,\,C} = \frac{\Delta U_{i,\,C}}{\Delta x} = \frac{\bar{U}_{i+1} - \bar{U}_{i-1}}{2\Delta x} \tag{2.42}$$

To avoid oscillations in the solution of U, which are arising from non-monotonicities induced by the linear reconstruction, the obtained slope is limited by an additional function φ which depends on $\bar{U}_{i-1}$, $\bar{U}_i$ and $\bar{U}_{i+1}$. This function is called the slope limiter and the expression (2.42) above is redefined, such that

$$m_i = \frac{\Delta U_i}{\Delta x} = \frac{\bar{U}_{i+1} - \bar{U}_{i-1}}{2\Delta x} \cdot \varphi_{(\bar{U}_{i-1},\,\bar{U}_i,\,\bar{U}_{i+1})} \quad \text{with} \quad \varphi_{\in}[0,1] \tag{2.43}$$

The extreme case $\varphi = 0$ corresponds to the piecewise constant method. In the Ramses code the Godunov scheme, with a piecewise linear reconstruction, is applied to solve the fluid dynamical equations of the baryonic gas. Two possibilities for the slope limiter are implemented in the code:

a) MinMod

First one defines two additional ways to reconstruct the slope in the i-th cell from the average values of the i-th cell itself and its two neighbouring ones.

$$m_{i,\,L} = \frac{\Delta U_{i,\,L}}{\Delta x} = \frac{\bar{U}_i - \bar{U}_{i-1}}{\Delta x} \quad \text{and} \quad m_{i,\,R} = \frac{\Delta U_{i,\,R}}{\Delta x} = \frac{\bar{U}_{i+1} - \bar{U}_i}{\Delta x} \tag{2.44}$$

It follows directly

$$m_{C\,i} = \frac{m_{i,\,L} + m_{i,\,R}}{2} \tag{2.45}$$

The MinMod slope limiter works the following way:

1. If $m_{i,L}$ and $m_{i,R}$ have opposite sign, then the slope of the considered cell m_i is set to zero. This corresponds to $\varphi = 0$.
2. If $m_{i,L}$ and $m_{i,R}$ have the same sign, then the one of them which is less steep, or equivalently the one with the smaller absolute, is chosen as m_i.
3. In the special case that $m_{i,L}$ and $m_{i,R}$ are equal, one has the central finite difference value back $m_{i,C}$. This corresponds to $\varphi = 1$.
4. In all other cases one of $m_{i,L}$ and $m_{i,R}$ is larger than the central finite difference approximation $m_{i,C}$. It follows then automatically from (2.45), that the other one is smaller than $m_{i,C}$ and therefore chosen by the algorithm. It is therefore automatically ensured that m_i can never exceed the finite difference approximation value $m_{i,C}$. Hence one gets a value of φ between 0 and 1.

The MinMod selection algorithm can be summarized as

$$m_i = \text{minmod}(m_{i,L}, m_{i,R}) \tag{2.46}$$

The minmod function is defined as zero if the two arguments have different signs. Otherwise it assumes the value of the minimum of the absolutes of the two arguments, multiplied by minus one if the common sign is negative.

b) MonCen (Monotonised Central)

This slope limiter, again uses the definitions from above for $m_{i,L}$, $m_{i,R}$ and $m_{i,C}$. Its goal is to ensure, that the values of the hydro variables, after the linear reconstruction, at the cell boundaries, do not exceed the average values of the neighbouring cells. Mathematically this can be formulated in the following way:

$$\bar{U}_{i-1} < \bar{U}_i - m_i \cdot \frac{\Delta x}{2} < \bar{U}_i \quad \text{and} \quad \bar{U}_i < \bar{U}_i + m_i \cdot \frac{\Delta x}{2} < \bar{U}_{i+1} \tag{2.47}$$

It can be shown that these constraints require

$$m_i < 2 \cdot m_{i,L} \quad \text{and} \quad m_i < 2 \cdot m_{i,R} \tag{2.48}$$

The MonCen slope limiter follows the following algorithm where these constraints are implemented:

1. If $m_{i,L}$ and $m_{i,R}$ have opposite sign, then the slope of the considered cell m_i is set to zero. This corresponds to $\varphi = 0$.
2. If $m_{i,L}$ and $m_{i,R}$ have the same sign, then two times the one of them which is less steep, or equivalently two times the one with the smaller absolute, is chosen as m_i.
3. If the absolute of the chosen value for m_i, which is either $2 \cdot m_{i,L}$ or $2 \cdot m_{i,R}$ is larger than the absolute of $m_{i,C}$, then the value of m_i is replaced with $m_{i,C}$. In other words, if the slope obtained from selecting two times the less steep one out of $m_{i,L}$ and $m_{i,R}$ is larger than $m_{i,C}$, then the latter is used as the value for m_i. This corresponds to $\varphi = 1$.

The MonCen selection algorithm can be summarized in the following way [TFD06]:

$$m_i = \text{minmod}[m_{i,C}, \text{minmod}(2 \cdot m_{i,L}, 2 \cdot m_{i,R})] \tag{2.49}$$

Hence the MonCen slope limiter gives back the maximum value of $m_{i,C}$ more often than the MinMod slope limiter, since in the latter one $m_{i,C}$ is given back only in the rare case that $m_{i,L}$ and $m_{i,R}$ are exactly the same. The MonCen slope limiter comes therefore closer to the original desire of using the finite difference approximation for reconstructing the slopes of the hydro variables within the grid cells, as it would be required for a piecewise linear scheme.
It follows that if the MonCen slope limiter is applied to a simulation, the slopes of the hydro variables within the grid cells will on average be steeper, than if the MinMod slope limiter is applied. Hence with the MonCen slope limiter one expects steeper gradients in the overall behaviour of the hydro variables, which would translate into a better resolution of small structures.
Key references on the implementation of grid based hydro solvers / Godunov schemes in Ramses are [Tey02] and [DBS+08].

2.5 Adaptive mesh refinement

One of the profound advantages that come with the discretisation of space on a grid, as in the PM and grid based hydro codes, is that the underlying grid is not required to have the same cell size everywhere. Or in other words, the grid does not have to be homogeneous. Instead regions of interest can be simulated with a higher resolution than surrounding ones, where in turn the resolution can be reduced as compared to a run with a homogeneous grid. To describe this hierarchy of grids mathematically and numerically one introduces the term level. The underlying idea is similar to the tree code method described above: The cubical simulation volume is divided and subsequently sub-divided into smaller cubical volumes. The total simulation cube corresponds to the grid on level $\ell = 0$, its next eight equally sized sub-volumes to level $\ell = 1$, and so forth. The mesh on which a homogeneous grid simulation would operate typically corresponds to $\ell = 10$. For a non-unigrid simulation a typical example would be a minimum level of $\ell_{min} = 9$ and a maximum level of $\ell_{max} = 18$. A density criterion is applied to decide whether a cell is refined into eight smaller ones, or in other words if one level higher than the current one is refined. The criterion which is used in the underlying study is the following: whenever the dark matter or baryon mass within a cell exceeds eight times the initial mass resolution, then the cell is split into 8 children cells. Therefore the baryonic mass of a cell always stays roughly constant (at the initial value). Since after the split one children cell has the same baryonic mass density as the father cell right after it was split from its father cell in turn. Or formulated otherwise the baryonic mass of cells never exceeds 8 times the initial value. Dark matter mass stays constant anyway because dark matter particles are never split after the initial grid (see below). But if the refinement happens, not all of the children cells must necessarily contain a dark matter particle. Another children cell could for example contain two. This strategy is called quasi-Lagrangian since the aim is to keep the mass contained in a cell at a fixed value, while the cell size itself is reduced.
As already mentioned above the dark matter particles keep their initial mass throughout the simulation run. This particle mass is determined by the coarsest level ℓ_{min} used in the simulation, as the initial conditions are specifically created for a simulation with this minimum level. Hence $\ell_{ini} = \ell_{min}$. Dark matter particle mass and ℓ_{min} are related via

$$m_{dm} = \bar{\rho} \cdot \frac{L^3}{2^{3 \cdot \ell_{min}}} = \bar{\rho} \cdot \frac{L^3}{8^{\ell_{min}}} \tag{2.50}$$

L is hereby the side length of the simulation volume. The refinement criterion is checked before every integration step and new oct cells are created in case the father cell fulfils the criterion. Likewise octs are removed, in case that the father cell no longer fulfils it. Hence the strategy is called dynamical refinement. The emerging picture is a cubical simulation volume which is sub-divided into smaller cubes of side lengths $1/2^{\ell}$, which are subsequently created and removed. As a consequence cubes of different volumes come to lie next to each other, and with that unequally size boundaries are shared at the interfaces. This requires sophistications of the algorithms presented above and the implementation of additional numerical methods.

The co-existence of different levels of spatial resolution in the simulation volume, also raises the not obvious question about the implementation of the time resolution. The two most obvious approaches are to either use the same time step on all levels, or to double the number of time steps with each subsequently higher level that is used. Both possibilities can be selected in the Ramses code. In the second case the synchronization of finer levels with coarser ones is required. In other words the sizes of the two time steps on level $\ell + 1$ need to add up to the size of the time step on level ℓ:

$$\Delta t_{\ell} = \Delta t^1_{\ell+1} + \Delta t^2_{\ell+1} \tag{2.51}$$

In the highest resolution simulations of this study $\ell = 7$ was chosen as the minimum level and $\ell = 20$ for the maximum one. No simulation however refined the grid beyond $\ell = 19$. For the first six levels $\ell = 7$ to $\ell = 12$ the same time step was used, and then the number of time steps was doubled with each subsequently higher level.

Aside from the above constraint (2.51), the size of the time step is determined independently for each level in the Ramses code. Four stability constraints are implemented for this purpose (see [Tey02] for details):

1. Gravitational evolution: Δt_ℓ should be smaller than a fraction of the minimum free fall time.
2. Particle dynamics: Particles should move only by a fraction of the local cell size. Therefore Δt_ℓ is required to be smaller than the cell size divided by the particle velocity.
3. Cosmic background evolution: The scale factor should not vary more than 10% over one time step.
4. Fluid dynamics: The Courant-Friedrich-Levy stability condition ensures that the fluid moves less than a fraction of the local cell size within one time step. For the fluid velocity, both bulk velocity and sound speed are taken into account.

2.6 The zoom-in technique

The result of the application of the adaptive mesh refinement (AMR) technique described in the previous section is a simulation volume in which all the high density regions are refined with smaller cell volumes, than the surrounding low density regions. Beyond this, it might be desirable to focus on one object only, e.g. one particular halo, and to simulate it with higher resolution than the rest of the entire box. In principle this could be achieved by simulating it as an isolated object, in a simulation with no other particles. That way however one would loose the information about how the surrounding structures influence the object under consideration gravitationally. A different technique has therefore been developed, and has found a successful application in cosmology: the zoom-in technique.
The halo of interest is identified at the desired redshift, in a regular none zoom-in run and the identities of all the particles which it contains are recorded. These particles are then identified in the initial configuration of the simulation and a bounding volume is fitted, such that they are all contained within it. In the case of this study an ellipsoid. The geometric information about this object is now passed on to the initial conditions program, which can then create modified initial conditions which contain higher resolved information about the region of interest. Meaning that already at the stage of the initial condition creation several levels of refinement $\ell_{ini,\,min} - \ell_{ini,\,max}$, and with that different particle masses, are introduced. The result is that the particles which will end up in the final halo, are simulated from the beginning with only a fraction of their original mass. This results in a higher mass resolution of the final object.
For the refined initial conditions one can use several levels of refinement and hence mass resolution. The coarsest level in the initial conditions must however be the same as the coarsest level in the simulation: $\ell_{ini,\,min} = \ell_{min}$. In our case we have chosen a coarsest level of $\ell_{ini,\,min} = 7$ and 4 additional levels in the initial conditions $\ell_{ini,\,max} = 11$, such that our highest resolved particles have only 8^{-4} or roughly 1/4000 of the particle mass of the unrefined particles. The three refinement levels in between are also represented with particle masses of 8^{-1}, 8^{-2} and 8^{-3} of the coarsest value, respectively. As in the non-zoom simulations, dark matter particles keep their initial masses during the simulations.

3 Results of simulations with purely non-radiative hydrodynamics

3.1 Preface and Declaration

We have simulated a statistically representative sample of 16 galaxy groups with the current state of the art simulation code Ramses [Tey02], and initial conditions code MUSIC [HA11]. Galaxy groups are mainly in our interest because they will give the strongest contribution to weak lensing effect, which serves as a probe of the cosmological structure [Sel00]. More specifically it is the distribution of mass within the galaxy groups, which will influence the spectrum of cosmological weak gravitational lensing significantly. Our simulations are performed on the supercomputer zbox4 of the Institute for Computational Science located at Irchel Campus, and also on the Piz Daint and Piz Dora machines at the Swiss National Supercomputing Centre (CSCS) in Lugano.

In [RT17] we report on the results from the first and second simulation phases, where the galaxy groups are modelled with gravitational physics only and gravitational physics plus non-radiative hydrodynamics, respectively.
We were motivated by the question, how numerically introduced uncertainties in our simulations compare to the ones arising from physical causes. We arrived at the satisfactory result, that the numerically introduced ones are smaller than the latter. With this we have proven that state of the art computer simulation are capable of resolving the scales under consideration and have paved the road for succeeding simulations containing even more complicated amounts of physics.
Further we have quantified the changes in the mass distribution induced by adding the hydrodynamical component to the simulations, in contrast to simulations with only gravitational interaction. The same can be done for the next steps, when additional physics enters the simulations. From this one can draw conclusions about the effectiveness of the different feedback mechanisms and implementations. On top of that the project also gave us new insights into the astrophysics of the intragroup medium, especially on the role of turbulent motion which is the source of non-thermal pressure support in galaxy clusters and groups. This topic is currently investigated by many researchers in the field because it has the potential of providing astrophysicist with a refined method for the determination of galaxy group and cluster masses.

All simulations mentioned in the publication were run by Manuel Rabold, and all of the analysis was performed by him. Further, all plots and maps were created by Manuel Rabold. The text of the article was almost entirely written by him, too. The exceptions are, slight modifications by Romain Teyssier, to a few sentences of the text, which did not change their scientific content, but only made them easier to read. These modifications were mainly in the form of shortening. A few sentences were also added by Romain Teyssier.

3.2 Precision cosmology with baryons: non-radiative hydrodynamics of galaxy groups

Monthly Notices
of the
ROYAL ASTRONOMICAL SOCIETY

MNRAS **467,** 3188–3211 (2017)
Advance Access publication 2017 February 1

doi:10.1093/mnras/stx266

Precision cosmology with baryons: non-radiative hydrodynamics of galaxy groups

Manuel Rabold[1,2]★ and Romain Teyssier[1,2]

[1]*Center for Theoretical Astrophysics and Cosmology, University of Zurich, Winterthurerstrasse 190, CH-8057 Zurich, Switzerland*
[2]*Institute for Computational Science, University of Zurich, Winterthurerstrasse 190, CH-8057 Zurich, Switzerland*

Accepted 2017 January 26. Received 2017 January 26; in original form 2016 November 24

ABSTRACT

The effect of baryons on the matter power spectrum is likely to have an observable effect for future galaxy surveys, like Euclid or Large Synoptic Survey Telescope (LSST). As a first step towards a fully predictive theory, we investigate the effect of non-radiative hydrodynamics on the structure of galaxy groups sized haloes, which contribute the most to the weak-lensing power spectrum. We perform high-resolution (more than one million particles per halo and one kilo-parsec resolution) non-radiative hydrodynamical zoom-in simulations of a sample of 16 haloes, comparing the profiles to popular analytical models. We find that the total mass profile is well fitted by a Navarro, Frenk & White model, with parameters slightly modified from the dark matter only simulation. We also find that the Komatsu & Seljak hydrostatic solution provides a good fit to the gas profiles, with however significant deviations, arising from strong turbulent mixing in the core and from non-thermal, turbulent pressure support in the outskirts. The turbulent energy follows a shallow, rising linear profile with radius, and correlates with the halo formation time. Using only three main structural halo parameters as variables (total mass, concentration parameter and central gas density), we can predict, with an accuracy better than 20 per cent, the individual gas density and temperature profiles. For the average total mass profile, which is relevant for power spectrum calculations, we even reach an accuracy of 1 per cent. The robustness of these predictions has been tested against resolution effects, different types of initial conditions and hydrodynamical schemes.

Key words: hydrodynamics – turbulence – methods: numerical – galaxies: groups: general – cosmology: theory – large-scale structure of universe.

1 INTRODUCTION

Our decade has seen cosmic microwave background (CMB) experiments dominate the field of observational cosmology, allowing us to determine cosmological parameters with unprecedented accuracy (Komatsu et al. 2011; Planck Collaboration et al. 2016). The next decade will be the era of precision cosmology based on large-scale galaxy surveys, like Euclid (Laureijs et al. 2011) and Large Synoptic Survey Telescope (LSST; LSST Dark Energy Science Collaboration 2012). In order for cosmological probes such as weak lensing (WL) or galaxy clustering (GC) to be really competitive, when compared to CMB data, it is required to achieve subpercent level accuracy in the determination of the matter power spectrum, at scales of comoving wavelength $0.1\,h\,\mathrm{Mpc}^{-1} < k < 10\,h\,\mathrm{Mpc}^{-1}$ (Huterer & Takada 2005). This brings considerable challenges to the instrumental design and to the data analysis of these future experiments, especially regarding the understanding and the control of systematic errors.

An important source of these systematic errors is coming from the theoretical predictions for both GC and WL probes. Although the matter distribution is well understood at the linear level, below modes of $0.1\,h\,\mathrm{Mpc}^{-1}$, this is not necessarily the case on smaller scales where non-linear effects become important. Collisionless N-body simulations, on one hand, have been successful in modelling dark matter only universes, with an accuracy better than 1 per cent at $k < 3\,h\,\mathrm{Mpc}^{-1}$ and better than 3 per cent at $k < 10\,h\,\mathrm{Mpc}^{-1}$ (Schneider et al. 2016). Baryonic effects, on the other hand, cannot be ignored on these scales: in the range of $1\,h\,\mathrm{Mpc}^{-1} < k < 10\,h\,\mathrm{Mpc}^{-1}$, baryonic physics can modify the total matter power spectrum (compared to the naive dark matter only case) up to 10 per cent (van Daalen et al. 2011; Schneider & Teyssier 2015), considering pessimistic but plausible scenarios.

To account for baryons in a cosmological simulation, we model them as a collisional fluid. As a first basic step, this gas component can be considered as purely non-radiative. From there, one

★ E-mail: manuel@physik.uzh.ch

can introduce additional physical processes to the baryonic gas, like radiative cooling, star formation, supernova feedback or active galactic nucleus (AGN) feedback (see Dolag et al. 2008, for a review). The latter, though still in an experimental, not really predictive phase, has proven very valuable in exploring strong baryonic effects on large scale, and in reproducing many observable properties of large galaxy clusters and groups. The ultimate goal for the inclusion of baryonic effects into the analysis of our cosmological data sets, would be to parametrize their influence on to the relevant spectra, in the form of one or a few key parameters, in addition to the set of standard cosmological parameters, so that we could fit those parameters together with the important dark sector parameters.

One of the advantages coming from the utilization of the cosmological WL technique, is its sensitivity on the late-time evolution of the Universe during the dark energy dominated era. So that a particular high expectation lies on the determination of the parameters relevant herein, like the dark energy equation-of-state parameter and the neutrino masses. Further, the corresponding redshift range relevant for cosmological WL translates, through the halo mass function, into the result that the strongest signal will come from galaxy group sized haloes (Seljak 2000). For this reason, our analysis focuses on the latter.

Since galaxy clusters are the standard testbeds for cosmological studies (Allen, Evrard & Mantz 2011; Borgani & Kravtsov 2011; Kravtsov & Borgani 2012), especially for the comparison of numerical predictions with observational results, galaxy group sized haloes, have played a subdominant role in the analysis of cosmological structure, mostly in combination with studies on cluster sized haloes. Indeed, from a naive view point, galaxy group haloes are scaled down versions of galaxy cluster, depending on the characteristic length-scales that are involved in the implemented physical processes. For purely non-radiative hydrodynamics, no characteristic length-scales exist, since both the gravitational and hydrodynamical equations of motion are scale free. On second thought, however, the difference in size between group and cluster haloes, translates into a different time-scale for their gravitational collapse. So that one could expect group sized haloes to be ahead of their cluster sized counterparts, in the collapse process, and to be more concentrated accordingly.

Our work is to our knowledge the first precision cosmology numerical study focusing entirely on group sized haloes. Previous work has been done in the area of galaxy formation physics within groups (Feldmann et al. 2010) and on testing of new implementations of AGN feedback (McCarthy et al. 2010). This, however, is not the focus of this paper. The analysis of this paper concentrates on the first basic step to include baryons: we investigate their influence as they are modelled as a purely non-radiative gas. Our aim is also to quantify the effect of numerical resolution, which is needed to resolve the inner regions of haloes $r < 10\,\mathrm{kpc}$ with the required precision. As a reference, we will use a well-known analytical model for the radial dependence of the thermodynamic quantities of the baryonic component, based on hydrostatic equilibrium (HSE) and a polytropic equation of state, from Komatsu & Seljak (2001).

A similar study about non-radiative hydro simulations of cluster and group sized haloes was reported in Ascasibar et al. (2003). There however the focus lay more on the testing of analytic models for the radial dependence of the thermodynamical properties of the baryonic component, commonly named the intracluster medium (ICM) and the intragroup medium (IGM). The ICM is an important source of information for observations of galaxy clusters, since it consist largely of ionized hydrogen, which is continuously emitting X-ray photons. The spectrum of these photons contains information, about the spatial distribution and thermodynamical state of the emitting baryonic gas.

Other important numerical studies of ICM/IGM profiles with non-radiative hydro simulations were done by Navarro, Frenk & White (1995), Eke, Navarro & Frenk (1998), Loken et al. (2002),Rasia, Tormen & Moscardini (2004), Roncarelli et al. (2006) and Nagai, Kravtsov & Vikhlinin (2007).

Aside from the intrinsic thermodynamical properties of the baryonic gas, we are also addressing its property of a non-thermal pressure component arising from turbulent motion in the gas. The question about how this additional pressure support enters into the assumption of HSE has been addressed before, in the studies of Rasia et al. (2004), Rasia et al. (2006), Roncarelli et al. (2006), Lau, Kravtsov & Nagai (2009) and Piffaretti & Valdarnini (2008). The importance of this issue comes from the fact that it leads to a mismatch in the mass estimate by X-ray observations of galaxy groups and clusters when the equation of HSE is applied, because there only the thermal pressure of the X-ray emitting gas is accounted for (Biffi, Dolag & Böhringer 2011). However, since the non-thermal component is more accessible in simulations, analytical fits have been proposed for its radial dependence. Recent works are Biffi et al. (2016), Martizzi & Agrusa (2016) and the paper series Shi & Komatsu (2014), Shi et al. (2015), and Shi et al. (2016).

Throughout the evolution of numerical astrophysical modelling, the quantification of numerical effects on to the simulation results has a long tradition. Already for the stage of pure *N*-body simulations, it is important to test for numerical convergence as was done by the studies of Power et al. (2003) and Heitmann et al. (2008). Also for non-radiative hydro simulations a series of code comparison projects were performed early on by Kang et al. (1994), Frenk et al. (1999) and O'Shea et al. (2005), and most recently in the nIFTy project (Sembolini et al. 2016). An established method here is to give a fixed set of initial conditions to each of the participating code developers, for each to run their simulation with their own choice of numerical parameters.

One important feature in these analyses is halo profiles and maps, which provide a common ground for the comparison of results from different numerical setups or codes. In the *N*-body case for density and mass and in the case where hydrodynamics is included also for thermodynamical quantities of the baryonic component like temperature, pressure or entropy. Our project focuses on halo profiles and maps alone. Further quantities used for comparisons could be the halo mass function, or the matter power spectrum itself.

The key questions that we address are as follows:

(i) How strong are the deviations of the numerical results from the analytic model, on average and for individual haloes?

(ii) How strong is the deviation from the numerical mean coming from the individual nature of the haloes? In other words: how strong is the scatter?

(iii) How strongly do numerical parameters e.g. the maximum resolution, or the initial conditions influence the results?

(iv) To which inner radius can the simulations be considered numerically converged?

(v) Are state of the art computer simulations capable of reaching the precision required by future observation?

Since these technical/numerical/systematic questions are the focus of this paper, we carry our analysis out for the simplest method of cosmological simulations, incorporating baryons: collisionless dark matter particles plus a non-radiative baryonic fluid. Parameter studies of cosmological hydrodynamic simulations including

radiative processes, star formation, stellar/AGN feedback and further subgrid physics will be presented in subsequent publications.

This paper is structured as follows: Section 2 describes our numerical simulations. Section 4 describes the analytical model to which we compare our findings. In Section 5, the selection criteria for our halo catalogue are discussed. In Section 6, we present the results in the form of halo profiles of the relevant physical quantities and in Section 7 correlations between the halo properties are depicted. The investigation of numerical effects is described in Section 8, while Section 9 concludes the paper.

2 SIMULATION PARAMETERS

All simulations were performed with the Adaptive Mesh Refinement code RAMSES (Teyssier 2002) in a cosmological periodic cubic box of side length $L = 100\,\mathrm{Mpc}\,h^{-1}$. Initially a reference run with dark matter only needed to be done, so that the halo regions of interest could be selected from it (see the particular section for the identification). Simulations of 16 individual haloes were undertaken with the use of the zoom-in technique. This allows us to refine the region of interest (in our case the $2\,r_{200}$ environment of each halo) with a higher resolution, than the rest of the box, while leaving the box size constant. The underlying cosmological model is characterized by the parameters listed in Table 1. Initial conditions for all simulations were provided by the MUSIC code (Hahn & Abel 2011). For the definition of r_{200}, the average matter density of the Universe $\bar{\rho}_\mathrm{m}$ is used.

The effective size of the reference run's initial grid was 512^3 ($\ell_\mathrm{min} = 9$). This translates into a mass resolution of $m_\mathrm{DM} = 9.34 \times 10^8\,\mathrm{M}_\odot$. During the run, seven more levels were added recursively. Once a halo of interest is found at $z = 0$, a bounding sphere of twice the haloes virial radius around the haloes centre of mass is set up, to account for all particles within it. The same particles are then identified in the initial grid at $z = 100$. A bounding ellipsoid of minimum size including all relevant particles is generated. Its geometric information is passed on to the MUSIC code, which in turn creates the multilevel initial conditions for the zoom-in run.

For the zoom-in runs, the levels of the initial grid ran from $\ell_\mathrm{ini} = 11$ in the region of interest, down to $\ell_\mathrm{min} = 7$ in the rest of the box. $\ell_\mathrm{ini} = 11$ corresponds to a mass resolution $m_\mathrm{DM} = 1.46 \times 10^7\,\mathrm{M}_\odot$ in dark matter only case, and to $m_\mathrm{DM} = 1.25 \times 10^7\,\mathrm{M}_\odot$ and $m_\mathrm{b} = 2.13 \times 10^6\,\mathrm{M}_\odot$ in the runs including hydrodynamics. The dynamical refinement is implemented in the following way (quasi-Lagrangian): when the dark matter mass or the baryon mass in a cell reaches eight times the initial mass resolution, during the run, the cell is split into eight children cells. This results in a nearly constant spatial resolution in physical units throughout the run. The chosen maximum refinement of level $\ell_\mathrm{max} = 18$ corresponds to a physical minimum cell size of $\Delta x_\mathrm{min} = L/2^{\ell_\mathrm{max}} = 1.1258$ kpc. We use for the hydro solver a second-order unsplit Godunov scheme based on the Harten-Lax-van Leer-Contact (HLLC) Riemann solver (Teyssier, Fromang & Dormy 2006) and the MinMod slope-type limiter (Fromang, Hennebelle & Teyssier 2006).

Table 1. Adopted cosmological parameters.

$\Omega_{\mathrm{b},0}$	0.048 25
$\Omega_{\mathrm{m},0}$	0.308
$\Omega_{\Lambda,0}$	0.692
h_0	0.6777
n_s	0.9611
σ_8	0.8288
w	−1

3 HALO FINDING

For halo detection, we applied the HOP halo finder (Eisenstein & Hut 1998; Skory et al. 2010) to the dark matter particles in our simulations. HOP calculates the density of each particle from a specified number of its nearest neighbours. With this information, it assigns each particle to a local density peak (densest neighbour), which is found after checking another specified number of neighbouring particles. Now all particles are assigned to a group defined by its densest particle, or they themselves are the densest of a number of particles (the group). In the next step, particles whose density is below a specified density contrast δ_outer are removed from these groups. This way it is decided, which particles belong to a halo and which do not. On top of that, the issue has to be addressed, that a dens spatial region could contain more than one density maximum. This means that such a region, which would in the physical sense corresponds to a halo, is artificially split into smaller groups, defined by their local density maxima, when the aforementioned steps are applied. To overcome this mishap, the groups found so far are merged together in another step, which introduces two additional density contrast parameters δ_saddle and δ_peak. Only a group, whose highest density lies above δ_peak can be an alone standing halo, otherwise it is merged into another halo, which is defined by a group, whose highest density exceeds δ_peak. The question, to which halo it should be merged is decided by, with which halo it shares the boundary of highest density. Further, two neighbouring groups whose highest densities both exceed δ_peak are merged together, if the density at their boundary exceeds the value δ_saddle. So typically one has $\delta_\mathrm{outer} < \delta_\mathrm{saddle} < \delta_\mathrm{peak}$. The most important parameter is δ_outer. We have selected the following set of density thresholds: $(\delta_\mathrm{outer}, \delta_\mathrm{saddle}, \delta_\mathrm{peak}) = (80, 200, 240)$. The resulting halo definition corresponds to the one of using a friends-of-friends halo finder, with linking length 0.2 Mpc (Eisenstein & Hut 1998). From the latter in turn, it is known that the resulting halo mass is a good estimate for M_{200}, defined with the average mass density of the Universe. Since the implementation of HOP used in this work does not output any information about substructure, we have not removed any particles from the found haloes in the following to unbind subhaloes.

4 THE ANALYTIC MODEL

The analytical model to which we compare our simulation data is based on the following principles. The density radial profile of the haloes overall matter distribution follows the NFW model (Navarro, Frenk & White 1996):

$$\rho_\mathrm{tot}(r) = \frac{\rho_\mathrm{s}}{\frac{r}{r_\mathrm{s}}\left(1+\frac{r}{r_\mathrm{s}}\right)^2}. \tag{1}$$

This model introduces two parameters ρ_s and r_s. The temperature and density radial profiles of the baryonic fraction follow the Komatsu & Seljak (2001) analytical hydrostatic and polytropic model:

$$T_\mathrm{gas}(r) = T_0 \frac{\ln(1+\frac{r}{r_\mathrm{s}})}{\frac{r}{r_\mathrm{s}}} \tag{2}$$

$$\rho_\mathrm{gas}(r) = \rho_0 \left(\frac{\ln(1+\frac{r}{r_\mathrm{s}})}{\frac{r}{r_\mathrm{s}}}\right)^{\frac{1}{\Gamma-1}}, \tag{3}$$

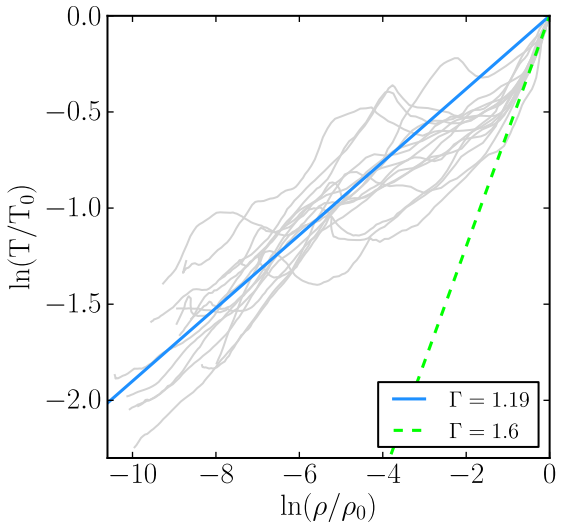

Figure 1. Logarithm of the temperature profile versus the logarithm of the density profile for all 16 haloes in our sample. For comparison, we show the polytropic relation with $\Gamma = 1.19$ as a solid line and another polytropic relation with $\Gamma = 1.6$, more adapted to the central regions of our sample.

where Γ is the adopted polytropic index used to represent the polytropic equation of state

$$P_{\rm gas}(r) \propto \rho_{\rm gas}(r)^{\Gamma} \tag{4}$$

Γ together with T_0 and ρ_0 add three additional parameters to the model. T_0 the normalization of the temperature profile is however determined already by the condition of zero pressure at infinity, which results in

$$T_0 = \frac{4\pi G \rho_{\rm s} r_{\rm s}^2 \mu m_p}{k_B} \frac{\Gamma - 1}{\Gamma}. \tag{5}$$

Let us explain how we determine the values of the various parameters for each halo. First, $\rho_{\rm s}$ and $r_{\rm s}$ can be extracted for each of the 16 haloes by fitting to their circular velocity curve. This is done by making a least-squares fit to the circular velocity squared curve:

$$L(r_{\rm s}, \rho_{\rm s}) = \sum_{i=1}^{N} \left(V_i^2 - F^2(r_i)\right)^2. \tag{6}$$

Here, r_i and V_i are data points of our halo profiles, and $F(r_i)$ is the circular velocity for the NFW case:

$$F^2(r) = 4\pi\, G\, \rho_{\rm s}\, r_{\rm s}^3 \frac{1}{r} \cdot \left[\ln(1 + \frac{r}{r_{\rm s}}) - \frac{r/r_{\rm s}}{1 + r/r_{\rm s}}\right]. \tag{7}$$

We give each data point pair an equal weight. The interval that we consider reaches from the resolution limit $\Delta x_{\rm min} = 1.1258$ kpc to $1.5\, r_{\rm HOP}$ (for the definition see Appendix A). This corresponds to between 550 and 600 data points, depending on the size of the halo. We have also tried the range [1.1258 kpc; $r_{\rm HOP}$] for comparison, but this affected the resulting values for $r_{\rm s}$ and $\rho_{\rm s}$ only insignificantly.

The next parameter T_0 follows directly from equation (5). We have explored various values for Γ with $1.15 < \Gamma < 1.21$. The value that we found to fit our numerical density and temperature curves the best is $\Gamma = 1.19$, very close to the value $\Gamma = 1.18$ suggested by Ascasibar et al. (2003). To confirm this, we plot the logarithm of the temperature versus the logarithm of the density for the radial profiles of all 16 haloes in Fig. 1. Note that in the very inner part, our simulations prefer a steeper value with $\Gamma = 1.6$, but our adopted value is better at reproducing the density/temperature relation over the entire range of densities. Finally, the gas profile normalization ρ_0 is fixed by assuming the additional constraint

$$M_{\rm gas}(r_{200}) = \frac{\Omega_{\rm b}}{\Omega_{\rm m}} M_{\rm tot}(r_{200}), \tag{8}$$

which translates into

$$\rho_0 = \frac{\Omega_{\rm b}}{\Omega_{\rm m}} \rho_{\rm s} \frac{\ln(1+c) - \frac{c}{1+c}}{\int_0^c \left(\frac{\ln(1+x)}{x}\right)^{\Gamma} x^2 {\rm d}x}, \tag{9}$$

which, for our adopted cosmology and for the whole range of interest $4 < c < 20$, translates into a simple approximation, accurate to ± 2 per cent,

$$\rho_0 \simeq 0.208 \rho_{\rm s}. \tag{10}$$

Note that r_{200} is determined for each halo through the function

$$\Delta(r) = \frac{3}{4\pi} \frac{M(<r)}{\bar{\rho}_{\rm m} r^3}. \tag{11}$$

r_{200} is simply the radius for which $\Delta(r) = 200$ in units of the average density in the Universe, and its value is fully fixed once the two parameters $\rho_{\rm s}$ and $r_{\rm s}$ have been found.

The halo mass M_{200} directly follows.

5 HALO SELECTION

We identified galaxy group sized haloes in the *N*-body unigrid simulation at $z = 0$. At this redshift, the simulation volume contained 73 947 haloes with masses in the mass range of interest $5 \times 10^{12}\,{\rm M}_\odot\, h^{-1} < M < 5 \times 10^{13}\,{\rm M}_\odot\, h^{-1}$. Please note that these are the masses given by the halo finder HOP. The masses of our selected haloes, listed in Table 2 as M_{200}, are however the ones which come out of the NFW model, once the halo parameters $r_{\rm s}$ and $\rho_{\rm s}$ have been derived. In Appendix A, we give all details about the different methods to obtain the halo masses, and hence halo radii r_{200}. For the remaining part of this paper, we always refer to the mass and radii given by the NFW model, with M_{200} and r_{200}. To the 73 947 found haloes, we applied a series of selection criteria to ensure that we have a representative sample of group sized haloes, considering their mass accretion history and their circular velocity curves (as a measure of their spatial mass distribution). Finally, we ensured that the entire mass range is represented, by selecting quasi-randomly 16 haloes with masses distributed over the entire interval. Our selection is not entirely random, as we preferentially select relatively isolated haloes, since isolated haloes are easier to handle in zoom-in simulations. For a detailed description of the selection process, we refer to Appendix B.

In Figs 2 and 3, we plot the mass accretion history and circular velocity profile of our 16 selected haloes. One can see from these two plots that haloes that have assembled their mass early on, are also systematically more concentrated at $z = 0$. This confirms the standard scenario of halo formation (Navarro, Frenk & White 1997; Wu et al. 2013a,b), in which haloes that had their last major merger early, had more time to absorb the substructure induced from smaller haloes falling in on them. Although haloes with a late last major merger are still in the process of absorbing subhaloes into their core through dynamical processes. This interpretation is confirmed by the density maps (Figs 4 and 5). The haloes with an early formation epoch have a clean spherical shape without large substructure. Some of the haloes, classified as average, have a significant number of relatively large subhaloes, but they also show a prominent high-density core. The four haloes in our sample with late formation

Table 2. Properties of our halo sample.

Designation	M_{200} (hydro) ($10^{13}\,M_\odot\,h^{-1}$)	r_{200} (hydro) (Mpc)	c (hydro)	r_{200} (*N*-body) (Mpc)	c (*N*-body)	$z_{\rm form}$	Assembly	Mass profile
1	5.59	1.36	9.31	1.37	8.48	0.96	Average	Average
2	5.31	1.34	12.9	1.31	13.5	1.17	Early	Concentrated
3	4.27	1.24	8.91	1.25	12.2	0.69	Average	Average
4	4.04	1.22	10.7	1.2	12.3	0.79	Average	Average
5	3.07	1.11	8.79	1.1	8.69	0.75	Average	Shallow
6	2.11	0.982	10.6	0.972	11.5	1.13	Average	Average
7	1.65	0.904	16.4	0.894	16.2	1.22	Early	Concentrated
8	1.56	0.888	6.85	0.862	8.58	0.49	Late	Shallow
9	1.46	0.869	14.1	0.859	14.7	1.5	Early	Concentrated
10	1.16	0.804	8.27	0.791	7.63	0.51	Late	Shallow
11	1.01	0.768	13.9	0.729	18	1.7	Early	Concentrated
12	0.789	0.706	14.5	0.7	16	1.56	Early	Concentrated
13	0.713	0.684	7.67	0.68	7.77	0.64	Late	Shallow
14	0.616	0.651	9.57	0.622	9.85	0.59	Late	Shallow
15	0.625	0.655	10.4	0.641	11	1.04	Average	Average
16	0.537	0.622	9.85	0.622	10.7	0.67	Average	Average

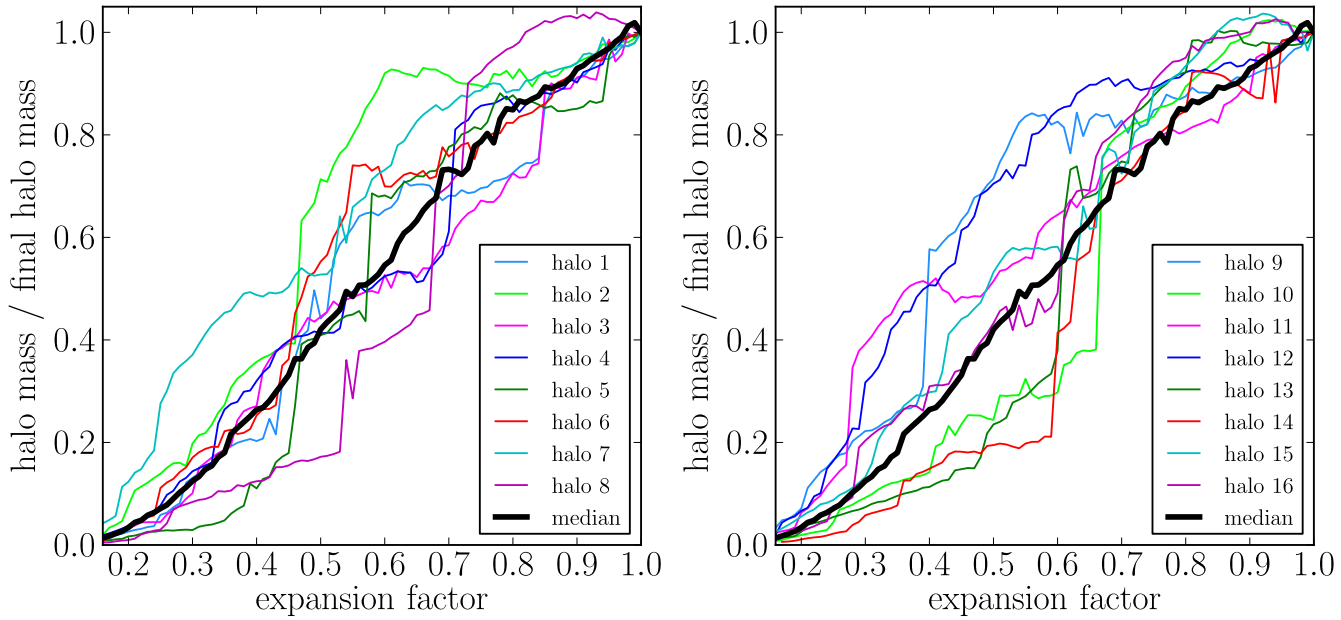

Figure 2. Halo mass as function of the expansion factor, in our N body unigrid run. This plot shows the mass accretion history of each of the 16 haloes in our sample. The black and thicker curve (labelled median) is the median of a larger sample of 108 halo within the same mass range.

epoch have less large subhaloes than the average case; however, they also lack a clearly defined high-density core. To quantify the time evolution of the haloes with a number, we define the formation redshift $z_{\rm form}$, as the redshift at which a halo has acquired 50 per cent of its final mass at $z = 0$.

A special case is depicted by halo 10. Although on the gas density map, it looks like a clean case without subhaloes, it actually consist of two subhaloes of similar mass in the process of merging, clearly visible in the dark matter projection map. Although it was identified by our halo finder as a relatively isolated halo in our adopted mass range, we did not take into account this exceptional case for our calculations of mean quantities. Nevertheless, we kept it in our sample as a typical example of a statistical outlier and quantified the deviation of its properties from the average of the other 15 haloes. The exceptional dynamical state of halo 10 can also be seen in the temperature map (Fig. 6), as a thin shock in between the two subhaloes. For the other haloes in our sample, the temperature maps show also typical signatures of strong shocks, but at larger distances from the halo centre. Old haloes (like halo 2, 7, 9 and 12) exhibit a very regular temperature structure, with a hotter core and a steady, quasi-spherically symmetric decline towards the external regions. Halo 11, on the other hand, formed early but suffered from a relatively late and massive merger, that can be seen nicely in the temperature map.

6 RESULTS

In this section, we present the results of our numerical experiment in the form of profile plots for the relevant thermodynamical and dynamical quantities. Our main points of interest are as follows:

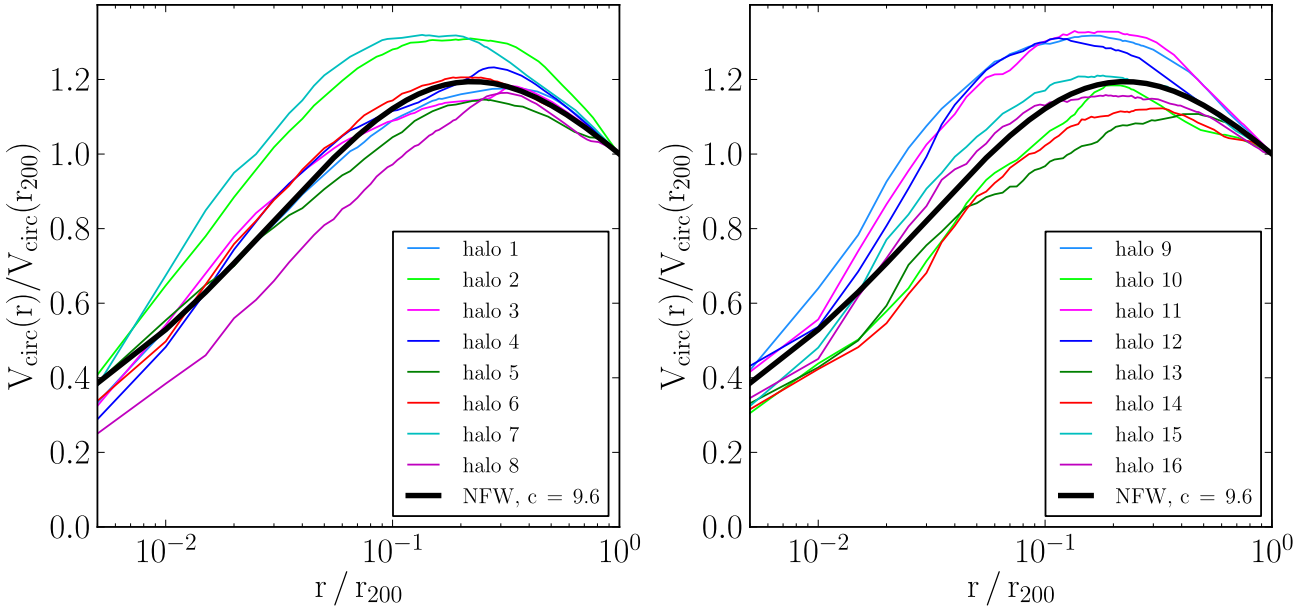

Figure 3. Circular velocity profile, in our *N*-body unigrid run. This plot shows the circular velocities of the 16 haloes in our sample. The black and thicker curve (labelled analytic) is the NFW model (Navarro et al. 1996) with a concentration parameter equal to $c = 9.6$, typical of our halo mass range (Klypin, Trujillo-Gomez & Primack 2011).

(i) How strongly do our results deviate from the analytical model we have adopted?
(ii) How strongly do individual haloes deviate from the mean?

We therefore plot the mean of our 15 haloes (excluding halo number 10) and the analytical curve together in the same plots, and quantify the variance of our sample by

$$\sigma = \sqrt{\frac{1}{N}\sum_{i=1}^{N}(x_i - \overline{x})^2} \tag{12}$$

and plot it as a shaded region around the mean curve. Furthermore, we estimate the error in our estimation of the mean by

$$\sigma_{\rm mean} = \frac{\sigma}{\sqrt{N}}. \tag{13}$$

This quantity is plotted as the error bars around the mean. The profiles were sampled with 109 radial bins in the range $0 < r < 1.5\,r_{200}$ for each halo and for all quantities, unless stated otherwise. The mean and standard deviation are also calculated at the same 109 coordinates. Values of r below the effective resolution of $\Delta x_{\rm min} = L/2^{\ell_{\rm max}} = 1.1258$ kpc are discarded.

6.1 Circular velocity profile

To characterize the radial distribution of the total mass found in our haloes, we plot the circular velocity normalized to $4\pi G\rho_{\rm s}r_{\rm s}^2$ versus the radius r normalized to $r_{\rm s}$ in Fig. 7. Our mean value is in excellent agreement with the NFW analytic model. The deviation of the mean from the analytic curve lies below 2 per cent for $r > 0.3\,r_{\rm s}$. For smaller r, it increases up to 7.5 per cent. The deviations of individual haloes from the analytical model are below 10 per cent for $r > 0.1\,r_{\rm s}$. For $r < 0.1\,r_{\rm s}$, they increase, but do not exceed 30 per cent. The variance in the total circular velocity profile reaches 30 per cent of the mean at the centre and decreases to less than 4 per cent in the outer regions. This result proves the constrained nature of the collisionless dark matter component in cosmological simulations. We conclude that, in our simulations, the total mass distribution follows the one predicted by the NFW model. The only small deviation of individual haloes from the mean can be interpreted as a resolution effect on very small scales.

6.2 Cumulative gas mass profile

The baryonic mass profile is the other integrated, cumulative quantity, and is in very good agreement with the analytical prediction (Fig. 7). The deviation of the mean profile from the analytical model lies below 20 per cent and reaches its largest value at $r_{\rm s}$. The deviations of each individual halo from the mean are all similar, except for one strong outlier, halo 10. For $r < 0.1\,r_{\rm s}$, these deviations appear as a constant offset, which for the strongest case corresponds to 40 per cent above or below the mean profile. With increasing radius, individual deviations gradually decrease to 10 per cent for $r > r_{\rm s}$. As a consequence, the variance in the gas mass profile decreases monotonically from 50 per cent of the mean at the centre to less than 1 per cent in the periphery ($r > 2\,r_{\rm s}$).

6.3 Gas density

The gas density profile is shown in the left-hand panel of Fig. 10, and exhibits a larger deviation to the mean than the cumulative mass profile.

The overall agreement with the analytical model is quite good. On closer look, however, it appears clearly that for $r < 2\,r_{\rm s}$, the analytic model underestimates systematically the simulated halo profiles, while for $r > 2\,r_{\rm s}$, the situation is reversed, and the analytical prediction systematically overestimates our numerical results. The deviation of the mean from the analytic profile is strongest at intermediate radii (around $r = 0.5\,r_{\rm s}$) with 25 per cent, where it appears larger than the standard deviation. This deviation of the analytical profile from our numerical mean is therefore significant around $r_{\rm s}$ and should be taken seriously.

The deviations of individual haloes from the mean have a maximum value of 50 per cent at the centre (not considering our outlier

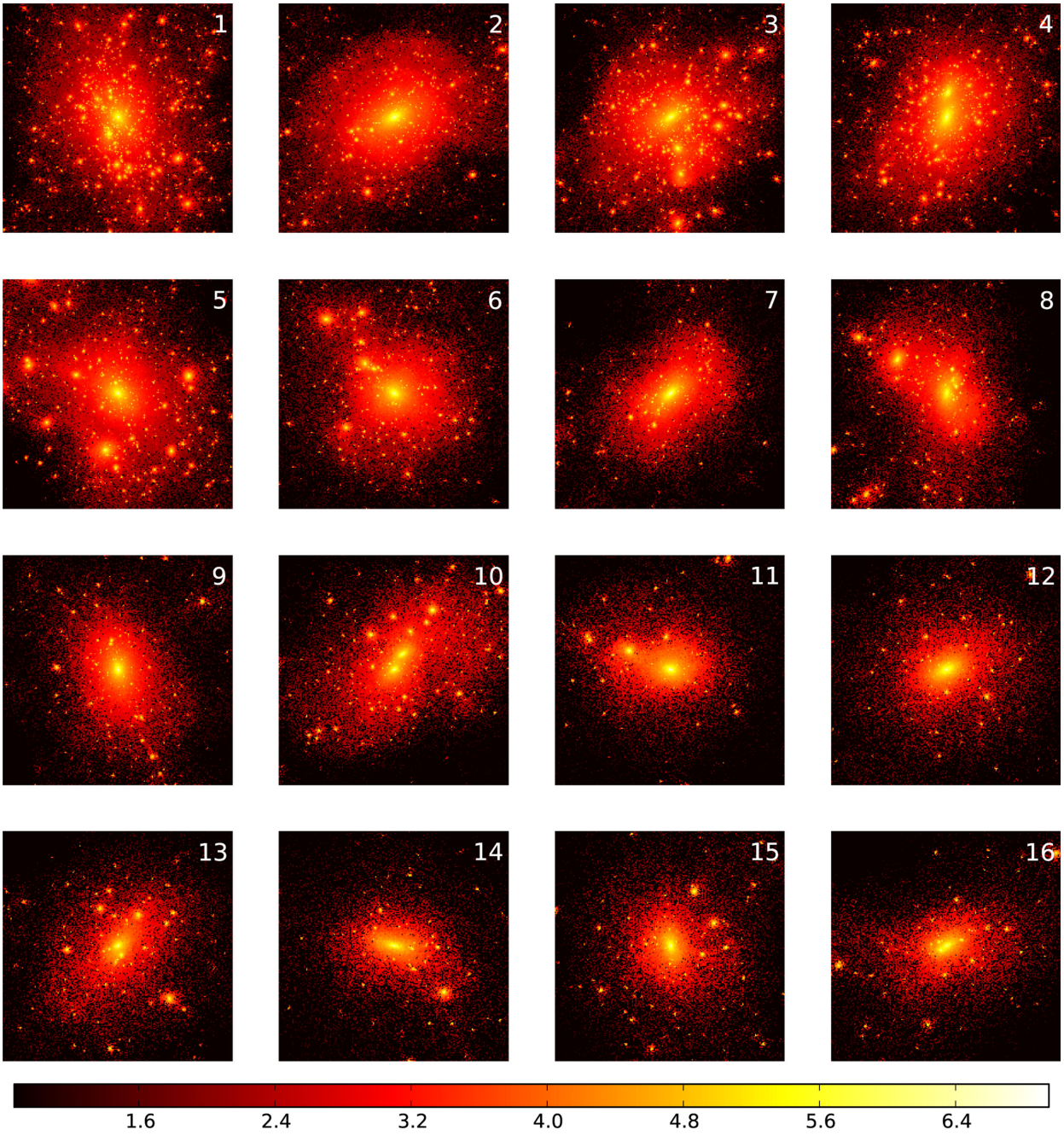

Figure 4. Dark matter density maps in our *N*-body zoom-in runs. The colour bar unit is $\log_{10}(\rho_{\rm m}/\bar{\rho}_{\rm m})$, where $\bar{\rho}_{\rm m}$ is the average matter density in the Universe. The side length of each map is $2R_{200}$, with the centre of the maps corresponding to the centre of mass of the halo.

halo 10), in the form of constant offsets. In the range $r > r_{\rm s}$ the deviations are smaller (around 20 per cent to 30 per cent), mostly in the form of random peaks for each of the 16 haloes. This translates into a standard deviation of 35 per cent in the periphery and 50 per cent in the centre.

The second feature can be explained by the existence of substructure in the outer parts of the haloes. The first one is less obvious. We interpret it as different levels of entropy after the last major mergers, due to different circumstances occurring at halo formation time. This argument was used by Hahn et al. (2015) to explain the dichotomy between cool core and non-cool core clusters. In our case, low angular momentum mergers would give rise to almost head-on collisions and higher post-shock entropy levels, resulting in a systematically higher temperature and lower density in the core. We will come back to this point in Section 7.

We find that our numerical average has a typical density core in the centre. In the non-radiative hydrodynamics simulations of the nIFTy comparison project by Sembolini et al. (2016), this feature is shown to be typical for grid-based and modern smoothed particle hydrodynamics (SPH) codes. The same authors report that classical SPH codes give gas density profiles which rise all the way to the centre, leading to a disagreement with grid-based codes of one order of magnitude.

Furthermore, our gas density profile is in agreement with the one from the earlier study of Ascasibar et al. (2003), where a modern,

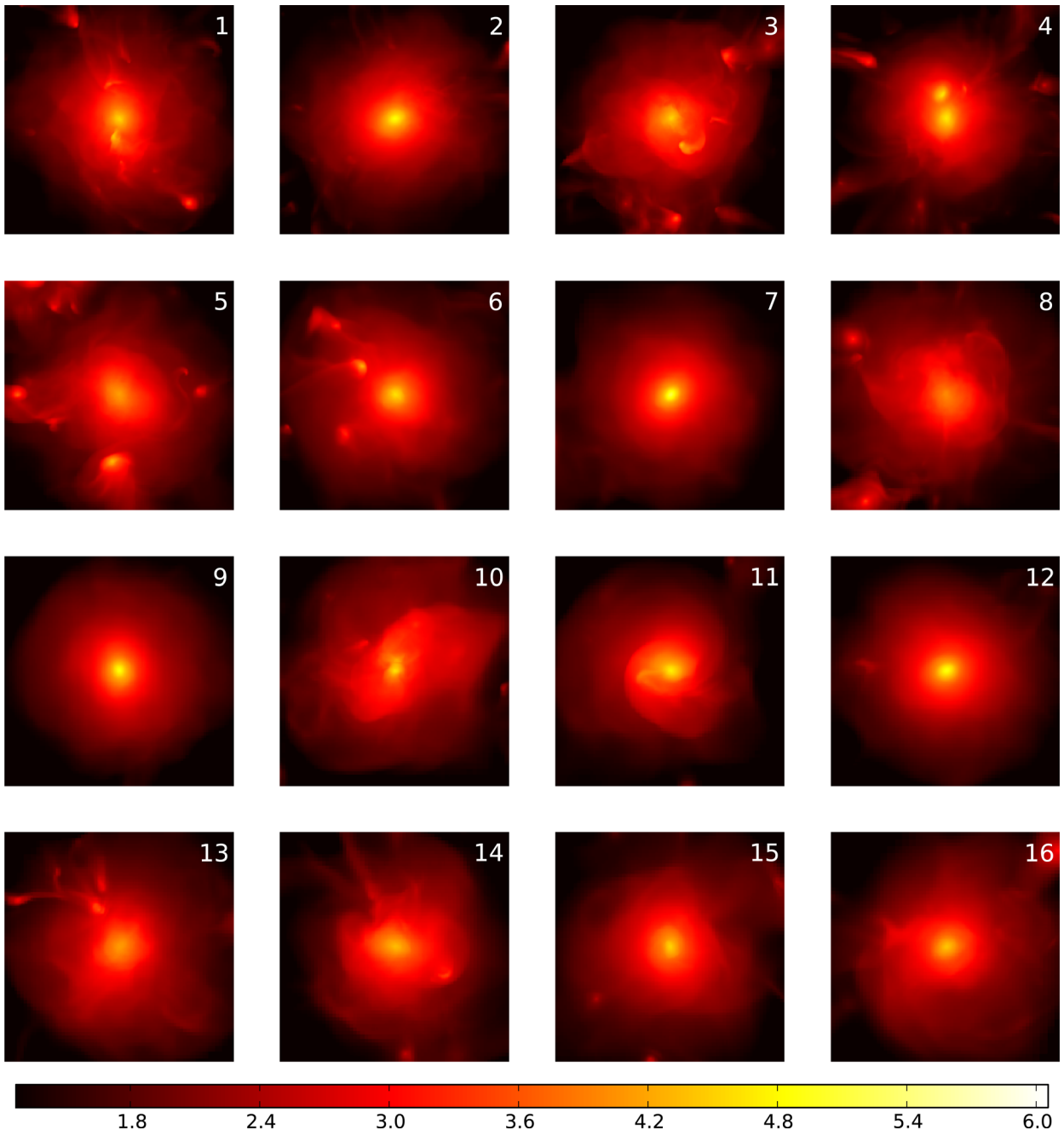

Figure 5. Gas density maps in our non-radiative hydrodynamics zoom-in runs. The colour bar unit is $\log_{10}(\rho_{\rm gas}/\bar{\rho}_{\rm b})$, where $\bar{\rho}_{\rm b}$ is the average baryon density in the Universe. The side length of each map is $2R_{200}$, with the centre of the maps corresponding to the centre of mass of the halo.

entropy conserving version of the SPH code GADGET was used. They also report a good agreement with the same analytical model, around 20 per cent. However, their gas density profile deviates mostly in the outer parts, whereas our numerical mean deviates mostly in the intermediate range $r \simeq r_{\rm s}$.

6.4 Gas temperature profile

We have computed for each halo the temperature profile by averaging the temperature from individual adaptive mesh refinement (AMR) cells within the same 109 spherical bins (with a mass-weighted average). We have then computed the mean of all 15 profiles (again excluding halo 10), as well as the variance. These are shown on Fig. 8 and compared to the analytical prediction (see equation 2). One clearly sees a small but systematic difference between the analytical model (red dashed curve in Fig. 8) and our measurement. As explained in Shaw et al. (2010) and Battaglia et al. (2012), we argue this is due to the contribution of the turbulent pressure in the halo, which is missing in the analytical model. To quantify the effect of turbulence, we have computed the turbulent energy profile, by averaging in each spherical bin the mass-weighted velocity dispersion as

$$v^2_{\rm turb}(r) = \frac{1}{3}\frac{1}{M}\int (v_x^2 + v_y^2 + v_z^2)\,\rho {\rm d}V, \qquad (14)$$

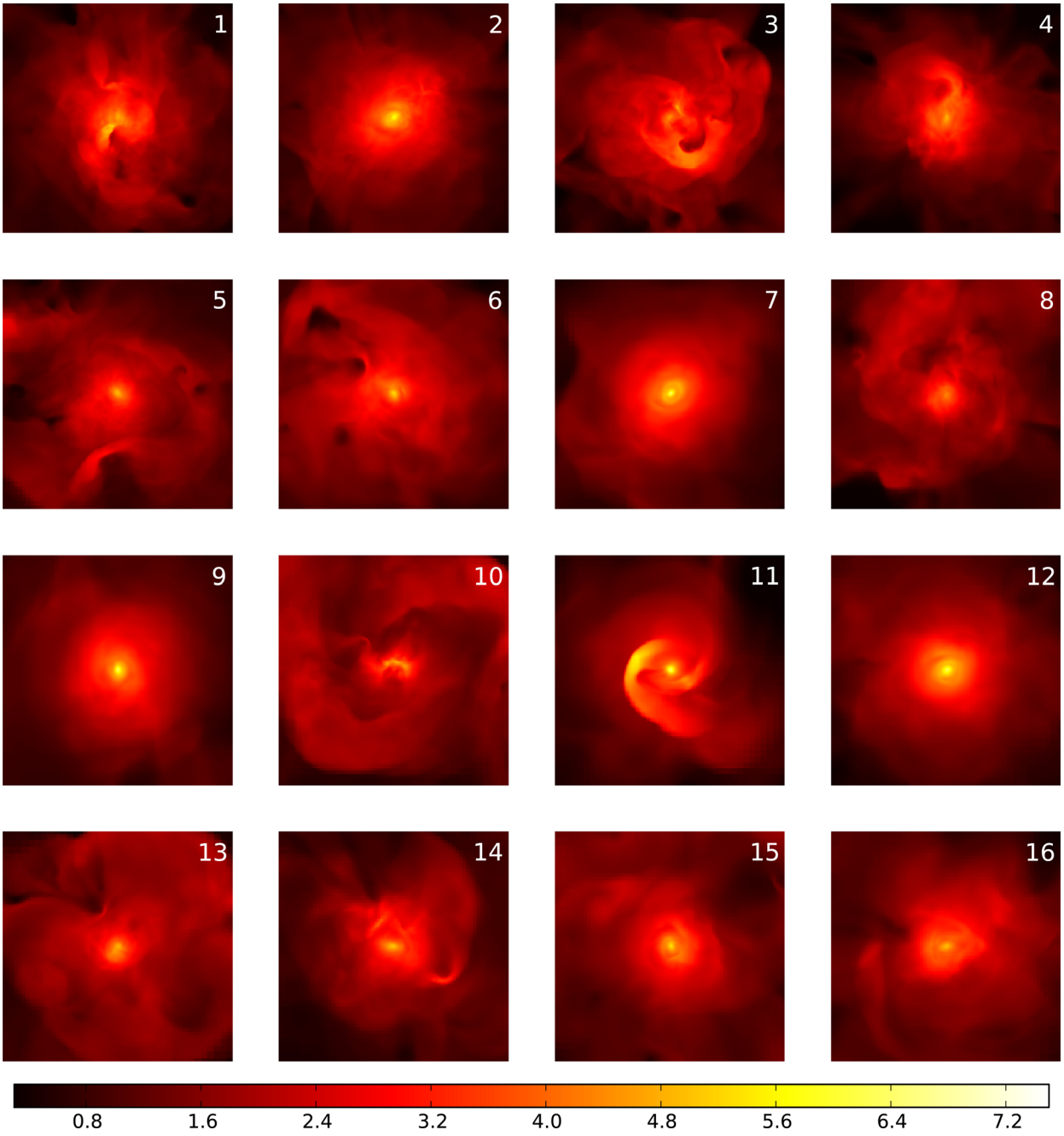

Figure 6. Gas temperature maps in our non-radiative hydrodynamics zoom-in runs. The colour bar unit is $T_{\rm gas}/T_{200}$, where T_{200} is computed for each individual halo as $T_{200} = \frac{1}{3}\frac{m_p}{k_B}\frac{G\,M_{200}}{R_{200}}$. The side length of each map is $2R_{200}$, with the centre of the maps corresponding to the centre of mass of the halo.

where the v_i are the components of the velocity of the gas in the frame of the halo centre of mass. We have then converted this velocity dispersion into a turbulent temperature as

$$T_{\rm turb}(r) = \frac{m_{\rm h}}{k_B} \cdot v^2_{\rm turb}(r). \tag{15}$$

The average turbulent temperature profile (with error bars) and its standard deviation are both plotted on Fig. 8. To first order, the turbulent specific energy appears as constant, with a mean value around $0.06\,T_0$. On closer look, it is in fact slightly rising with radius, with a central value around $0.03\,T_0$, reaching in the outer parts $0.10\,T_0$. We propose the following fitting function for the turbulent temperature

$$T^{\rm fit}_{\rm turb}(r) = \left(0.03 + 0.007\frac{r}{r_{\rm s}}\right) T_0, \tag{16}$$

shown as the green solid line in the right-hand panel of Fig. 8. When one now subtracts from the analytical temperature profile this fit for the turbulent, non-thermal energy

$$T^{\rm cor}_{\rm gas}(r) = T_{\rm ana}(r) - T^{\rm fit}_{\rm turb}(r), \tag{17}$$

one gets much better agreement with our numerical data (see the green solid curve in the left-hand panel of Fig. 8), especially in the outer parts where turbulence is the strongest.

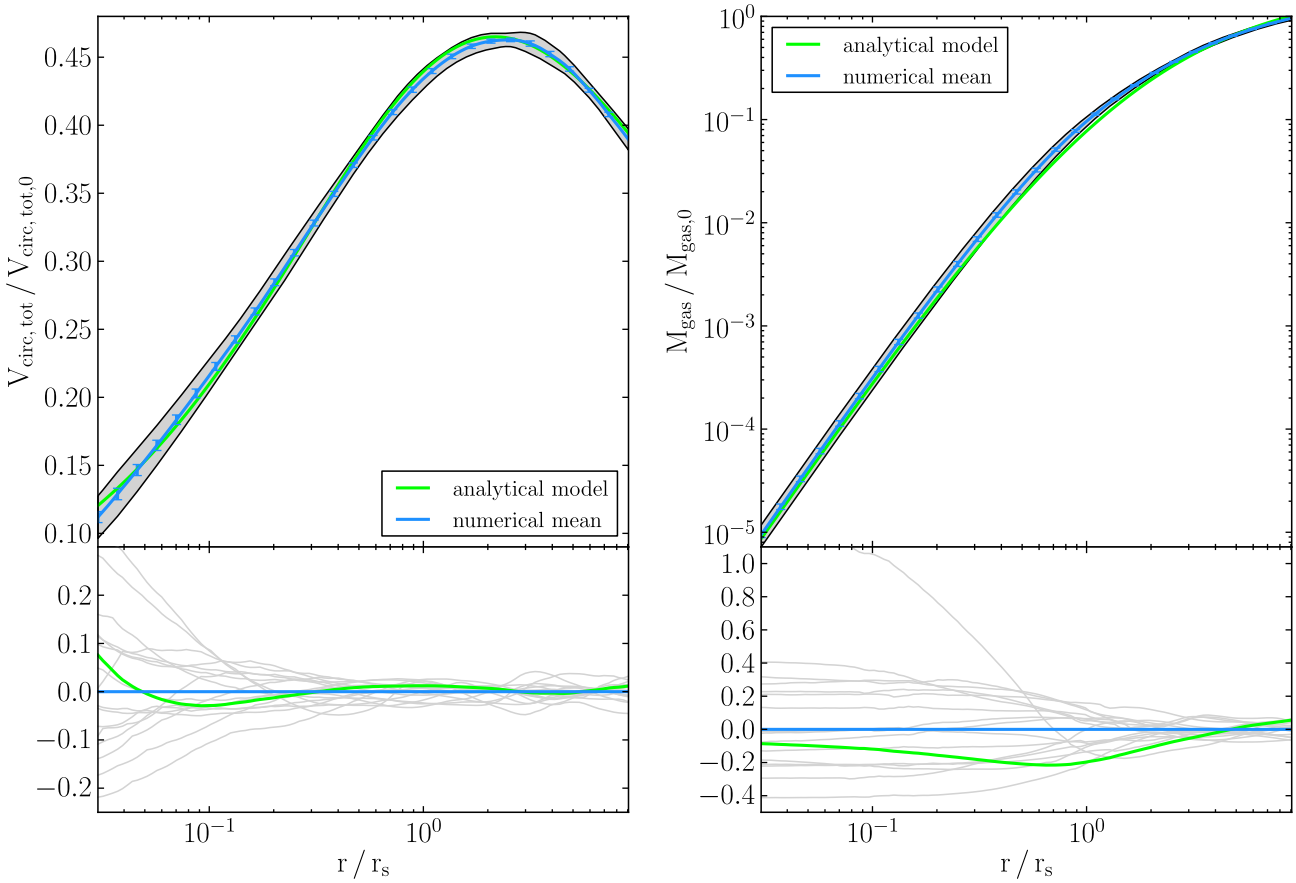

Figure 7. Total circular velocity and gas mass profiles: in the upper plot, the blue curve with error bars is the numerical mean of the 15 haloes, the grey shaded area is the variance of the numerical mean and the blue error bars indicate the error of the mean. The analytic prediction is plotted in green. In the lower panel, the deviations from the numerical mean are plotted. Green is again the analytic value and the individual haloes' deviations are depicted as thin grey lines.

The final agreement between our corrected analytical model and the numerical data is quite good (less than 15 per cent) but is far from perfect. The maximum disagreement lies around r_s and peaks at 15 per cent. At this radius, the numerical gas temperature lies significantly below the analytical prediction. It is worth noticing that this radius corresponds also to the maximum discrepancy observed in the gas density profile, where this time the numerical gas density lies significantly above the analytical prediction.

Individual halo temperature profiles deviate from the mean in the centre with an almost constant offset, never exceeding 15 per cent. This constant offset in the central temperature is related to the constant offset we have discovered in the central density. This is again due to different merger circumstances at halo formation time (see Section 6.3). In the outer parts, $r > r_s$ the deviations are characterized by peaks and troughs, which we associate with the presence of both substructure and turbulence. At these radii, the deviations from the mean can reach 35 per cent in the extreme cases.

The variance in the gas temperature profile is also constant in the centre with a value close to 16 per cent of the mean for $r < 0.5\,r_s$ and decreases from there to less than 10 per cent at $r \simeq r_s$, only to increase again to 35 per cent around $r \simeq 3\,r_s$. Finally it reduces to 10 per cent in the outermost range.

The temperature profiles measured in Ascasibar et al. (2003) show a much better agreement with the hydrostatic analytical model. The variance of the temperature profile appears also much more regular and slightly smaller (around 20 per cent). From a first naive look, a possible interpretation for the smoother profiles in these earlier SPH simulations could be coming from the selection strategy in Ascasibar et al. (2003), where major mergers were first identified and then removed from the sample. In our work, only halo 10 classifies as a major merger in this sense. And since we excluded it from the computation of the numerical average (as mentioned above), the difference in the temperature variance, between the two works, cannot arise from the removing of major mergers. For the better agreement with the uncorrected analytical profile, we argue that the SPH method used in Ascasibar et al. (2003) is known to dissipate subsonic turbulence too efficiently. Indeed, as demonstrated nicely in Bauer & Springel (2012), standard SPH techniques underestimate the turbulent energy by a factor between 2 and 10, depending on the scales considered. This reduces artificially the non-thermal pressure support, especially in the outer parts where turbulence is the strongest, and as a consequence provides a better but spurious match to the strict hydrostatic model. Interestingly, Loken et al. (2002) have also found a universal temperature profile (using mock X-ray observations) using non-radiative AMR simulations similar to ours. Ascasibar et al. (2003) have directly compared their SPH simulations to the AMR simulations of Loken et al. (2002) and have found a systematic 10 per cent positive difference between SPH and AMR results, explained by the stronger turbulence support in the AMR case.

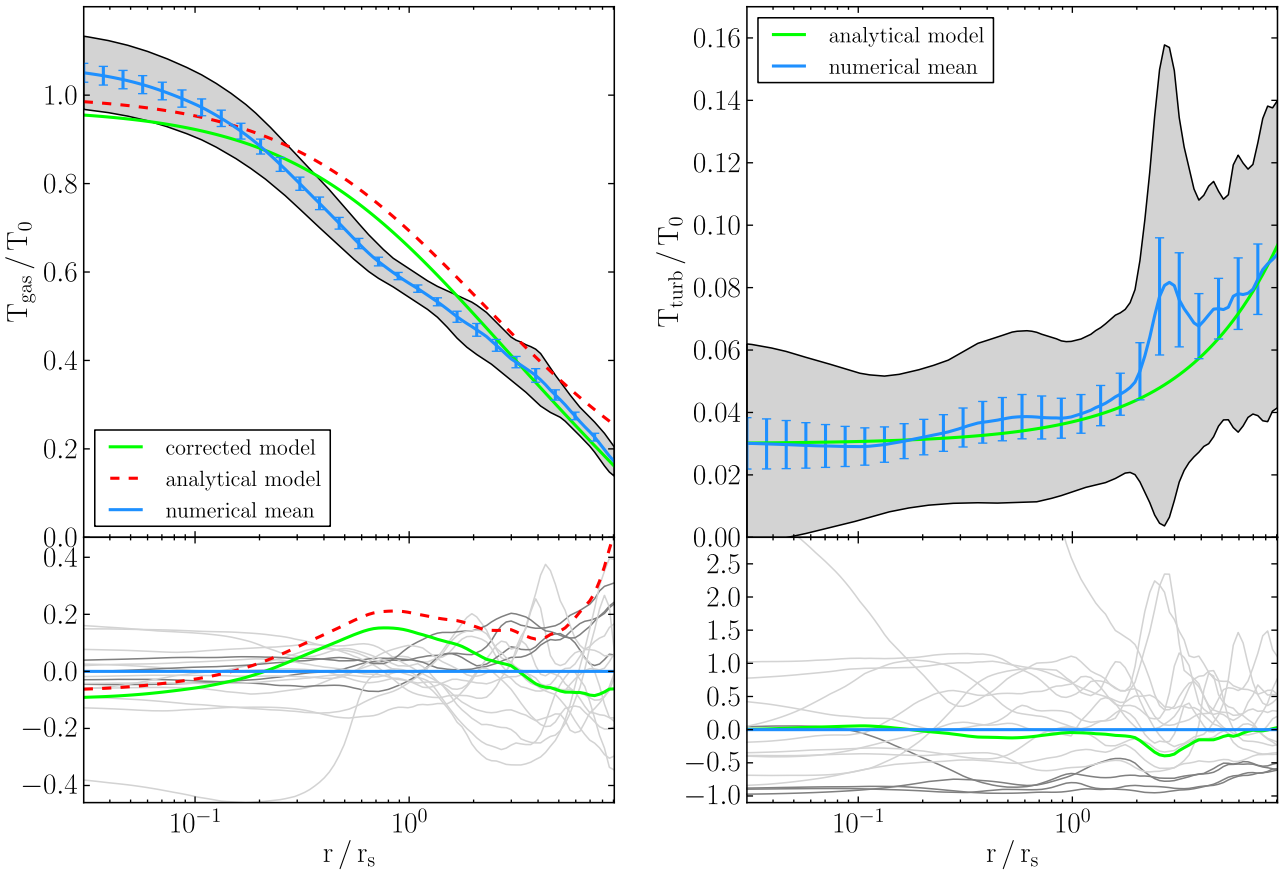

Figure 8. Gas temperature and turbulent gas temperature profiles: the green line in the turbulent temperature plot is the fitted analytical model and the green line in the temperature plot is the corresponding corrected analytical model. In addition, the uncorrected analytic curve of the gas temperature is plotted in dashed red, in the plot of the gas temperature. The colour code of the individual halo deviations is explained in the text.

6.5 Turbulence and substructure

As already presented in the previous section, the level of turbulent energy in our simulated haloes is relatively low and uniform, between 3 per cent and 10 per cent of the thermal energy, estimated here as the central temperature T_0. This is agreement with Lau et al. (2009) and Martizzi & Agrusa (2016), who report very similar values. Note that for the latter work, the authors used a model with a constant turbulent specific energy, while in our case, we see a clear, although not very strong, increase of the turbulence specific energy with radius, confirming the analytical theory presented in Shi & Komatsu (2014) and Shi et al. (2015). From individual halo turbulent profiles (see Fig. 8), one can see pronounced peaks in the profiles for $r > r_s$. This is a direct consequence of substructure in the outer regions of the haloes. This translates in a very large variance for the turbulence, usually up to 100 per cent, but even larger in some cases.

In our catalogue, we have a subsample of four haloes with very low levels of turbulence: haloes 2, 7, 9 and 12, which all show very smooth gas density maps (Fig. 5) and were classified as early formation epoch. We have highlighted this subset (halo 2, 7, 9 and 12) with a darker grey line in Fig. 8, to show that these four haloes have a significant and almost constant deficit of turbulence compared to the mean. This comparison directly indicates a strong correlation between turbulence and substructure on one hand, and concentration and formation epoch, on the other hand. The latter is because haloes which have had their last major merger early have had more time to see the turbulence decay. As a result, these haloes are well virialized, with low levels of turbulence and have temperature profiles closer to the uncorrected analytical model. To support further these conclusions, we have investigated possible correlations between the thermodynamical properties, the concentration parameter c and the formation redshift z_{form} in Section 7.

The complementary viewpoint is given by our outlier halo 10, which consist of two subhaloes of similar mass in the merging process at $z = 0$. In this case, the gas temperature in the centre shows a deficit with respect to the mean as high as 50 per cent. The turbulent energy, on the other hand, overshoots the mean value by a factor of 10, meaning that in the case of this halo, the turbulent energy in the centre is almost 30 per cent of T_0, accounting for almost all the missing thermal energy, which is needed to balance the HSE situation. This kinetic energy is stored in the velocity of the relative motion of the two merging subhaloes, waiting to be dissipated into heat when their orbital separation will shrink to zero. This shows, that when the kinetic energy of the turbulence is taken into account, even haloes which are far from being virialized (like halo 10), can still be compared to a model of HSE.

6.6 Pressure

Since the gas pressure is proportional to the product of gas temperature and gas density, it could be considered in a sense as a redundant

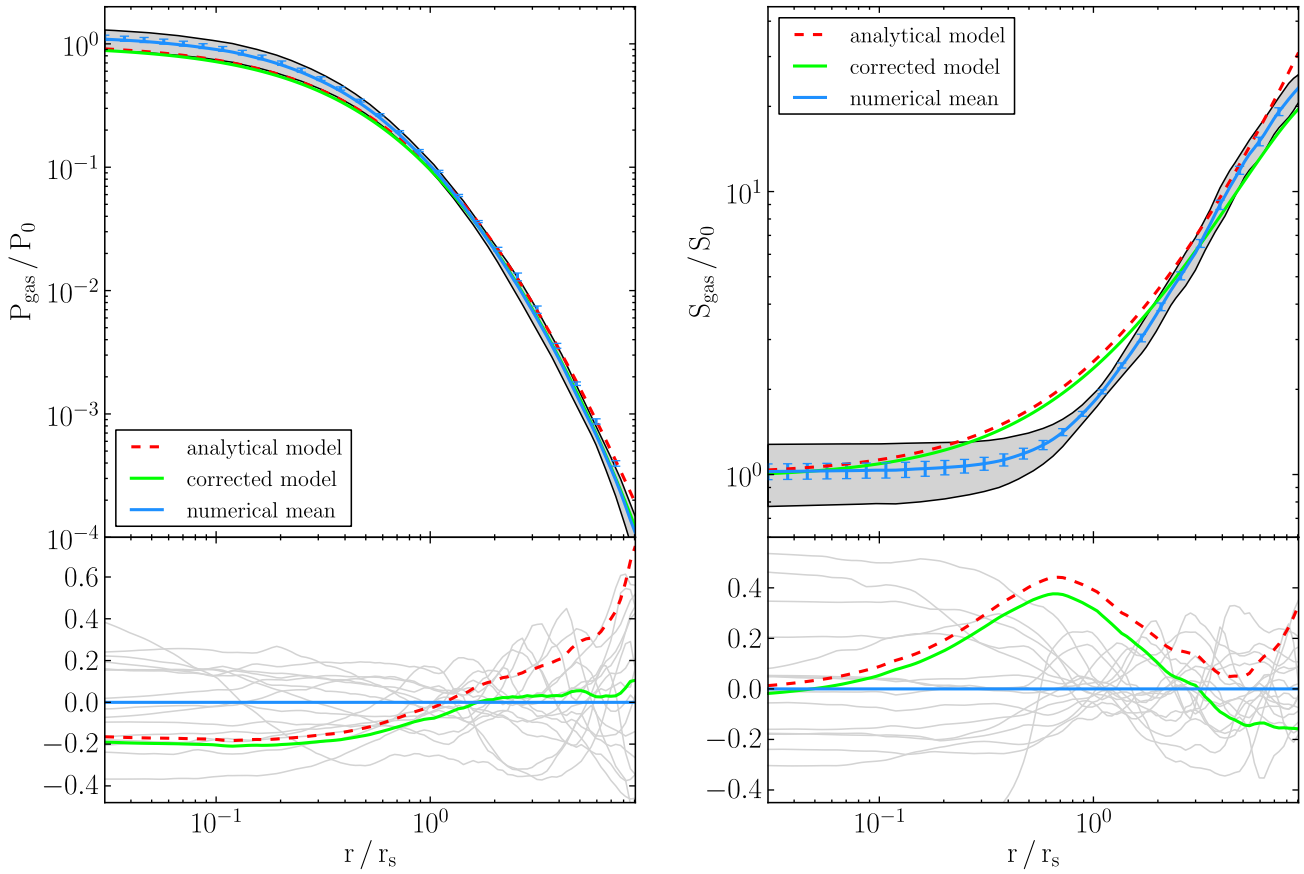

Figure 9. Gas pressure and gas entropy profiles: the green line in the pressure plot is the corrected analytical model. In addition the uncorrected analytic curve of the gas temperature is plotted in dashed red. The colour code of the entropy profile is the same.

quantity. We nevertheless plot it in Fig. 9 to emphasize three distinct features.

First, while it shows quantitatively the same behaviour as the gas density, the variance being significantly smaller in the central region. Secondly, the agreement of our mean profile with the corrected analytical model is quite good, especially in the outer parts $r > r_s$ (less than 10 per cent), and still good in the inner parts $r < r_s$ with less than 20 per cent. We do not see a significant disagreement particularly around $r \simeq r_s$, like for the density and the temperature profiles. Thirdly, the peaks and the troughs in the outer regions are more pronounced than for the density and the temperature, as they reach 60 per cent for the pressure, while for the density (respectively the temperature) they reach only 20 per cent (respectively 35 per cent).

We interpret the first two features as coming from the close connection between the gas pressure and the total mass distribution through the HSE equation. The small deviations in the pressure profile reflect the small deviations in the circular velocity profile of the total mass, just as the good agreement with the corrected analytical model for the pressure reflects the good agreement with the analytical model of the total mass circular velocity. The third feature is due to shocks associated with substructure collapsing through the main halo and converting their kinetic energy into heat.

The difference between the corrected and uncorrected analytical model is barely visible for $r < r_s$ (less than 5 per cent). But it increases significantly in the outer regions, where it reaches 60 per cent. The obvious interpretation is the existence of an additional pressure support in the form of turbulent pressure in the outer parts, which is not taken into account by the original analytical model, but which is captured correctly by the corrected version (see Section 6.4).

6.7 Gas entropy profile

The gas entropy profile, highly relevant for X-ray observations, is defined as

$$S_{gas}(r) = \frac{T_{gas}(r)}{\rho_{gas}(r)^{2/3}} \tag{18}$$

and is plotted in Fig. 9. We find two different regimes: a constant entropy core for $r < 0.5\, r_s$ and a steep entropy increase for $r > 0.5\, r_s$. This increase of the entropy in the outer parts is predicted by our analytical model, but it fails at reproducing the sharp transition towards a flat core that we observe in our simulations.

Nevertheless, the agreement between the model and our numerical mean is quite good, it shows again a significant (40 per cent) deviation around r_s. The deviation of each individual halo from the mean profile follows from the structure of the density and temperature profiles: a constant offset in the centre (with up to 50 per cent deviation for some haloes) and several low amplitude peaks and troughs at large radii ($r > r_s$) due to substructures.

The constant entropy core in the centre and the steep increase in the outer parts are consistent with our finding that the relation

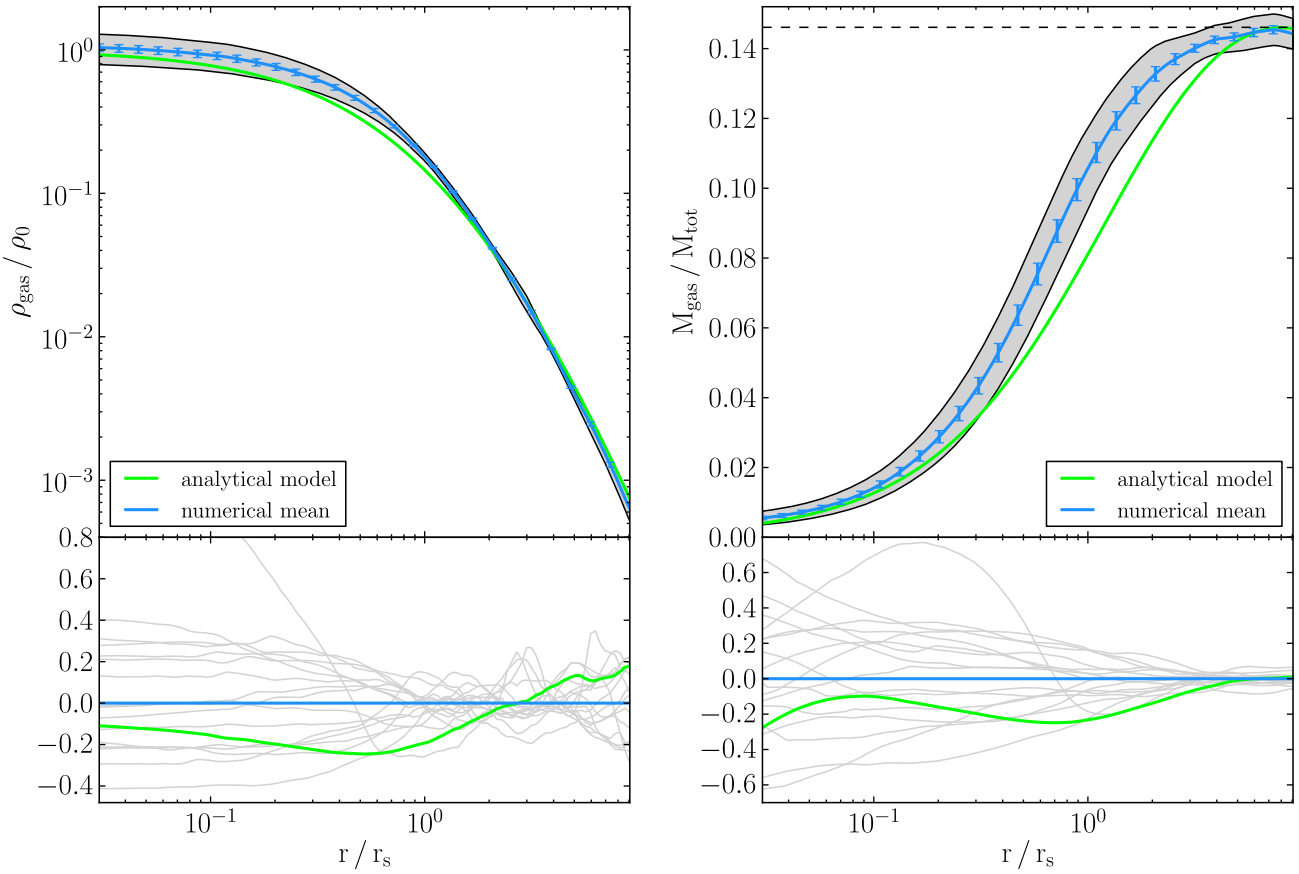

Figure 10. Gas density and mass fraction profiles: the colour code is the same as in Fig. 7. For a better comparison with observational results, we have plotted the unnormalized gas mass fraction profile (right-hand panel). The analytical curve of it is plotted for the case of $c = 8$. The dashed line indicates the universal mass ratio of baryons to total matter.

between the density and the temperature revealed in Fig. 1 seems to exhibit two regimes:

(i) the core regime, at high density, for which the entropy is nearly uniform, as a consequence of the strong mixing following substructure mergers, and resulting in a polytropic law of $\Gamma \simeq 5/3$,
(ii) the halo regime, at low density, for which the entropy is rising with increasing radius, as a result of the evolution of the accretion shock leaving behind a stratified, convectively stable atmosphere with $\Gamma \simeq 1.2$.

This bi-modal, core–halo evolution is at odd with the main assumption of the polytropic analytical model, namely a unique value for $\Gamma = 1.19$. This explains why we see significant deviation between our numerical mean and the analytical model around $r \simeq r_s$.

In Sembolini et al. (2016), the constant entropy core is reported for all grid-based and modern SPH codes. Classical SPH implementations, on the other hand, show a continued steep decrease towards the centre. This dichotomy has been discovered first by Frenk et al. (1999), but with the caveat that the resolution was quite limited for most of the participating codes. In the outer parts, however, all codes seem to agree on the steep increase of entropy. The grid-based simulation analysis of Nagai et al. (2007) confirmed the presence of a flat entropy core in non-radiative simulations.

In the work of Ascasibar et al. (2003), the agreement between the measured entropy profiles and the analytical model is better than in our case, around 30 per cent, with the analytical model lying below the numerical profiles. We believe that these differences are due to different level of entropy mixing in the central region, leading to a less pronounced constant entropy core in the Ascasibar et al. (2003) results.

6.8 Cumulative gas mass fraction

Another important observable for X-ray astronomy is the cumulative gas fraction defined as

$$f_{\rm gas}(<r) = \frac{M_{\rm gas}(<r)}{M_{\rm tot}(<r)}. \tag{19}$$

Within our analytical framework, this quantity is not strictly self-similar, and varies very weakly as a function of the concentration parameter c. We plot the gas fraction as a function of the scaled radius in Fig. 10, and compare it to our analytical solution for the specific case $c = 8$. Other models with values of c between 4 and 20 are very close (within 2 per cent) to this reference curve.

The agreement between the mean profile and the analytical model is quite good, but we see again a clear difference, larger than the standard deviation, in the range $0.5\,r_s < r < 2\,r_s$. Note that we recover exactly the universal baryon fraction (shown as the horizontal dashed line) already at $r \simeq 3\,r_s$. The analytical model satisfies the same constraint by construction (see Section 4). The variance in the numerical prediction is quite small, less than 20 per cent, except again for the outlier halo 10.

When comparing again to Ascasibar et al. (2003), we note that their SPH results barely reach 90 per cent of the universal baryon

fraction at $r \simeq 10\,r_s$. This is a significant difference with our results. Sembolini et al. (2016) have reported the same discrepancy between different codes, with SPH codes showing a systematic deficit of baryons at large radii, while grid-based codes reaching the universal baryon fraction already at relatively small radii, and in most cases even overshooting it. One could speculate that because dark matter is collisionless, dark matter particle are splashing back to larger radii after their first pericentre passage, and because gas is collisional, it gets shocked and remains trapped at smaller radii. Both facts combined, this could lead to a deficit of dark matter and an excess of baryon in the halo outer regions, as we observe in our non-radiative simulations and in Sembolini et al. (2016) for grid-based codes.

6.9 Summary

We have quantified the dispersion of our profiles with respect to the average profile by measuring the variance with typical values of 10–20 per cent of the numerical mean. In extreme cases, it can reach up to 35–50 per cent. Individual halo profiles deviate up to 20–40 per cent from the mean, and are mostly in the form of constant offsets in the centre and in the form of peaks and troughs in the outer regions.

We have also estimated how well the numerical results reproduce the analytical profiles predicted by the model introduced in Section 4. We find an overall good agreement for all quantities. In the case of the gas temperature, however, our numerical results significantly underestimated the analytical prediction. We argued that we have to include to the pressure support a significant contribution of the turbulence, especially in the outer regions. We have fitted the turbulent specific energy with a simple linear function of the radius, and subtracted it from the analytical temperature profile. After this correction, the deviations of the analytical model from the numerical mean remain smaller than 20 per cent.

We have confirmed the results of Ascasibar et al. (2003), namely that the analytical hydrostatic and polytropic gas profiles resulting from an NFW total mass distribution (equations 2 and 3) are good estimates for the actual numerical profiles. Note that we have observed a very good agreement between the total mass profile (gas and dark matter combined) and the NFW model. We would like to point out, however, that Ascasibar et al. (2003) fitted the NFW model to the dark matter mass distribution, ignoring the baryons. This could partly explain why, in their case, they seem to find an excellent agreement between the numerical temperature profile and the uncorrected analytical model, without the need for invoking turbulence. We have checked this issue by extracting the NFW parameters r_s and ρ_s from the circular velocity plot of the dark matter mass only, as in the previous work by Ascasibar et al. (2003). Our assumption was partly confirmed, since we found a better agreement between the uncorrected analytical and numerical curves in the intermediate range $0.5\,r_s < r < 5\,r_s$. Above and below this interval, however, the differences between the two curves became even larger. The other possibility is that their SPH simulations are underestimating by a factor of 2 (or more) the level of residual turbulent energy. Note that our mass resolution is higher by a factor of 20 than was achievable more than 10 yr ago. The size of their sample is similar to ours, with 15 haloes, but they are distributed over a wider mass range and contain also galaxy cluster sized objects.

We also noticed that Ascasibar et al. (2003) measured a smaller variance for the profiles than we did. A possible underestimation of the turbulence, could explain this discrepancy. Our results agree also very well with the fig. 1 of Nagai et al. (2007) obtained with a sample of 16 galaxy clusters simulated with the Eulerian code ART. For the gas density and temperature profiles, we have reproduced the behaviour at small radii reported in Sembolini et al. (2016), for grid-based codes and modern SPH codes, namely a core of constant entropy in the centre, in contrast to this classical SPH codes with an entropy profile decreasing all the way to the centre.

7 CORRELATIONS BETWEEN HALOES STRUCTURAL PARAMETERS

In the previous section, we have compared our sample of 16 haloes to an hydrostatic analytical profile. For a given halo mass, usually defined by M_{200}, one needs to introduce an important structural parameter, namely the concentration parameter c. The statistic of this parameters has been well studied using N-body simulations (Bullock et al. 2001), and can be considered as an independent random variable. Once M_{200} and c have been chosen, we can deduce the corresponding values for r_s and ρ_s, and the hydrostatic equations give us immediately T_0 and ρ_0 (see Section 4).

In order to improve the quality of the fit for a given halo, we now introduce two new structural parameters $\rho_{\rm gas}$ and $T_{\rm gas}$, which denotes the central gas density and the central gas temperature. We have seen in Sections 6.3 and 6.4 that each individual halo profile was offset with respect to the analytical prediction ρ_0 and T_0 by a fixed amount. We interpreted this constant offset in the centre as different entropy levels reached at halo formation time. We now consider these two new parameters $\rho_{\rm gas}$ and $T_{\rm gas}$ as two possible independent random variables, and will study now their correlation properties.

In the previous section, we have used the turbulent energy to correct the analytical gas temperature, in order to account for non-thermal pressure support, and we have identified a correlation between the amount of turbulent energy in each halo and its formation epoch. The level of turbulence in the halo is therefore another new and important structural parameter. We define it as

$$\frac{k_{\rm B}T_{\rm turb}}{m_{\rm H}} = \frac{1}{M(<r_{\rm max})}\int_0^{r_{\rm max}} v^2_{\rm turb}(r)\rho(r)4\pi r^2{\rm d}r, \qquad (20)$$

where $r_{\rm max} = 10.8\,r_s$ is used as upper bound of the integral because 10.8 is the average c value. For comparison, we have also calculated the integral by using the $r_{200} = c \cdot r_s$ value of each individual halo as upper limit. This had only an insignificant influence on the result.

We now show the correlation of the various pairs of the following five possibly independent random variables ($\rho_{\rm gas}$, $T_{\rm gas}$, $T_{\rm turb}$, c, $z_{\rm form}$) in Fig. 11. To quantify the correlations between two random variables, we calculate the Pearson correlation coefficient C and show it in the corresponding panel.

The correlation between c and $z_{\rm form}$ is very high, with a Pearson coefficient of 0.85. These well-known properties (see for example Bullock et al. 2001) reveal that concentrated haloes have formed at an earlier epoch. As we have already anticipated, we also have strong anticorrelations between $T_{\rm turb}$ and c with a Pearson coefficient of -0.7 and, similarly between $T_{\rm turb}$ and $z_{\rm form}$ with a correlation coefficient of -0.6. For the particular cases of haloes 2, 7, 9 and 12 (labelled with numbers in Fig. 11), one can see that they form a subset of haloes that formed particularly early, with a rather high concentration and a rather low level of turbulence. The opposite is true for halo 8, which formed late, has a low concentration and a large amount of turbulence.

While there is no correlation between the central gas parameters $\rho_{\rm gas}$ and $T_{\rm gas}$ and the halo structural parameters c and $z_{\rm form}$, the central gas quantities themselves are strongly anticorrelated with a

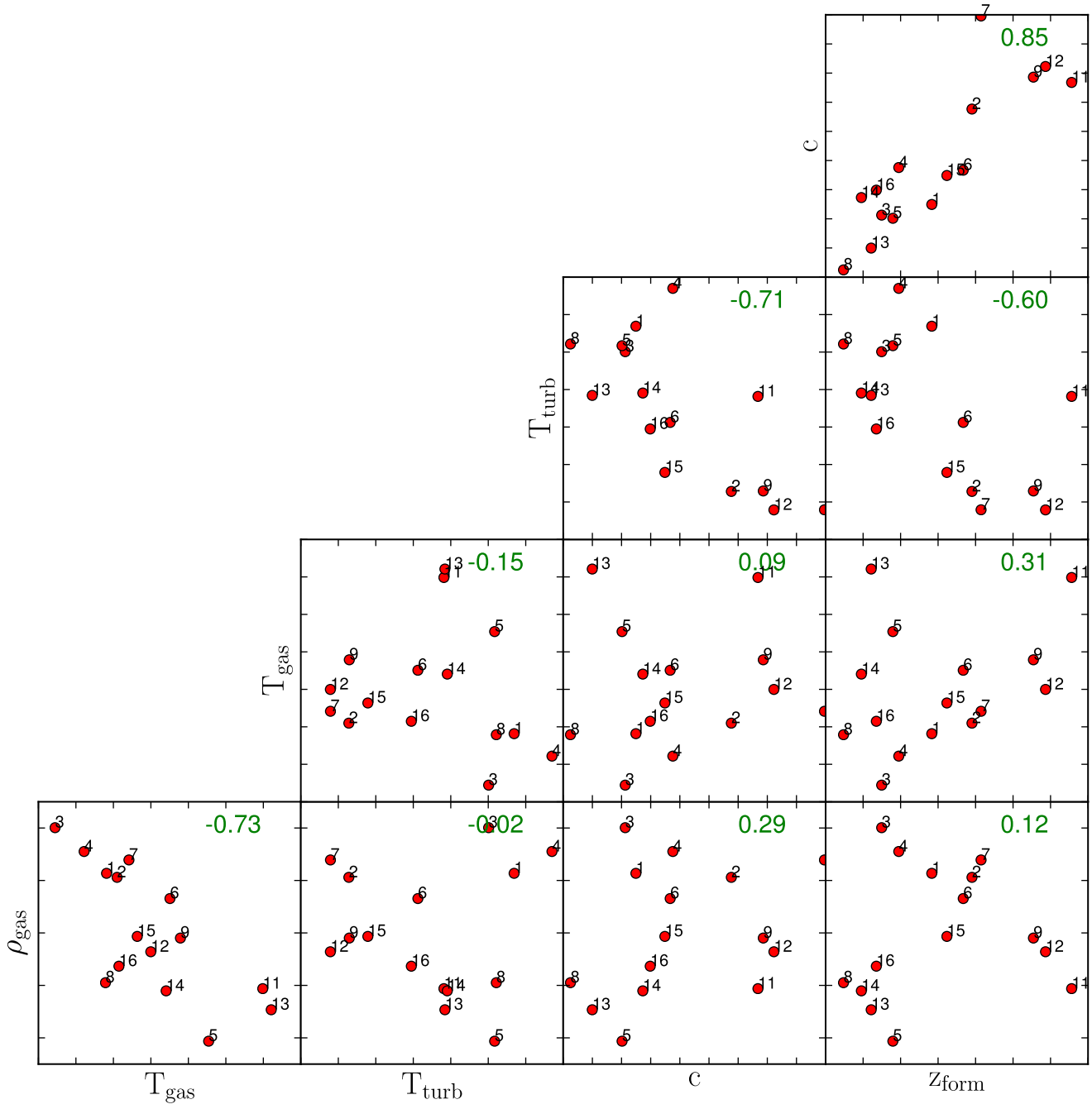

Figure 11. This plot shows the correlation between the three structural parameters of the gas (central density, central temperature and average turbulent temperature) and the two structural parameters of the halo (formation redshift and concentration). The number in the upper right of each panel is the respective Pearson correlation coefficient, computed without halo 10.

Pearson coefficient of −0.73. We interpret this anticorrelation as the consequence of different merger scenarios at halo formation time, with almost head-on collisions leading to higher entropy levels (with a lower density and a higher temperature) and with higher angular momentum collisions leading to lower entropy levels (with a higher density and a lower temperature). In our sample, halo 10 is a prototypical example of such head-on collisions, while halo 11 shows a nice case of a merger with a high angular momentum clump. This interpretation was proposed first by Hahn et al. (2015) as a possible origin for the cool core/non-cool core dichotomy observed in X-ray clusters.

In conclusion, once we know M_{200}, we can draw the concentration parameter c from a lognormal statistic (Bullock et al. 2001). We can immediately deduce the expected level of turbulence using the observed correlation between $T_{\rm turb}$ and c in Fig. 11. We then draw another random variable for $\rho_{\rm gas}$, with a 40 per cent variance around ρ_0, and deduce immediately the central gas temperature using the observed correlation between $T_{\rm gas}$ and $\rho_{\rm gas}$ in Fig. 11. This strategy

could be used to generate a mock catalogue with very accurate and realistic non-radiative gas properties.

8 EFFECT OF NUMERICAL PARAMETERS

We have presented so far the radial profiles of various quantities, comparing the mean value of a sample of 15 haloes to a reference analytical profile. The variance from halo to halo gives the upper envelope of the required accuracy for the analytical model. We have found that the analytical model deviates significantly (more than the measured variance) from our numerical mean around the scaled radius r_s, leading us to the conclusion that the single polytropic model is probably too naive, and does not reflect the bi-modal, core–halo structure of our simulated haloes.

We now want to test the robustness of these conclusions against possible numerical errors. For this, we selected one halo in our sample, halo 2, and re-ran a series of zoom-in simulations, varying the following numerical parameters: mass and spatial resolution, type of initial conditions, ingredients of the hydrodynamics solver. We then compare the resulting profiles with the fiducial run, using the same quantities discussed in Section 6. To assess if numerical errors are significant, we again use the variance of the profiles of the 15 haloes.

8.1 Effect of resolution

To ensure that our simulation are numerically converged, we ran two additional zoom-in simulations for halo 2, where only the maximum level of the initial condition was reduced from our fiducial value $\ell_{\rm ini} = 11$ (high resolution), down to $\ell_{\rm ini} = 10$ (medium resolution) and $\ell_{\rm ini} = 9$ (low resolution). This translates into mass resolutions of $m_{\rm DM} = 8.2 \times 10^6\,{\rm M}_\odot\,h^{-1}$, $m_{\rm gas} = 1.6 \times 10^6\,{\rm M}_\odot\,h^{-1}$ (high resolution) $m_{\rm DM} = 6.6 \times 10^7\,{\rm M}_\odot\,h^{-1}$, $m_{\rm gas} = 1.2 \times 10^7\,{\rm M}_\odot\,h^{-1}$ (medium resolution) and $m_{\rm DM} = 5.3 \times 10^8\,{\rm M}_\odot\,h^{-1}$, $m_{\rm gas} = 1.0 \times 10^8\,{\rm M}_\odot\,h^{-1}$ (low resolution).

The radial profiles for the runs with non-radiative hydrodynamics are shown in Fig. 12. The high-resolution profiles are considered here as the reference profiles, and we used the variance over the 15 haloes to estimate the required level of accuracy to test for convergence. One can see that the medium- and high-resolution runs are both within the shaded area for all quantities, meaning that the measurements are converged within the target accuracy. Since halo 2 has a mass of $M_{200} = 5.3 \times 10^{13}\,{\rm M}_\odot\,h^{-1}$, this means we need at least 1 million particles within R_{200} to have fully converged profiles over the radius range 0.1–10 in units of r_s. In the low-mass range of our sample, this requirement is only reached at high resolution, hence validating the adopted resolution for the entire sample.

8.2 Effect of the initial conditions

Our initial conditions were generated using the MUSIC code (Hahn & Abel 2011). Several options are offered to the users of MUSIC to generate the initial particle positions and velocities, as well as the initial gas density and velocity fields. In this paper, we considered the same transfer function for the combined dark matter and baryonic fluid. We do not explore the possibility to use different transfer functions for the two fluids, as it is likely to have a small effect on the large scales we consider in this paper.

We have still the option to compute the particle positions using either the Zel'dovich approximation, also referred to as first-order Lagrangian perturbation theory (1LPT), or the second-order Lagrangian perturbation theory (2LPT). It has been argued (Reed et al. 2013) that the latter is required for relatively late starting redshift ($z_{\rm ini} \simeq 50$), while 1LPT is enough for early starting redshift ($z_{\rm ini} \geq 100$). Note that for zoom-in simulation using AMR, it is particularly important to start as late as possible, to make sure that the truncation errors in the potential calculation remain smaller than the initial physical perturbations, justifying the use of 2LPT in this context.

For the gas, we have also two options offered by MUSIC. Either we use the Gaussian random density fluctuations linearly extrapolated to the starting redshift, using in a sense first-order Eulerian perturbation theory, or we use the density field corresponding to the adopted Lagrangian Perturbation Theory for dark matter. The second option is referred to a local Lagrangian approximation (LLA), and ensures that the gas density fluctuations are consistent with the slightly non-Gaussian dark matter density field. For more details and references, we point the interested reader to Hahn & Abel (2011).

The various options, 1LPT or 2LPT for dark matter, and with or without LLA for baryons, result in four different combinations summarized in Table 3. For our group catalogue, we use as fiducial choice 2LPT without LLA. We justify this choice in this section, showing that our results are not sensitive to the details in the initial conditions, given the target accuracy set by the relatively variance in the profiles. For further studies requiring a better accuracy, we argue that the best combination would be however to choose 2LPT with LLA.

The simulated profiles using the different initial conditions (see Fig. 13) show only small deviations from the profile of the reference run for all four quantities. Please, note that deviations in the temperature profile appear larger, since it is plotted with linear scale, whereas the other plots use a logarithmic scale. Nevertheless, deviations remain always smaller than the grey shaded area indicating the variance in the corresponding profile, meaning that the details of the initial conditions generator do not play a role in this paper.

8.3 Effect of the hydrodynamics solver

We would like to test the robustness of our results with respect to the numerical parameters of the Godunov solver used in the RAMSES code. As explained in Fromang et al. (2006), these are the adopted Riemann solver, which can be either LLF or HLLC, and the slope limiter, either MinMod or MonCen. For the Riemann solver, we have adopted the less diffusive one, the HLLC Riemann solver, and discarded completely LLF, because it is notoriously diffusive. For the slope limiter, we explored the MinMod scheme, which is more diffusive but also more robust (our fiducial choice) and MonCen, which is more accurate but also less robust.

We show in Fig. 14 the maps of the gas density distribution and in Fig. 15 the maps of the temperature distribution for halo 2, using our two slope limiters and our three different resolutions. We see much more substructures for the more accurate, MonCen slope limiter, while for the more diffusive slope limiter MinMod, substructures seem to have been washed away, although, on closer look, they are still visible but very weak. To quantify this spectacular effect, we have plotted in Fig. 16 the effect of the slope limiters on the measured profiles. It appears now clearly that both slope limiters are converging to the same result, MonCen converging from above while MinMod is converging from below. Interestingly enough, the a priori more accurate scheme systematically overestimate the mean converged profile, while the a priori more diffusive scheme converges faster to the right solution, systematically

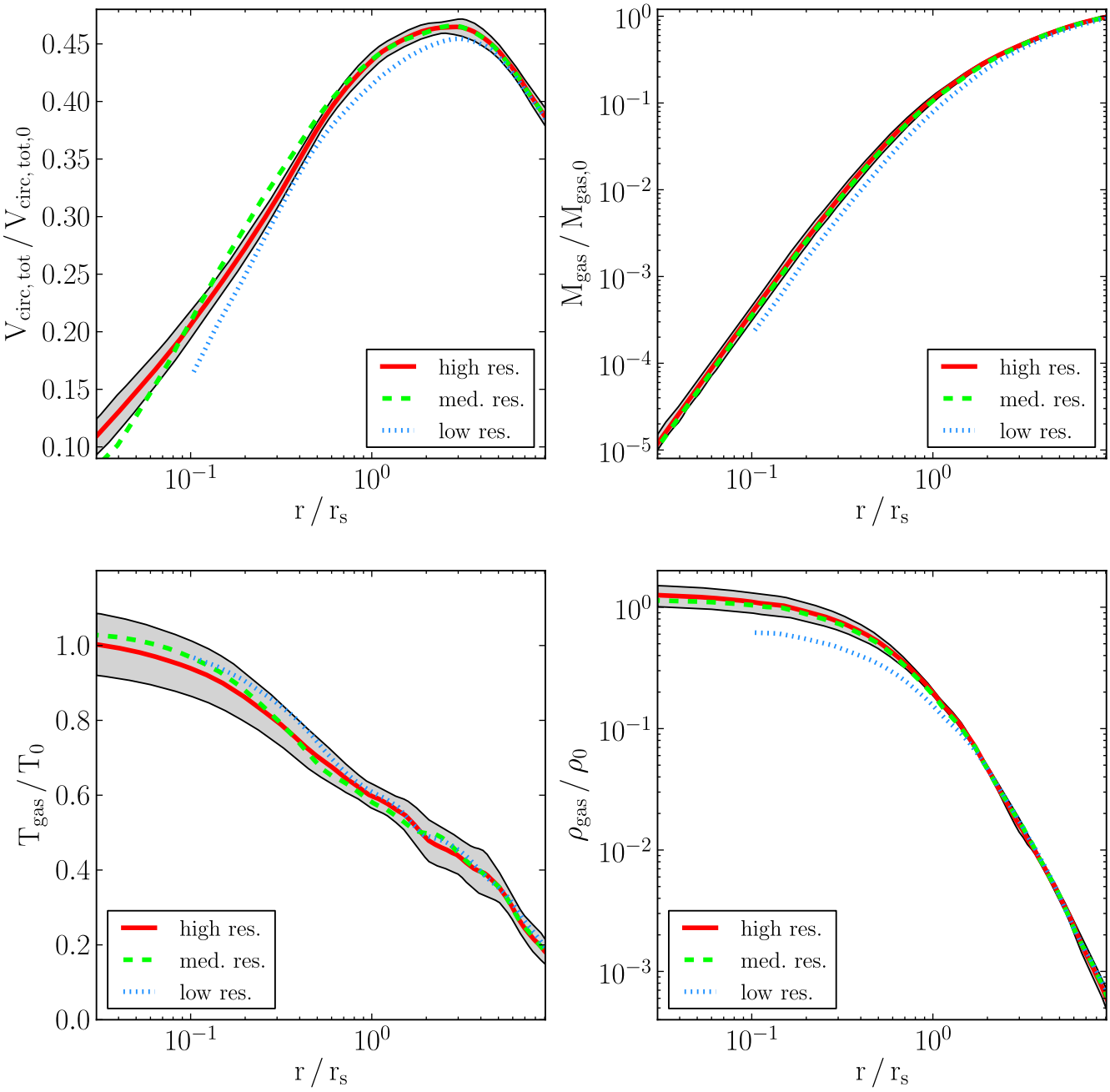

Figure 12. The total circular velocity, gas mass, gas temperature and gas density profiles of halo 2 for the three different resolutions under consideration. For comparison the variance of the numerical mean of the 15 haloes, as it is defined in Section 5, is also plotted as grey shaded area.

Table 3. MUSIC numerical parameters.

2LPT	LLA	Run name
Yes	No	2LPT, no LLA
Yes	Yes	2LPT, with LLA
No	No	1LPT, no LLA
No	Yes	1LPT, with LLA

underestimating the right answer. Our conclusion is therefore that once one uses enough resolution elements, namely one million particles per halo, the influence of the slope limiter becomes smaller than the variance (shown in Fig. 16 as the grey shaded area).

Since we have related the presence of substructure to the strength of turbulence, a very subtle effect, we would like to quantify the effect of the slope limiters to the level of turbulence in the halo. In Fig. 15, one can see small and cold clumps with a clear bow shock structure ahead of them. This nicely resolved shocks could inject kinetic energy and power turbulence. We show in Fig. 17 the turbulent temperature profile for our two slope limiters and our three resolutions. One can see again that the more diffusive slope limiter gives us a smoother turbulence distribution, while the more accurate slope limiter preserves the substructure longer, giving rise to spikes in the turbulent energy in the vicinity of the substructure. Note that the overall profiles remain very similar, independently of the adopted resolution and slope limiter, especially if one considers

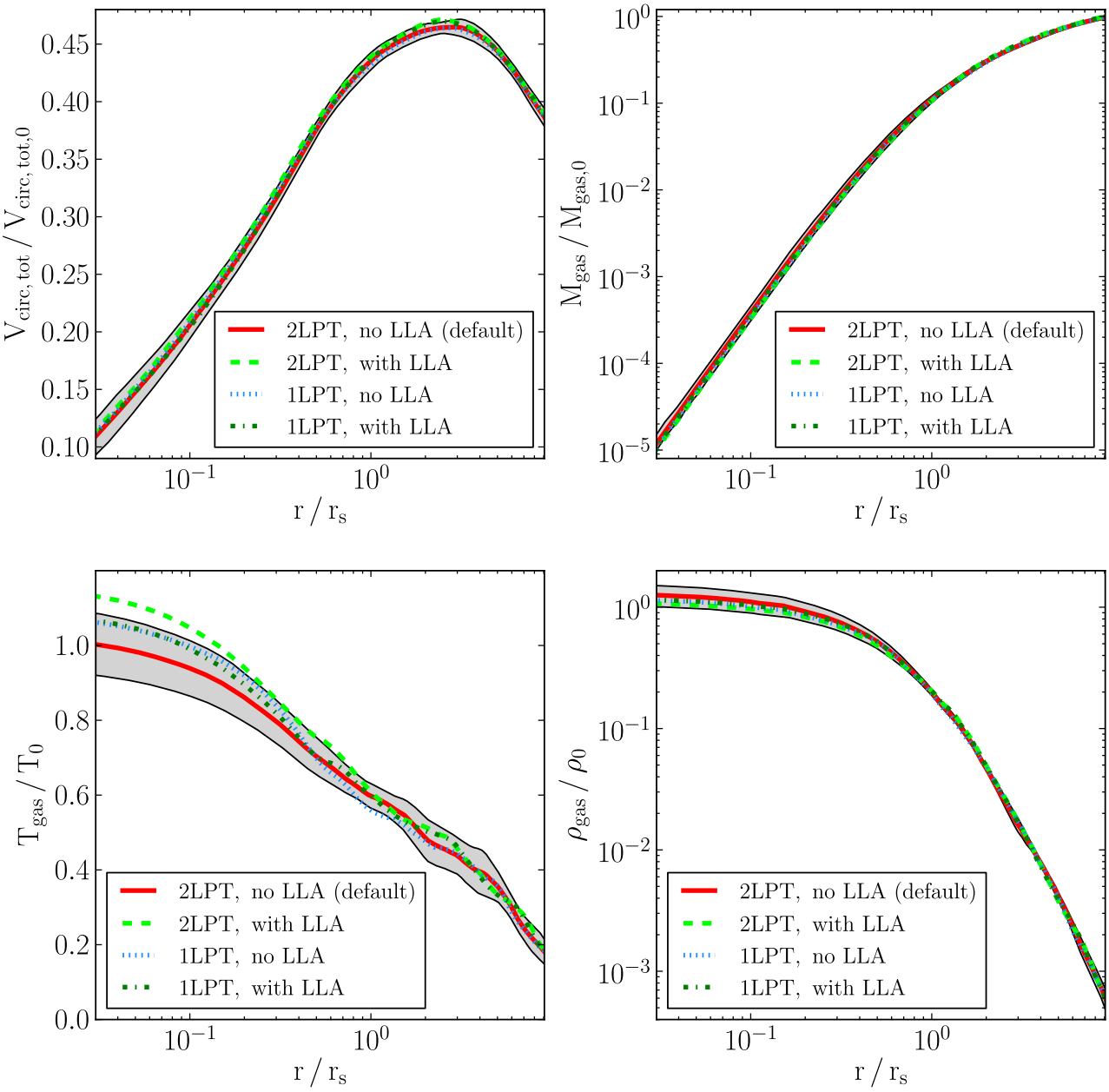

Figure 13. The total circular velocity, gas mass, gas temperature and gas density profiles of halo 2 for the four different initial condition settings under consideration. For comparison the variance of the numerical mean of the 15 haloes, as it is defined in Section 6, is also plotted as grey shaded area.

the very large variance we observe in the various turbulence profiles. Interestingly, our highest resolution temperature profiles show a rather large difference in the central region between MinMod and MonCen, the latter being colder than the former. A similar but opposite effect is seen in the turbulent temperature profile, proving that this is a minor transient feature. Indeed, at the exact time we have analysed our simulation's snapshot, turbulence was not entirely dissipated in the case of the MinMod slope limiter, while the MonCen slope limiter gives us a slightly more evolved snapshot for which kinetic energy has been transformed into heat.

8.4 Summary

We showed in this section, that changing the resolution to lower levels can have an effect on to the profiles of halo 2 mostly around 10 per cent. The medium-resolution profile deviations, from the high-resolution profile, are far less than the variance coming from the individual halo nature. The low-resolution profiles reach deviations from the high resolution ones, which are in the order of magnitude of the variance.

Altering the initial condition settings has only a minor effect on to the profiles of the four quantities considered, leading to deviations that are smaller than the extend of the individual halo variance, for almost all *r*-values.

The variation of the hydro solver slope limiter also causes deviations, which are smaller than the ones of the variance (of the order of 10 per cent), but only when the highest resolution is applied. In case of the medium resolution, the deviations are of the order of magnitude of the variance, and for the lowest resolution they are considerably larger. A very interesting

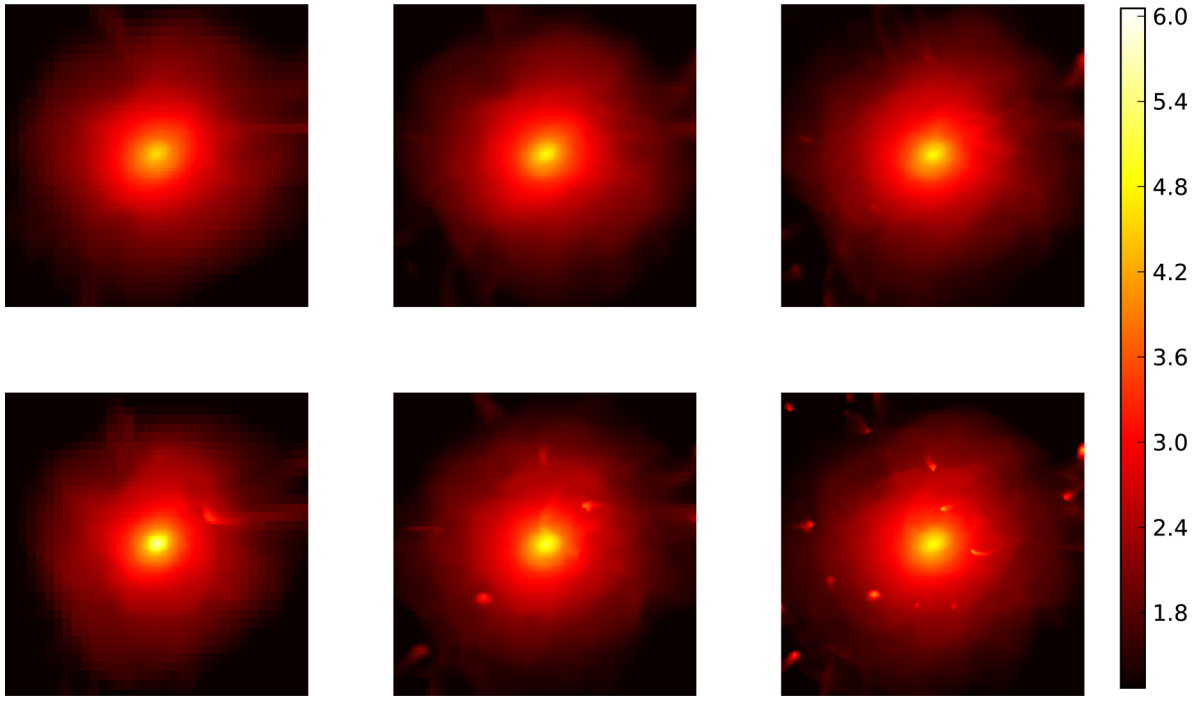

Figure 14. Baryon density maps of halo 2 for the two slope-type specifications: the upper three maps correspond to MinMod slope type and the lower three to MonCen slope type. The resolution is increasing from left to right: low ($\ell_{\rm ini} = 9$), medium ($\ell_{\rm ini} = 10$) and high ($\ell_{\rm ini} = 11$). The colour bar unit is $\log_{10}(\rho_{\rm b}/\bar{\rho}_{\rm b})$, where $\bar{\rho}_{\rm b}$ is the baryon density of the Universe. The side length of each map is $2r_{200}$, while the centre of the maps correspond to the centre of mass of the halo.

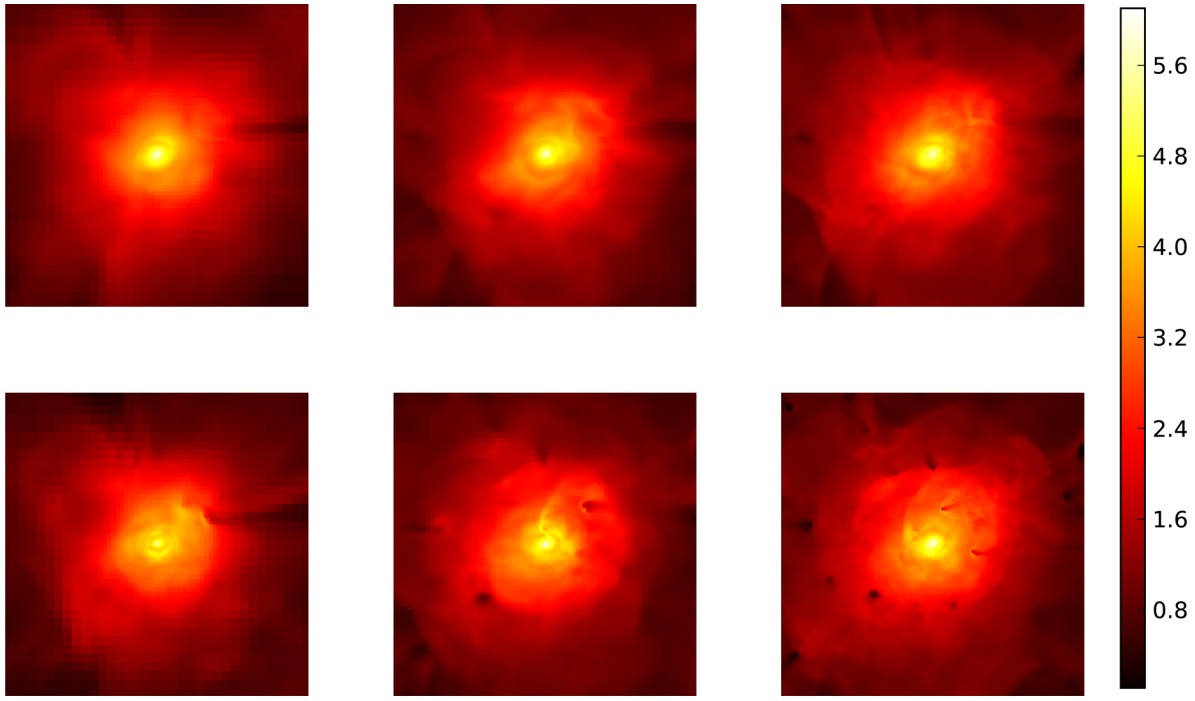

Figure 15. Baryon thermal temperature maps of halo 2 for the two slope-type specifications: the upper three maps correspond to MinMod slope type and the lower three to Moncen slope type. The resolution is increasing from left to right: low ($\ell_{\rm ini} = 9$), medium ($\ell_{\rm ini} = 10$) and high ($\ell_{\rm ini} = 11$). The colour bar unit is $T_{\rm gas}/T_{200}$, where T_{200} is defined as $T_{200} = \frac{1}{3}\frac{m_p}{k_B}\frac{G\,M_{200}}{R_{200}}$. The side length of each map is $2r_{200}$, while the centre of the maps correspond to the centre of mass of the halo.

feature of the hydro solver comparison plot (Fig. 16) is that for MonCen the two lower resolution curves converge towards the high resolution one from above, whereas for the MinMod setting, they converge from below. In the latter case they also converge faster. The most noticeable feature however is that the MonCen runs show more substructure, and hence turbulence, than the runs with MinMod. This effect increases with increasing resolution.

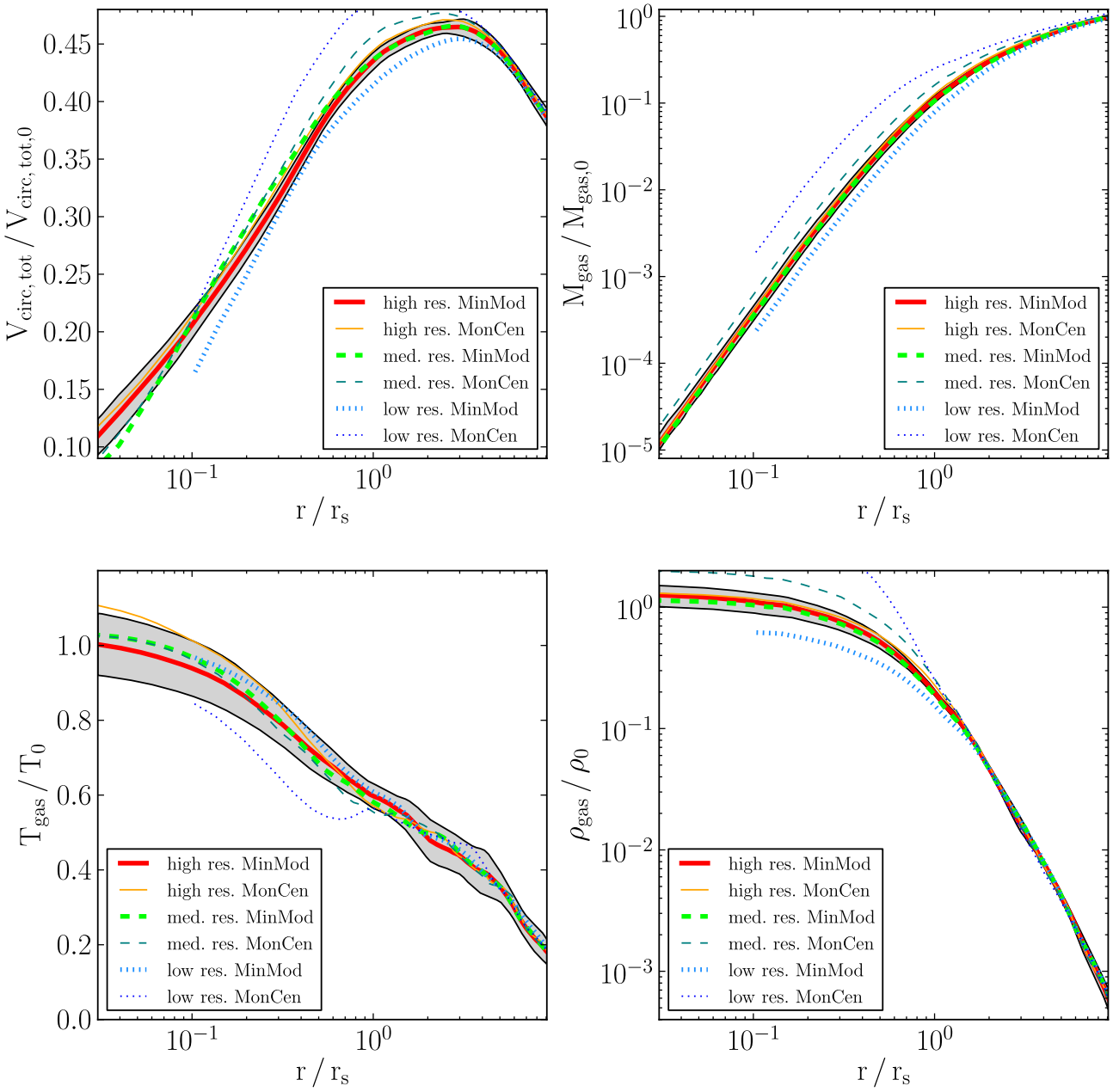

Figure 16. The total circular velocity, gas mass, gas temperature and gas density profiles of halo 2 for the two different slope-type hydro solver specifications, and, respectively, three different resolutions, under consideration. For comparison the variance of the numerical mean of the 15 haloes, as it is defined in Section 6, is also plotted as grey shaded area.

With the analysis of this section, we showed that generally the alteration of numerical parameters within the RAMSES code and the initial conditions (ICs) provided by MUSIC can have a 10–20 per cent effect on to the profiles. A further step would be to quantify the effects, that the use of different codes would have, on to the profiles. This is however beyond the scope of this paper. Instead we estimate the variance coming from the use of different codes through the results of the first nIFTy paper (Sembolini et al. 2016): from the profile plots therein, it can be seen that for the quantities relevant in this analysis the individual deviations in the subset of grid based and modern SPH codes, are of the order of 10–20 per cent, of the average. And mostly the agreement is better for the outer radii than for the inner ones.

9 CONCLUSIONS

Novel methods in precision observational cosmology, like WL and GC, will enable observers to determine the matter power spectrum with high accuracy, down to relatively small scales, where non-linearities and baryonic effects will play an important role ($1\,h\,\mathrm{Mpc}^{-1} < k < 10\,h\,\mathrm{Mpc}^{-1}$). This will challenge theoreticians to compute the predicted power spectrum in this k-range with similar accuracy.

In the present analysis, we have studied the internal structure of 16 galaxy group sized haloes with purely non-radiative hydrodynamics. The mass range was chosen because the mass distribution within groups will give the strongest contribution to the WL signal. In addition, the scale-free nature of non-radiative dynamics

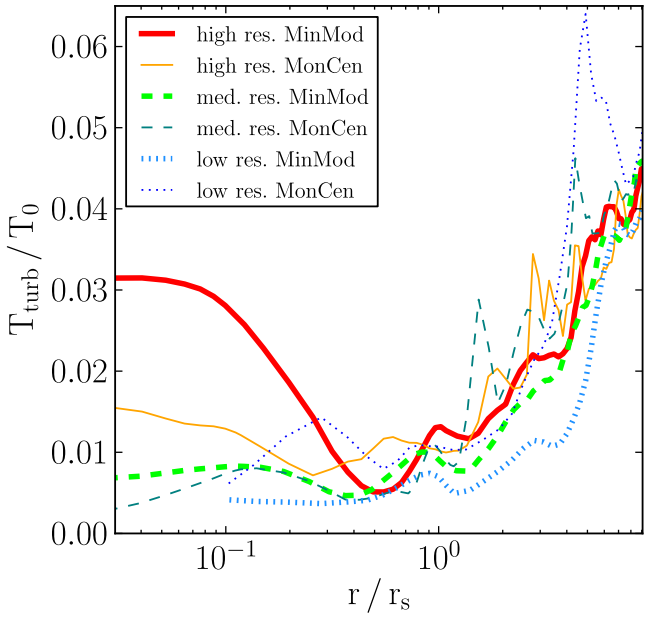

Figure 17. The turbulent gas temperature of halo 2 for the two different slope-type hydro solver specifications, and, respectively, three different resolutions, under consideration.

has the advantage that we can rescale our halo profiles, compute the average profiles and compare them with analytical predictions. By computing the 1σ standard deviation on the numerical mean profiles, we have found a variance of 20 per cent for the most important gas quantities. This was interpreted as being due to different histories and internal dynamics of individual haloes. While this effect is of physical origin, changes in the numerical parameters on the other hand, lead also to measurable differences in the profiles, which are generally smaller than the variance. We conclude from this, that our simulations, with the highest resolution of $\Delta x_{\rm min} \simeq 1$ kpc and more than one million particles per halo, are accurate enough to reproduce the physics of galaxy group sized haloes.

In a further step, we have compared our numerical result to analytical profiles predicted by a classical theoretical model based on a polytropic gas in HSE within the NFW mass profile. We found an excellent agreement for the total circular velocity, with less than 10 per cent deviation between the numerical mean and the analytical profile. With this result, we confirm that the NFW model is capable of describing the total mass distribution within haloes, also when a collisional gas component is added to the dominant collisionless component, and that it provides a reliable analytical mass prediction for computing the power spectrum within the halo model approach (see also Rudd, Zentner & Kravtsov 2008).

For the thermodynamical properties of the gas component, we found a stronger disagreement between the analytical curve and the numerical mean. However, this deviation is generally smaller than 20 per cent, when the corrections due to the turbulent energy are taken into account, as we have done in our proposed corrected analytical model. Its main ingredient is a shallow but outwardly increasing turbulent temperature (equivalent to the specific turbulent energy profile). This behaviour was also found in the analytical analysis of Shi & Komatsu (2014) and Shi et al. (2015), in which the authors derived their result from a set of differential equations describing the evolution of non-thermal, random motions in haloes. A slightly different approach was used in Martizzi & Agrusa (2016), who used what corresponds in our case to a constant turbulent temperature. Being able to understand better and describe more accurately the non-thermal contribution to the HSE, would be highly beneficial for mass estimates of galaxy groups and clusters based on X-ray observations, since these notoriously suffer from underestimation of the total pressure support (a problem known as the hydrostatic mass bias).

Nevertheless, even after correcting the analytical model, we observe the strongest deviation from the numerical mean around $r = r_{\rm s}$, consistently in all baryonic quantities. The gas entropy profile has provided us with an indication on the physical origin of this disagreement. We have indeed found two different thermodynamical regimes separated by the critical radius $r \simeq r_{\rm s}$. In the central high-density region, where merging of clumps and substructures leads to efficient mixing, we see a core of constant entropy. Here, isentropic evolution of an ideal gas with adiabatic index $\Gamma \simeq 5/3$ is recovered. In the outer part, however, we observe an atmosphere of decreasing density and increasing entropy, as predicted by our polytropic model with $\Gamma \simeq 1.2$.

Hence the polytropic model of the baryonic component based on the HSE equation and the NFW distribution of the total mass, captures the essence of the dominant physical processes, but it also has its limitations: first, it does not take into account the additional non-thermal pressure support and secondly, it cannot predict the core of constant entropy we have observed. While for the first problem we have suggested an analytic correction, a detailed refactoring of the analytical model would be necessary to address the second issue, and is left for future work.

Furthermore, we have estimated the error on to our numerical mean profiles as the variance scaled with the inverse square root of the number of simulated haloes. For the total circular velocity, we have found the error on the mean to be less than 1 per cent, for the range $r > 0.2\, r_{\rm s}$. This is good news for future projects on precision cosmology and the matter power spectrum. In the central region, the error increases however to 7 per cent. We conclude from this that the required 1 per cent precision is achieved within our non-radiative simulations down to very small scales. In order to estimate the possible bias due to resolution effects, we have calculated the numerical mean of the 15 haloes also for the medium resolution case. For the circular velocity, we found that its deviation from the high-resolution mean profile lies below 2 per cent for $r > 0.2\, r_{\rm s}$ (see Fig. 18). This indicates that our highest resolution results are converged within the estimated 1 per cent error bars.

Overall, we can quantify the modification of the mass distribution due to the non-radiative baryonic gas component compared to pure dark matter simulations using the main halo structural parameters c and r_{200}. While for the N-body only runs we find an averages for these parameters $c = 11.7$ and $r_{200} = 913$ kpc, in the case of hydrodynamical runs we get $c = 10.8$ and $r_{200} = 991$ kpc. This indicates that, in the hydro simulations, haloes are slightly more extended and less concentrated (see Table 2). We have found the decrease in the concentration parameter to be $\Delta c \simeq 1$ in average, which is significant even if this value is much smaller than the variance, with different haloes having concentrations ranging $c = 8$–18.

The idea to apply the NFW model to the total (gas + dark matter) mass, with different concentration parameters with or without a baryonic component, was introduced by Rudd et al. (2008). These authors found almost no difference in the average c value between their non-radiative and N-body simulations. However, their work is focused on the direct computation of the matter power spectrum, and hence they do not apply the zoom-in technique as we do, so that their

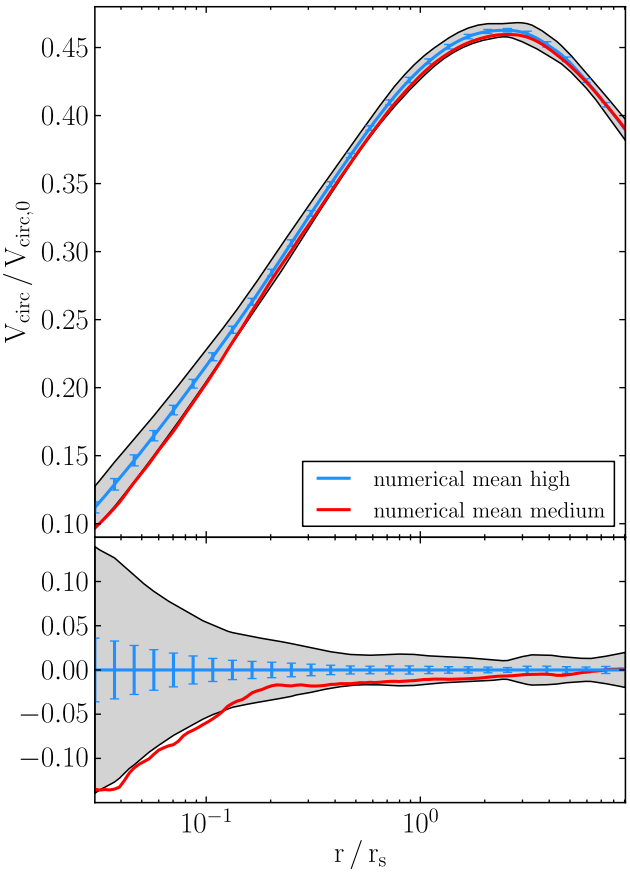

Figure 18. Deviation between the high- and the medium-resolution mean profile of the total circular velocity, the grey 1σ variance region and the blue error bars on the mean are calculated, as described in Section 6.

mass resolution is much lower with $m_{DM} \simeq 10^9\,M_\odot$. Accordingly, they only have 10 000 particles per halo, in the considered halo mass range. Hence, our results are likely to be more accurate.

Beyond non-radiative hydrodynamics, the inclusion of additional baryonic processes like cooling, star formation and feedback mechanisms is likely to produce stronger deviations into the mass profiles especially in the centre, or increase the variance of the profiles even further. In a follow-up paper, we will explore these effects using various new physical processes on the same halo sample.

ACKNOWLEDGEMENTS

The simulations for this work were performed on the zBox4 supercomputer at the University of Zurich. We thank S3IT for providing the infrastructure for this machine. We also thank the anonymous referee for greatly improving the quality of this paper, through constructive comments.

REFERENCES

Allen S. W., Evrard A. E., Mantz A. B., 2011, ARA&A, 49, 409
Ascasibar Y., Yepes G., Müller V., Gottlöber S., 2003, MNRAS, 346, 731
Battaglia N., Bond J. R., Pfrommer C., Sievers J. L., 2012, ApJ, 758, 75
Bauer A., Springel V., 2012, MNRAS, 00, 00
Biffi V., Dolag K., Böhringer H., 2011, MNRAS, 413, 573
Biffi V. et al., 2016, ApJ, 827, 112
Borgani S., Kravtsov A., 2011, Adv. Sci. Lett., 4, 204
Bullock J. S. et al., 2001, MNRAS, 00, 00
Dolag K., Borgani S., Schindler S., Diaferio A., Bykov A. M., 2008, Space Sci. Rev., 134, 229
Eisenstein D. J., Hut P., 1998, ApJ, 498, 137
Eke V. R., Navarro J. F., Frenk C. S., 1998, ApJ, 503, 569
Feldmann R., Carollo C. M., Mayer L., Renzini A., Lake G., Quinn T., Stinson G. S., Yepes G., 2010, ApJ, 709, 218
Frenk C. S. et al., 1999, ApJ, 525, 554
Fromang S., Hennebelle P., Teyssier R., 2006, A&A, 457, 371
Hahn O., Abel T., 2011, MNRAS, 415, 2101
Hahn O., Martizzi D., Wu H.-Y., Evrard A. E., Teyssier R., Wechsler R. H., 2015, preprint (arXiv:e-prints)
Heitmann K. et al., 2008, Comput. Sci. Discovery, 1, 015003
Huterer D., Takada M., 2005, Astropart. Phys., 23, 369
Kang H., Ostriker J. P., Cen R., Ryu D., Hernquist L., Evrard A. E., Bryan G. L., Norman M. L., 1994, ApJ, 430, 83
Klypin A. A., Trujillo-Gomez S., Primack J., 2011, ApJ, 740, 102
Komatsu E., Seljak U., 2001, MNRAS, 327, 1353
Komatsu E. et al., 2011, ApJS, 192, 18
Kravtsov A. V., Borgani S., 2012, ARA&A, 50, 353
Lau E. T., Kravtsov A. V., Nagai D., 2009, ApJ, 705, 1129
Laureijs R. et al., 2011, preprint (arXiv:1110.3193)
Loken C., Norman M. L., Nelson E., Burns J., Bryan G. L., Motl P., 2002, ApJ, 579, 571
LSST Dark Energy Science Collaboration 2012, preprint (arXiv:1211.0310)
McCarthy I. G. et al., 2010, MNRAS, 406, 822
Martizzi D., Agrusa H., 2016, preprint (arXiv:1608.04388)
Nagai D., Kravtsov A. V., Vikhlinin A., 2007, ApJ, 668, 1
Navarro J. F., Frenk C. S., White S. D. M., 1995, MNRAS, 275, 720
Navarro J. F., Frenk C. S., White S. D. M., 1996, ApJ, 462, 563
Navarro J. F., Frenk C. S., White S. D. M., 1997, ApJ, 490, 493
O'Shea B. W., Nagamine K., Springel V., Hernquist L., Norman M. L., 2005, ApJS, 160, 1
Piffaretti R., Valdarnini R., 2008, A&A, 491, 71
Planck Collaboration XIII, 2016, A&A, 594, A13
Power C., Navarro J. F., Jenkins A., Frenk C. S., White S. D. M., Springel V., Stadel J., Quinn T., 2003, MNRAS, 338, 14
Rasia E., Tormen G., Moscardini L., 2004, MNRAS, 351, 237
Rasia E. et al., 2006, MNRAS, 369, 2013
Reed D. S., Smith R. E., Potter D., Schneider A., Stadel J., Moore B., 2013, MNRAS
Roncarelli M., Ettori S., Dolag K., Moscardini L., Borgani S., Murante G., 2006, MNRAS, 373, 1339
Rudd D. H., Zentner A. R., Kravtsov A. V., 2008, ApJ, 672, 19
Schneider A., Teyssier R., 2015, J. Cosmology Astropart. Phys., 12, 049
Schneider A. et al., 2016, J. Cosmology Astropart. Phys., 4, 047
Seljak U., 2000, MNRAS, 318, 203
Sembolini F. et al., 2016, MNRAS, 457, 4063
Shaw L. D., Nagai D., Bhattacharya S., Lau E. T., 2010, ApJ, 725, 1452
Shi X., Komatsu E., 2014, MNRAS, 442, 521
Shi X., Komatsu E., Nelson K., Nagai D., 2015, MNRAS, 448, 1020
Shi X., Komatsu E., Nagai D., Lau E. T., 2016, MNRAS, 455, 2936
Skory S., Turk M. J., Norman M. L., Coil A. L., 2010, ApJS, 191, 43
Teyssier R., 2002, A&A, 385, 337
Teyssier R., Fromang S., Dormy E., 2006, J. Comput. Phys., 218, 44
van Daalen M. P., Schaye J., Booth C. M., Dalla Vecchia C., 2011, MNRAS, 415, 3649
Wu H.-Y., Hahn O., Wechsler R. H., Mao Y.-Y., Behroozi P. S., 2013a, ApJ, 763, 70
Wu H.-Y., Hahn O., Wechsler R. H., Behroozi P. S., Mao Y.-Y., 2013b, ApJ, 767, 23

APPENDIX A: HALO MASS DEFINITIONS

Given the information about the haloes which we obtain after running the HOP halo finder: the HOP halo masses and centres of mass of the haloes, we can extract the halo profiles from the simulation outputs. With these data, there are now three principle ways to find

the halo mass M_{200} and corresponding r_{200} (defined with respect to the average mass density of the Universe):

Method 1 (HOP mass): use the HOP mass $M_{\rm HOP}$ as M_{200} and calculate r_{200} from it via the relation:

$$M_{(<r_{200})} = \frac{4\pi}{3} \cdot \bar{\rho} \cdot 200 \cdot r_{200}^3 \tag{A1}$$

$$\Longrightarrow r_{200} = \sqrt[3]{\frac{3}{4\pi} \cdot \frac{1}{\bar{\rho}} \cdot \frac{1}{200} \cdot M_{(<r_{200})}} \tag{A2}$$

$$\Longrightarrow r_{\rm HOP} = \sqrt[3]{\frac{3}{4\pi} \cdot \frac{1}{\bar{\rho}} \cdot \frac{1}{200} \cdot M_{\rm HOP}} \tag{A3}$$

Method 2 [spherical overdensity (SOD) meaning spherical overdensity]: use the halo total mass profile $M_{(<r)}$ extracted from the simulation as function of r:

$$M_{(<r)} = \frac{4\pi}{3} \cdot \bar{\rho} \cdot \Delta \cdot r^3 \tag{A4}$$

$$\Longleftrightarrow \frac{M_{(<r)}}{r^3} = \frac{4\pi}{3} \cdot \bar{\rho} \cdot \Delta \tag{A5}$$

$$\Longleftrightarrow \Delta = \frac{3}{4\pi} \cdot \frac{1}{\bar{\rho}} \cdot \frac{M_{(<r)}}{r^3}. \tag{A6}$$

When $\Delta = 200$ one finds r_{200} and $M_{(<r_{200})}$.

Method 3 (NFW mass profile): use the NFW mass profile $M_{(<r)}^{\rm NFW}$ as function of r. The NFW parameters of the halo $\rho_{\rm s}$ and $r_{\rm s}$ need to be known (in our case we have extracted them from fitting the NFW circular velocity squared to the numerical profile):

$$M_{(<r)}^{\rm NFW} = 4\pi \cdot \rho_{\rm s} \cdot r_{\rm s}^3 \cdot \left(\ln(1 + r/r_{\rm s}) - \frac{r/r_{\rm s}}{1 + r/r_{\rm s}} \right). \tag{A7}$$

Inserting $\frac{M_{(<r)}^{\rm NFW}}{r^3}$ as $\frac{M_{(<r)}}{r^3}$ into the expression for Δ (A6):

$$\Delta = \frac{3}{4\pi} \cdot \frac{1}{\bar{\rho}} \cdot \frac{M_{(<r)}^{\rm NFW}}{r^3} \tag{A8}$$

$$= 3 \cdot \frac{\rho_{\rm s}}{\bar{\rho}} \cdot \left(\frac{r_{\rm s}}{r} \right)^3 \cdot \left(\ln(1 + r/r_{\rm s}) - \frac{r/r_{\rm s}}{1 + r/r_{\rm s}} \right). \tag{A9}$$

Evaluating this expression at $r = r_{200}$ gives

$$200 = 3 \cdot \frac{\rho_{\rm s}}{\bar{\rho}} \cdot \left(\frac{r_{\rm s}}{r_{200}} \right)^3 \cdot \left(\ln(1 + r_{200}/r_{\rm s}) - \frac{r_{200}/r_{\rm s}}{1 + r_{200}/r_{\rm s}} \right). \tag{A10}$$

So one finds $r = r_{200}$ when $\Delta = 200$ and can insert the value into $M_{(<r)}^{\rm NFW}$ to obtain $M_{(<r_{200})}^{\rm NFW}$.

The resulting masses are displayed in Table A1 and Fig. A1. The average deviation between the NFW and SOD halo mass is 5 per cent, however no bias is observable. The HOP halo mass lies 13 per cent below SOD mass on average and a clear bias exists.

The HOP mass appears in our work because it is the one defining the haloes, when we select our sample from the unigrid run. Though the spherical overdensity mass is the one which is used the most in literature, we give the NFW mass in Table 2 of the main text. The reason is simply that this mass corresponds to the other parameters which characterize our haloes (r_{200}, $r_{\rm s}$, $\rho_{\rm s}$, T_0 etc.), as they are all connected through the assumption of HSE. Any other definition of M_{200} would result in a slightly different value for r_{200} and hence lead to a mismatch, when mixed with the other NFW parameters, as can be seen for example, in the definition of $c = r_{200}/r_{\rm s}$.

Table A1. Comparison of halo mass definitions. All masses are stated in $10^{13}\,{\rm M}_\odot\,h^{-1}$.

Halo	$M_{\rm HOP}$ (nbody)	$M_{200}^{\rm SOD}$ (hydro)	$M_{200}^{\rm NFW}$ (hydro)
1	4.48	5.28	5.59
2	4.11	4.7	5.31
3	3.76	4.35	4.27
4	3.16	3.65	4.04
5	2.7	3.15	3.07
6	1.78	2.08	2.11
7	1.39	1.57	1.65
8	1.37	1.49	1.56
9	1.2	1.37	1.46
10	1.05	1.16	1.16
11	0.778	0.869	1.01
12	0.663	0.768	0.789
13	0.614	0.69	0.713
14	0.451	0.528	0.616
15	0.517	0.608	0.625
16	0.479	0.538	0.537

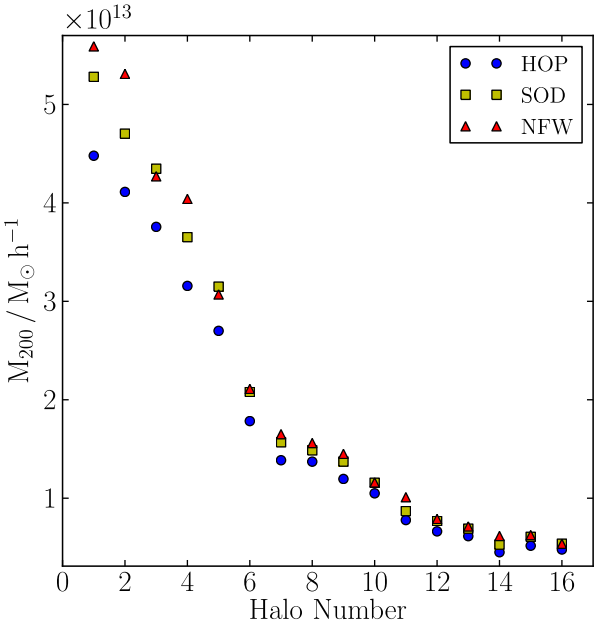

Figure A1. Halo masses M_{200} for the three different methods to obtain them: HOP (blue dots), SOD (yellow squares), NFW (red triangles).

APPENDIX B: HALO SELECTION DETAILS

In this appendix, we describe in more detail how we arrived at the 16 haloes of our sample, from the initially 73 947 haloes found in the considered mass range $5 \times 10^{12}\,{\rm M}_\odot\,h^{-1} < M < 5 \times 10^{13}\,{\rm M}_\odot\,h^{-1}$, in the unigrid run at $z = 0$.

Since it is easier for the zoom-in simulations and the overall analysis process, that the halo candidates are relatively isolated, we applied the following isolation selection criterion on to the 73 947 found haloes, with masses in the mass range of interest $5 \times 10^{12}\,{\rm M}_\odot\,h^{-1} < M < 5 \times 10^{13}\,{\rm M}_\odot\,h^{-1}$, in the first step:

(i) check for each main halo (labelled with 1), if it has another halo (labelled with 2) within radius $r_{12} = a(r_{200,\,1} + r_{200,\,2})$;

(ii) if this is the case, the mass ratios of the halo under consideration and the haloes in its vicinity of radius r_{12} are checked;

(iii) if $M_1 > b \cdot M_2$ then the main halo is kept in the sample, otherwise it is discarded completely.

As conservative minimum values of the selection parameters a and b, we chose $(a, b) = (5, 3)$. This criterion was fulfilled by 117 of the 73 947 group sized haloes. Among the other 73 830 haloes were still extremely isolated ones, with a large value for either a or b, e.g. $(a, b) = (13, 1)$ for halo 1 and halo 14. Those cases were identified individually, so that another 26 haloes were found and added to the 117 selected for the analysis. Table B1 shows the number of haloes found for each parameter pair (a, b).

Another step of selection was done by looking at the assembly history and the circular velocity curves of the 143 haloes we have found so far: late mergers that had not yet accumulated 70 per cent of their final mass at $z = 0.175$ were removed from the sample, as well as haloes that showed atypical behaviour in their circular velocity plots. From the remaining 108 haloes, we selected 16 which were lying close, above or below the average time evolution and circular velocity curves, to ensure that we have a sample representative of the typical behaviour of present-day galaxy groups (see Table 2 and Figs 2 and 3). While as average for the time evolution selection, we used the median of the 108 haloes, for the average circular velocity curve we used the analytical expression from the NFW model (Navarro et al. 1996), with the concentration parameter chosen as $c = 9.6$ (Klypin et al. 2011). Further we ensured that the masses of the 16 selected haloes represent the entire mass interval under consideration.

Table B1. Halo isolation criteria table: number of haloes found for each parameter pair (a, b). The parameter a increases vertically and the parameter b horizontally.

(a, b)	1	2	3	4	5	6	7	8	9	10	11	12	∞
1	883	874	862	854	845	834	831	822	819	813	805	802	195
2	735	655	610	572	538	513	496	467	448	433	419	406	**21**
3	552	436	360	316	273	252	233	213	193	180	173	163	1
4	404	273	222	179	146	131	114	95	85	79	74	66	0
5	283	157	**117**	83	65	56	49	42	34	31	29	26	0
6	201	105	78	49	36	28	21	17	12	10	10	10	0
7	133	64	44	23	17	14	13	10	9	7	7	7	0
8	81	39	21	13	10	8	7	4	4	3	3	2	0
9	50	23	10	5	4	3	3	3	3	2	2	1	0
10	30	13	5	3	2	1	1	0	0	0	0	0	0
11	16	4	2	2	2	1	1	0	0	0	0	0	0
12	11	4	2	2	2	1	1	0	0	0	0	0	0
13	**6**	1	1	0	0	0	0	0	0	0	0	0	0
14	2	0	0	0	0	0	0	0	0	0	0	0	0
15	1	0	0	0	0	0	0	0	0	0	0	0	0
16	0	0	0	0	0	0	0	0	0	0	0	0	0
17	0	0	0	0	0	0	0	0	0	0	0	0	0

This paper has been typeset from a TEX/LATEX file prepared by the author.

3.3 Afterword

The primary purpose for the study described in the previous subsection, was to ascertain, that the precision of numerical simulations with Ramses, reaches the accuracy required by the observations. It was shown that numerical effects only play a sub-dominant role, and do not change the results in a significant way. This matter is therefore completed and will not be referred to in the rest of the analysis.
However, an equally important point of the analysis described in Subsection 3.2, was to find a baseline for the quantification of baryonic effects in the subsequent steps, where more baryonic physics is implemented. The results on the distribution of the baryonic mass in the halos from the simulations described in Subsection 3.2, are therefore used in the rest of the work of this thesis.
As a secondary result important physical properties of galaxy group size halos, were also identified and quantified; mainly the importance of non-thermal pressure support. This quantity is closely related to the assembly history of the halos. Non-thermal pressure support is highly relevant also in feedback processes. The classification of the 16 halos in Subsection 3.2, according to this quantity and other halo properties, might give an indication for which halos are more susceptible to feedback processes, than others.
The results of Subsection 3.2 are therefore not only relevant, but also a necessary requirement, for the further study, described below, which includes sub-grid physics.

4 Sub-grid physics: the baryonic matter component beyond non-radiative hydrodynamics

4.1 Overview

The before mentioned interactions of baryons like radiative cooling, star formation and feedback processes are the next steps in the modelling of this cosmological component, beyond the non-radiative hydrodynamics described in the previous section. Introducing the first of these processes to the simulations brings along the necessity to implement the next one, and subsequently all the other ones, in order to be able to compare the simulation results with observations. The first step is the implementation of cooling. With this the baryonic gas looses much of its random thermal motion, and reaches high densities at the centre of the halos. This is where stars are born in the real universe, hence the transition of the baryonic gas component into a stellar simulation component is required. Implementing this scenario without any further physics leads to an over-production of stars and an over-cooling of the gas component, as compared to observations where galaxies at the centre of halos consist of much fewer stars and far less gas accumulates near the centres. It is therefore necessary to introduce processes which quench the formation of stars and heat the gas, thereby preventing it from falling to the halo centres. Physically motivated scenarios to achieve these goals are the so called feedback processes. Feedback denotes hereby the secondary effect of a process on the environment, which causes the primary process itself to slow down. Stellar feedback for example is the result of star formation. One consequence of the formation of stars is the emission of energetic radiation from these stars during their existence. Another one is the death of stars in supernova explosions. Both processes inject thermal energy as well as bulk kinetic energy into the surrounding baryonic gas, e.g. in the form of highly energetic radiation, thereby hindering the formation of further stars. The stellar feedback scenario has been successful in the description of dwarf galaxy halos. For larger systems, like galaxy groups or clusters, however its energy injection process is insufficient to reproduce the observed properties. A more energetic feedback mechanism has therefore been proposed, in the form of Active Galactic Nucleus feedback. Here the systems which inject the energy into the surrounding gas are black holes at the centre of galaxies, which are surrounded by accretion discs of gas. The idea is that collisions of gas particles at the inner edge of the accretion disk are so highly relativistic, that they emit radiation and particle fountains which are even more energetic, than in the stellar feedback case.
The equations of motion and relevant objects of these processes, e.g. the quantum mechanical emission of radiation by atoms, or the formation of stars in giant molecular clouds, are taking place on scales far smaller, than the minimum cell size of the simulations. An effective description of these processes and objects is therefore necessary. Hence one generally speaks of sub-grid physics. The individual implementation steps in the Ramses code are described in the following.

4.2 Cooling and Heating

The internal energy of the gas is affected by the exchange of radiation with the environment. This process is physically accounted for by adding two source terms to the right hand side of the energy conservation equation of fluid dynamics. These terms depend on the density and temperature of the gas and are called heating (ζ) and cooling function (λ), respectively.

$$\frac{\partial(\rho \cdot e)}{\partial t} + \nabla(\rho \cdot \vec{v} \cdot e) = -\nabla(\vec{v} \cdot P) - \rho \cdot \nabla\Phi \cdot \vec{v} + \zeta_{(\rho,T)} + \lambda_{(\rho,T)} \tag{4.1}$$

The cooling function is implemented with the recipe by Sutherland and Dopita from 1993 [SD93], and heating of the gas through a homogeneous UV background, to mimic the re-ionization of the universe, as suggested by Haardt and Madau in 1996 [HM96]. As the beginning of the re-ionization era we have chosen $z = 10$ in this thesis work. Within an individual hydro cell the UV background is exponentially suppressed depending on the gas density of the cell. The efficiency of the cooling and heating processes depends on the chemical composition of the gas, since the emission and absorption of radiation depend on the atomic properties. Species in addition to hydrogen are implemented in the code as a hydro variables. Helium is the only other individual element which is simulated. All of the elements which are heavier than Helium are described as a single hydro variable called metals. The mass fractions of the gas which each of these three chemical species contributes are determined by the physics of the early universe: Hydrogen 75%, Helium 25% and Metals 0.1%.

4.3 Star formation

The formation of stars takes place in the universe in regions where the baryonic gas is highly dens and cool, so that it cannot counteract the collapse under its own gravity with its pressure. These dens regions are called giant molecular clouds (GMCs) and cannot be resolved by the simulations of this study, since they are smaller than the minimum cell size. The idea is therefore to model the formation of stars through a density threshold ρ_{star}. If the gas density within a hydro cell increases above ρ_{star} in a cell from one time step to another, then a star particle is formed by converting the baryonic gas mass in the cell into a star particle with mass m_{star}, with the rate given by a Schmidt law [Sch59]:

$$\dot{\rho}_{star} = \epsilon_{star} \cdot \frac{\rho_{gas}}{t_{ff}} \quad \text{with} \quad t_{ff} = \frac{1}{\sqrt{G\rho}} \quad \text{the free fall time.} \tag{4.2}$$

ϵ_{star} is an efficiency parameters and set to 0.02 in the underlying study. The formation of a star particle takes place from one time step to another. To mimic the star formation rate, the following is done: every time when the density threshold is crossed (and the star formation criterion is met), a star particle is created or not, depending on a probability assigned to it. So that overall the number of stars will be the same as if the individual stars were formed with the rate $\dot{\rho}_{star}$ over several time steps [RT06]. The mass of the resulting star is given by m_{star}. It is the fraction of baryonic mass, in the cell which exceeded the density threshold, that is converted into a star particle. This does not have to be the same mass every time, since the threshold can be crossed, with multiples of it. $m_{star} = 1.0$ means that all the baryonic mass is converted into a star particle. Since the formed star particles are collisionless they are numerically treated as an n-body problem. They follow the same equations of motions as the dark matter particles described above.

4.4 Stellar feedback

Stellar feedback summarizes the interactions which stars have with their environment, thereby giving thermal energy to the surrounding gas. The most important contribution comes from supernova explosions.
These are modelled with a universal thermal energy transfer of 10^{44} J , or 10^{51} erg, per 10 $M_\odot$ star to the neighbouring gas cells. Aside from that also the mass of the stellar component participating in the explosion is given back to the gas cells. And further, their metal fraction is increased by 10% of the stellar mass transferred with the supernova. The enrichment with metals has direct consequences for the gas' cooling behaviour.
Giant molecular clouds are the stages within galaxies, at which the birth and interactions of stars with the environment happen. Since the typical scales of of these objects, 5 to 200 pc, cannot be resolved in our simulations the thermal energy release from young stars would be too smoothly distributed. Because if each formed star particle would become a supernova, the distribution of supernovas can be too smooth. Therefore the process of a star becoming a supernova is implemented stochastically, to make these events sparser. In this model not every star becomes a supernova, but only the ones whose previously assigned random variable, between 0 and 1, is smaller than the star particle's mass divided by M_{GMC}, the mass of a typical GMC. This quantity is a parameter of the model. The energy released by the individual supernova is then scaled by M_{GMC} divided by the star particle's mass so that the overall supernova energy is conserved, in a statistical sense. If the mass of star particles is larger than M_{GMC}, then the distribution of star particles and hence supernova is not too smooth anyway, because the star particles and hence supernovae are very sparse [RTA$^+$14]. For this work the we have set $M_{GMC} = 10^7 M_\odot$.
If the thermal energy from stellar feedback would be injected directly into gas cells, then it would result in strong dilution of the energy and also cooling, which radiates it away. Therefore the energy is stored in the cells as a non-thermal energy component, which could be seen e.g. as not resolved turbulence. This non-thermal component is decaying with a fixed rate, over a time determined by the time scale parameter t_{diss}, which was chosen as 20 Myr. This is the typical lifetime of GMCs. As long as the non-thermal energy component of the cells is larger than the thermal one, cooling is turned of for these cells. Once the non-thermal component drops below the thermal one, the first is converted into the latter, and cooling is turned back on. A similar scheme, called delayed cooling was first introduced by [SSK$^+$06].
Detailed information about the stellar feedback implementation in the Ramses code can be found in [TPDR13] and [RTA$^+$14].

4.5 Radiative feedback

The transfer of thermal energy from the stars to the gas described above, which mimics the feedback mechanism of supernova explosions, is only a small fraction of the total transfer. Especially young stars interact strongly with the surrounding gas, namely their GMC, through their emission of Ultra Violet (UV) radiation. This radiation gets then absorbed by dust and is re-emitted as infrared (IR) radiation. The radiation pressure provided by this mechanism is able to dissolve the GMC, and consequently halt further star formation [MQT10]. In addition baryonic mass is removed from halos, as it reaches the escape velocity through the additional energy.
In the Ramses code this scenario is modelled by injecting energy into the gas cells which contain these young stars. This happens in two steps. First, the fraction of energy absorbed by the dust of the cell through the UV radiation is given by

$$E_{UV} = E_{rad} \cdot (1 - e^{-\kappa_{UV} \rho_{dust} \Delta x}) \tag{4.3}$$

A fraction of this energy is re-emitted in the IR range and transferred to the gas

$$E_{IR} = E_{UV} \cdot (1 - e^{-\kappa_{IR} \rho_{dust} \Delta x}) \tag{4.4}$$

Here $E_{rad} = 10^{46}$ J, or 10^{53} erg, per 10 $M_\odot$ star and ρ_{dust} is determined by the metal fraction and the gas density. κ_{UV} is the dust opacity in the UV range, which is taken to be $10^3 \mathrm{cm}^2 \mathrm{g}^{-1}$. κ_{IR} is the counterpart in the corresponding IR band, and the parameter which determines the amount of energy, which is given to the gas.
The energy transfer from the radiative feedback itself is implemented such that it happens together with the one from the supernovae, as described in the previous section.
The radiative feedback implementation in the Ramses code is described in more detail in [RTA$^+$14].

4.6 AGN feedback

4.6.1 Active galactic nuclei

Supernova explosions are among the most luminous events in the universe. However, their implementation as feedback mechanism in astrophysical simulations, has not been able to remedy the mismatch between observations and simulations, in the stellar, as well as gas mass fractions, of galaxy groups and clusters. Researchers have therefore suggested the only objects which are more luminous than supernovae, to provide the energy required to push the baryons out of the halo centres and disrupt the formation of new stars: active galaxies, or more specifically the nuclei of active galaxies.

Classifications of active galaxies are based on observational characteristics, and are not directly related to the physical processes at work. The most common type of observed active galaxies are Seyfert galaxies which are characterized by a continuous emission spectrum on all frequencies, plus a number of characteristic broad emission lines. Examples are the galaxy Meyssier 51 A (Figure 4.1) and NGC 1275, at distances of 11 Mpc and 70 Mpc, respectively, from the Milky way. A second category of active galaxies, which is common and important is the class of quasars. These objects, though similar to Seyfert galaxies in their emission spectra, are even more luminous than the latter. This high emission rate makes these objects important probes of high distances, or in other words the early universe. The most distant quasar known today is ULAS J1120+0641 at 9 Gpc distance.

Figure 4.1: **The Seyfert galaxy Messier 51 A or NGC 5194 at roughly 7 Mpc distance from the Milky Way (left). It is interacting with its companion dwarf galaxy Messier 51 B or NGC 5195 (upper right). Both are members of the M51 group. Image Credit: NASA/ESA**

The proposed physical mechanism, at work in the active galactic nuclei, which gives rise to the high luminosities, is an accreting black hole. These objects are end products of certain classes of high mass stars. Those collapse under their own gravity, when their fuel supply for nuclear fusion is exhausted, such that the remaining pressure support can no longer counteract the gravitational force. The mass of the former star becomes thereby so highly concentrated, that nothing, not even light, can escape from it, ones it has crossed a certain limit in the black hole's proximity. This radius, called the event horizon is a sphere, which surrounds the black hole. The strong gravitational forces which a black hole exerts onto its environment, attracts surrounding stellar objects and gas. Stars orbiting the black holes are in high velocity orbits. When they loose kinetic energy and fall into the event horizon, the rest mass of the black hole increases. The same is true for baryonic gas which is drawn towards a black hole. In dissipative processes the gas looses kinetic energy and falls towards the centre, where its mass is also converted into additional rest mass of the black

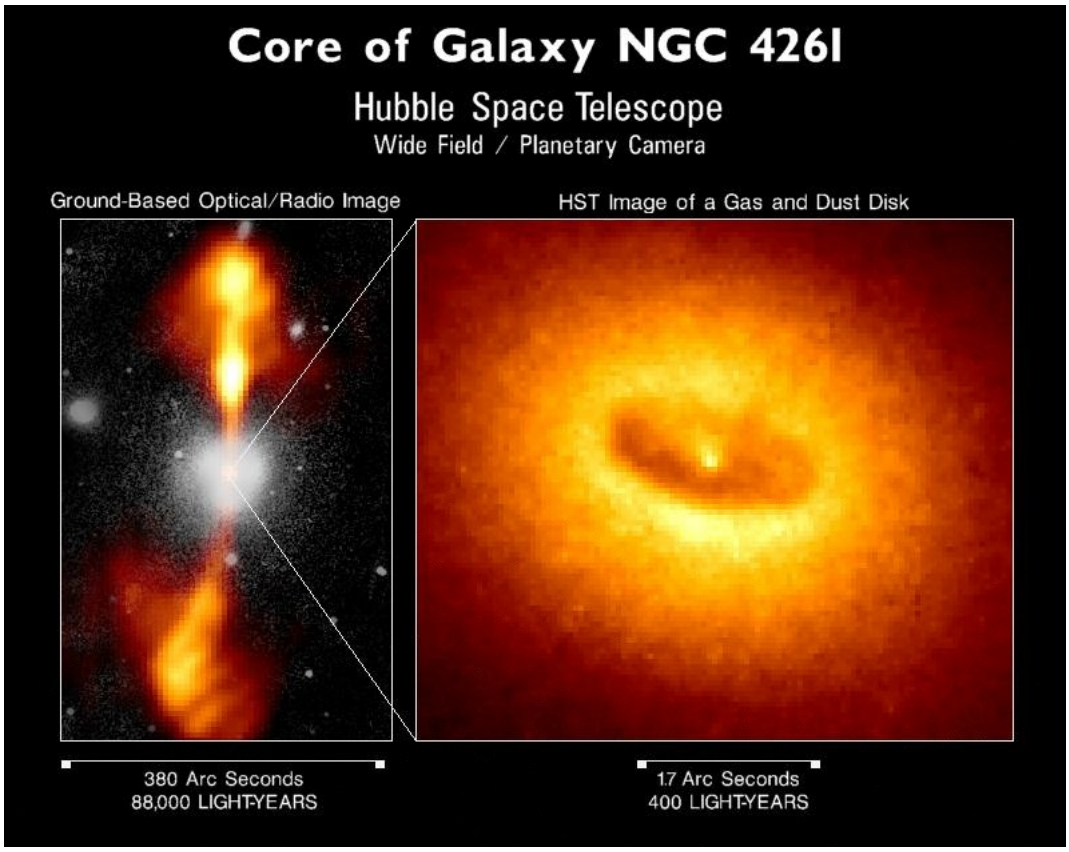

Figure 4.2: **The active galactic nucleus at the centre of the elliptical galaxy NGC 4261, located behind the Virgo Cluster, at 30 Mpc distance from the Milky Way. Visible in the right image is what is presumed to be a torus of dust around the accretions disk at the centre. In the left image one can see two radio jets perpendicular to the disk. Dimensions are indicated, 1 light-year = 3.262 pc. The mass estimates for the black hole, which is assumed to be at the centre of the object, are in the magnitude of 10^7 to $10^8 M_\odot$, [CO07]. Image Credit: NASA/ESA/Hubble Space Telescope.**

hole. Although the gravitational attraction is in principle spherically symmetric, dissipative process and angular momentum conservation lead to the development of a spinning disk of gas, whose angular momentum direction is determined by the initial conditions. This disk structure is the famous accretion disk of a black hole.
Black holes themselves, do by definition not emit any radiation. However, the accreted gas close to the event horizon is contracted to such high densities and accelerated to such high relative velocities, that high energy particle collision processes take place in the baryonic material, in large numbers. For these processes synchrotron emission and inverse Compton scattering have been proposed, since these two would be capable of producing high energy photons, up to the wavelengths of X-rays. Both processes involve highly relativistic electrons, which emit the high energy photons.
These described mechanism have not yet been proven observationally, as by construction dens gas encloses the black hole and the accretion disk. An observational indication was nevertheless reported in the Seyfert galaxy NGC 1275 at the centre of the Perseus cluster, at a distance of 70 Mpc from the Milky way [Fab12]. Another indication comes from an observation by the Hubble space telescope (HST) of the centre of the elliptical galaxy NGC 4261 located behind the Virgo cluster, at 30 Mpc distance from the Milky Way: Figure 4.2 shows an image of what is interpreted as its torus of dust around its accretions disk. Aside from that, the existence of black holes at the centres of massive galaxies is confirmed indirectly through the orbital velocities of close stars. From this kind of observation, a black hole existing at the centre of the Milky Way was inferred.

The question is now: how to model, first, the transfer of mass from the gas component to the black hole, and second, the transfer of energy from the accretion disk to the surrounding baryonic gas, in astrophysical simulations. Accretion disks are much smaller than the cell size. Necessarily, their implementation in cosmological simulations falls into the category sub-grid physics. The problem can be divided into four main parts.

4.6.2 Black hole seeding

Since cosmological simulations start at high redshift the entire life cycle of an active galactic nucleus needs to be modelled in principle. The origin of the black holes in galaxy centres are unclear to this date. Two scenarios are mainly considered by astrophysicists: in the first, the black holes have formed from collapsing stars in the early universe (Population III) stars [MR01]. In the second, the black holes are a result of the direct collapse of baryonic gas in the early universe [BVR06], so that the intermediate step, of the baryons forming stars, is skipped. In the Ramses code the origin of black holes is modelled by placing them into mass accumulations, ones these cross a specified mass threshold [BTB17]. These mass accumulation or clumps are identified while the simulation is running, with the Phew clump finder [BTCM15]. It can be chosen which species, dark matter, baryonic gas or stars, should be used for the identification of the clumps. In the underlying study the baryonic gas was used for the mass threshold, with a value of $10^9 M_\odot$. A third parameter to be specified is the initial mass of the black hole. In [BVR06] and [BS09] a value of $10^5 M_\odot$ is suggested, which is also used in the default model of this thesis. Other values are also tested.

4.6.3 Mass accretion onto the black hole

Accretion disks are complex systems and a variety of physical processes takes place in them. To understand and model them is therefore an own field of study. Fortunately, effective descriptions for accretion rates, which can be applied to cosmological simulations, have already been developed in the mid of the 20th century by astrophysicists Arthur Eddington, Hermann Bondi [Bon52] and Fred Hoyle [HL41]. As the rate of mass transfer from the gas

to the black hole, the Bondi model is used, in this study:

$$\dot{M}_B = \frac{4\pi G^2 M_{BH}^2 \tilde{\rho}}{\tilde{v}^3} \tag{4.5}$$

It is based on the assumption, that the increase in mass of the black hole is given by an area times velocity times a density. The parameters which enter into Equation (4.5) are for the black hole its mass M_{BH}, and for the surrounding baryonic gas its density $\tilde{\rho}$. The velocity $\tilde{v}$ is a combination of the sound speed of the gas c_s and the relative velocity of the black hole with respect to the gas.
While the mass of the black hole, as a scalar quantity, is fairly easy to keep track of, it is a more complicated question how to assess the properties of the gas surrounding the black hole, for the computation of the accretion rate. For this purpose a spherical region around the black hole is defined, in which a distribution of equidistantly positioned test particles, denoted as cloud particles, probes the properties of the gas. These cloud particles move rigidly with the black hole, as it evolves in time. The so defined spherical region describes numerically the black holes sphere of influence, as the gas cells which fall within its radius, are used to sample the gas properties and are participating in the exchange of mass and energy, between the black hole and the gas. The sphere is also called sink sphere, as black holes are called sink particles in the simulation community. The radius of the sphere is one parameter of the AGN model and was chosen in this work, as four times the minimum cell size used in the simulation ($4\Delta x$). This idea of the spherical influence/accretion region, around the black hole particles, was first developed by [KMK04] for grid based hydro codes. With this tool at hand, the density which enters into the equation of the Bondi accretion rate (4.5) $\tilde{\rho}$, can be taken as the average gas density within the sink sphere $\bar{\rho}_{gas}$. In the model applied in this thesis, in addition a parametrisation of whether the accretion flow is sub- or supersonic, enters into the definition of the density.

$$\tilde{\rho} = \frac{\bar{\rho}_{gas}}{\alpha} \tag{4.6}$$

With α being a function which describes the state of the accretion flow. The other parameter in (4.5), which can now be described with the sink sphere is the velocity $\tilde{v}$. It is defined as

$$\tilde{v} = \sqrt{v_{rel}^2 + c_s^2} = \sqrt{(\vec{v}_{BH} - \vec{\bar{v}})^2 + c_s^2} \quad \text{with} \quad \vec{v}_{rel} = \vec{v}_{BH} - \vec{\bar{v}} \tag{4.7}$$

where $\vec{v}_{BH}$ is the velocity of the black hole, $\vec{\bar{v}}$ is the average velocity of the gas within the sink sphere and c_s is the local sound speed of the gas.
Already in the first implementations of AGN feedback [BS09] an additional factor was introduced into Equation (4.5), to boost the Bondi accretion rate. With the justification of taking unresolved temperature and density fluctuations into account, that way. In the model used in this work these effects are described in a novel way, by reducing the local sound speed, which is redefined as

$$c_s \rightarrow c_s/\beta \tag{4.8}$$

The factor β is a function of the gas density ρ_{gas} and addition depends on the density threshold parameter for star formation ρ_{star}.
The two main components of the underlying picture of AGN feedback are, first, the accretion of gas onto a central object, and second, the radiative heating of the surrounding gas, which pushes the gas radially away from the accreting body. Therefore by construction, the second process counteracts the first one. In other words, the more gas is pushed outwards radially, the less gas remains near the black hole to be accreted and the less radiation is produced in particle collisions to push the gas outwards. One consequently expects a kind of equilibrium

configuration, towards which the system evolves.
A similar situation was studied by Arthur Eddington, namely the balance between radiation pressure and gravitational force in a star, from which he concluded a limit for the star's luminosity

$$L_E = \frac{4\pi G m_{star} m_p c}{\sigma_T} \tag{4.9}$$

The Eddington limit is derived from the assumption, that a gas made up of hydrogen is in hydrostatic equilibrium (1.55), with the Newtonian gravitational field of the star, and that all the pressure is contributed by the radiation which gives rise to the stars luminosity.
The same principle can also be applied to a black hole's luminosity, which in turn can be related to its mass accretion rate via

$$W = \frac{G M_{BH} N m_p}{r} \quad \Longrightarrow \quad \frac{dW}{dt} = L = \frac{G M_{BH}}{r}\dot{M} \tag{4.10}$$

Here the underlying assumption, is that as a particle of mass m_p falls towards the black hole from radius r. The potential energy which it looses thereby is transformed into kinetic energy of the particle and ultimately in the collision process into radiative energy. One can summarize the effect of the gravitational potential by defining

$$\epsilon_r = \frac{L}{\dot{M}c^2} \quad \text{hence} \quad \epsilon_r = \frac{G M_{BH}}{c^2 r} \tag{4.11}$$

The factor ϵ_r is a parametrisation, introduced to describe the radiative efficiency of the system, it is chosen in this study as $\epsilon_r = 0.1$. Finally one is left with the expression for the Eddington accretion rate

$$\dot{M}_E = \frac{4\pi G M_{BH} m_p}{\epsilon_r \sigma_T c} \tag{4.12}$$

This is applied to the simulations as a maximum accretion rate, or likewise an upper bound of how much mass can be transferred from the gas within the sink sphere to the black hole per time. If the value of the Bondi accretion rate lies below the Eddington limit, then the black hole accretes with the Bondi rate. In the opposite case, that the Bondi accretion rate lies above the Eddington limit, then the black hole accretes only with the Eddington rate.

$$\dot{M} = \min(\dot{M}_B, \dot{M}_E) \tag{4.13}$$

The numerical implementation of this is done by transferring the mass, given by the accretion rate and the length of the time step, from the sink sphere to the black hole.

$$\Delta M_{BH} = \dot{M}\Delta t \quad \text{and} \quad \Delta M_{gas} = -\dot{M}\Delta t \tag{4.14}$$

Within the sink sphere the gas mass removed from the i-th cell is taken by the density weighted scheme,

$$\Delta\rho_i = \rho_i \frac{\Delta M_{gas}}{M_{gas}} \ , \tag{4.15}$$

where M_{gas} is the total gas mass of the sink sphere. This approach presents a novelty in the development of the AGN model in the Ramses code, as in previous version a volume weighted scheme was applied, for the removal of mass from the i-th cell, within the sink sphere.

4.6.4 Black hole dynamics

Black holes are objects, which need to described through General Relativity, in situations which involve high relative velocities, or small distances to the event horizon. For the kinematic behaviour in cosmological simulation, however a treatment through the Newtonian equations of motion is sufficient. In the Ramses code the integration of their motion in time is therefore the same as for the collisionless particles, of dark matter and stars. The gravitational force, which the black holes exert onto the other objects in the simulation, is also computed by the particle mesh method described above. However this is only the case for black holes whose mass is smaller than $10^7\,M_\odot$. For any black hole, whose mass has grown above this threshold, through the accretion, the gravitational interaction with all other objects is computed through direct summation.
Aside from the gravitational force, the black holes are also subject to a drag force, as they move through the gas component. They do not only accrete the mass of the gas, but also its momentum. In addition, the underlying version of the Ramses code, applies a novel implementation, in which the drag force is modelled as arising from the redistribution of mass within the sink sphere, when the accretion rate is Eddington limited. The difference between Bondi and Eddington accretion rate, together with the momentum conservation equations for the black hole and the gas within a sink sphere, give the relevant equations of motion. A detailed description of the model can be found in [BTB17].

4.6.5 Energy transfer onto the gas

The AGN feedback energy is injected into the gas cells contained in the sink sphere in each fine time step as thermal energy. Its amount is given by

$$\Delta W = \epsilon_c \cdot L \cdot \Delta t = \epsilon_c \cdot \epsilon_r \cdot c^2 \cdot \dot{M} \cdot \Delta t \tag{4.16}$$

The newly introduced factor ϵ_c, describes how efficiently the radiation, emitted in the inner edge of the accretion disk, transfers its energy onto the gas. It is called the coupling efficiency and is one of the key parameters of the model. For the deposition of the energy in the i-th cell, again a density weighted scheme is used, as was described above, for the gas mass removal. However, the thermal energy is not directly injected into the gas cells. Instead it is stored and accumulated until it is larger than the threshold

$$W_{min} = \frac{3}{2} \cdot M_{gas} \cdot k_B \cdot T_{min} \tag{4.17}$$

given by the gas mass within the sink sphere M_{gas} and the minimum feedback temperature T_{min}. The latter is an additional parameter of the model and chosen as $T_{min} = 10^7$ K, in this study. The purpose of this temperature threshold is to prevent the gas from immediately diluting the injected energy through cooling. For this reason its value should be chosen such that it lies in a temperature range, in which the cooling through metals is not efficient.

Key works in the numerical modelling of black hole physics and AGN feedback are [SDH05], [SSDH07] and [BS09]. Also the models applied in this study, are partly based on these works, for example the description of the growth of black holes was originally proposed in [BS09]. However, in the mentioned publications, the underlying code is based on the SPH hydrodynamics method. Since Ramses uses a grid based hydro solver, the sub-grid models needed to be converted into this framework. Important publications about the implementation and testing of AGN feedback specifically in the Ramses code are [DDST10], [DDTS11], [TMM$^+$11], [DDST12] and the aforementioned [BTB17].

5 Sub-grid physics: results

5.1 Exploring the limits and robustness of stellar feedback

5.1.1 Overview

As mentioned above AGN feedback is the main mechanism which has been proposed by astrophysicists, to alleviate the mismatch between theory and observation, in the baryon and stellar fraction, of halos in the mass range of galaxy groups and clusters. Stellar feedback on the other hand has been successful in the description of the considered mass fractions for smaller halos. Any simulation which involves AGN feedback, necessarily also needs a working model of stellar feedback (SF). Ultimately, the two mechanism will be applied together, and are expected to have qualitatively similar effects. Although in principle they could influence each other, and one could reduce the effectiveness of the other. For example in [DVS$^+$15] it is reported, that at high redshift stellar feedback efficiently prevents the infall of gas into the central regions of halos, thereby reducing the accretion onto the central black holes. The mentioned study is also done in the context of the stellar and AGN feedback implementation in Ramses.

It is therefore necessary to check the effects which stellar feedback alone has, onto the relevant quantities which describe the mass distribution within the galaxy group halos, before any model of AGN feedback is applied. Since an established model of stellar feedback already exists for the Ramses code, it is necessary to record its impact on the relevant quantities, as this model serves as a baseline reference. Further, it should be explored how strongly variations of this model would affect these quantities. Since computational resources and time are limited, only extreme cases can be tested. Finally, it is worth exploring the possibility, that individual halos could be more susceptible to certain types of feedback, than others. Relevant halo properties might be, most intuitively, the mass, but also their assembly history and dynamical state.

We have tested four different models, our default model and three additional ones, which resulted from changing one parameter at a time:

- SF Default model:
  This is the model which was already described in subsection 4.4, and also used in all the runs which include AGN feedback. Key parameters are: first, the thermal energy injected into the neighbouring cells, per supernova explosion of 10^{44} J per 10 $M_\odot$ star, and second, the enrichment with metals of 10% of the stellar mass transferred with the supernova. Third, the GMC mass of $10^7 M_\odot$ for the stochastic model of supernova explosions. Finally, the dissipation time for the delayed cooling scheme is $t_{diss} = 20$ Myr.
- SF Model 1: no stellar feedback
  Neither energy, nor metals are injected into the neighbouring cells, with the supernova explosions. In other words: stellar feedback is turned of completely.
- SF Model 2: no energy from stellar feedback but metals
  Like in Model 1, no energy is injected into the neighbouring cells, but the injection of metals is kept at the value of the default model (10% of the stellar mass).
- SF Model 3: default model plus radiative feedback
  The default model is used and in addition radiative feedback is applied. For the latter, the two key parameters are $E_{rad} = 10^{46}$ J per 10 $M_\odot$ star and the dust opacity in the IR range κ_{IR}, which is chosen as $20\,\mathrm{cm^2 g^{-1}}$.

5.1.2 Stellar to halo mass (SHM) relation

One key observational quantity, which should be reproduced by numerical simulations, is the fraction of baryonic mass within the stars of the central galaxy M_{star}, in a halo of given total mass M. On one hand this quantity represents a fundamental relation which characterises the large scale structure, as it connects the properties of galaxies to their host halo. On the other hand, in the numerical context, it is a measure for the effectiveness of implemented feedback processes, in the quenching of star formation. The stellar-halo-mass (SHM) relation can be described by the stellar mass within $0.1 r_{200,c}$. Here $r_{200,c}$ is defined with respect to the critical density of the universe. The stellar mass is set in relation to the total mass of the halo, which is defined by the mass within $r_{200,c}$.
Attempts to derive the relation from first principle of galaxy dynamics have been made, and also semi-analytical methods have been developed. A numerical technique to estimate the relation is the abundance matching method. Here the halo population of simulations are linked to the observed population of galaxies, via the assumption

$$n_{(M)} = n_{gal\,(M_{star})} \tag{5.1}$$

This technique was used by Benjamin Moster and others in 2010, to fit an analytical function for the SHM relation [MSM+10] and later generalized to multiple cosmological times [MNW13]. The results of this thesis are compared with this function, which is given by

$$M_{star\,(M)} = 2N \cdot M \cdot \left[\left(\frac{M}{M_1} \right)^{-\beta} + \left(\frac{M}{M_1} \right)^{\gamma} \right]^{-1} \tag{5.2}$$

The parameters N, M_1, β and γ are taken from [MNW13] and listed in Appendix B. The function is plotted in the left panel of Figure 5.1 for $z = 0$. The right panel shows stellar mass fraction of halos, predicted by this model. As can be seen the function peaks at roughly $6 \cdot 10^{11} M_\odot$, which means that galaxy sized halos have the largest fractions of stars. This

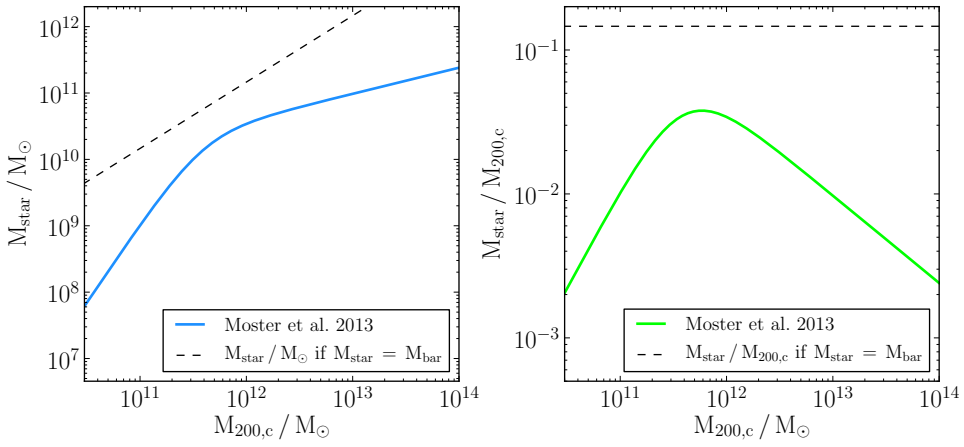

Figure 5.1: **Left panel: The SHM relation as found by [MNW13] in blue. For comparison the dashed line shows $M_{star\,(M)}$ if all baryons would be converted into stars. Right panel: The stellar mass fraction of halos, described by the function of Equation (5.2) divided by the halo mass. The dashed line shows the universal baryon fraction.**

is however below the mass range considered in this thesis, which is for the simulations of the 16 halos, involving feedback mechanism $5 \times 10^{12} M_{\odot} < M < 6.5 \times 10^{13} M_{\odot}$. Figure 5.2 shows the SHM relation for the four tested models of stellar feedback. All results and plots in the remaining part of this thesis, are taken at redshift $z = 0$, unless stated otherwise. The colour code remains the same in all plots.

The first feature which meets the eye in Figure 5.2 is that, the relation between stellar mass and halo mass is indeed close to linear for all four SF models. The trend is slightly broken by the high mass halos. The default model (red) is close to a relation in which 45% of the universal baryon budget is converted into stars (dot-dashed line), or in other words, the stars make up 6.5% of the halo mass. Since in the underlying cosmological model, the baryons make make up 14.6% of the total mass in the universe (dashed line).
Second, it can be seen, when the four SF models are compared with each other, that the

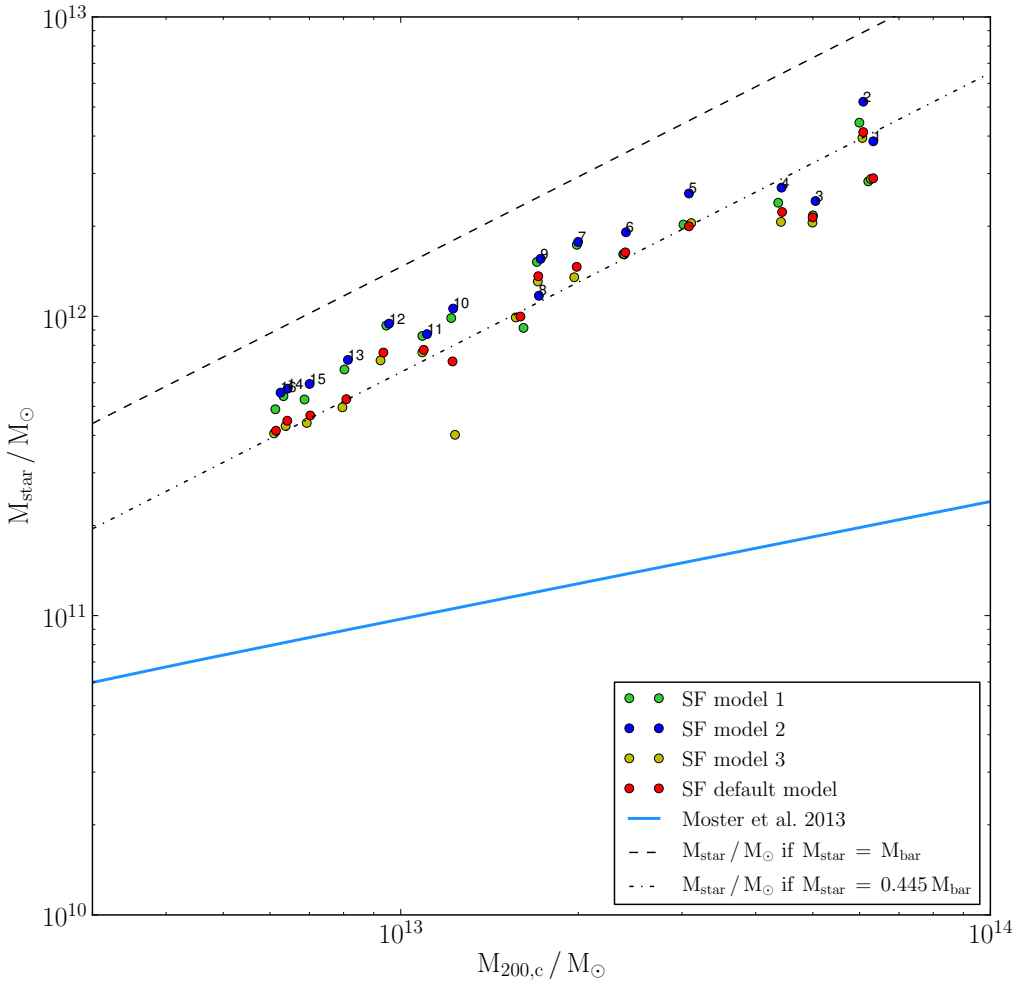

Figure 5.2: **The numerical result for the SHM relation, for simulations involving the four models of stellar feedback.**

ones for which the stellar feedback is turned of partially (blue) and fully (green) are less effective in quenching star formation than the default model, as the halos have larger stellar masses. Slightly more efficient than the default model is however the SF model 3, in which radiative feedback is included (yellow). Halo 10 is particularly affected by the addition of this mechanism. It is interesting to note, that for SF model 2 (blue) the halos have significantly more stellar mass than for SF model 1 (green). The difference between the two is that in the case of SF model 2, the metals from supernova explosions are still injected into the gas. The behaviour in the plot can therefore be explained by the effectiveness of cooling, which is higher if a larger fraction of metals is present. This leads to a higher rate of star formation as opposed to SF model 1, where the cooling is less effective since fewer metals are present in the gas.
Compared to the fit from Moster et al. 2013 (bright blue), all four stellar feedback models overshoot the stellar masses by roughly a factor of eight at the low mass end at roughly a factor of 20 at the high mass end.
To summarize the insight from Figure 5.2 it can be said, that the effectiveness of stellar feedback in the quenching of star formation is largely independent of the halo mass. The logarithmic slope of the analytic fit to observations by Moster et al. 2013, however requires a feedback mechanism to be more effective towards higher halo masses.

5.1.3 Half mass radius of the central galaxies

The abundance matching technique was also applied by Andrey Kravtsov in 2013, to relate the $r_{200,c}$ value to the half mass radius r_{hm} of their central galaxies. In [Kra13] he derived this value pairs for an observational catalogue of galaxies and found a linear fit to them:

$$r_{hm} = 0.015 \cdot r_{200,c} \tag{5.3}$$

The half mass radius of a galaxy r_{hm} is defined as the radius which contains half of the galaxy's stellar mass. In accordance to the above definition, to estimate the stellar mass of the galaxy as the stellar mass within $0.1r_{200,c}$, we define r_{hm} as the radius, which contains 50% of the stellar mass within $0.1r_{200,c}$. We have ascertained that this is reliable estimate, by looking at the stellar mass profiles of the halos. The SF default model can reproduce the linearity of the Kravtsov 2013 fit but has a slightly higher proportionality constant of 0.0225 (dashed line). The radiative feedback model (SF model 3) also shows the linear

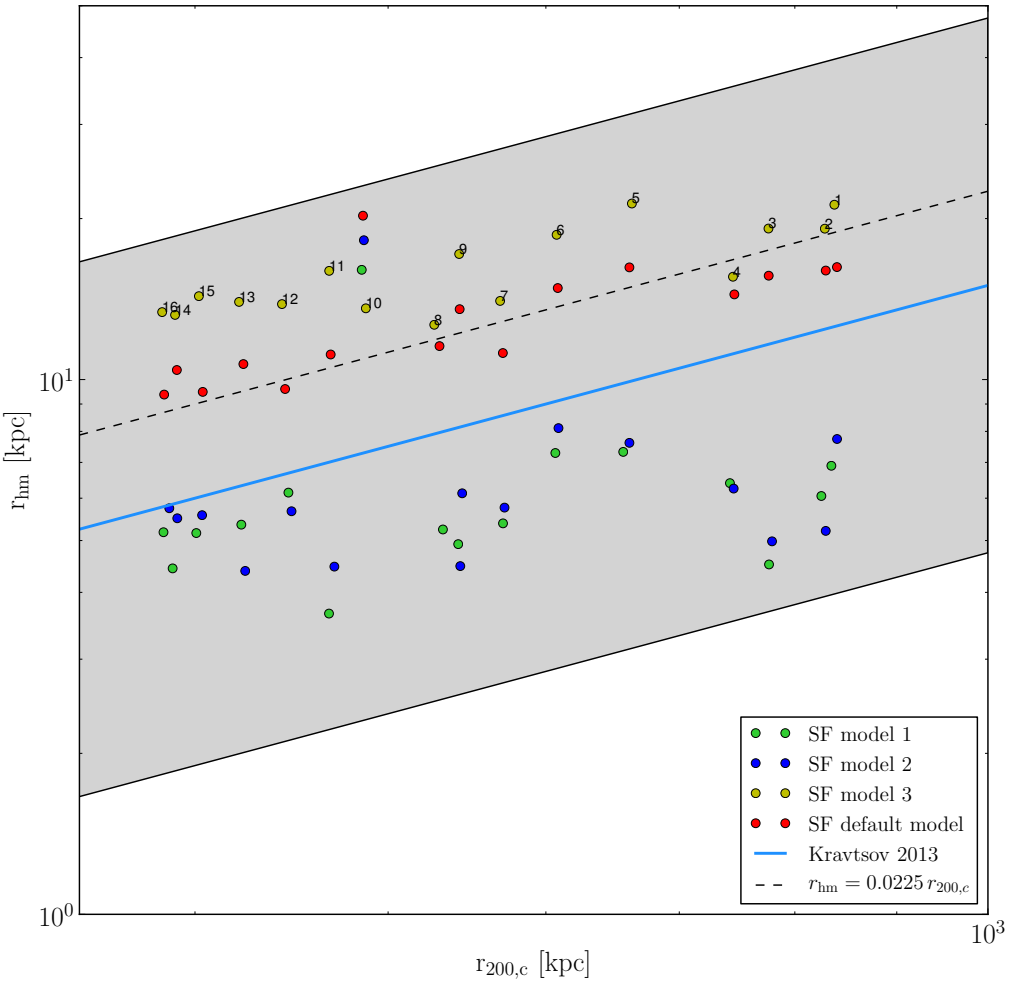

Figure 5.3: **The numerical result for the half mass radius to $r_{200,c}$ relation, for simulations involving the four models of stellar feedback.**

characteristic, but not as clear as the default model, especially towards the high mass end. The scatter is also significantly higher than for the default model, as is the difference to the Kravtsov 2013 fit in the slope. The two models without feedback energy (SF model 1 and SF model 2), both underestimate the slope of the fit and have significantly higher scatter than the models with feedback. A linear relation is hardly recognisable for them. If a functional dependence is to be guessed, it would rather be a constant one. There is also no indication for whether SF model 1 or SF model 2 would have larger half mass radii for any given halo mass interval.
All four models lie within the variance band of $\sqrt{10}$ kpc, suggested by Kravtsov 2013 (grey shaded area). In this context it would be interesting to analyse the effect of the stellar feedback onto the morphologies of the galaxies. However since this is not the main topic of this study, and since time is limited, a brief glimpse was possible for only one of the halos: Halo 2.
In the two cases of SF model 1 and SF model 2 the central galaxy, has the shape of a concentrated disk, with a clearly noticeable bulge. With the application of stellar feedback in the default model, the disk structure is strongly dissolved, but still recognisable. The height of the bulge is reduced and the disc itself thicker in total. With the addition of radiative feedback (SF model 3) the galaxy becomes an elliptical or irregular one. No indication of a disk structure is present. The maps of the central galaxies are shown in Appendix C.
To summarize, the feedback extends the size of the galaxies, additional feedback like in the case of SF model 3 increases their size even more. An outlier presents again Halo 10, but only for the default model, SF model 1 and SF model 2.

5.1.4 Baryonic gas mass fraction

Besides the stellar mass contained in the halos, the second important quantity for the characterization the baryonic mass distribution in halos, is the fraction of baryonic gas mass of the total of halo mass. Here the observational information sources are primarily X-ray surveys like *XMM-Newton* or *Chandra*. In Figure 5.4 the results of the simulation with stellar feedback are compared to the X-ray survey results from Gonzales et al. 2013 [GSZZ13], Sun et al. 2009 [SVD+09] and [VKF+06]. These observations are limited to the central part of the halo, where the baryonic gas is hot enough to emit the X-rays. Therefore the mass distribution in the outer parts is not well detectable and the gas mass and total mass are quantified by their value within r_{500}. This radius is defined with respect to the critical density of the universe. The subscript c is dropped however, as no other definition of r_{500}

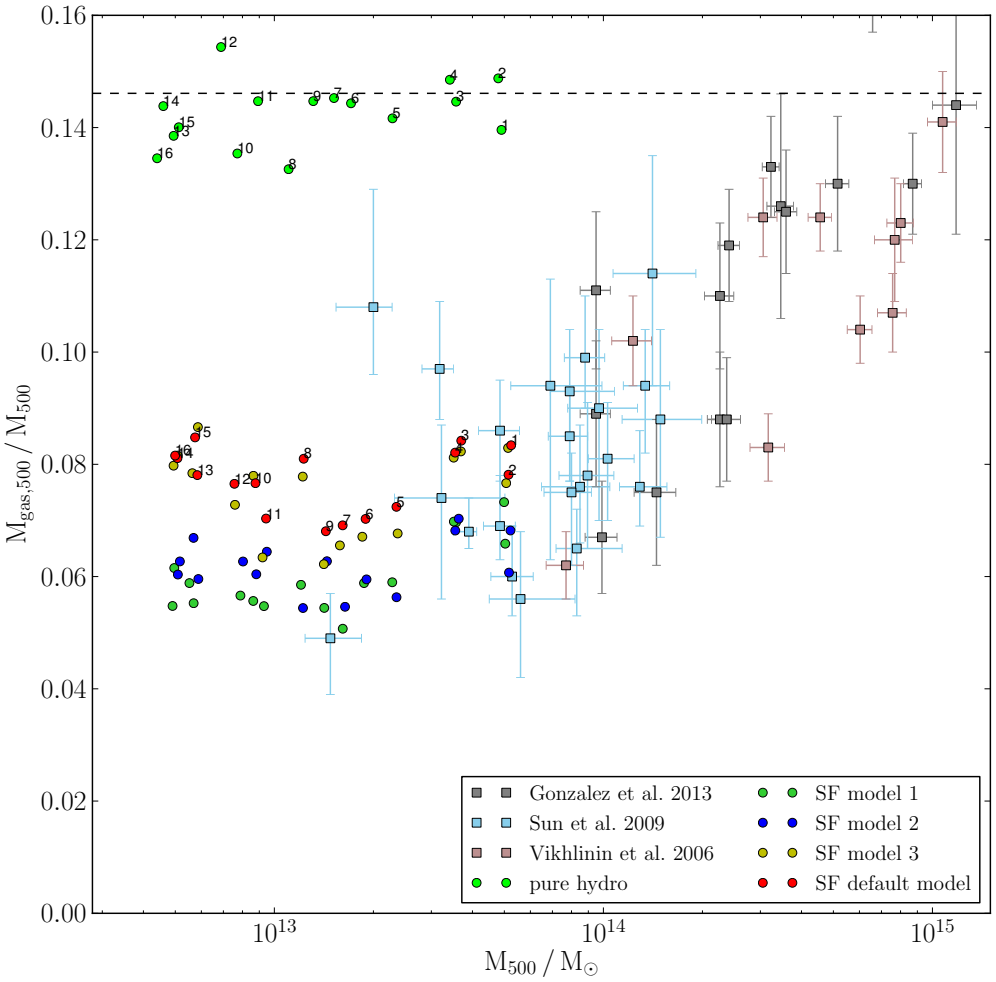

Figure 5.4: **The numerical result for the baryon fraction within r_{500}, for simulations involving the four models of stellar feedback. For comparison, the result from the non-radiative hydrodynamics (pure hydro) simulations are also plotted, as well as the universal baryon fraction (dashed line).**

was used before in the text.

The halo mass range probed by the mentioned X-ray surveys is a slightly higher than the one in the underlying study. Not much overlap is therefore present. Nevertheless it is possible to compare the simulated high mass halos to the X-ray results. But for the small mass end the comparison becomes difficult. In particular, it is unclear whether the detectable slope of the $M_{gas,500}/M_{500}$ to M_{500} relation remains the same towards mass ranges of $M_{500} \approx 10^{12} M_{\odot}$ or if it becomes shallower.
Given the scatter in the observational data points, all four SF models seem to agree with the empirical data, for the four largest halos. When comparing the four SF model with each other, it is clearly visible that a hierarchy is present over the entire mass range, where the default model (red) has the largest baryon fractions, followed by the model with radiative feedback (yellow). Then comes the model without energy feedback, but metals (blue) and finally the model with no stellar feedback at all (green), which has the smallest baryon fractions. For the half of the halos with higher masses (Halo 1 - 9), a trend of increasing gas mass fraction towards higher halo mass is present. This could be interpreted as in agreement with the trend in the observational data. For the lower mass half (Halos 10 - 16) however, this is not the case. These halos rather cluster around constant values of $M_{gas,500}/M_{500} = 0.06$ and $M_{gas,500}/M_{500} = 0.08$, or even show signs of decrease towards higher halo masses, for the case of the two models with feedback.
The baryon fractions from the purely non-radiative halo run (bright green), which are plotted for comparison, cluster all around the universal baryon fraction of 0.1461.

5.1.5 Stellar and gas mass fractions within the same radii

Probably the most important question about the effectiveness of any feedback process is, if its effect is solely to quench star formation. In that case the gas which was not transformed into stars still remains within the halos and even though the stellar mass fraction might be lower than without feedback, the gas fraction will generally be to high. What is required from the feedback process, is that in addition the overabundant gas is pushed out of the halos.
To check whether the latter process is present, or if there is just a trade-off between stars and gas, one needs to look at gas and stellar fractions within the same radii, and compare them. The results plotted in Figures 5.5 - 5.8, are not directly compared to observations, but rather serve the purpose of comparing code internally apples with apples.

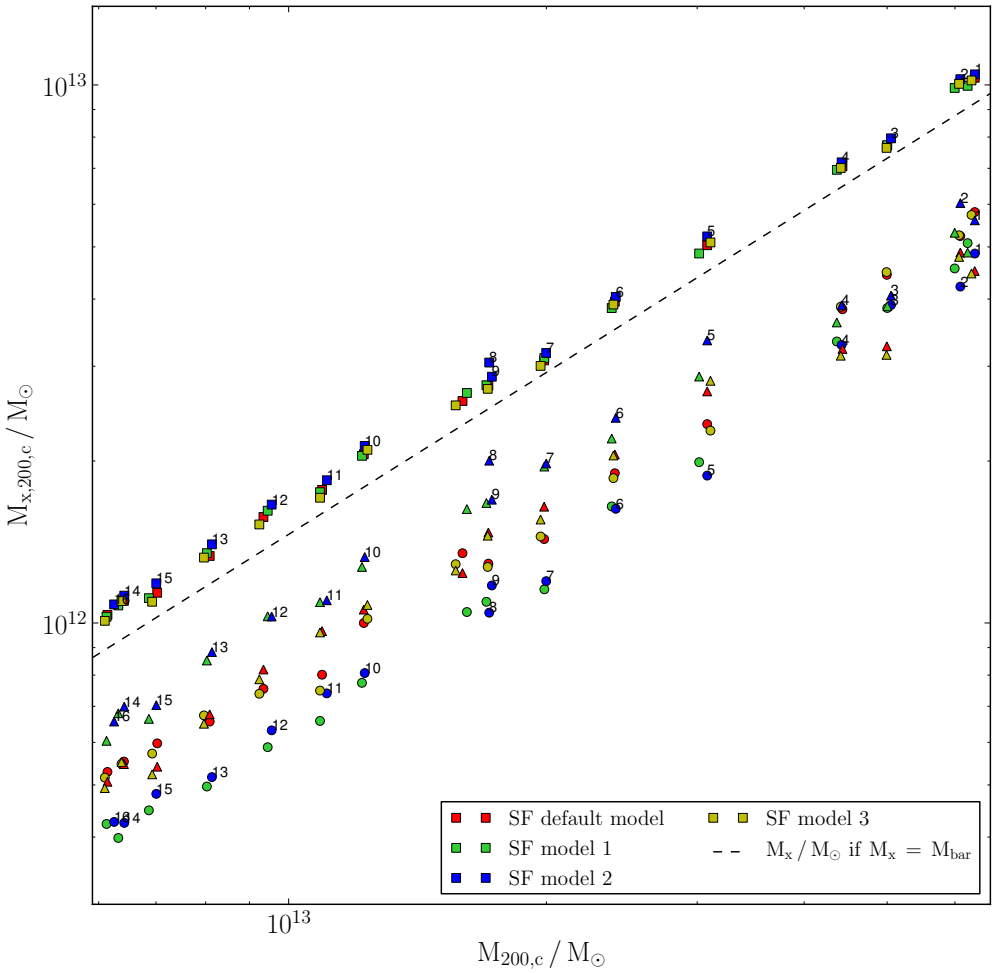

Figure 5.5: **The stellar, gas and total baryonic masses within $r_{200,c}$. Circles denoted the gas mass, triangle denote the stellar mass and squares denote the total baryonic mass. The dashed line is the universal baryon fraction. The colour code is the same as in the previous plots of this section.**

Within $r_{200,c}$ the total baryonic mass fraction of the total halo mass, overshoots the universal baryon fraction by a factor of 10/9.
For the models with stellar feedback turned of (green and blue), two different trends are observable from Figure 5.6, for two separate halo mass ranges. Halos 5 - 16 have almost 1.5 times as much stellar mass as gas mass. For Halos 1 - 4 the differences are smaller. The two models with full stellar feedback (red and yellow), show three distinct trends: Halos 10 - 16 have roughly equal stellar and gas mass fractions, Halos 5 - 9 have more stellar mass than gas mass, except Halo 8. Halos 1 - 4 have more gas mass than stellar mass.
Figures 5.7 and 5.8 show that within r_{500}, all four models overshoot the universal baryon fraction even more than for the case within $r_{200,c}$, namely by a factor of 5/4. Although,

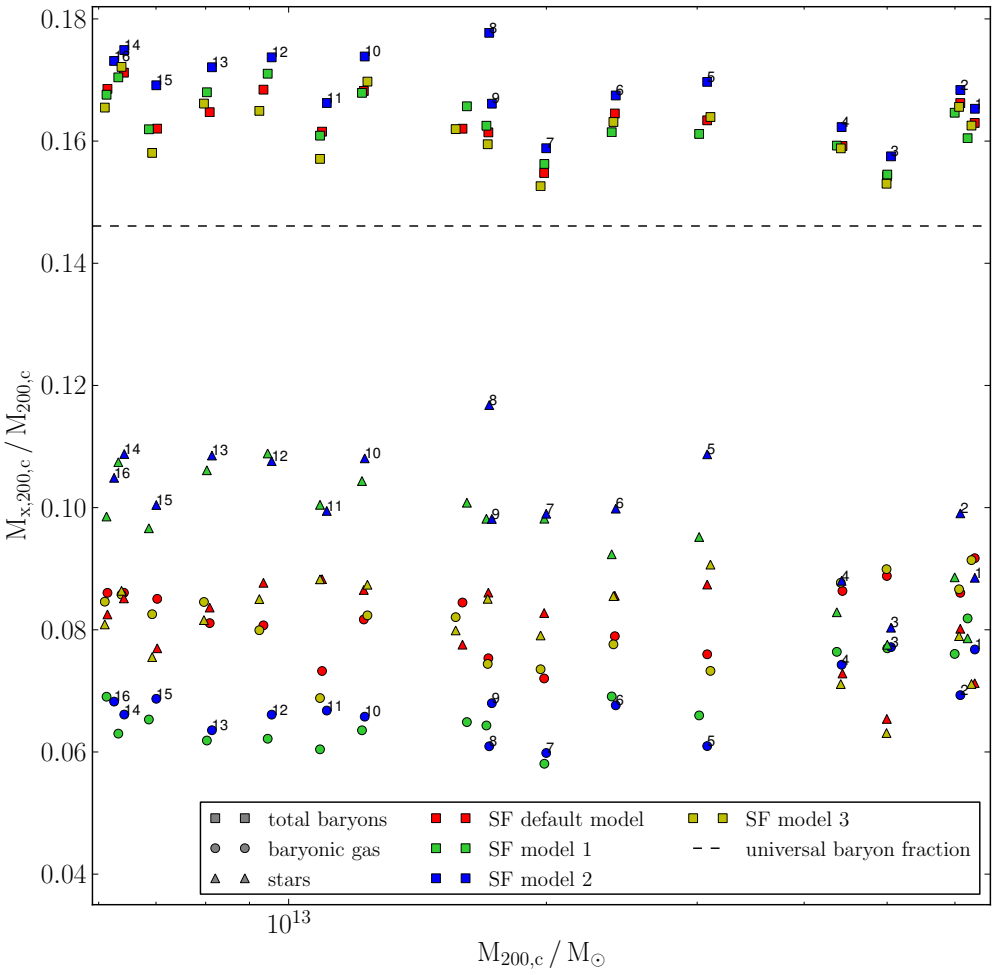

Figure 5.6: **The stellar, gas and total baryonic mass fractions within $r_{200,c}$. Circles denoted the gas mass fraction, triangle denote the stellar mass fraction and squares denote the total baryonic mass fraction. The dashed line is the universal baryon fraction. The colour code is the same as in the previous plots of this section.**

towards the high mass end, there is a decrease in the total baryon fraction towards the value of 10/9 of the universal baryon fraction, like in the $r_{200,c}$ case.
For almost all 16 halos the stellar mass fraction is higher than the one of the gas. Again, two distinct trends are visible in two different mass regimes. For Halos 5-16 the two models with feedback turned of have twice as much stellar mass as gas mass. The two models with full stellar feedback have around 1.3 times as much stellar mass as gas mass. For Halo 1-4 this overall behaviour is still present, but the differences between the stellar and gas mass are smaller.
Given the fact, that for both $r_{200,c}$ and r_{500}, the enclosed total baryonic masses of the halos are smaller for the SF default model and SF model 3, than for SF model 2, it can be said, that stellar feedback actually pushes the baryons out of the halos, but not in a significant

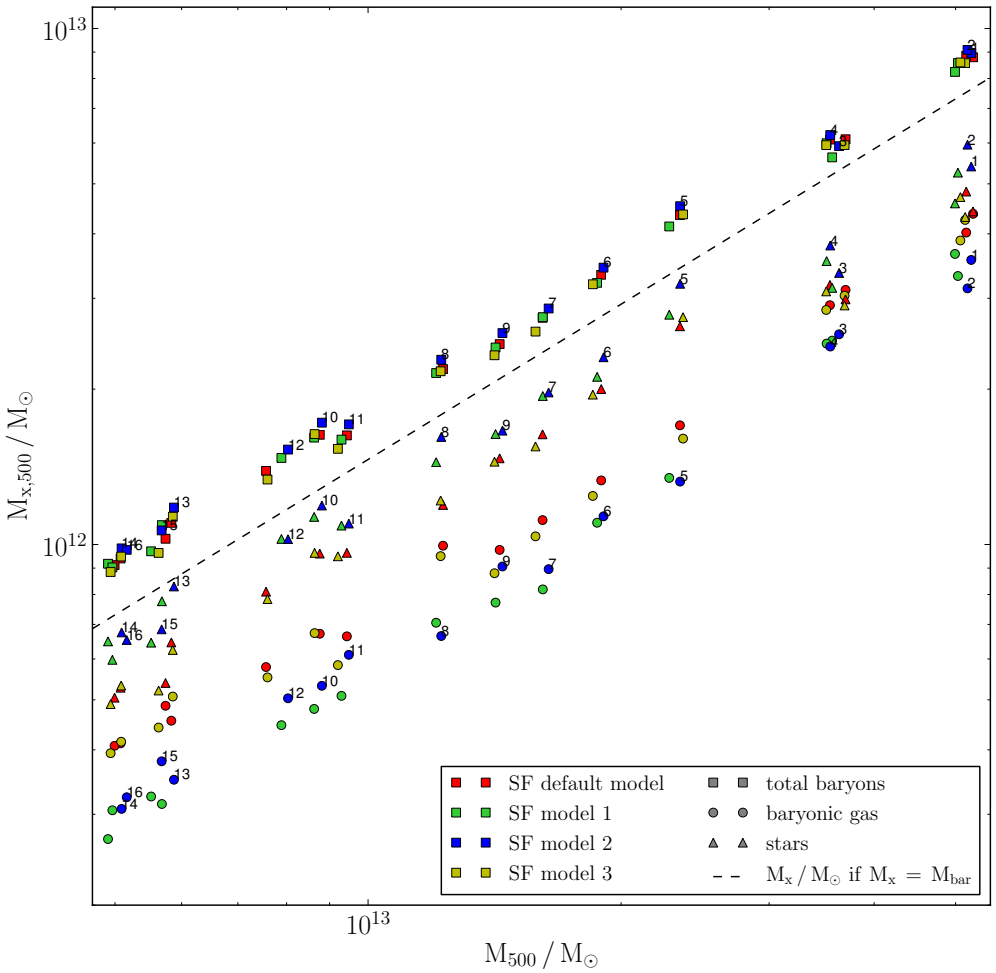

Figure 5.7: **The stellar, gas and total baryonic masses within r_{500}. Circles denoted the gas mass, triangle denote the stellar mass and squares denote the total baryonic mass. The dashed line is the universal baryon fraction. The colour code is the same as in the previous plots of this section.**

fashion. SF model 2 ironically mimics the two models with full stellar feedback in this respect, as its absence of supernova induced metals makes the cooling of the gas inefficient and therefore prevents it from falling into the halos. The most important difference between the two models with feedback and the two without, are however, the stellar and gas mass fraction. As the models with feedback have significantly less stellar mass, but therefore more gas mass, the primary effect of the stellar feedback process, is indeed the quenching of star formation for a given amount of gas, and not pushing the gas out of the halos.
A slight difference exists between the two models with feedback, the one which also includes radiative feedback (yellow) has slightly smaller total baryon fractions. The stellar mass fractions are however roughly the same for the two models. The gas mass fraction is in

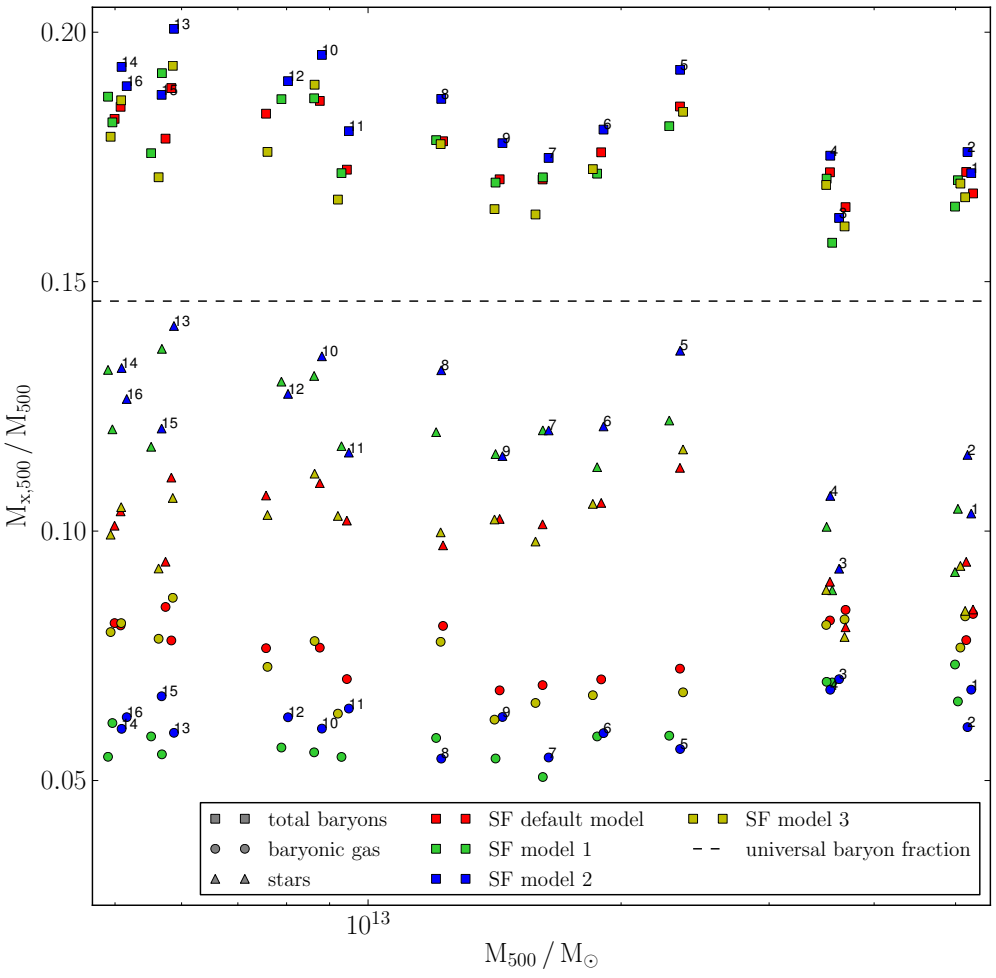

Figure 5.8: **The stellar, gas and total baryonic mass fractions within r_{500}. Circles denoted the gas mass fraction, triangle denote the stellar mass fraction and squares denote the total baryonic mass fraction. The dashed line is the universal baryon fraction. The colour code is the same as in the previous plots of this section.**

some cases lower for the model with radiative feedback. This would be consistent with a picture where the effect resulting from the addition of radiative feedback, is indeed to keep the baryonic mass out of the halos, but also that SF model 3 must be a bit more efficient in the formation of stars, as it has less baryonic mass available to do so.
SF model 1 and 2 also have similar stellar fractions in most cases, and therefore the SF model 2 has slightly higher gas mass fractions. This means, that SF model 1 is a bit more efficient in forming stars, since it has less baryonic mass available in the halos, than SF model 2.

5.1.6 Summary and Conclusions

Stellar feedback alone is far from reproducing the stellar mass fractions, required to match observations, as it overshoots the latter. Regarding the gas mass fractions the situation looks better in the sense that the implementations of stellar feedback tested in this study, are indeed in the right range to match the observations. However, this comes only because the star formation is so efficient, that a too large fraction of the baryonic mass is converted into stars, as was shown in the plots of this section. Further, the direct comparison is difficult for the low mass halos, as the experimental data required of a comparison is missing.
Most importantly the main effect of stellar feedback, is to quench star formation, for a given amount of available baryons in a halo. Only as a secondary effect the stellar feedback also removes the baryonic gas from the halos. The addition of radiative feedback amplifies this process slightly.
Aside from these properties, the effect of the stellar feedback, onto the considered mass fractions, is fairly independent of the halo mass. Also the two models with feedback turned off, show mass fraction properties which are halo mass independent. It might be possible to describe the mass distributions of halos in simulations including cooling, star formation or even stellar feedback, also with a scale free analytical model, like in the case of non-radiative hydrodynamics (see Section 3).

5.1.7 Halo maps

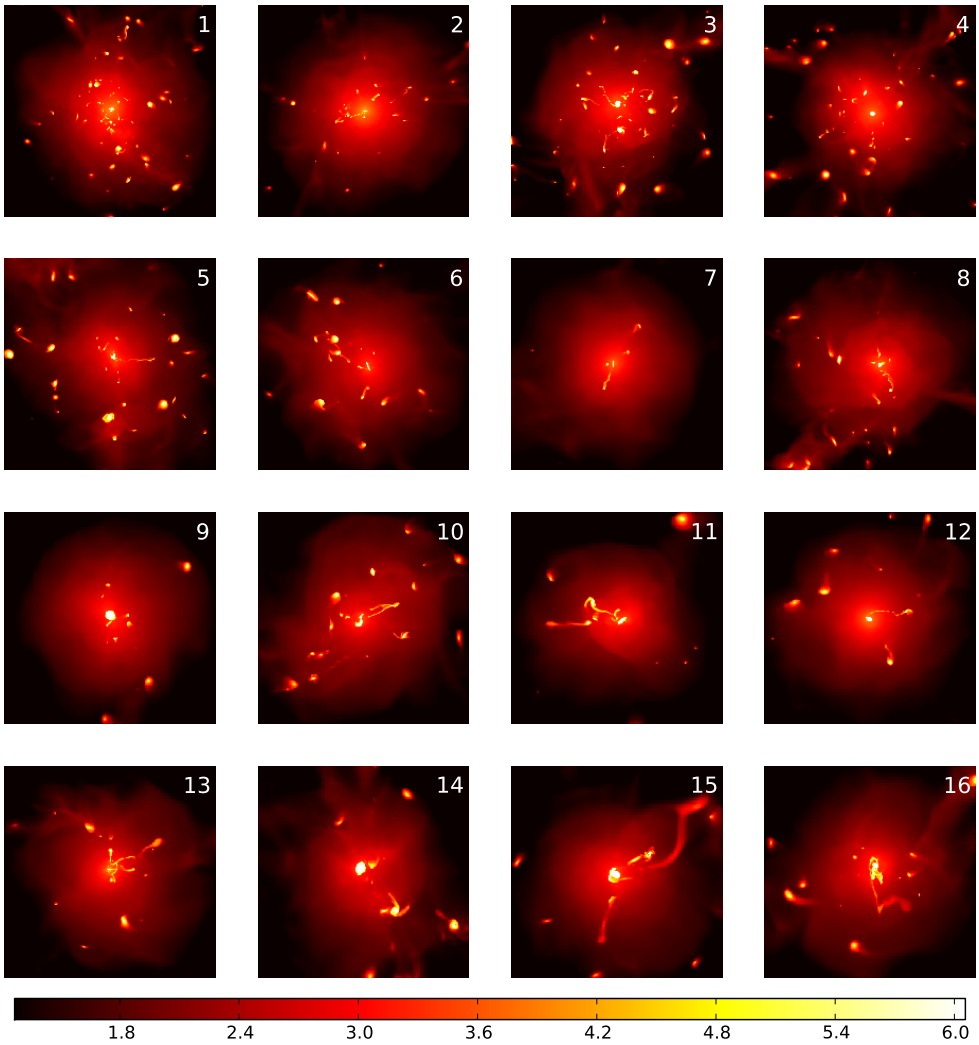

Figure 5.9: **Gas density maps for the default stellar feedback model. The colour bar unit is $\log_{10}(\rho_{gas}/\bar{\rho}_b)$, where $\bar{\rho}_b$ is the average baryon density in the universe. The side length of each map is $2r_{200}$, with the centre of the maps corresponding to the centre of mass of the halo.**

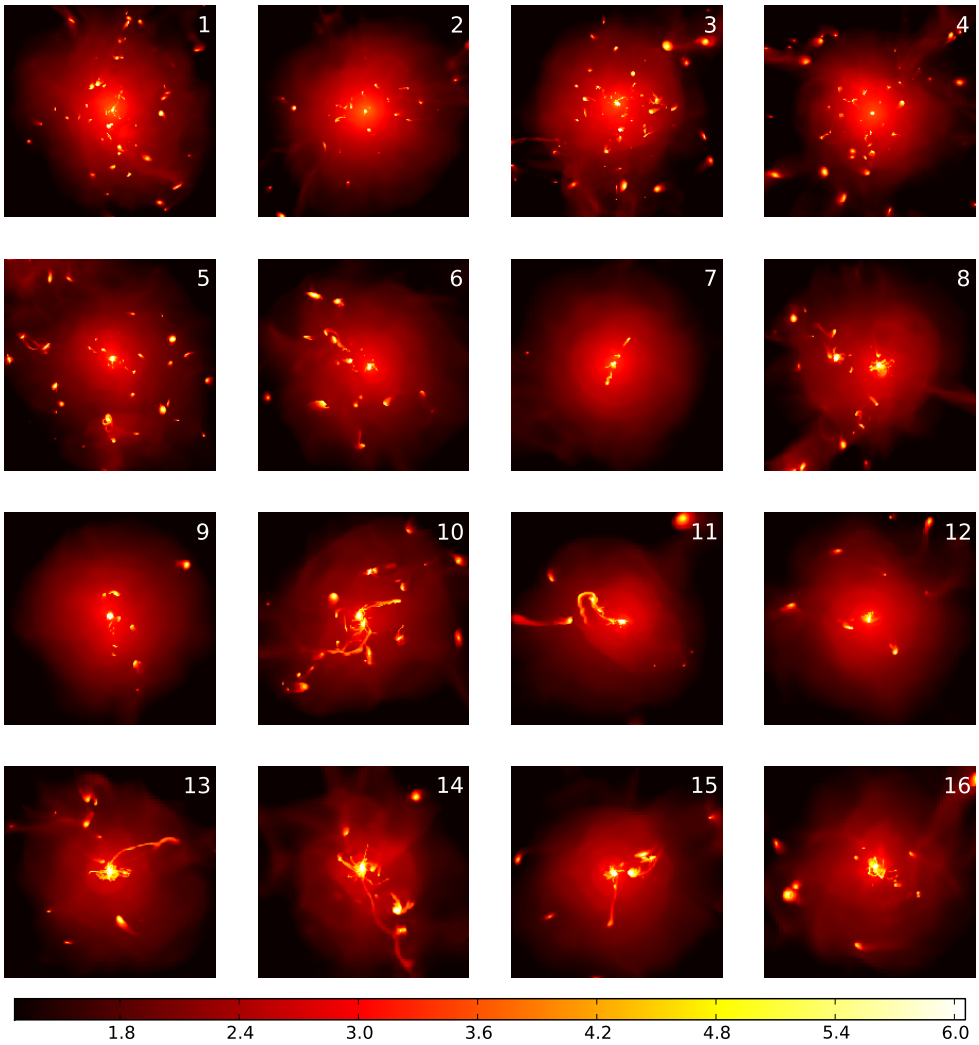

Figure 5.10: **Gas density maps for the SF model 3. The colour bar unit is $\log_{10}(\rho_{gas}/\bar{\rho}_b)$, where $\bar{\rho}_b$ is the average baryon density in the universe. The side length of each map is $2r_{200}$, with the centre of the maps corresponding to the centre of mass of the halo.**

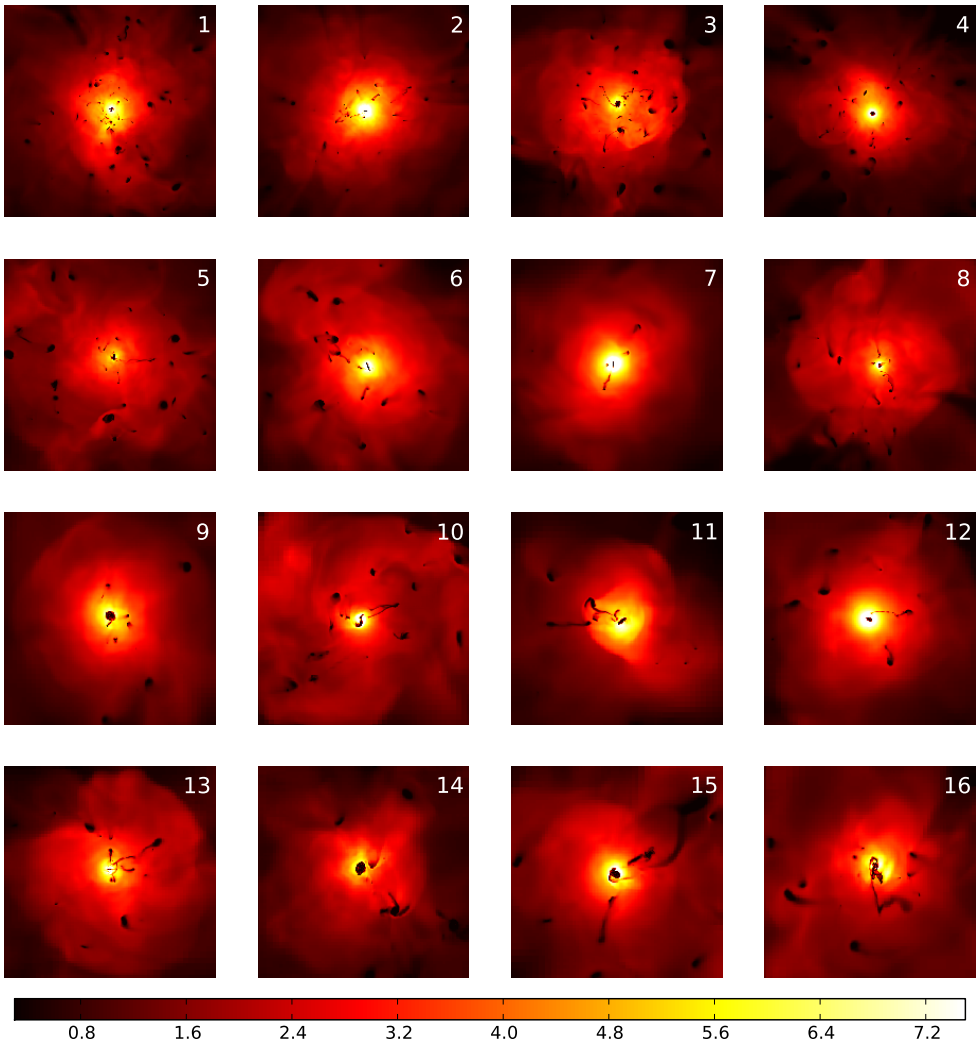

Figure 5.11: **Gas temperature maps the default stellar feedback model. The colour bar unit is T_{gas}/T_{200}, where T_{200} is computed for each individual halo as $T_{200} = \frac{1}{3}\frac{m_p}{k_B}\frac{G\,M_{200}}{r_{200}}$. The side length of each map is $2r_{200}$, with the centre of the maps corresponding to the centre of mass of the halo.**

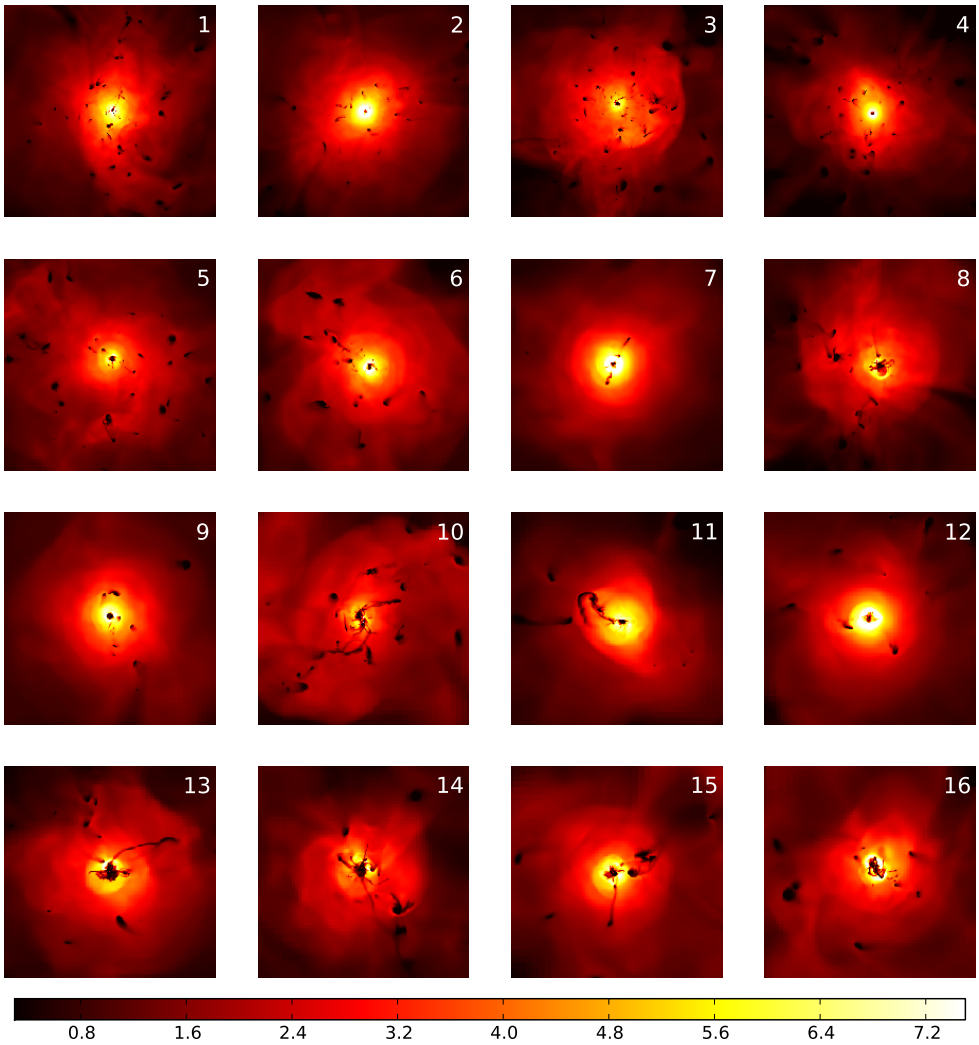

Figure 5.12: **Gas temperature maps for the SF model 3. The colour bar unit is T_{gas}/T_{200}, where T_{200} is computed for each individual halo as $T_{200} = \frac{1}{3}\frac{m_p}{k_B}\frac{G\,M_{200}}{r_{200}}$. The side length of each map is $2r_{200}$, with the centre of the maps corresponding to the centre of mass of the halo.**

5.2 Exploring the parameter space of AGN feedback

5.2.1 Overview

While on the level of n-body physics and non-radiative hydro dynamics the equations of motion, which are derived from first principles, can be implemented and the results compared with observations, the situation is more complicated if sub-grid physics is involved. The point is that the parameters of the sub-grid models need to be gauged with observational results. Hence the simulation has no predictive power, if the same results are reproduced by it. However, it is possible to gauge the parameters of a sub-grid model with observational results of a certain astrophysical / cosmological situation or magnitude and then apply the sub-grid model with the newly found parameters, to a different situation or magnitude.
In this work the simulation results of the mass fractions of stellar and baryonic gas within the halos are compared to observational data, and simulation parameters of the Active Galactic Nucleus feedback (AGNF) model are adjusted to match the latter.
Starting from a physically motivated default model, the space of the two key parameters, the black holes seed mass M_{seed} and the coupling efficiency ϵ_c, was explored, as far as time and computational resources permitted it. Mainly four additional models could be tested, however not all of the 16 halos for either one. The values of the two key parameters, M_{seed} and ϵ_c, are listed in 5.1, for each of the five models.

Table 5.1: **The parameters values of the tested AGN feedback models.**

Model	$M_{seed}/M_{\odot}$	ϵ_c
Default Model	10^5	0.15
AGN Model 1	10^7	1
AGN Model 2	10^5	10
AGN Model 3	10^5	1000
AGN Model 4	10^7	10

It should be pointed out, that any value of ϵ_c, that is larger than one is unphysical, in the sense of the definition in Subsection 4.6. Nevertheless, this parameter range was explored in three of our models, since the coupling between radiation and gas is the pivotal process for the heating of the latter.

5.2.2 Stellar to halo mass (SHM) relation

Compared to stellar feedback default model (dot-dashed line), the addition of AGN feedback in the AGNF default model (magenta), reduces the stellar mass within $0.1 r_{200,c}$ by a factor of three at the low mass end, and by a factor of four at the high mass end. The logarithmic slope is however roughly the same for the two models. In an analysis by Martizzi et al. from 2012 [MTM12], a preceding version of the underlying Ramses AGN implementation was applied to a galaxy cluster size halo of roughly $10^{14}\, M_{\odot}$. The stellar feedback model in their analysis was however the same as in this work. They arrived at a factor of 20, in the difference of the stellar mass within the central galaxy, between their model which included AGN feedback and the one with only the stellar feedback. Also in [DGPS13], the authors quantify the differences in the SHM relation between a related model of AGN feedback implemented in Ramses and the same model of stellar feedback as in the underlying study, for five halos in the same mass range. They find a reduction in stellar mass by a factor of

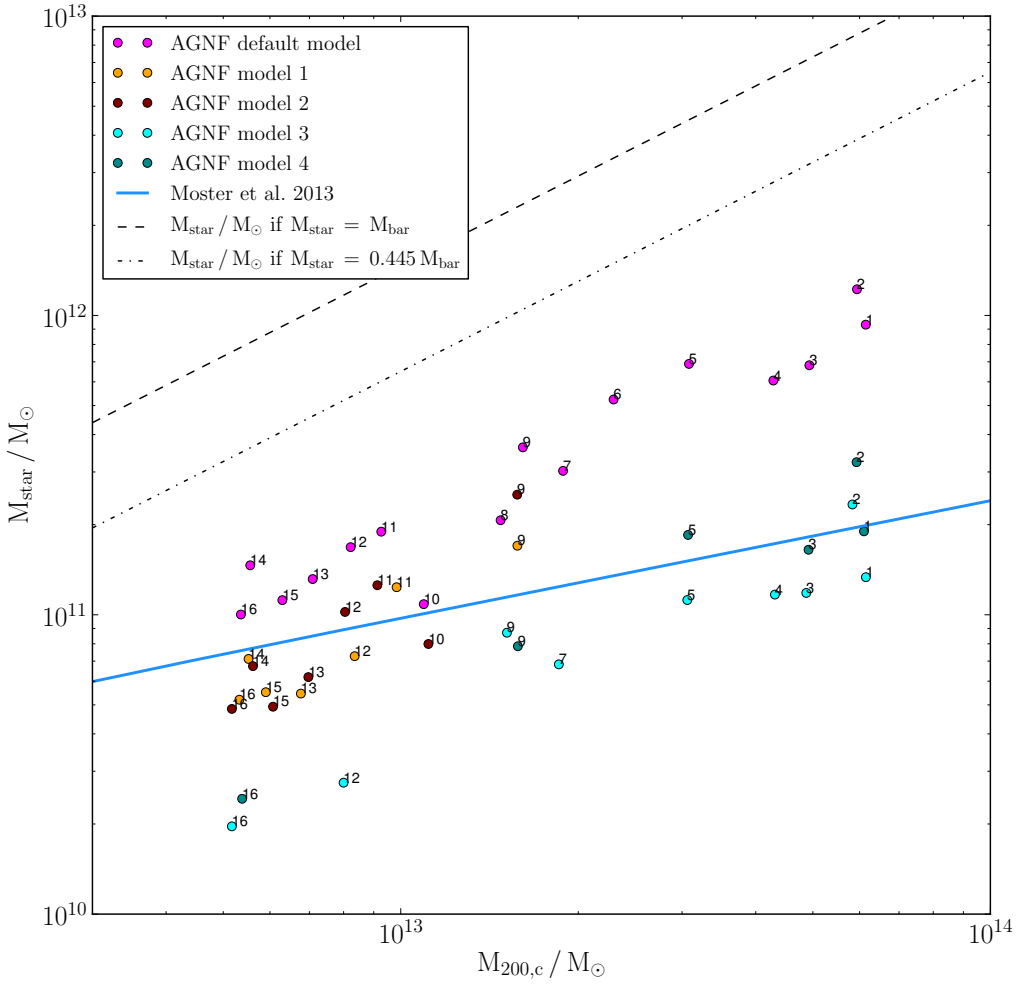

Figure 5.13: **The numerical result for the SHM relation, for simulations involving the four models of stellar feedback.**

eight, for the case with AGN feedback.
The AGNF default model overshoots the relation from Moster et al. 2013 by a factor of 1.3 at the low mass end and by a factor of 5 at the high mass end. The shallow logarithmic slope of the analytic model cannot be reproduced by the simulations with the AGNF default model. For the other four models it can be seen that they reduce the stellar mass, compared to the default. However, none of them seems to have changed the logarithmic slope. For models AGNF 1 (orange) and AGNF 2 (maroon) this featured is, of course, not conclusive because of the few data points, but for model AGNF 3 (cyan) and AGNF 4 (dark green), the trend is clearly present.
The result of Figure 5.13 would hence suggest, that for the higher half of the sampled mass range AGNF model 3 and AGNF model 4 would be good choices. AGNF model 4 stands on more solid physical ground, of course, because of its more realistic value of ϵ_c. For the low mass range (Halo 9 - 16), AGNF model 1 comes closest to the analytic fit. However to few data points are available to make a well warranted statement.
In [BBP$^+$10] an AGN feedback model, in which the feedback efficiency depends on the stellar mass within a certain radius and on the redshift, was tested in the context of SPH simulations. It would be interesting to test this model in an AMR framework, like the one of Ramses.
The conclusion from Figure 5.13 is that, $M_{seed} = 10^7$ seems to be a good choice over the entire mass range considered. $\epsilon_c = 1$ can reproduce the stellar masses for the low mass half, and $\epsilon_c = 10$ for the high mass half. Both values for ϵ_c are of course not well motivated physically, as $\epsilon_c = 1$ would mean that all the energy from the emitted accretion disk radiation can be converted into gas energy, without any losses. And $\epsilon_c = 10$ would in the context of the above derivation of the model not make physical sense at all, as more energy in the gas would be produced, than is in the radiation budget. However, the value of $\epsilon_c = 10$ gives an indication, for what parameters could be alternated in additional tests of models, as in Equation (4.16), for the energy injected into the gas, ϵ_c and ϵ_r are degenerate parameters. A value pair of $\epsilon_c = 10$ and $\epsilon_r = 0.1$, like it is the case in AGNF model 1, would therefore be the same as $\epsilon_c = 1$ and $\epsilon_r = 1$ in this equation. However, the efficiency ϵ_r, which describes how the potential energy of an infalling particle is transformed into radiative energy, also enters into the equation describing the Eddington accretion rate (Equation (4.12)) and needs therefore to be changed correspondingly.
In the analysis of [DVS14] the authors discuss the dependence of the radiative efficiency ϵ_r, on the spin of the black hole, in the context of AGN feedback simulations with Ramses.

5.2.3 Half mass radius of the central galaxies

All five models including AGN feedback, lie above the default model of stellar feedback (red) in the entire mass interval, except Halo 10. The AGN models also lie above the analytic fit, but within the variance region (grey shaded area) of $\sqrt{10}$ kpc. For the default AGN model a clear slope is difficult to infer because of the large scatter, however the indication points more towards a constant relation between r_{hm} and $r_{200,c}$, than to a linear dependence. AGNF model 3 (cyan) and AGNF model 4 (dark green), on the other hand seem to reproduce the linear relation and attain a similar value range for the half mass radius, as the AGNF default model.
Although, the r_{hm}-$r_{200,c}$ gives some indication for which AGN feedback models might be preferred over others, a utilization of galaxy properties for the purpose of ruling out models, would require a full analysis of the morphologies of the central galaxies. This is beyond the scope of this work.

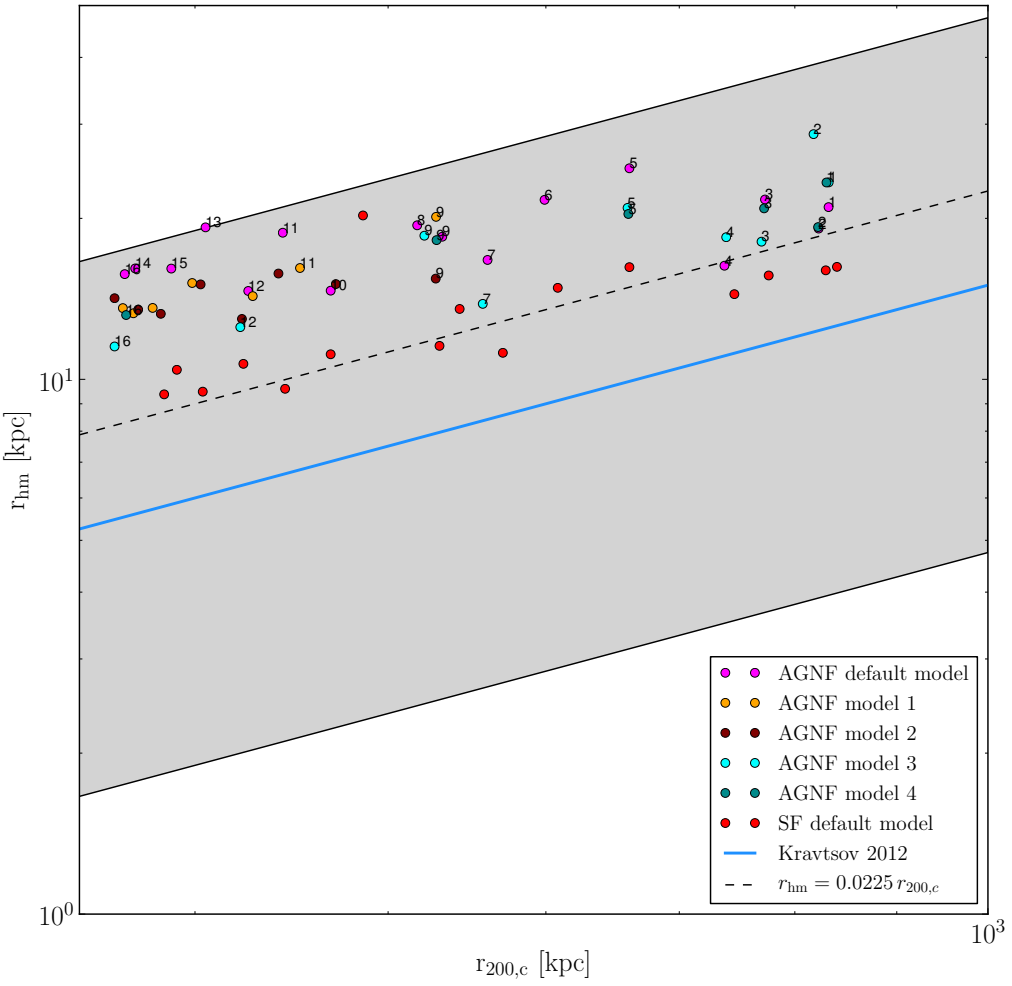

Figure 5.14: **The numerical result for the half mass radius to $r_{200,c}$ relation, for simulations involving the four models of stellar feedback.**

However, in the cosmological simulation analysis of [DGPS13] a different version of the AGN feedback model of Ramses was applied onto a halo sample, in roughly the same mass range as in this study. These authors describe the differences in the morphology of the central galaxy, between simulations with AGN feedback and without. Among many other results they report, that if AGN feedback is activated, then ellipticals are produced instead of disk galaxies, and that observational scaling laws are matched better.

5.2.4 Baryonic gas mass fraction

The first noticeable feature of the plot, is that at the high mass end (Halo 1 to 5) all three AGN models tested in this range, default AGNF (magenta), AGNF 3 (cyan) and AGNF 4 (dark green), overshoot the observational data points. Second, these three models are characterised by a steep increase towards higher masses, throughout the entire range under consideration. The same trend seems to apply to AGNF model 1 (orange). Therefore, the three mentioned AGN models overshoot the default model of stellar feedback by far, for the sampled cases from Halo 1 to 7, and lie below the SF default model for the range of Halo 10 to 16. Between the 3 mentioned AGN models, exist also differences, as AGNF model 3 lies above the default AGNF model, and AGNF model 4 in turn lies above AGNF model 3 in the high mass range. For Halo 2, AGNF model 4 even has a larger gas fraction, than

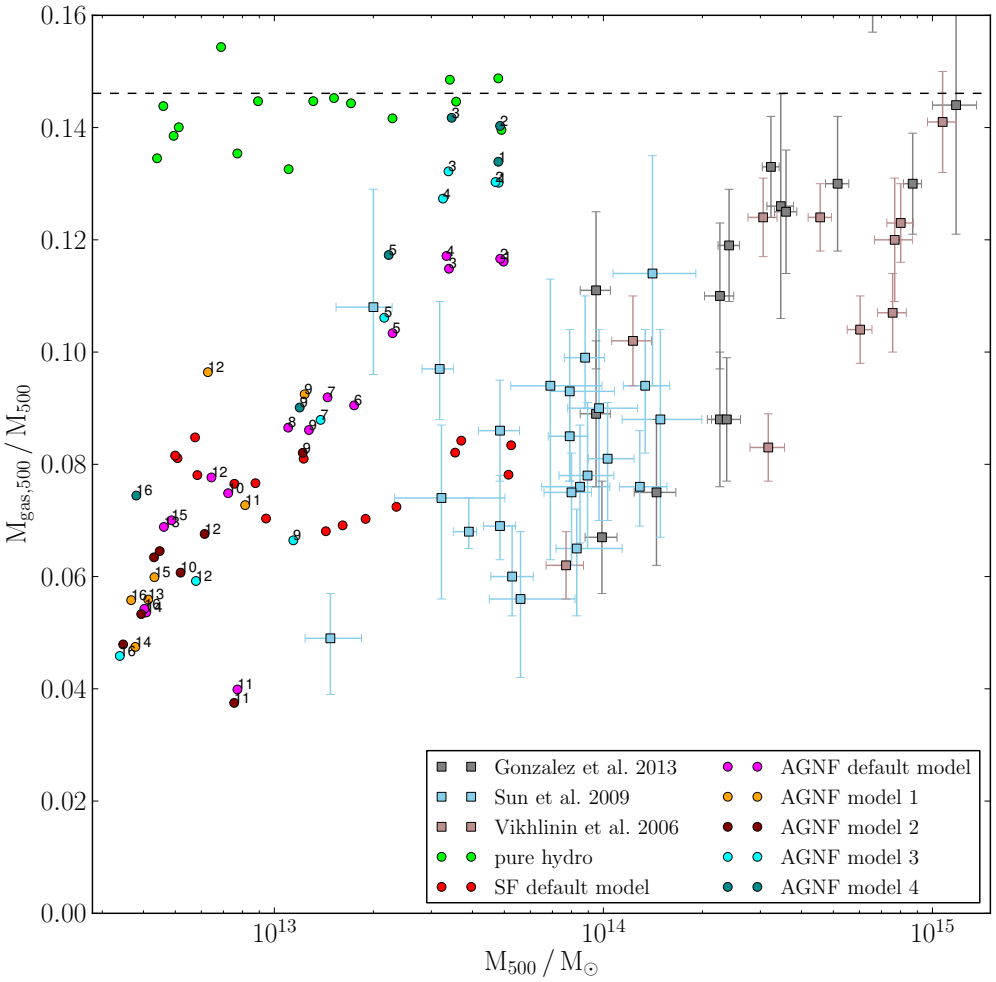

Figure 5.15: **The numerical result for the baryon fraction within r_{500}, for simulations involving the four models of stellar feedback. For comparison, the result from the non-radiative hydrodynamics (pure hydro) simulations are also plotted, as well as the universal baryon fraction (dashed line).**

the non-radiative simulation. For the low mass halos on the other hand AGNF model 3 lies below the default AGNF model.
What can be deducted from Figure 5.15, for the validity of the tested AGNF models? For the high mass halos, where overlap with the observations exist, the observational baryonic gas fractions cannot be reproduced by any of the AGNF models. In the low mass range from Halo 9 to 16 both the default AGNF model and AGNF model 3 might be good parametrisations, if the slope of observational data would become shallower towards small masses. The same might be true for AGNF model 1, but more tests are necessary. An outlier with a low gas mass fraction presents Halo 11, which however was tested only for the default AGNF model. To summarize, at the mass range around $M_{500} = 4 \cdot 10^{13}\, M_{\odot}$ none of the AGNF models successfully reproduces the considered observational data, inferred from X-ray surveys. In the mass range around $M_{500} = 4 \cdot 10^{12}\, M_{\odot}$ however, two of the tested AGNF models might be able to do that, but more observational data is required, to make a reliable statement.

5.2.5 Stellar and gas mass fractions within the same radii

For the gas mass and total baryonic mass fraction, the simulations including AGN feedback do not share the self similar behaviour of the simulations, which included only stellar feedback. Only for the stellar mass fraction the scale free behaviour is reproduced.
The total baryonic mass of every halo is however smaller, for AGNF models than for the SF ones. Nevertheless, the AGNF models still reach total baryon fractions which are slightly larger than the universal baryon fraction at the high mass end. Both total baryonic and gas mass decrease towards lower halo masses. This decrease is steeper for the r_{500} fractions, than for the $r_{200,c}$ ones.
All mass fractions strongly depend on the AGNF model. While AGNF model 3 (cyan) and 4 (dark green) are very close in the stellar mass fractions of the halos. They have differences

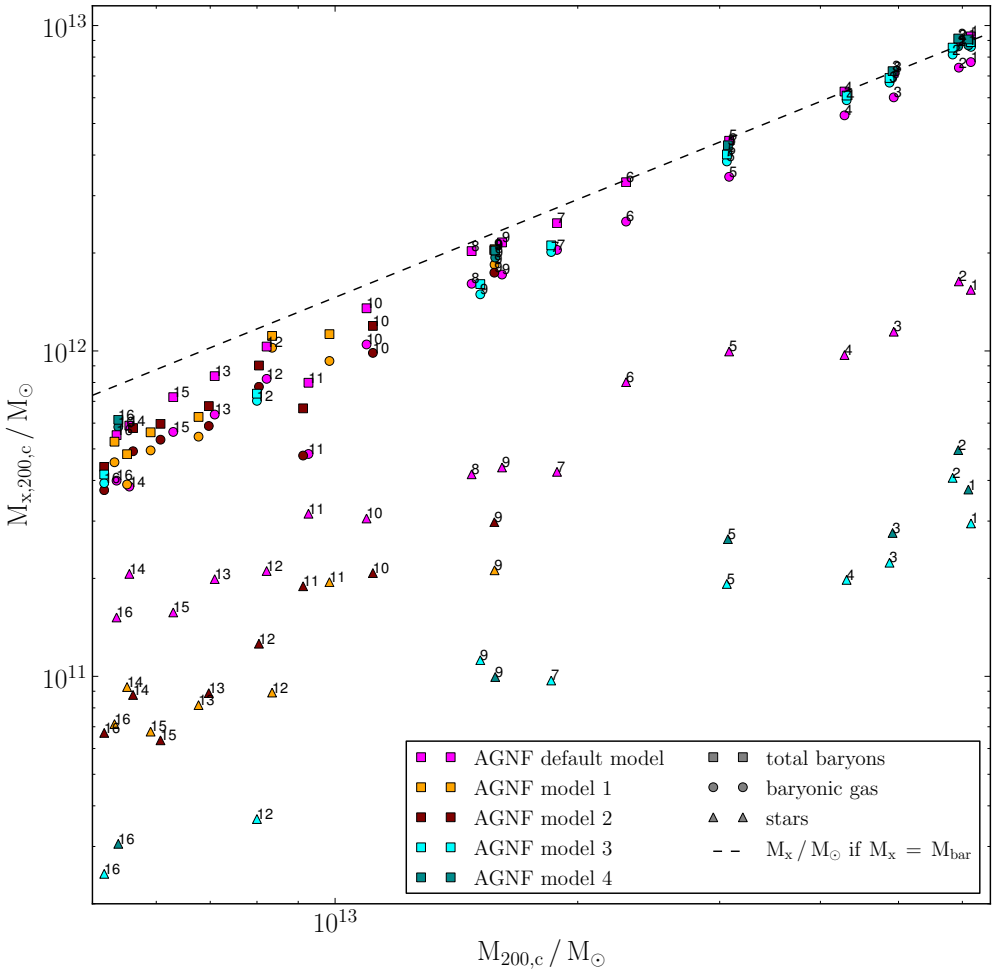

Figure 5.16: **The stellar, gas and total baryonic masses within $r_{200,c}$. Circles denoted the gas mass, triangle denote the stellar mass and squares denote the total baryonic mass. The dashed line is the universal baryon fraction. The colour code is the same as in the previous plots of this section.**

in the gas and total baryon fractions, as AGNF model 3 has smaller ones. Interestingly, the differences between gas and total baryonic mass, are very similar for both models. From these properties it follows directly, that AGNF model 3 is more efficient in pushing the baryonic gas out of the halos. This is mostly likely because of the high value of $\epsilon_c = 1000$. The default model of AGN feedback (magenta), lies above the two mentioned models with the stellar masses, by a factor of 3 or 4. For the gas mass it reaches similar values as the AGNF model 3 in the low mass half of the halos and lies below AGNF model 3 by a factor of 6/7 at the high mass end. Regarding the total baryonic mass the AGNF default model has slightly higher values than AGNF model 3 for Halos 1 - 4, but significantly higher ones for Halos 5 - 16. Its total baryon masses are similar to the ones of AGNF model 4. The

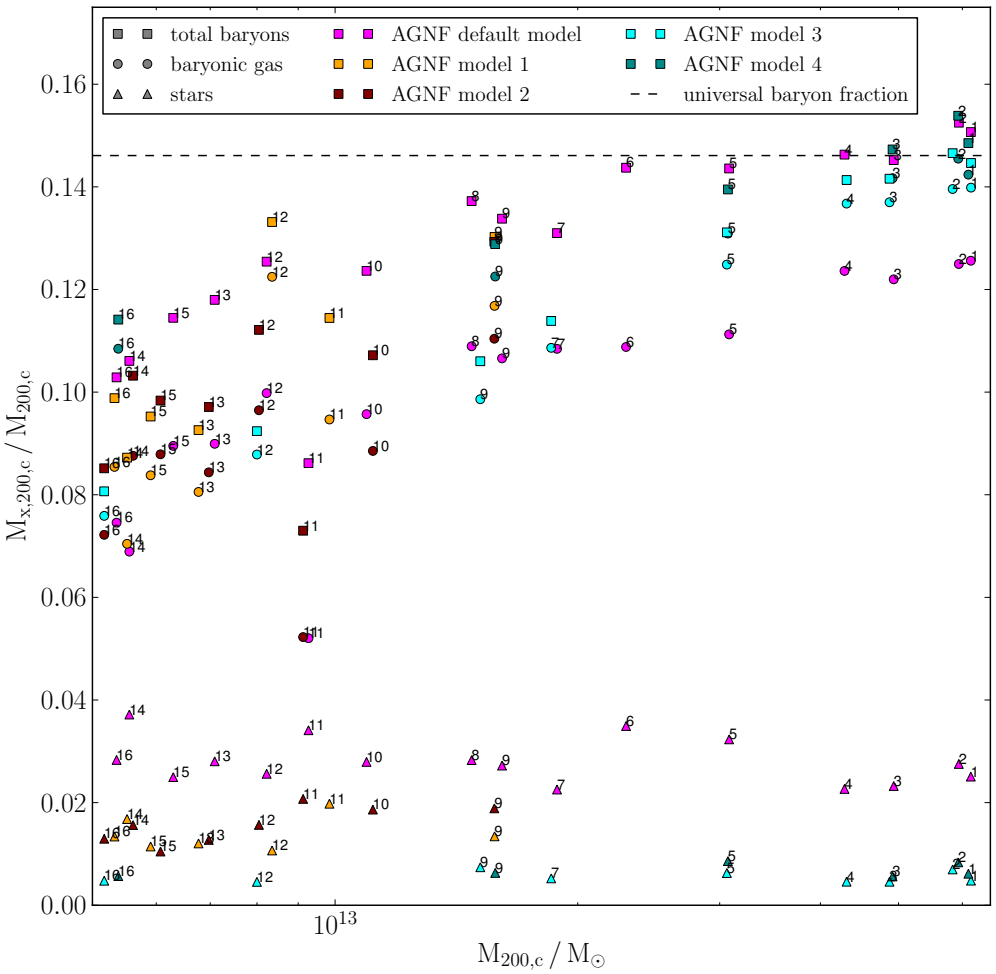

Figure 5.17: **The stellar, gas and total baryonic mass fractions within $r_{200,c}$. Circles denoted the gas mass fraction, triangle denote the stellar mass fraction and squares denote the total baryonic mass fraction. The dashed line is the universal baryon fraction. The colour code is the same as in the previous plots of this section.**

baryon excess which the default model has over AGNF model 3 is hence in the form of stars. Since the two models have the same value for the black hole seed mass, the large difference in their stellar mass fractions, must hence come from the different value of ϵ_c, which is approximately 7000 higher for AGNF model 3.
Unlike the stellar feedback models, the AGNF models produce gas mass fractions, which are significantly higher, than the stellar mass fractions. This difference between the two mass fractions is larger for $r_{200,c}$ than for r_{500}. While the stellar mass fractions are approximately the same for both radii, large amounts of gas mass are located specifically between r_{500} and $r_{200,c}$. The AGNF models have gas mass fractions which are 1.6 times as high as the ones of the SF models for the high mass halos. These are decreasing towards the low mass end, where they reach values similar to the ones of stellar feedback for $r_{200,c}$, for the AGNF

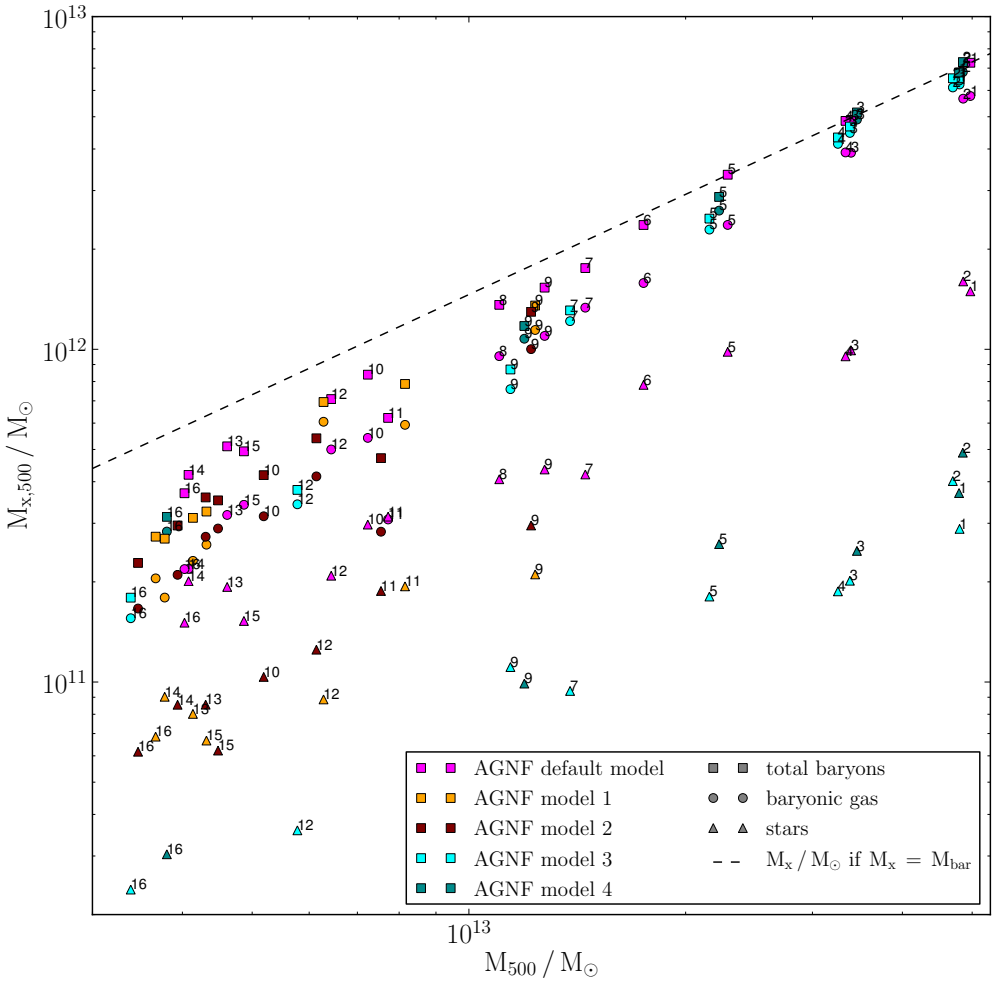

Figure 5.18: **The stellar, gas and total baryonic masses within r_{500}. Circles denoted the gas mass, triangle denote the stellar mass and squares denote the total baryonic mass. The dashed line is the universal baryon fraction. The colour code is the same as in the previous plots of this section.**

default model, AGNF models 1 and 3. Within r_{500} the gas mass fractions of these three AGNF models are even lower than the SF ones, by a factor of 0.6. For AGNF model 4 the gas mass fractions remain higher than the SF ones, also for the low mass halos.
From this one can conclude, that the inclusion of AGN feedback, results in both the quenching of star formation and the removal baryonic mass from the halos. For the first process it is very efficient throughout the entire mass range considered, as the AGNF default model reduces the stellar mass fraction by a factor of 1/2 compared to the SF model. The AGNF model 3 and 4 reach even factors of 1/10 to 1/16, for r_{500} and $r_{200,c}$ respectively.
While this effectiveness of star formation quenching is almost independent of the halo mass, the removal of baryonic mass from the halos, by AGN feedback, is much more efficient for

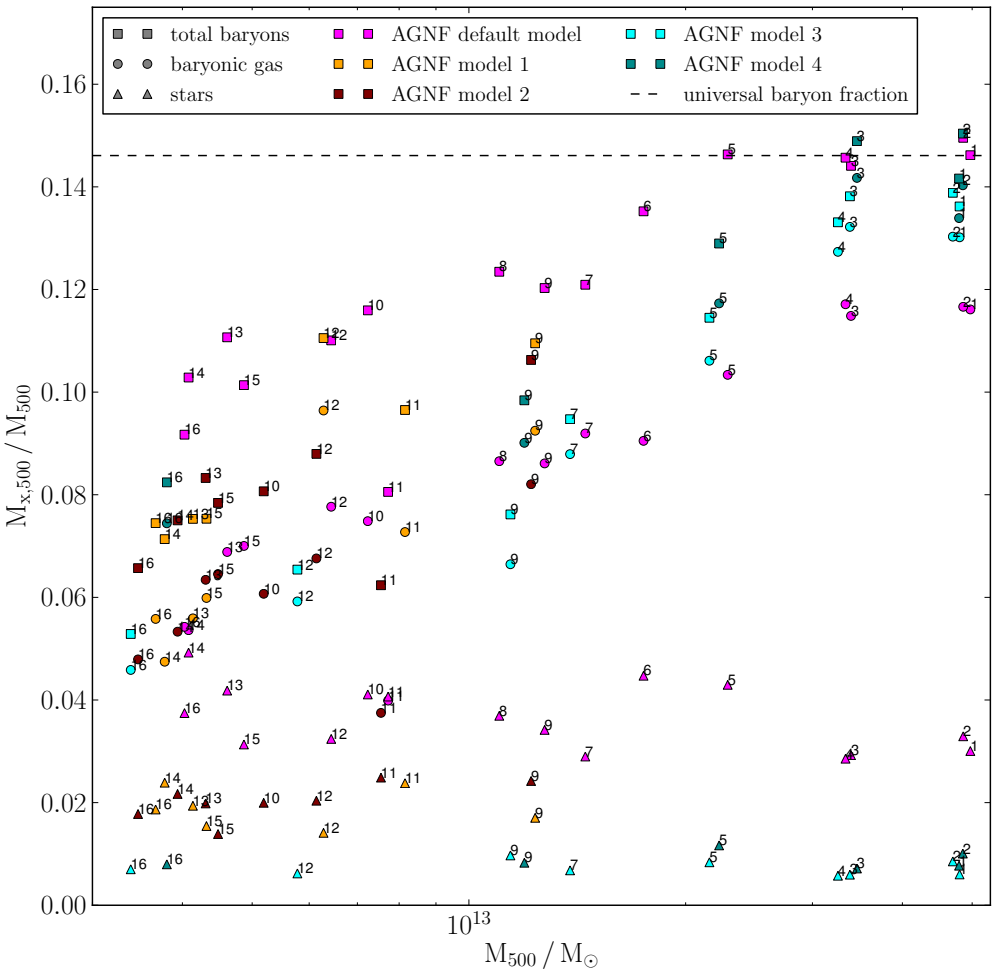

Figure 5.19: **The stellar, gas and total baryonic mass fractions within r_{500}. Circles denoted the gas mass fraction, triangle denote the stellar mass fraction and squares denote the total baryonic mass fraction. The dashed line is the universal baryon fraction. The colour code is the same as in the previous plots of this section.**

the small halos, than for the large ones.
The quenching of star formation seems indeed to be the primary effect, which comes out of the addition of AGN feedback. For the halos with smaller mass, however the removal of baryonic mass also becomes an equally effective process. The AGNF model 3 is capable of reducing the baryonic mass fraction by a factor of 1/4 compared to SF models, for the smallest halos. Again, this is only because of its unrealistically high value of $\epsilon_c = 1000$.

5.2.6 Central black hole mass

The masses of the central black holes seem to be fairly independent of the halo mass, except for the default AGNF model (magenta), where some oscillations exist at the low mass range. The mean values are however clearly separated between the models.
Observational estimates for black hole masses lie around $M_{BH} = 10^7\,M_\odot$ to $M_{BH} = 10^8\,M_\odot$ as stated e.g. in [CO07] and [GRG+09a]. AGNF model 3 (cyan) and AGNF model 4 (dark green) appear to be closer to these, with black hole masses of around $M_{BH} = 4 \cdot 10^6\,M_\odot$ and $M_{BH} = 4 \cdot 10^7\,M_\odot$, respectively, than the AGNF default model, with black hole masses around $M_{BH} = 10^9\,M_\odot$. For a description of mass estimation methods for central black holes in galaxies, see for example the latter reference [GRG+09a].
If the mass of the central black hole is a reliable observable, to be compared to observations, might however be a matter of opinion. As it is a quantity of the experimental sub-grid physics implementation of AGN feedback itself, unlike the stellar mass, gas mass etc., which

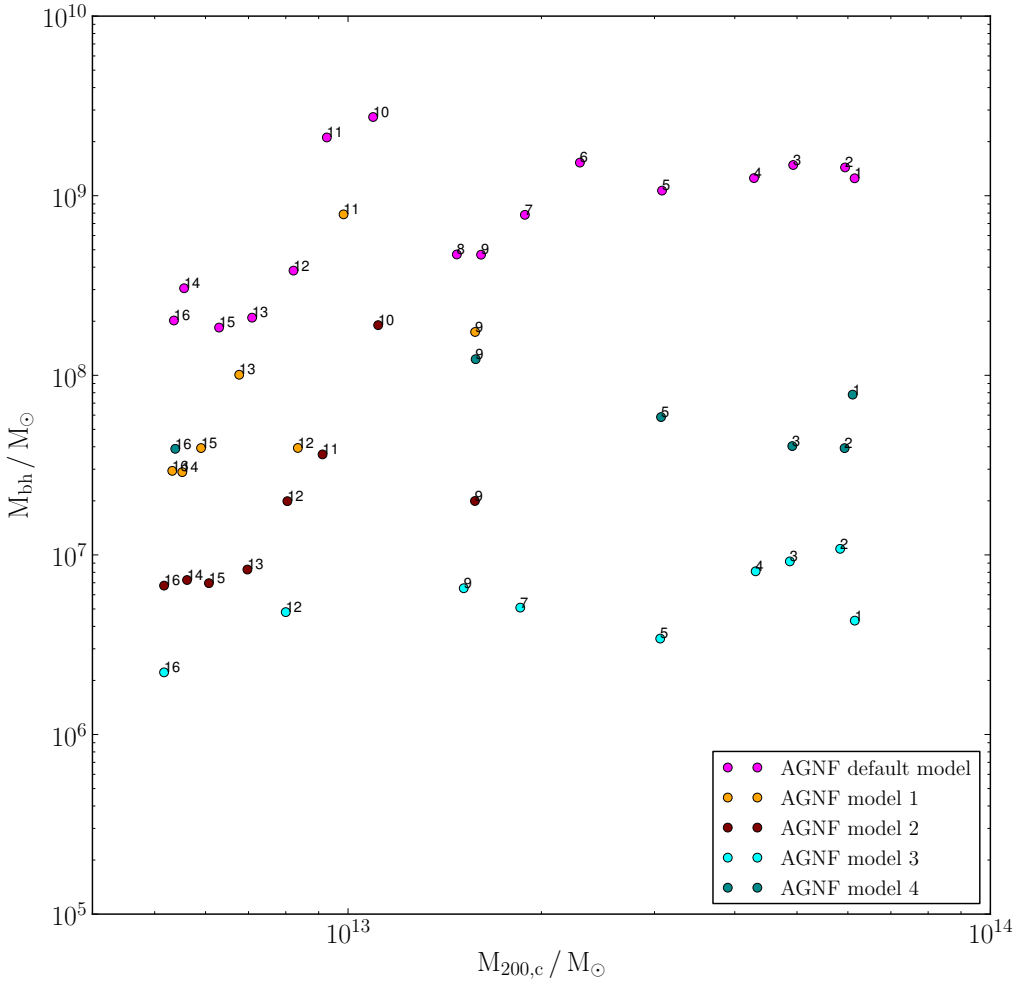

Figure 5.20: **The mass of the central black hole as a function of the halo mass for the five considered AGNF models.**

are quantities only affected by this model. It strongly depends on the seed mass parameters, as well as on the Bondi and Eddington accretion rates, which are effective descriptions only. Nevertheless, the black hole mass can be used for an internal consistency check, of the underlying AGN feedback implementation. The AGNF default model and AGNF model 3 have the same seed mass, but lie a factor of 100 to 200 apart from each other in the black hole masses. The difference between the two is the value of ϵ_c, which is a factor of roughly 7000, higher for AGNF model 3 than for the default model.
Ultimately the goal is to have a model for AGN feedback, where the black hole mass itself is also described correctly. To validate such a model the correlation between the mass of a galaxy's central black hole and the velocity dispersion of the stars in the galactic bulge [GBB$^+$00] [GRG$^+$09b] is a key observational reference to be reproduced by the simulations.

5.2.7 Summary and Conclusions

The application of the AGN feedback mechanism breaks the scale invariance, which is present in the baryonic mass fractions when only stellar feedback is applied in the simulations. While its effect onto the stellar mass fraction is indeed largely independent of the halo mass, and much more efficient, than for the SF models, the impact of the AGNF in the removal of baryonic mass is significant for small mass halos only. For the ones with larger masses it is present only as a smaller effect.
The strong quenching of star formation is hence the primary effect following from the inclusion of AGN feedback. The removal of baryons is secondary only and also halo mass dependent. As a result the large halos have unrealistically high gas mass fractions, which cannot match the observational results (Figure 5.15). The smaller halos on the other hand can, specifically for the AGNF default model, as well as AGNF model 1 and AGNF model 3.
The stellar mass of the halos, was the primary quantity to which our parameter values were calibrated. None of the five tested models was able to reproduce the analytic fit values by Moster at al. 2013, over the entire mass range, sampled by the 16 halos. The logarithmic slope of the AGNF simulation results in the stellar to halo mass plot (Figure 5.13), remained the same as for the SF models and the universal baryon fraction. This fact is also reflected by the plots of Figures 5.16 - 5.19, where the stellar mass fraction remain constant throughout the considered mass range. Judging from the stellar mass in the halo mass range between $5 \cdot 10^{12}\, M_\odot$ and $5 \cdot 10^{13}\, M_\odot$ the AGNF model 1 appears to be the best choice. Also the default model comes reasonably close to the analytic fit. The other three models however overshoot this relation.
In the high halo mass range of $5 \cdot 10^{13}\, M_\odot$ to $7 \cdot 10^{13}\, M_\odot$, both AGNF models 3 and 4 make sound estimates for the stellar masses within $0.1 r_{200,c}$. AGNF model 4 would seem to be the better choice from Figure 5.13. It also has a value of ϵ_c which is physically more sound with 10, than the one of AGNF model 3 which is 1000.
When however the baryon gas fractions within r_{500} are considered, as in Figure 5.15, this choice seems no longer a good one. As for the high mass halos AGNF model 3 and 4 lie far above the observational data points; AGNF model 4 even more than AGNF model 3. Also around the mid of the considered mass interval AGNF model 1 overshoots the gas fraction within Halo 9 and 12. Only towards the low mass end, with Halo 16, it is able to give a gas fraction value which seems in agreement with observations.
A good agreement for the gas mass fractions of the low mass half, has however AGNF model 3. It seems that the extreme value of $\epsilon_c = 1000$ is required to push the baryons outside of the halos. This value is unphysical, in the underlying framework, where the radiation emitted from the inner edge of the accretion disk, is coupling to the surrounding gas, through processes described in Section 4 and with an efficiency of ϵ_c, which therefore cannot be larger than one, if energy conservation is not to be violated.
A way out of this, might offer the consideration about how the energy of the accreted gas particles is transformed into the emitted radiation. The effectiveness of this process is described by another efficiency parameter ϵ_r, which is defined in equation (4.11), as the ratio between the luminosity of the emitted radiation and the rest mass energy equivalent of the accretion rate.

$$\epsilon_r = \frac{L}{\dot{M} c^2} \tag{5.4}$$

There is a priori no reason, why ϵ_r should lie between zero and one, nor why the relation between L and $\dot{M}$ should be linear, as various energy forms from the infalling gas can be converted into emitted radiation, or additional black hole mass.
The important point to note, is that ϵ_r, in the underlying model is not derived from the assumption of the Eddington Luminosity limit (see Section 4). This model itself is derived

from the assumption of hydrostatic equilibrium, where the gravitation is provided by a central spherically symmetric mass and the pressure by radiation. Hence, the luminosity of the emitted radiation is determined solely by the mass of the central object. In addition now the relation (4.11) is introduced, to relate the mass accretion rate to the luminosity. This parameter will therefore influence the value of the black hole mass and with that the luminosity, but will itself cancel out in the computation of the feedback energy or luminosity. This is for the case of Eddington accretion only. For the case of Bondi accretion, ϵ_r will not influence the accretion rate and black hole mass in any way, but will enter into the final calculation for the feedback energy as a parameter which has exactly the same effect as ϵ_c. Some physical intuition for the parameter ϵ_r can nevertheless be found if one assumes that the energy of the emitted radiation is coming from the conversion of the potential energy which a particle at distance r from the black hole has. If this particle is removed from there, to fall into the black hole and thereby increase the mass of the latter by its rest mass m_p, luminosity and accretion rate are related by the gravitational potential:

$$W = \frac{GM_{BH}Nm_p}{r} \quad \Longrightarrow \quad \frac{dW}{dt} = L = \frac{GM_{BH}}{r}\dot{M} \tag{5.5}$$

It should be noted that this assumption is not part of the Eddington model. Nevertheless, if it is applied ϵ_r comes out as the ratio between the initial potential energy of an infalling particle, and its rest mass energy.

$$\frac{L}{c^2 \cdot \dot{M}} = \frac{GM_{BH}}{r \cdot c^2} = \frac{GM_{BH}m_p}{r \cdot m_p c^2} \tag{5.6}$$

With this relation, a value of ϵ_r between zero and one is certainly the outcome. $\epsilon_r = 0.1$ is indeed often quoted in literature on the subject, e.g. in [CO07] or [MvW10]. The assumptions going into this calculation are however rather strong ones, that the increase in black hole mass is given only by the rest mass of the infalling particles, and that the energy of the emitted radiation is given only by their potential energy. Not only could both energy sources be distributed differently onto black hole mass and radiation, respectively, but certainly are also other energy forms present. Kinetic energy is not neglectable if the particles on the inner edge of the accretion disk are supposed to be highly relativistic. Altogether the non-general-relativistic description of the above derivation might be inappropriate, but a verification is beyond the scope and given time of this thesis.

The results of the AGNF model 3 are a good match to observations in many cases. The high value of ϵ_c of this model might be an indication, that actually a higher value of ϵ_r is required, as these two parameters are degenerate. Especially for the case of Bondi accretion they have the exact same effect, and there is no difference whether the one or the other is altered. For the case of Eddington accretion however, the black hole masses might turn out differently, for a different value of ϵ_r.

Another key parameter which might have a similar effect onto the results, as ϵ_c, is the threshold energy W_{min}, defined in (4.17). Since it determines how often the accumulated energy is released into the gas. A higher value of W_{min} will lead to a situation where the energy releases happen less frequent, but with higher energy. This might provide a better effectiveness for pushing the baryons out of the halos.

The next step would be to test a higher value of T_{min}, and to analyse the possibilities of varying ϵ_r instead of ϵ_c. Another problem might exist for the situation of Eddington accretion. The assumption of hydrostatic equilibrium in a situation, where mass accretion onto the central object is happening has its flaws, as the HSE gives rather narrow constraints onto the radial velocities of the particles, which are necessary for an accretion flow. This can be seen from Equation (1.57), where hydrostatic equilibrium requires

$$\frac{d\dot{r}}{dt} = \frac{(r\,\dot{\theta})^2}{r} + \frac{(\sin\,\theta\, r\,\dot{\phi})^2}{r} \tag{5.7}$$

This condition will generally not be fulfilled. For the physical application one could argue, that the mass movement due to the accretion flow is neglectable, for the HSE situation. As it concerns only the accretion disk, which is a small part of the entire system of the black hole and the surrounding gas. Also the time scales for the accretion process is a different one than that of the processes, maintaining the HSE of the gas. Nevertheless, for the implementation in cosmological simulations, the two time scales might be smaller than the time step. And further the spatial dimensions of the accretion disk are not resolved in any case. In the underlying model the mass which is accreted and the mass which is in HSE, are described by the same physical scale: the sink sphere. Therefore the considerations above become relevant.

5.2.8 Halo maps

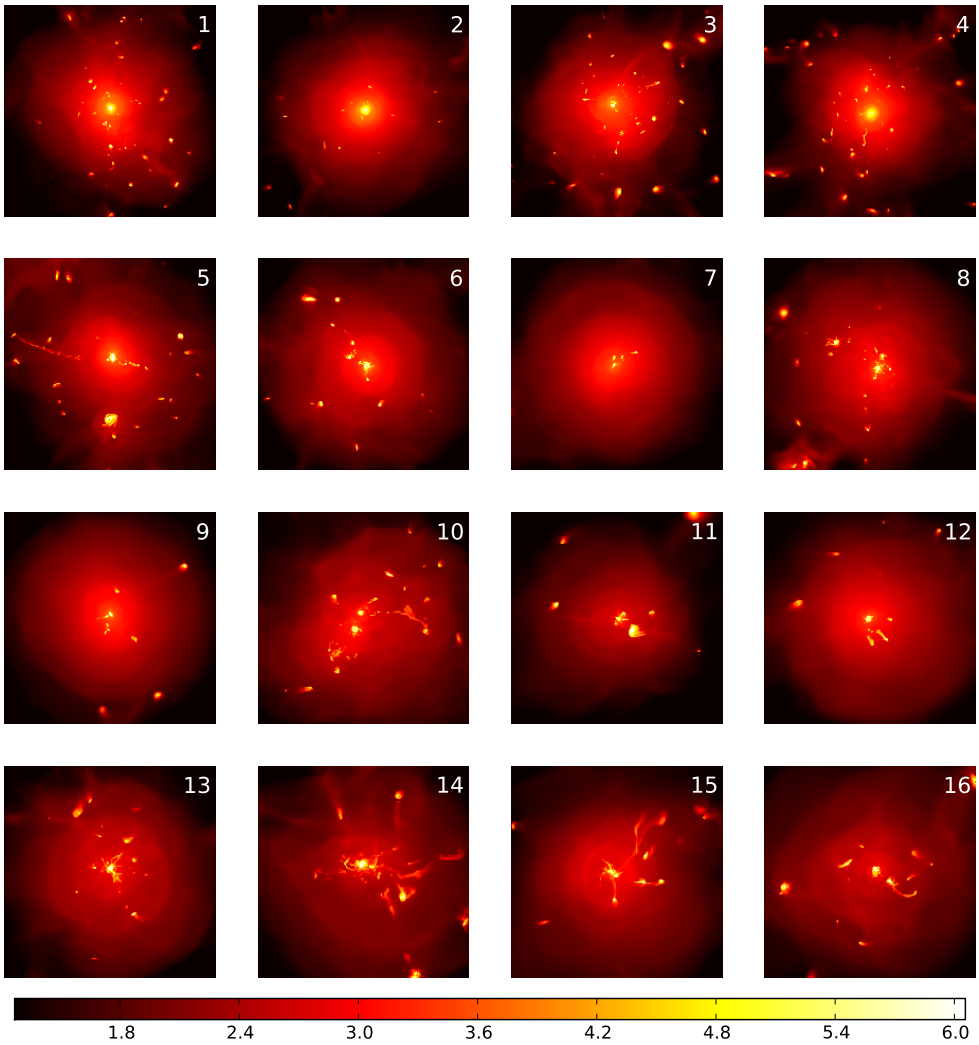

Figure 5.21: **Gas density maps for the default AGN feedback model. The colour bar unit is $\log_{10}(\rho_{gas}/\bar{\rho}_b)$, where $\bar{\rho}_b$ is the average baryon density in the universe. The side length of each map is $2r_{200}$, with the centre of the maps corresponding to the centre of mass of the halo.**

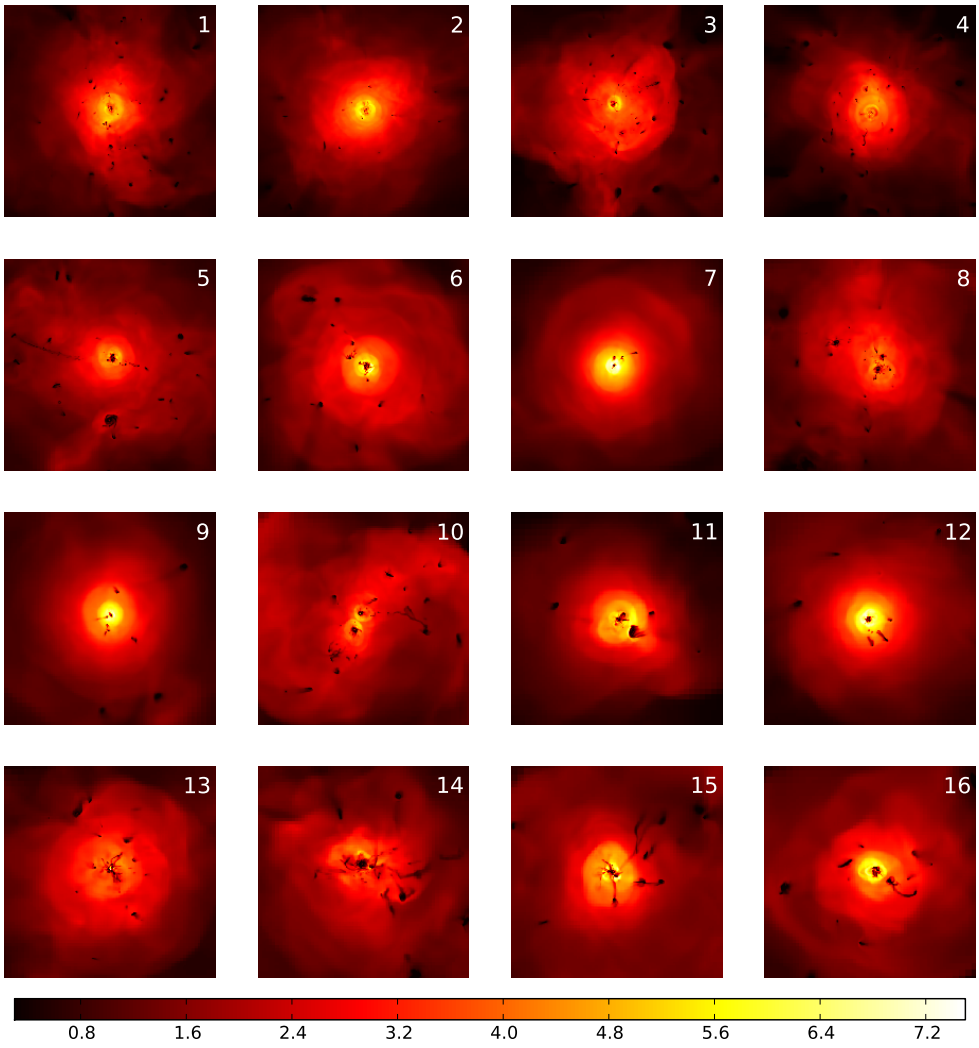

Figure 5.22: **Gas temperature maps the default AGN feedback model. The colour bar unit is T_{gas}/T_{200}, where T_{200} is computed for each individual halo as $T_{200} = \frac{1}{3}\frac{m_p}{k_B}\frac{G\,M_{200}}{r_{200}}$. The side length of each map is $2r_{200}$, with the centre of the maps corresponding to the centre of mass of the halo.**

6 Summary, Conclusions and Outlook

The goal of this thesis work, was to explore how numerical simulations run with the Ramses code, and with cosmological initial conditions from the MUSIC code, can contribute to the quest of computing the cosmological observables, mainly the matter power spectrum, with sufficient accuracy. Since baryonic effects play an important role at the relevant scales of these observables, the influence of baryonic physics onto the simulation results needed to be tested and quantified. Because of the high use of computational resources in such simulations, it was necessary to restrict the numerical experiments to the scales, from which the largest contribution to the desired quantities is expected: galaxy group sized halos. The work consists of three main parts:

1. The first main task was to test the simulations including a baryonic component described by hydrodynamics on the level, where no other physical processes like cooling or star formation are present. This is described in Section 3. It was found that the applied numerical techniques are robust enough, such the results are uninfluenced by the resolution, the details about the computation of the initial conditions, and the tested hydro solver property (slope limiter for the linear reconstruction). In fact the scatter introduced by the individual nature of the 16 halos is larger, than these numerical effects. A further result of this simulation phase, was the important role of the non-thermal pressure component, for the physics of galaxy group sized halos, which was analysed and quantified.

2. The next step, was the test of the already established model of stellar feedback in the Ramses code on the 16 galaxy group halos. Here a set of four different models, the default one and three others, mimicking extreme cases, were tested on all 16 Halo. The results were as expected. The default model was verified for the use in the following runs, including AGN. Aside from this the results of the other three models provided valuable insights into the astrophysics of cooling, star formation and feedback processes in general. These gave some hints for the future development of the AGN feedback modelling.

3. Finally the implementation of AGN feedback in the Ramses code was tested, for different sets of parameters. The results were compared to observations, with the goal to gauge the model parameters with them. Thereby none of the tested models has been successful in matching all of the considered observational results. Instead different parameter sets are required for different mass ranges. Nevertheless, the tested models gave important information, about which parameters influence which baryonic quantities (gas mass or stellar mass for example). This information is highly relevant for a code internal understanding of the feedback processes. With, this analysis we have explored only the tip of the iceberg. Further parameter sets could be tested, and modifications to the AGN feedback model could be made. Suggestions for future work are described below.

Finally it was the goal of the project to arrive at the mass profiles of dark matter, baryonic gas and stars for an observationally verified model of AGN feedback in Ramses. With the use of these profiles, the changes between a pure n-body simulation and a simulation with the full model of AGN feedback could be quantified, by describing how the respective profiles differ. This method was suggested in [ST15]. It would require the knowledge of the AGN induced changes, at least for the mass interval considered in this analyses, but knowing them also for higher halo masses, might become a requirement, for some desired accuracies. The simplest way to envision the quantification of this changes in the profiles, is as a function radius r which also depends on the parameter of the halo mass M. This might not be a sufficient parametrisation, as was shown in Section 3. The halo profiles also depend

on other characteristics, such as their assembly history, which is in turn closely related to the amount of substructure and non-thermal pressure support in the halos. Including all of this information into one model might be possible, but to arrive at the relevant information through high performance computer simulation might prove to be a daunting task. Since not only the relevant mass ranges, but also the relevant other quantities going into this halo description must be explored by simulations, such that a statistically representative sample is produced, from which conclusions can be drawn. Moreover it requires a model of AGN feedback which is valid for all of these circumstances. Since the effectiveness of any feedback model, or sub-grid physics model in general, depends on the resolution, the simulations to test the model cannot be performed with a lower one, as the desired resolution. In this analyses we have found that the AGN models tested are, if at all applicable, only work for narrow ranges of halo masses. Nevertheless, to have a practical estimate of how AGN feedback influences the halos this might be sufficient already, as there are not many possibilities, to change a function of one variable only. Namely the profiles, whose overall radial dependence is already known. A few suggestion to improve the situation within the framework of the Ramses code, but also in general, are made in the following.

The most direct step to connect to the analysis of this thesis and take it further, would be to test further AGN feedback parameter values, with the same AGN feedback implementation. As already pointed out in the summary of the previous section: ϵ_c, ϵ_r and T_{min} are the most important parameters for the effectiveness of the model to push baryons out of the halos. The first of the next steps is necessarily to test different values of T_{min}, starting from AGNF model 1, or from the default model. In a second step, variations of ϵ_r should be tested for these two models. The remaining parameter, for which it was shown that its value influences the resulting mass fractions within the halos is, the black hole seed mass M_{seed}. Since the goal is to increase the energy released by the AGNs, this parameter lies at the other end of the model, and in between are the two models for the black hole accretion rates, Bondi and Eddington. Before the seed mass value range can be explored in a reasonable way, and possibly also the halo mass threshold at which the black holes are seeded, it is prudent to first check the influence of these two accretion models, and possibly try alternatives, as both are effective descriptions. With that of course another barrel is opened, namely the modification of the AGN feedback implementation itself, in its equations and algorithms, and not just the alteration of its parameters.

As was already mentioned in the result section (Section 5). The applied assumption, that the increase in black hole mass is only coming from the rest mass of the accreted gas, is not required physically. Neither is the assumption, that the radiation energy emitted by the accretion process is coming only from the potential energy of the infalling gas particles. If this restriction is alleviated, then ϵ_r can have values larger than one. The full discussion is in Subsection 5.2.7 and shall not be repeated here. Since for the case of Bondi accretion, ϵ_r influences the result only in a way which is degenerate with ϵ_c, having $\epsilon_r > 1$ should significantly improve the impact of the AGN feedback, in this accretion phase. A glimpse into this scenario is provided by the results of AGNF model 3. For the case of Eddington accretion, ϵ_r will cancel out for the computation of the feedback energy, but it will directly influence the rate of mass accretion onto the black hole and thereby indirectly through the mass of the black hole, also the feedback energy. A lager value of ϵ_r, would therefore also mean more feedback energy and again at least a partial degeneracy with ϵ_c is present. The picture which becomes apparent, is that the parameter ϵ_r actually serves two purposes. In case of the Bondi accretion it scales the feedback energy, which is proportional to the accretion rate and with that to M_{BH}^2. In the case of Eddington accretion it scales the accretion rate itself, which is proportional to M_{BH}. It might improve the analysis of the situation, to

parametrise these two distinct processes with two different parameters. They became entangled, since accretion rate and feedback energy, or luminosity, are proportional to each other, in the underlying model. It might also be worth the effort to reconsider this assumption.

What can be learned from the results of simulations with pure stellar physics and no AGN feedback described in Subsection 5.1?

The addition of radiative feedback to the default SF model, which was tested with SF model 3, has produced results which show that this ingredient helps to push the baryonic mass out of the halos. It should prove worthwhile to activate this already implemented process also for the simulations including AGN feedback. In other words one could replace the SF default model with SF model 3, for the run with AGN feedback added. The removal of gas from the halos through the pressure of radiation, emitted from their centre is also the central concept of AGN feedback. Even though the two processes might have different physical sources (young stars and accretion disks respectively) and differing numerical implementation, it might be interesting to analyse their commonalities and quantify their effects. Maybe a unification of the two and with that a numerical simplification is possible. In [DQM11] the authors implement a model of radiative AGN feedback into an SPH code. The physical picture which underlies their work, is the absorption of UV radiation from the AGN by dust. Subsequently it is re-emitted in the IR band and finally absorbed by the baryonic gas around the nuclear region. This is in essence the AGN counterpart of the radiative SF process of the underlying study. In [DQM11] however the energy form which is injected into the gas during the described process, is not thermal energy but instead bulk kinetic energy or equivalently momentum.
An important part in the stellar feedback model is provided, by the contribution from the non-thermal pressure component in the delayed cooling scheme. Non-thermal pressure support has already proven to be an important concept for the distribution of the baryonic gas mass, in the non-radiative hydro simulations, described in Section 3. It might be possible to include the idea of a non-thermal pressure component released by AGN feedback into the sub-grid physics of the AGNF model. Especially, since the energy threshold W_{min} for the release of AGN feedback energy has some commonalities in purpose to the delayed cooling scheme of stellar feedback. A comparison of the two mechanisms, independent of weather the physical context is stellar or AGN physics, could be done. Eventually there might also be the possibility of unification. The non-thermal contribution to AGN feedback from the physical cause of cosmic ray flows was studied by [FO11].
It has been shown with the stellar as well as the AGN feedback model simulations, that some halos are more susceptive to the feedback effects, than others. A particular example is Halo 10, which has a large fraction of non-thermal pressure support, as it is a halo in the merging process. It would be interesting to analyse, in which way non-thermal pressure support amplifies the effectiveness of the feedback processes. In particular, it could be tested code internally, which subroutines of the feedback algorithms are called more often, in simulations of such halos with large non-thermal pressure, than in the other cases, and why.

The Ramses code also offers the possibility to apply a feedback mechanism of the AGNF model, in which bulk kinetic energy, in addition to the thermal one, is also injected into the gas. This component of the feedback model is commonly referred to as mechanical feedback, or momentum feedback. The physical phenomenon, which this model describes are polar jets, which are emitted from the black holes, perpendicular to the accretion disks. The details about their cause and composition are unknown, but the most common idea are highly relativistic particles, which follow trajectories, determined by strong magnetic fields

existing in the black hole vicinity. The interaction of these jets with the surrounding gas medium, give rise to cavity like structures, often called lobes [BVF$^+$93]. The implementation of momentum feedback in Ramses was outlined in [CT07]. The process was generalised to cosmological applications in [DDST12] based on a model by [OBBS04]. The jet implementation is tested and developed further in subsequent works by Yohan Dubois et al., e.g. [DDTS11] and [DDST12].

What other projects exist in the direction of AGN-feedback within the Ramses code ?

In the Horizon-AGN cosmological simulation, one of the latest versions of the AGN feedback implementation of Ramses, was used to create a catalogue of more than 150.000 galaxies at redshifts $1.2 < z < 1.8$ [DPW$^+$14]. The simulation volume is the same as in the cases of this thesis 100 Mpc h^{-1}. The main motivation for the Horizon-AGN simulation is to study the alignment of galaxy spins with the cosmic filaments. The authors find that AGN plays a key role in these alignments, through the prevention of baryons falling into the halos and the quenching of star formation after mergers. Other aspects are galaxy morphologies themselves, and the correlations between galaxy shapes and spins, as well as the evolution of the black holes [VDPD16]. The alignment of galaxies with the cosmic web is slightly problematic for the utilization of the weak lensing signal, described in Section 1.2 [CCL$^+$15]. Since there the alignments between images of galaxies are assumed to be induced mainly through the gravitational effects of matter onto the emitted light from the galaxies.

Another project which uses the AGN implementation of Ramses is the Rhapsody-G collaboration [HMW$^+$15], [MHW$^+$16], [WEH$^+$15]. The authors of this paper series have simulated ten massive galaxy clusters ($M \sim 10^{15} M_\odot$) in cosmological zoom-in simulations and studied their baryonic and stellar properties, as well as correlations between the two. One of their main results is the existence of a dichotomy in the core temperatures of the clusters, arising from their merger history, in particular from the angular momenta involved in the merger events. The detailed analysis contains further information about the gas profiles and global properties of the halos.

The most important point about the implementation of feedback processes, is that their primary purpose is to counteract the effects of other sub-grid processes like cooling and star formation. Because the sole application of the latter does not give the right results, when compared to observations, as too many stars are formed and too much baryonic mass ends up in the halos. In some cases a better match with the observational data is indeed found, when only non-radiative hydrodynamics is applied. Instead of implementing more and more sub-grid physics, to reproduce results which are similar to those of simulations with no sub-grid physics at all, one could try a different approach: start from a model which contains as little sub-grid physics as possible, find a set of its parameters which matches the observations and then interpret and parametrize this model in the context of the physical process, which is thought to be responsible for the observational results, e.g. feedback. A glimpse into such an approach, is given by the results of SF model 1. Despite that the stellar feedback was turned off completely in this model, the fractions of baryons within the halos were close to, and in some cases even lower than, in the cases of the models with full stellar feedback. The reason is that the cooling of the gas is less efficient in the absence of metals injected from the supernova explosions. Matching the observations by adjusting the cooling efficiency or star formation density threshold parameters, might therefore be possible. The interpretation of the parameter values found this way, is of course not straight forward. The purpose is more to understand the code intrinsic processes which lead to the right results, in the light of physics which is as simple as possible. More complicated algorithms to sim-

ulate additional physics, together with the parameters describing them, can then still be implemented in subsequent steps. Always with the goal to first reproduce the result, which fits the observations, before more physical processes are implemented. In [TMM+11] the authors also applied this method, by comparing the results from their AGNF and SF implementations to a model, in which star formation is artificially suppressed. This approach might ultimately be an alternative to the current process of applying a number of physically motivated processes at the same time, which come with a large number of parameter values. In principle these have to be chosen consistent with the physically motivated models, which they represent. However, often unphysical values for these parameters are necessary to make the models work. A similar issue is the introduction of so called boost factors into the equations of the sub-grid physics, which are justified with the proposition, that they mimic some unresolved process relevant for the model. The predictive power of such implementations is therefore limited. Even worse, the presence of several physical processes acting and counteracting each other in the simulations, makes it difficult to disentangle them and quantify their individual impact onto the simulation results. A good starting ground in this context might be the AGN feedback model described in the study of [BBP+10], where the underlying equations and physical processes of the feedback are kept simpler. It might be a prudent step to implement this model, which is based on SPH simulations, into the AMR framework of Ramses and try it there. Aside from the physical results, the simplicity of the model, might allow a glimpse into the differences, of how SPH and AMR hydrodynamics respond to the same feedback mechanism.

Another way of verifying that simulations are accurately describing the underlying physics, is by comparing results from complementary approaches to the implementation. This method provides an additional consistency check. In code comparison projects the results of several different implementations can be compared to each other, after they are applied to simulations with the same initial conditions, e.g. the ones of a zoom-in simulation on a galaxy cluster. One example of such a project, which also includes AGN feedback mechanisms is the nIFTy collaboration [SEP+16] [CPK+16].

There are many other simulation collaborations with cosmological applications and the field of the development of AGN models is vast.

One of the largest simulation projects in contemporary research is the Illustris collaboration [VGS+14a], [VGS+14b], which consists of a suite of cosmological simulations of different resolutions, with and without baryonic physics. They are performed with the moving mesh simulation technique. The authors report significant effects onto the mass distribution on large scales arising from AGN feedback. These are relevant in the context of precision cosmology with weak lensing. Another part of the Illustris project is devoted to the analysis of the evolution of black holes [SVG+15]. The main focus of the project however lies on the study of galaxy properties, e.g. their morphology, gas properties and abundance.
Another example is the EAGLES (Evolution and assembly of galaxies and their environments) collaboration [SCB+15]. Its aim is also to reproduce the properties of galaxies, groups and clusters with simulations including AGN feedback. They report in detail on the necessity of calibrating the parameters of such a model with observational results [CSB+15]. Their simulations are run with the Tree / SPH based code GADGET-3 [Spr05].
Also worth mentioning is the OWLS (Overwhelmingly large simulations) project [SDB+10], which describes a suite of cosmological simulations of different sizes and resolutions, performed also with GADGET-3. These simulations contain the physical processes described in Section 4 up to stellar and AGN feedback. One of the first applications of this suite was the study of the cosmic star formation history [SDB+10] and the global properties of galaxy

groups [MSP+10]. Later in 2011, the simulation were used in analyses by Marcel van Daalen [vSBD11], to directly compute the matter power spectrum from them and to quantify the impacts of baryonic physics, like AGN feedback onto it. In this respect van Daalen's work presents a complementary approach to the method of this thesis work. As he and his collaborators explicitly use the non-zoom-in cosmological simulations of the OWLS project. From such simulations the matter power spectrum can be computed directly, since they do not suffer the numerical bias existing for zoom-in simulations, on small scales, arising from the difference in resolution between the zoomed region and the rest of the simulation box.

Despite that there are some set backs and shortcomings in the results of this thesis, the possibilities given by the use of Ramses and other codes for simulating the universe are many. Ones a valid model is found for the computation of the relevant quantities, the effects onto the relevant spectra can be quantified. Baryons give in this regard certainly the most important contribution, however also other species like neutrinos are present. Already a lot can be learned from pure n-body simulations. With a analytic or semi-analytic description of the named effects, onto the particles in such simulations, computational effort can be reduced, severely. Finally it should be noted, that the description of the expanding universe, which is in fact inhomogeneous, is done through a model which relies on a background expansion determined by the assumption of homogeneity. Such a method certainly has its value, but also its limits. At the level of precision reached by future experiments mentioned above, these limits might become relevant. It is possible, that effects of General Relativity need to be included in future simulations.
Cosmological simulation as the ones described in this thesis have proven to be a valuable and reliable tool, for the understanding of the universe. In the sense that they allow the comparison of theory to observation. This is the key process in the current era of precision cosmology, where models of the universe, described by the values of their cosmological parameters, need to be ruled out in this comparison.
The determination of these parameters with uncertainties as small as possible is indeed the quest of precision cosmology. The model of an overall homogeneous, expanding universe and with composition described by ΛCDM is established in the cosmology community. No surprising results which would indicate this model to be wrong have been found so far. Nor has there been any discovery which would have redefined the view of physics on the world, or indicated the existence of some unknown physical forces in almost a century. Except maybe for the one which led to the introduction of dark energy. Any effect which would reveal unknown physics, e.g. at scales, where gravitation and quantum field theory need to be considered both, is out of reach for feasible experiments.
Some unknowns still exist on the scales which can be probed at present. Not everything is explained in the context of ΛCDM cosmology e.g. the scenarios of galaxy formation. Indeed the idea that ΛCDM is the wrong model occasional comes up in the astrophysics community. It is important to remember, that dark matter and dark energy are only parametrisations. They have been introduced into the equations describing the universe like Equations (1.2), to reproduce the observed dynamical state of the latter. Their properties were chosen such that they fulfil these requirements. These properties give physicist hints about their microscopic nature. It is therefore difficult to imagine, that anything else than smoothly distributed dark matter elementary particles, could reproduce the observed velocity curves of galaxies, or hold together entire halos with their gravitation, or be responsible for the gravitational lensing of light from galaxies. Nevertheless, no dark matter particle has been found in a direct detection process, in one of the experiments build for this purpose, nor has one been produced and detected in a particle accelerator.
Dark energy is supposed to be an even more evasive substance, in the sense that no valid particle interpretation exists for it, and that clustering is not in its nature. A direct detec-

tion might therefore never be possible.
It should be recalled, that velocities and distances in cosmology are inferred from the properties of the light emitted by galaxies, supernovae and the initial cosmic plasma. The apparent accelerated expansion of the universe, which is dynamically accounted for by the introduction of dark energy, might be originating in a cause, which is yet not considered in the equations of the universe, but has an effect which is effectively described by the addition of the Λ-term. Such a cause could for example be, the inhomogeneity of the universe. This observational fact has so far been treated only perturbatively, with the assumption of a homogeneous background expansion.

On one hand experimental evidence for utterly new physics is out of reach, and on the other hand still many mysteries in the current scenario of an expanding universe have to be solved. The refinement of the experimental methods, by the observational community and the improvement of numerical simulations, by theorists, are certainly the ways to go, for the future.
It should be kept in mind though, by any physicist, that a homogeneously expanding universe is not the measure of all things, and that ΛCDM is not the last word spoken.

I close with the words of a better known and more successful physicists than I am:

"Cosmologists are often in error, but never in doubt."

Lev Landau

References

[AAA+16] L. Amendola, S. Appleby, A. Avgoustidis, D. Bacon, T. Baker, M. Baldi, N. Bartolo, A. Blanchard, C. Bonvin, S. Borgani, E. Branchini, C. Burrage, S. Camera, C. Carbone, L. Casarini, M. Cropper, C. de Rham, J. P. Dietrich, C. Di Porto, R. Durrer, A. Ealet, P. G. Ferreira, F. Finelli, J. Garcia-Bellido, T. Giannantonio, L. Guzzo, A. Heavens, L. Heisenberg, C. Heymans, H. Hoekstra, L. Hollenstein, R. Holmes, O. Horst, Z. Hwang, K. Jahnke, T. D. Kitching, T. Koivisto, M. Kunz, G. La Vacca, E. Linder, M. March, V. Marra, C. Martins, E. Majerotto, D. Markovic, D. Marsh, F. Marulli, R. Massey, Y. Mellier, F. Montanari, D. F. Mota, N. J. Nunes, W. Percival, V. Pettorino, C. Porciani, C. Quercellini, J. Read, M. Rinaldi, D. Sapone, I. Sawicki, R. Scaramella, C. Skordis, F. Simpson, A. Taylor, S. Thomas, R. Trotta, L. Verde, F. Vernizzi, A. Vollmer, Y. Wang, J. Weller, and T. Zlosnik. Cosmology and Fundamental Physics with the Euclid Satellite. *ArXiv e-prints*, June 2016.

[AEM11] S. W. Allen, A. E. Evrard, and A. B. Mantz. Cosmological Parameters from Observations of Galaxy Clusters. *ARAA*, 49:409–470, September 2011.

[AYMG03] Y. Ascasibar, G. Yepes, V. Müller, and S. Gottlöber. The radial structure of galaxy groups and clusters. *MNRAS*, 346:731–745, December 2003.

[BBKS86] J. M. Bardeen, J. R. Bond, N. Kaiser, and A. S. Szalay. The statistics of peaks of Gaussian random fields. *ApJ*, 304:15–61, May 1986.

[BBM+16] V. Biffi, S. Borgani, G. Murante, E. Rasia, S. Planelles, G. L. Granato, C. Ragone-Figueroa, A. M. Beck, M. Gaspari, and K. Dolag. On the Nature of Hydrostatic Equilibrium in Galaxy Clusters. *ApJ*, 827:112, August 2016.

[BBP+10] N. Battaglia, J. R. Bond, C. Pfrommer, J. L. Sievers, and D. Sijacki. Simulations of the Sunyaev-Zel'dovich Power Spectrum with Active Galactic Nucleus Feedback. *ApJ*, 725:91–99, December 2010.

[BBPS12] N. Battaglia, J. R. Bond, C. Pfrommer, and J. L. Sievers. On the Cluster Physics of Sunyaev-Zel'dovich and X-Ray Surveys. II. Deconstructing the Thermal SZ Power Spectrum. *ApJ*, 758:75, October 2012.

[BCGS02] F. Bernardeau, S. Colombi, E. Gaztañaga, and R. Scoccimarro. Large-scale structure of the Universe and cosmological perturbation theory. *Physics Reports*, 367:1–248, September 2002.

[BDB11] V. Biffi, K. Dolag, and H. Böhringer. Velocity structure diagnostics of simulated galaxy clusters. *MNRAS*, 413:573–584, May 2011.

[Ber01] E. Bertschinger. Multiscale Gaussian Random Fields and Their Application to Cosmological Simulations. *ApJS*, 137:1–20, November 2001.

[BH86] J. Barnes and P. Hut. A hierarchical O(N log N) force-calculation algorithm. *Nature*, 324:446–449, December 1986.

[BH88] F. R. Bouchet and L. Hernquist. Cosmological simulations using the hierarchical tree method. *ApJS*, 68:521–538, December 1988.

[BK11] S. Borgani and A. Kravtsov. Cosmological Simulations of Galaxy Clusters. *Advanced Science Letters*, 4:204–227, February 2011.

[BLW+13] C. L. Bennett, D. Larson, J. L. Weiland, N. Jarosik, G. Hinshaw, N. Odegard, K. M. Smith, R. S. Hill, B. Gold, M. Halpern, E. Komatsu, M. R. Nolta, L. Page, D. N. Spergel, E. Wollack, J. Dunkley, A. Kogut, M. Limon, S. S. Meyer, G. S. Tucker, and E. L. Wright. Nine-year Wilkinson Microwave Anisotropy Probe (WMAP) Observations: Final Maps and Results. *ApJS*, 208:20, October 2013.

[Bon52] H. Bondi. On spherically symmetrical accretion. *MNRAS*, 112:195, 1952.

[Bou96] F. R. Bouchet. Introductory Overview of Eulerian and Lagrangian Perturbation Theories. In S. Bonometto, J. R. Primack, and A. Provenzale, editors, *Dark Matter in the Universe*, page 565, 1996.

[BS09] C. M. Booth and J. Schaye. Cosmological simulations of the growth of supermassive black holes and feedback from active galactic nuclei: method and tests. *MNRAS*, 398:53–74, September 2009.

[BT08] J. Binney and S. Tremaine. *Galactic Dynamics: Second Edition*. Princeton University Press, 2008.

[BT14] A. Bleuler and R. Teyssier. Towards a more realistic sink particle algorithm for the RAMSES CODE. *MNRAS*, 445:4015–4036, December 2014.

[BTB17] P. Biernacki, R. Teyssier, and A. Bleuler. On the Dynamics of Supermassive Black Holes in Gas-Rich, Star-Forming Galaxies: the Case for Nuclear Star Cluster Coevolution. *ArXiv e-prints*, January 2017.

[BTCM15] A. Bleuler, R. Teyssier, S. Carassou, and D. Martizzi. PHEW: a parallel segmentation algorithm for three-dimensional AMR datasets. Application to structure detection in self-gravitating flows. *Computational Astrophysics and Cosmology*, 2:5, June 2015.

[BVF+93] H. Boehringer, W. Voges, A. C. Fabian, A. C. Edge, and D. M. Neumann. A ROSAT HRI study of the interaction of the X-ray-emitting gas and radio lobes of NGC 1275. *MNRAS*, 264:L25–L28, October 1993.

[BVR06] M. C. Begelman, M. Volonteri, and M. J. Rees. Formation of supermassive black holes by direct collapse in pre-galactic haloes. *MNRAS*, 370:289–298, July 2006.

[CBB04] TV-Series *"Star Trek: Enterprise"*, Episode 3.12 *"Chosen Realm"*, First aired on January 14th, 2004 on UPN, Executive Producers: Rick Berman and Brannon Braga, Written by Manny Coto, Directed by Roxann Dawson, Star Trek and Star Trek: Enterprise are trademarks of CBS Studios Inc., all rights reserved by CBS Studios Inc., 2004.

[CCL+15] N. Chisari, S. Codis, C. Laigle, Y. Dubois, C. Pichon, J. Devriendt, A. Slyz, L. Miller, R. Gavazzi, and K. Benabed. Intrinsic alignments of galaxies in the Horizon-AGN cosmological hydrodynamical simulation. *MNRAS*, 454:2736–2753, December 2015.

[CO07] B. W. Carroll and D. A. Ostlie. *An introduction to modern astrophysics, Second Edition*. Pearson, July 2007.

[CPK+16] W. Cui, C. Power, A. Knebe, S. T. Kay, F. Sembolini, P. J. Elahi, G. Yepes, F. Pearce, D. Cunnama, A. M. Beck, C. Dalla Vecchia, R. Davé, S. February, S. Huang, A. Hobbs, N. Katz, I. G. McCarthy, G. Murante, V. Perret, E. Puchwein, J. I. Read, A. Saro, R. Teyssier, and R. J. Thacker. nIFTy galaxy cluster simulations - IV. Quantifying the influence of baryons on halo properties. *MNRAS*, 458:4052–4073, June 2016.

[CS02] A. Cooray and R. Sheth. Halo models of large scale structure. *Physics Reports*, 372:1–129, December 2002.

[CSB+15] R. A. Crain, J. Schaye, R. G. Bower, M. Furlong, M. Schaller, T. Theuns, C. Dalla Vecchia, C. S. Frenk, I. G. McCarthy, J. C. Helly, A. Jenkins, Y. M. Rosas-Guevara, S. D. M. White, and J. W. Trayford. The EAGLE simulations of galaxy formation: calibration of subgrid physics and model variations. *MNRAS*, 450:1937–1961, June 2015.

[CT07] A. Cattaneo and R. Teyssier. AGN self-regulation in cooling flow clusters. *MNRAS*, 376:1547–1556, April 2007.

[DAA+16] Dark Energy Survey Collaboration, T. Abbott, F. B. Abdalla, J. Aleksić, S. Allam, A. Amara, D. Bacon, E. Balbinot, M. Banerji, K. Bechtol, A. Benoit-Lévy, G. M. Bernstein, E. Bertin, J. Blazek, C. Bonnett, S. Bridle, D. Brooks, R. J. Brunner, E. Buckley-Geer, D. L. Burke, G. B. Caminha, D. Capozzi, J. Carlsen, A. Carnero-Rosell, M. Carollo, M. Carrasco-Kind, J. Carretero, F. J. Castander, L. Clerkin, T. Collett, C. Conselice, M. Crocce, C. E. Cunha, C. B. D'Andrea, L. N. da Costa, T. M. Davis, S. Desai, H. T. Diehl, J. P. Dietrich, S. Dodelson, P. Doel, A. Drlica-Wagner, J. Estrada, J. Etherington, A. E. Evrard, J. Fabbri, D. A. Finley, B. Flaugher, R. J. Foley, P. Fosalba, J. Frieman, J. García-Bellido, E. Gaztanaga, D. W. Gerdes, T. Giannantonio, D. A. Goldstein, D. Gruen, R. A. Gruendl, P. Guarnieri, G. Gutierrez, W. Hartley, K. Honscheid, B. Jain, D. J. James, T. Jeltema, S. Jouvel, R. Kessler, A. King, D. Kirk, R. Kron, K. Kuehn, N. Kuropatkin, O. Lahav, T. S. Li, M. Lima, H. Lin, M. A. G. Maia, M. Makler, M. Manera, C. Maraston, J. L. Marshall, P. Martini, R. G. McMahon, P. Melchior, A. Merson, C. J. Miller, R. Miquel, J. J. Mohr, X. Morice-Atkinson, K. Naidoo, E. Neilsen, R. C. Nichol, B. Nord, R. Ogando, F. Ostrovski, A. Palmese, A. Papadopoulos, H. V. Peiris, J. Peoples, W. J. Percival, A. A. Plazas, S. L. Reed, A. Refregier, A. K. Romer, A. Roodman, A. Ross, E. Rozo, E. S. Rykoff, I. Sadeh, M. Sako, C. Sánchez, E. Sanchez, B. Santiago, V. Scarpine, M. Schubnell, I. Sevilla-Noarbe, E. Sheldon, M. Smith, R. C. Smith, M. Soares-Santos, F. Sobreira, M. Soumagnac, E. Suchyta, M. Sullivan, M. Swanson, G. Tarle, J. Thaler, D. Thomas, R. C. Thomas, D. Tucker, J. D. Vieira, V. Vikram, A. R. Walker, R. H. Wechsler, J. Weller, W. Wester, L. Whiteway, H. Wilcox, B. Yanny, Y. Zhang, and J. Zuntz. The Dark Energy Survey: more than dark energy - an overview. *MNRAS*, 460:1270–1299, August 2016.

[DBS+08] K. Dolag, S. Borgani, S. Schindler, A. Diaferio, and A. M. Bykov. Simulation Techniques for Cosmological Simulations. *Space Science Reviews*, 134:229–268, February 2008.

[DDST10] Y. Dubois, J. Devriendt, A. Slyz, and R. Teyssier. Jet-regulated cooling catastrophe. *MNRAS*, 409:985–1001, December 2010.

[DDST12] Y. Dubois, J. Devriendt, A. Slyz, and R. Teyssier. Self-regulated growth of supermassive black holes by a dual jet-heating active galactic nucleus feedback mechanism: methods, tests and implications for cosmological simulations. *MNRAS*, 420:2662–2683, March 2012.

[DDTS11] Y. Dubois, J. Devriendt, R. Teyssier, and A. Slyz. How active galactic nucleus feedback and metal cooling shape cluster entropy profiles. *MNRAS*, 417:1853–1870, November 2011.

[DGPS13] Y. Dubois, R. Gavazzi, S. Peirani, and J. Silk. AGN-driven quenching of star formation: morphological and dynamical implications for early-type galaxies. *MNRAS*, 433:3297–3313, August 2013.

[Dod03] S. Dodelson. *Modern cosmology*. Academic Press, 2003.

[DPW+14] Y. Dubois, C. Pichon, C. Welker, D. Le Borgne, J. Devriendt, C. Laigle, S. Codis, D. Pogosyan, S. Arnouts, K. Benabed, E. Bertin, J. Blaizot, F. Bouchet, J.-F. Cardoso, S. Colombi, V. de Lapparent, V. Desjacques, R. Gavazzi, S. Kassin, T. Kimm, H. McCracken, B. Milliard, S. Peirani, S. Prunet, S. Rouberol, J. Silk, A. Slyz, T. Sousbie, R. Teyssier, L. Tresse, M. Treyer, D. Vibert, and M. Volonteri. Dancing in the dark: galactic properties trace spin swings along the cosmic web. *MNRAS*, 444:1453–1468, October 2014.

[DQM11] J. Debuhr, E. Quataert, and C.-P. Ma. The growth of massive black holes in galaxy merger simulations with feedback by radiation pressure. *MNRAS*, 412:1341–1360, April 2011.

[DVS14] Y. Dubois, M. Volonteri, and J. Silk. Black hole evolution - III. Statistical properties of mass growth and spin evolution using large-scale hydrodynamical cosmological simulations. *MNRAS*, 440:1590–1606, May 2014.

[DVS+15] Y. Dubois, M. Volonteri, J. Silk, J. Devriendt, A. Slyz, and R. Teyssier. Black hole evolution - I. Supernova-regulated black hole growth. *MNRAS*, 452:1502–1518, September 2015.

[EH98a] D. J. Eisenstein and W. Hu. Baryonic Features in the Matter Transfer Function. *ApJ*, 496:605–614, March 1998.

[EH98b] D. J. Eisenstein and P. Hut. HOP: A New Group-Finding Algorithm for N-Body Simulations. *ApJ*, 498:137–142, May 1998.

[ENF98] V. R. Eke, J. F. Navarro, and C. S. Frenk. The Evolution of X-Ray Clusters in a Low-Density Universe. *ApJ*, 503:569–592, August 1998.

[Fab12] A. C. Fabian. Observational Evidence of Active Galactic Nuclei Feedback. *ARAA*, 50:455–489, September 2012.

[FCM+10] R. Feldmann, C. M. Carollo, L. Mayer, A. Renzini, G. Lake, T. Quinn, G. S. Stinson, and G. Yepes. The Evolution of Central Group Galaxies in Hydrodynamical Simulations. *ApJ*, 709:218–240, January 2010.

[FHT06] S. Fromang, P. Hennebelle, and R. Teyssier. A high order Godunov scheme with constrained transport and adaptive mesh refinement for astrophysical magnetohydrodynamics. *A&A*, 457:371–384, October 2006.

[FO11] Y. Fujita and Y. Ohira. Stable Heating of Cluster Cooling Flows by Cosmic-Ray Streaming. *ApJ*, 738:182, September 2011.

[FWB+99] C. S. Frenk, S. D. M. White, P. Bode, J. R. Bond, G. L. Bryan, R. Cen, H. M. P. Couchman, A. E. Evrard, N. Gnedin, A. Jenkins, A. M. Khokhlov, A. Klypin, J. F. Navarro, M. L. Norman, J. P. Ostriker, J. M. Owen, F. R. Pearce, U.-L. Pen, M. Steinmetz, P. A. Thomas, J. V. Villumsen, J. W. Wadsley, M. S. Warren, G. Xu, and G. Yepes. The Santa Barbara Cluster Comparison Project: A Comparison of Cosmological Hydrodynamics Solutions. *ApJ*, 525:554–582, November 1999.

[GBB+00] K. Gebhardt, R. Bender, G. Bower, A. Dressler, S. M. Faber, A. V. Filippenko, R. Green, C. Grillmair, L. C. Ho, J. Kormendy, T. R. Lauer, J. Magorrian, J. Pinkney, D. Richstone, and S. Tremaine. A Relationship between Nuclear Black Hole Mass and Galaxy Velocity Dispersion. *ApJL*, 539:L13–L16, August 2000.

[GRG+09a] K. Gültekin, D. O. Richstone, K. Gebhardt, T. R. Lauer, J. Pinkney, M. C. Aller, R. Bender, A. Dressler, S. M. Faber, A. V. Filippenko, R. Green, L. C. Ho, J. Kormendy, and C. Siopis. A Quintet of Black Hole Mass Determinations. *ApJ*, 695:1577–1590, April 2009.

[GRG+09b] K. Gültekin, D. O. Richstone, K. Gebhardt, T. R. Lauer, S. Tremaine, M. C. Aller, R. Bender, A. Dressler, S. M. Faber, A. V. Filippenko, R. Green, L. C. Ho, J. Kormendy, J. Magorrian, J. Pinkney, and C. Siopis. The M-σ and M-L Relations in Galactic Bulges, and Determinations of Their Intrinsic Scatter. *ApJ*, 698:198–221, June 2009.

[GSZZ13] A. H. Gonzalez, S. Sivanandam, A. I. Zabludoff, and D. Zaritsky. Galaxy Cluster Baryon Fractions Revisited. *ApJ*, 778:14, November 2013.

[HA11] O. Hahn and T. Abel. Multi-scale initial conditions for cosmological simulations. *MNRAS*, 415:2101–2121, August 2011.

[HE88] R. W. Hockney and J. W. Eastwood. *Computer simulation using particles*. CRC Press, 1988.

[HL41] F. Hoyle and R. A. Lyttleton. On the accretion theory of stellar evolution. *MNRAS*, 101:227, 1941.

[HLF+08] K. Heitmann, Z. Lukić, P. Fasel, S. Habib, M. S. Warren, M. White, J. Ahrens, L. Ankeny, R. Armstrong, B. O'Shea, P. M. Ricker, V. Springel, J. Stadel, and H. Trac. The cosmic code comparison project. *Computational Science and Discovery*, 1(1):015003, October 2008.

[HLK+13] G. Hinshaw, D. Larson, E. Komatsu, D. N. Spergel, C. L. Bennett, J. Dunkley, M. R. Nolta, M. Halpern, R. S. Hill, N. Odegard, L. Page, K. M. Smith, J. L. Weiland, B. Gold, N. Jarosik, A. Kogut, M. Limon, S. S. Meyer, G. S. Tucker, E. Wollack, and E. L. Wright. Nine-year Wilkinson Microwave Anisotropy Probe (WMAP) Observations: Cosmological Parameter Results. *ApJS*, 208:19, October 2013.

[HM96] F. Haardt and P. Madau. Radiative Transfer in a Clumpy Universe. II. The Ultraviolet Extragalactic Background. *ApJ*, 461:20, April 1996.

[HMW+15] O. Hahn, D. Martizzi, H.-Y. Wu, A. E. Evrard, R. Teyssier, and R. H. Wechsler. Rhapsody-G simulations I: the cool cores, hot gas and stellar content of massive galaxy clusters. *ArXiv e-prints*, September 2015.

[HT05] D. Huterer and M. Takada. Calibrating the nonlinear matter power spectrum: Requirements for future weak lensing surveys. *Astroparticle Physics*, 23:369–376, May 2005.

[Kar05] I. D. Karachentsev. The Local Group and Other Neighboring Galaxy Groups. *AJ*, 129:178–188, January 2005.

[KB12] A. V. Kravtsov and S. Borgani. Formation of Galaxy Clusters. *ARAA*, 50:353–409, September 2012.

[KMK04] M. R. Krumholz, C. F. McKee, and R. I. Klein. Embedding Lagrangian Sink Particles in Eulerian Grids. *ApJ*, 611:399–412, August 2004.

[KOC+94] H. Kang, J. P. Ostriker, R. Cen, D. Ryu, L. Hernquist, A. E. Evrard, G. L. Bryan, and M. L. Norman. A comparison of cosmological hydrodynamic codes. *ApJ*, 430:83–100, July 1994.

[Kra13] A. V. Kravtsov. The Size-Virial Radius Relation of Galaxies. *ApJL*, 764:L31, February 2013.

[KS01] E. Komatsu and U. Seljak. Universal gas density and temperature profile. *MNRAS*, 327:1353–1366, November 2001.

[KSD+11] E. Komatsu, K. M. Smith, J. Dunkley, C. L. Bennett, B. Gold, G. Hinshaw, N. Jarosik, D. Larson, M. R. Nolta, L. Page, D. N. Spergel, M. Halpern, R. S. Hill, A. Kogut, M. Limon, S. S. Meyer, N. Odegard, G. S. Tucker, J. L. Weiland, E. Wollack, and E. L. Wright. Seven-year Wilkinson Microwave Anisotropy Probe (WMAP) Observations: Cosmological Interpretation. *ApJS*, 192:18, February 2011.

[KTP11] A. A. Klypin, S. Trujillo-Gomez, and J. Primack. Dark Matter Halos in the Standard Cosmological Model: Results from the Bolshoi Simulation. *ApJ*, 740:102, October 2011.

[LAA+11] R. Laureijs, J. Amiaux, S. Arduini, J. . Augueres, J. Brinchmann, R. Cole, M. Cropper, C. Dabin, L. Duvet, A. Ealet, and et al. Euclid Definition Study Report. *ArXiv e-prints*, October 2011.

[LC11] A. Lewis and A. Challinor. CAMB: Code for Anisotropies in the Microwave Background. Astrophysics Source Code Library, February 2011.

[LKN09] E. T. Lau, A. V. Kravtsov, and D. Nagai. Residual Gas Motions in the Intracluster Medium and Bias in Hydrostatic Measurements of Mass Profiles of Clusters. *ApJ*, 705:1129–1138, November 2009.

[LNN+02] C. Loken, M. L. Norman, E. Nelson, J. Burns, G. L. Bryan, and P. Motl. A Universal Temperature Profile for Galaxy Clusters. *ApJ*, 579:571–576, November 2002.

[LSS12] LSST Dark Energy Science Collaboration. Large Synoptic Survey Telescope: Dark Energy Science Collaboration. *ArXiv e-prints*, November 2012.

[MA16] D. Martizzi and H. Agrusa. Mass modeling of galaxy clusters: quantifying hydrostatic bias and contribution from non-thermal pressure. *ArXiv e-prints*, August 2016.

[MB95] C.-P. Ma and E. Bertschinger. Cosmological Perturbation Theory in the Synchronous and Conformal Newtonian Gauges. *ApJ*, 455:7, December 1995.

[MHW+16] D. Martizzi, O. Hahn, H.-Y. Wu, A. E. Evrard, R. Teyssier, and R. H. Wechsler. RHAPSODY-G simulations - II. Baryonic growth and metal enrichment in massive galaxy clusters. *MNRAS*, 459:4408–4427, July 2016.

[MNW13] B. P. Moster, T. Naab, and S. D. M. White. Galactic star formation and accretion histories from matching galaxies to dark matter haloes. *MNRAS*, 428:3121–3138, February 2013.

[MQT10] N. Murray, E. Quataert, and T. A. Thompson. The Disruption of Giant Molecular Clouds by Radiation Pressure & the Efficiency of Star Formation in Galaxies. *ApJ*, 709:191–209, January 2010.

[MR01] P. Madau and M. J. Rees. Massive Black Holes as Population III Remnants. *ApJL*, 551:L27–L30, April 2001.

[MSM+10] B. P. Moster, R. S. Somerville, C. Maulbetsch, F. C. van den Bosch, A. V. Macciò, T. Naab, and L. Oser. Constraints on the Relationship between Stellar Mass and Halo Mass at Low and High Redshift. *ApJ*, 710:903–923, February 2010.

[MSP+10] I. G. McCarthy, J. Schaye, T. J. Ponman, R. G. Bower, C. M. Booth, C. Dalla Vecchia, R. A. Crain, V. Springel, T. Theuns, and R. P. C. Wiersma. The case for AGN feedback in galaxy groups. *MNRAS*, 406:822–839, August 2010.

[MTM12] D. Martizzi, R. Teyssier, and B. Moore. The formation of the brightest cluster galaxies in cosmological simulations: the case for active galactic nucleus feedback. *MNRAS*, 420:2859–2873, March 2012.

[MVV14] E. Massara, F. Villaescusa-Navarro, and M. Viel. The halo model in a massive neutrino cosmology. *JCAP*, 12:053, December 2014.

[MvW10] H. Mo, F. C. van den Bosch, and S. White. *Galaxy Formation and Evolution*. Cambridge University Press, May 2010.

[NFW95] J. F. Navarro, C. S. Frenk, and S. D. M. White. Simulations of X-ray clusters. *MNRAS*, 275:720–740, August 1995.

[NFW96] J. F. Navarro, C. S. Frenk, and S. D. M. White. The Structure of Cold Dark Matter Halos. *ApJ*, 462:563, May 1996.

[NFW97] J. F. Navarro, C. S. Frenk, and S. D. M. White. A Universal Density Profile from Hierarchical Clustering. *ApJ*, 490:493–508, December 1997.

[NKV07] D. Nagai, A. V. Kravtsov, and A. Vikhlinin. Effects of Galaxy Formation on Thermodynamics of the Intracluster Medium. *ApJ*, 668:1–14, October 2007.

[OBBS04] H. Omma, J. Binney, G. Bryan, and A. Slyz. Heating cooling flows with jets. *MNRAS*, 348:1105–1119, March 2004.

[ONS+05] B. W. O'Shea, K. Nagamine, V. Springel, L. Hernquist, and M. L. Norman. Comparing AMR and SPH Cosmological Simulations. I. Dark Matter and Adiabatic Simulations. *ApJS*, 160:1–27, September 2005.

[PAA+16] Planck Collaboration, P. A. R. Ade, N. Aghanim, M. Arnaud, M. Ashdown, J. Aumont, C. Baccigalupi, A. J. Banday, R. B. Barreiro, J. G. Bartlett, and et al. Planck 2015 results. XIII. Cosmological parameters. *A&A*, 594:A13, September 2016.

[PAG+99] S. Perlmutter, G. Aldering, G. Goldhaber, R. A. Knop, P. Nugent, P. G. Castro, S. Deustua, S. Fabbro, A. Goobar, D. E. Groom, I. M. Hook, A. G. Kim, M. Y. Kim, J. C. Lee, N. J. Nunes, R. Pain, C. R. Pennypacker, R. Quimby, C. Lidman, R. S. Ellis, M. Irwin, R. G. McMahon, P. Ruiz-Lapuente, N. Walton, B. Schaefer, B. J. Boyle, A. V. Filippenko, T. Matheson, A. S. Fruchter, N. Panagia, H. J. M. Newberg, W. J. Couch, and T. S. C. Project. Measurements of Ω and Λ from 42 High-Redshift Supernovae. *ApJ*, 517:565–586, June 1999.

[PNJ+03] C. Power, J. F. Navarro, A. Jenkins, C. S. Frenk, S. D. M. White, V. Springel, J. Stadel, and T. Quinn. The inner structure of ΛCDM haloes - I. A numerical convergence study. *MNRAS*, 338:14–34, January 2003.

[PPA+08] S. Prunet, C. Pichon, D. Aubert, D. Pogosyan, R. Teyssier, and S. Gottloeber. Initial Conditions For Large Cosmological Simulations. *ApJS*, 178:179–188, October 2008.

[PV08] R. Piffaretti and R. Valdarnini. Total mass biases in X-ray galaxy clusters. *A&A*, 491:71–87, November 2008.

[PW65] A. A. Penzias and R. W. Wilson. A Measurement of Excess Antenna Temperature at 4080 Mc/s. *ApJ*, 142:419–421, July 1965.

[RED+06] M. Roncarelli, S. Ettori, K. Dolag, L. Moscardini, S. Borgani, and G. Murante. Simulated X-ray galaxy clusters at the virial radius: Slopes of the gas density, temperature and surface brightness profiles. *MNRAS*, 373:1339–1350, December 2006.

[REM+06] E. Rasia, S. Ettori, L. Moscardini, P. Mazzotta, S. Borgani, K. Dolag, G. Tormen, L. M. Cheng, and A. Diaferio. Systematics in the X-ray cluster mass estimators. *MNRAS*, 369:2013–2024, July 2006.

[RFC+98] A. G. Riess, A. V. Filippenko, P. Challis, A. Clocchiatti, A. Diercks, P. M. Garnavich, R. L. Gilliland, C. J. Hogan, S. Jha, R. P. Kirshner, B. Leibundgut, M. M. Phillips, D. Reiss, B. P. Schmidt, R. A. Schommer, R. C. Smith, J. Spyromilio, C. Stubbs, N. B. Suntzeff, and J. Tonry. Observational Evidence from Supernovae for an Accelerating Universe and a Cosmological Constant. *AJ*, 116:1009–1038, September 1998.

[RT06] Y. Rasera and R. Teyssier. The history of the baryon budget. Cosmic logistics in a hierarchical universe. *A&A*, 445:1–27, January 2006.

[RT17] M. Rabold and R. Teyssier. Precision cosmology with baryons: non-radiative hydrodynamics of galaxy groups. *MNRAS*, 467:3188–3211, May 2017.

[RTA+14] R. Roškar, R. Teyssier, O. Agertz, M. Wetzstein, and B. Moore. A systematic look at the effects of radiative feedback on disc galaxy formation. *MNRAS*, 444:2837–2853, November 2014.

[RTM04] E. Rasia, G. Tormen, and L. Moscardini. A dynamical model for the distribution of dark matter and gas in galaxy clusters. *MNRAS*, 351:237–252, June 2004.

[Ryd03] B. Ryden. *Introduction to cosmology*. Pearson, 2003.

[RZK08] D. H. Rudd, A. R. Zentner, and A. V. Kravtsov. Effects of Baryons and Dissipation on the Matter Power Spectrum. *ApJ*, 672:19–32, January 2008.

[SCB+15] J. Schaye, R. A. Crain, R. G. Bower, M. Furlong, M. Schaller, T. Theuns, C. Dalla Vecchia, C. S. Frenk, I. G. McCarthy, J. C. Helly, A. Jenkins, Y. M. Rosas-Guevara, S. D. M. White, M. Baes, C. M. Booth, P. Camps, J. F. Navarro, Y. Qu, A. Rahmati, T. Sawala, P. A. Thomas, and J. Trayford. The EAGLE project: simulating the evolution and assembly of galaxies and their environments. *MNRAS*, 446:521–554, January 2015.

[Sch59] M. Schmidt. The Rate of Star Formation. *ApJ*, 129:243, March 1959.

[SD93] R. S. Sutherland and M. A. Dopita. Cooling functions for low-density astrophysical plasmas. *ApJS*, 88:253–327, September 1993.

[SDB+10] J. Schaye, C. Dalla Vecchia, C. M. Booth, R. P. C. Wiersma, T. Theuns, M. R. Haas, S. Bertone, A. R. Duffy, I. G. McCarthy, and F. van de Voort. The physics driving the cosmic star formation history. *MNRAS*, 402:1536–1560, March 2010.

[SDH05] V. Springel, T. Di Matteo, and L. Hernquist. Modelling feedback from stars and black holes in galaxy mergers. *MNRAS*, 361:776–794, August 2005.

[Sel00] U. Seljak. Analytic model for galaxy and dark matter clustering. *MNRAS*, 318:203–213, October 2000.

[SEP+16] F. Sembolini, P. J. Elahi, F. R. Pearce, C. Power, A. Knebe, S. T. Kay, W. Cui, G. Yepes, A. M. Beck, S. Borgani, D. Cunnama, R. Davé, S. February, S. Huang, N. Katz, I. G. McCarthy, G. Murante, R. D. A. Newton, V. Perret, E. Puchwein, A. Saro, J. Schaye, and R. Teyssier. nIFTy galaxy cluster simulations - II. Radiative models. *MNRAS*, 459:2973–2991, July 2016.

[SK14] X. Shi and E. Komatsu. Analytical model for non-thermal pressure in galaxy clusters. *MNRAS*, 442:521–532, July 2014.

[SKNL16] X. Shi, E. Komatsu, D. Nagai, and E. T. Lau. Analytical model for non-thermal pressure in galaxy clusters - III. Removing the hydrostatic mass bias. *MNRAS*, 455:2936–2944, January 2016.

[SKNN15] X. Shi, E. Komatsu, K. Nelson, and D. Nagai. Analytical model for non-thermal pressure in galaxy clusters - II. Comparison with cosmological hydrodynamics simulation. *MNRAS*, 448:1020–1029, March 2015.

[SNBL10] L. D. Shaw, D. Nagai, S. Bhattacharya, and E. T. Lau. Impact of Cluster Physics on the Sunyaev-Zel'dovich Power Spectrum. *ApJ*, 725:1452–1465, December 2010.

[Spr05] V. Springel. The cosmological simulation code GADGET-2. *MNRAS*, 364:1105–1134, December 2005.

[SSDH07] D. Sijacki, V. Springel, T. Di Matteo, and L. Hernquist. A unified model for AGN feedback in cosmological simulations of structure formation. *MNRAS*, 380:877–900, September 2007.

[SSK+06] G. Stinson, A. Seth, N. Katz, J. Wadsley, F. Governato, and T. Quinn. Star formation and feedback in smoothed particle hydrodynamic simulations - I. Isolated galaxies. *MNRAS*, 373:1074–1090, December 2006.

[ST15] A. Schneider and R. Teyssier. A new method to quantify the effects of baryons on the matter power spectrum. *JCAP*, 12:049, December 2015.

[STNC10] S. Skory, M. J. Turk, M. L. Norman, and A. L. Coil. Parallel HOP: A Scalable Halo Finder for Massive Cosmological Data Sets. *ApJS*, 191:43–57, November 2010.

[STP+16] A. Schneider, R. Teyssier, D. Potter, J. Stadel, J. Onions, D. S. Reed, R. E. Smith, V. Springel, F. R. Pearce, and R. Scoccimarro. Matter power spectrum and the challenge of percent accuracy. *JCAP*, 4:047, April 2016.

[SVD+09] M. Sun, G. M. Voit, M. Donahue, C. Jones, W. Forman, and A. Vikhlinin. Chandra Studies of the X-Ray Gas Properties of Galaxy Groups. *ApJ*, 693:1142–1172, March 2009.

[SVG+15] D. Sijacki, M. Vogelsberger, S. Genel, V. Springel, P. Torrey, G. F. Snyder, D. Nelson, and L. Hernquist. The Illustris simulation: the evolving population of black holes across cosmic time. *MNRAS*, 452:575–596, September 2015.

[SYP+16] F. Sembolini, G. Yepes, F. R. Pearce, A. Knebe, S. T. Kay, C. Power, W. Cui, A. M. Beck, S. Borgani, C. Dalla Vecchia, R. Davé, P. J. Elahi, S. February, S. Huang, A. Hobbs, N. Katz, E. Lau, I. G. McCarthy, G. Murante, D. Nagai, K. Nelson, R. D. A. Newton, V. Perret, E. Puchwein, J. I. Read, A. Saro, J. Schaye, R. Teyssier, and R. J. Thacker. nIFTy galaxy cluster simulations - I. Dark matter and non-radiative models. *MNRAS*, 457:4063–4080, April 2016.

[SZ96] U. Seljak and M. Zaldarriaga. A Line-of-Sight Integration Approach to Cosmic Microwave Background Anisotropies. *ApJ*, 469:437, October 1996.

[Tey02] R. Teyssier. Cosmological hydrodynamics with adaptive mesh refinement. A new high resolution code called RAMSES. *A&A*, 385:337–364, April 2002.

[TFD06] R. Teyssier, S. Fromang, and E. Dormy. Kinematic dynamos using constrained transport with high order Godunov schemes and adaptive mesh refinement. *Journal of Computational Physics*, 218:44–67, October 2006.

[TMM+11] R. Teyssier, B. Moore, D. Martizzi, Y. Dubois, and L. Mayer. Mass distribution in galaxy clusters: the role of Active Galactic Nuclei feedback. *MNRAS*, 414:195–208, June 2011.

[TPDR13] R. Teyssier, A. Pontzen, Y. Dubois, and J. I. Read. Cusp-core transformations in dwarf galaxies: observational predictions. *MNRAS*, 429:3068–3078, March 2013.

[VDPD16] M. Volonteri, Y. Dubois, C. Pichon, and J. Devriendt. The cosmic evolution of massive black holes in the Horizon-AGN simulation. *MNRAS*, 460:2979–2996, August 2016.

[VGS+14a] M. Vogelsberger, S. Genel, V. Springel, P. Torrey, D. Sijacki, D. Xu, G. Snyder, S. Bird, D. Nelson, and L. Hernquist. Properties of galaxies reproduced by a hydrodynamic simulation. *Nature*, 509:177–182, May 2014.

[VGS+14b] M. Vogelsberger, S. Genel, V. Springel, P. Torrey, D. Sijacki, D. Xu, G. Snyder, D. Nelson, and L. Hernquist. Introducing the Illustris Project: simulating the coevolution of dark and visible matter in the Universe. *MNRAS*, 444:1518–1547, October 2014.

[VKF+06] A. Vikhlinin, A. Kravtsov, W. Forman, C. Jones, M. Markevitch, S. S. Murray, and L. Van Speybroeck. Chandra Sample of Nearby Relaxed Galaxy Clusters: Mass, Gas Fraction, and Mass-Temperature Relation. *ApJ*, 640:691–709, April 2006.

[vSBD11] M. P. van Daalen, J. Schaye, C. M. Booth, and C. Dalla Vecchia. The effects of galaxy formation on the matter power spectrum: a challenge for precision cosmology. *MNRAS*, 415:3649–3665, August 2011.

[Wal97] R. M. Wald. *General relativity, Second Edition.* The University of Chicago Press, 1997.

[WEH+15] H.-Y. Wu, A. E. Evrard, O. Hahn, D. Martizzi, R. Teyssier, and R. H. Wechsler. RHAPSODY-G simulations: galaxy clusters as baryonic closed boxes and the covariance between hot gas and galaxies. *MNRAS*, 452:1982–1991, September 2015.

[WHW+13a] H.-Y. Wu, O. Hahn, R. H. Wechsler, P. S. Behroozi, and Y.-Y. Mao. Rhapsody. II. Subhalo Properties and the Impact of Tidal Stripping From a Statistical Sample of Cluster-size Halos. *ApJ*, 767:23, April 2013.

[WHW+13b] H.-Y. Wu, O. Hahn, R. H. Wechsler, Y.-Y. Mao, and P. S. Behroozi. Rhapsody. I. Structural Properties and Formation History from a Statistical Sample of Re-simulated Cluster-size Halos. *ApJ*, 763:70, February 2013.

[Yep97] G. Yepes. Cosmological Numerical Simulations. In D. Valls-Gabaud, M. A. Hendry, P. Molaro, and K. Chamcham, editors, *From Quantum Fluctuations to Cosmological Structures*, volume 126 of *Astronomical Society of the Pacific Conference Series*, page 279, September 1997.

[Zen07] A. R. Zentner. The Excursion Set Theory of Halo Mass Functions, Halo Clustering, and Halo Growth. *International Journal of Modern Physics D*, 16:763–815, 2007.

[Zwi33] F. Zwicky. Die Rotverschiebung von extragalaktischen Nebeln. *Helvetica Physica Acta*, 6:110–127, 1933.

[Zwi37] F. Zwicky. On the Masses of Nebulae and of Clusters of Nebulae. *ApJ*, 86:217, October 1937.

Appendix

Appendix A: Euler equations

Continuity / Mass conservation:

$$\frac{d\rho_{(\vec{x},t)}}{dt} = -\rho_{(\vec{x},t)} \cdot \nabla \vec{v}_{(\vec{x},t)}$$

$$\frac{\partial \rho_{(\vec{x},t)}}{\partial t} + \vec{v}_{(\vec{x},t)} \cdot \nabla \rho_{(\vec{x},t)} = -\rho_{(\vec{x},t)} \cdot \nabla \vec{v}_{(\vec{x},t)}$$

$$\frac{\partial \rho_{(\vec{x},t)}}{\partial t} + \vec{v}_{(\vec{x},t)} \cdot \nabla \rho_{(\vec{x},t)} + \rho_{(\vec{x},t)} \cdot \nabla \vec{v}_{(\vec{x},t)} = 0$$

$$\frac{\partial \rho_{(\vec{x},t)}}{\partial t} + \nabla(\rho_{(\vec{x},t)} \cdot \vec{v}_{(\vec{x},t)}) = 0 \tag{A.1}$$

Velocity conservation / momentum conservation:

$$\frac{dv_{i\,(\vec{x},t)}}{dt} = -\frac{1}{\rho_{(\vec{x},t)}} \cdot \nabla P_{(\vec{x},t)} - \nabla \Phi_{(\vec{x},t)}$$

$$\frac{\partial v_{i\,(\vec{x},t)}}{\partial t} + \vec{v}_{(\vec{x},t)} \cdot (\nabla v_{i\,(\vec{x},t)}) = -\frac{1}{\rho_{(\vec{x},t)}} \cdot \nabla_i P_{(\vec{x},t)} - \nabla_i \Phi_{(\vec{x},t)}$$

$$\rho_{(\vec{x},t)} \cdot \frac{\partial v_{i\,(\vec{x},t)}}{\partial t} + \rho_{(\vec{x},t)} \cdot \vec{v}_{(\vec{x},t)} \cdot (\nabla v_{i\,(\vec{x},t)}) = -\nabla_i P_{(\vec{x},t)} - \rho_{(\vec{x},t)} \cdot \nabla_i \Phi_{(\vec{x},t)}$$

$$\rho_{(\vec{x},t)} \cdot \frac{\partial v_{i\,(\vec{x},t)}}{\partial t} + \rho_{(\vec{x},t)} \cdot \vec{v}_{(\vec{x},t)} \cdot (\nabla v_{i\,(\vec{x},t)}) +$$
$$+ v_{i\,(\vec{x},t)} \cdot \frac{\partial \rho_{(\vec{x},t)}}{\partial t} + v_{i\,(\vec{x},t)} \cdot \vec{v}_{(\vec{x},t)} \cdot \nabla \rho_{(\vec{x},t)} + v_{i\,(\vec{x},t)} \cdot \rho_{(\vec{x},t)} \cdot \nabla \vec{v}_{(\vec{x},t)} =$$
$$= -\nabla_i P_{(\vec{x},t)} - \rho_{(\vec{x},t)} \cdot \nabla_i \Phi_{(\vec{x},t)}$$

$$\frac{\partial(\rho_{(\vec{x},t)} \cdot v_{i\,(\vec{x},t)})}{\partial t} +$$
$$+ \rho_{(\vec{x},t)} \cdot \vec{v}_{(\vec{x},t)} \cdot (\nabla v_{i\,(\vec{x},t)}) + v_{i\,(\vec{x},t)} \cdot \vec{v}_{(\vec{x},t)} \cdot \nabla \rho_{(\vec{x},t)} + v_{i\,(\vec{x},t)} \cdot \rho_{(\vec{x},t)} \cdot \nabla \vec{v}_{(\vec{x},t)} =$$
$$= -\nabla_i P_{(\vec{x},t)} - \rho_{(\vec{x},t)} \cdot \nabla_i \Phi_{(\vec{x},t)}$$

$$\frac{\partial(\rho_{(\vec{x},t)} \cdot v_{i\,(\vec{x},t)})}{\partial t} +$$
$$+ \rho_{(\vec{x},t)} \cdot v_{j\,(\vec{x},t)} \cdot \nabla_j v_{i\,(\vec{x},t)} + v_{i\,(\vec{x},t)} \cdot v_{j\,(\vec{x},t)} \cdot \nabla_j \rho_{(\vec{x},t)} + v_{i\,(\vec{x},t)} \cdot \rho_{(\vec{x},t)} \cdot \nabla_j v_{j\,(\vec{x},t)} =$$
$$= -\nabla_i P_{(\vec{x},t)} - \rho_{(\vec{x},t)} \cdot \nabla_i \Phi_{(\vec{x},t)}$$

$$\frac{\partial(\rho_{(\vec{x},t)} \cdot v_{i\,(\vec{x},t)})}{\partial t} + \nabla_j(\rho_{(\vec{x},t)} \cdot v_{j\,(\vec{x},t)} \cdot v_{i\,(\vec{x},t)}) = -\nabla_i P_{(\vec{x},t)} - \rho_{(\vec{x},t)} \cdot \nabla_i \Phi_{(\vec{x},t)} \tag{A.2}$$

Energy conservation equation:

$$\frac{dE_{(\vec{x},t)}}{dt} = -\frac{P_{(\vec{x},t)}}{\rho_{(\vec{x},t)}} \cdot \nabla \vec{v}_{(\vec{x},t)}$$

$$\rho_{(\vec{x},t)} \cdot \frac{dE_{(\vec{x},t)}}{dt} + \nabla(P_{(\vec{x},t)} \cdot \vec{v}_{(\vec{x},t)}) - (\nabla P_{(\vec{x},t)}) \cdot \vec{v}_{(\vec{x},t)} = 0$$

$$\begin{aligned}\rho_{(\vec{x},t)} \cdot \frac{dE_{(\vec{x},t)}}{dt} + \nabla(P_{(\vec{x},t)} \cdot \vec{v}_{(\vec{x},t)}) - (\nabla P_{(\vec{x},t)}) \cdot \vec{v}_{(\vec{x},t)} - \rho_{(\vec{x},t)} \cdot \nabla \Phi_{(\vec{x},t)} \cdot \vec{v}_{(\vec{x},t)} = \\ = -\rho_{(\vec{x},t)} \cdot \nabla \Phi_{(\vec{x},t)} \cdot \vec{v}_{(\vec{x},t)}\end{aligned}$$

$$\begin{aligned}\rho_{(\vec{x},t)} \cdot \frac{dE_{(\vec{x},t)}}{dt} + \left[-(\nabla P_{(\vec{x},t)}) - \rho_{(\vec{x},t)} \cdot (\nabla \Phi_{(\vec{x},t)})\right] \cdot \vec{v}_{(\vec{x},t)} = \\ = -\nabla(P_{(\vec{x},t)} \cdot \vec{v}_{(\vec{x},t)}) - \rho_{(\vec{x},t)} \cdot \nabla \Phi_{(\vec{x},t)} \cdot \vec{v}_{(\vec{x},t)}\end{aligned}$$

After using the momentum conservation equation one finds

$$\rho_{(\vec{x},t)} \cdot \frac{dE_{(\vec{x},t)}}{dt} + \rho_{(\vec{x},t)} \cdot \frac{d\vec{v}_{(\vec{x},t)}}{dt} \cdot \vec{v}_{(\vec{x},t)} = -\nabla(P_{(\vec{x},t)} \cdot \vec{v}_{(\vec{x},t)}) - \rho_{(\vec{x},t)} \cdot \nabla \Phi_{(\vec{x},t)} \cdot \vec{v}_{(\vec{x},t)}$$

$$\rho_{(\vec{x},t)} \cdot \frac{dE_{(\vec{x},t)}}{dt} + \rho_{(\vec{x},t)} \cdot \frac{1}{2} \cdot \frac{dv^2_{(\vec{x},t)}}{dt} = -\nabla(P_{(\vec{x},t)} \cdot \vec{v}_{(\vec{x},t)}) - \rho_{(\vec{x},t)} \cdot \nabla \Phi_{(\vec{x},t)} \cdot \vec{v}_{(\vec{x},t)}$$

$$\begin{aligned}\rho_{(\vec{x},t)} \cdot \frac{\partial E_{(\vec{x},t)}}{\partial t} + \rho_{(\vec{x},t)} \cdot \vec{v}_{(\vec{x},t)} \cdot (\nabla E_{(\vec{x},t)}) + \\ + \rho_{(\vec{x},t)} \cdot \frac{1}{2} \cdot \frac{\partial v^2_{(\vec{x},t)}}{\partial t} + \rho_{(\vec{x},t)} \cdot \vec{v}_{(\vec{x},t)} \cdot (\nabla \frac{1}{2} \cdot v^2_{(\vec{x},t)}) = \\ = -\nabla(P_{(\vec{x},t)} \cdot \vec{v}_{(\vec{x},t)}) - \rho_{(\vec{x},t)} \cdot \nabla \Phi_{(\vec{x},t)} \cdot \vec{v}_{(\vec{x},t)}\end{aligned}$$

Adding the mass conservation equation times the internal energy per mass and volume

$$\begin{aligned}E_{(\vec{x},t)} \cdot \frac{\partial \rho_{(\vec{x},t)}}{\partial t} + E_{(\vec{x},t)} \cdot \nabla(\rho_{(\vec{x},t)} \cdot \vec{v}_{(\vec{x},t)}) + \\ + \rho_{(\vec{x},t)} \cdot \frac{\partial E_{(\vec{x},t)}}{\partial t} + \rho_{(\vec{x},t)} \cdot \vec{v}_{(\vec{x},t)} \cdot (\nabla E_{(\vec{x},t)}) + \\ + \rho_{(\vec{x},t)} \cdot \frac{1}{2} \cdot \frac{\partial v^2_{(\vec{x},t)}}{\partial t} + \rho_{(\vec{x},t)} \cdot \vec{v}_{(\vec{x},t)} \cdot (\nabla \frac{1}{2} \cdot v^2_{(\vec{x},t)}) = \\ = -\nabla(P_{(\vec{x},t)} \cdot \vec{v}_{(\vec{x},t)}) - \rho_{(\vec{x},t)} \cdot \nabla \Phi_{(\vec{x},t)} \cdot \vec{v}_{(\vec{x},t)}\end{aligned}$$

Adding the mass conservation equation times the bulk kinetic energy per mass and volume

$$\begin{aligned}
E_{(\vec{x},t)} \cdot \frac{\partial \rho_{(\vec{x},t)}}{\partial t} + E_{(\vec{x},t)} \cdot \nabla(\rho_{(\vec{x},t)} \cdot \vec{v}_{(\vec{x},t)}) + \\
+\rho_{(\vec{x},t)} \cdot \frac{\partial E_{(\vec{x},t)}}{\partial t} + \rho_{(\vec{x},t)} \cdot \vec{v}_{(\vec{x},t)} \cdot (\nabla E_{(\vec{x},t)}) + \\
+\frac{1}{2} \cdot v^2_{(\vec{x},t)} \cdot \frac{\partial \rho_{(\vec{x},t)}}{\partial t} + \frac{1}{2} \cdot v^2_{(\vec{x},t)} \cdot \nabla(\rho_{(\vec{x},t)} \cdot \vec{v}_{(\vec{x},t)}) + \\
+\rho_{(\vec{x},t)} \cdot \frac{1}{2} \cdot \frac{\partial v^2_{(\vec{x},t)}}{\partial t} + \rho_{(\vec{x},t)} \cdot \vec{v}_{(\vec{x},t)} \cdot (\nabla \frac{1}{2} \cdot v^2_{(\vec{x},t)}) = \\
= -\nabla(P_{(\vec{x},t)} \cdot \vec{v}_{(\vec{x},t)}) - \rho_{(\vec{x},t)} \cdot \nabla \Phi_{(\vec{x},t)} \cdot \vec{v}_{(\vec{x},t)}
\end{aligned}$$

$$\begin{aligned}
E_{(\vec{x},t)} \cdot \frac{\partial \rho_{(\vec{x},t)}}{\partial t} + E_{(\vec{x},t)} \cdot (\nabla \rho_{(\vec{x},t)}) \cdot \vec{v}_{(\vec{x},t)} + E_{(\vec{x},t)} \cdot \rho_{(\vec{x},t)} \cdot (\nabla \vec{v}_{(\vec{x},t)}) + \\
+\rho_{(\vec{x},t)} \cdot \frac{\partial E_{(\vec{x},t)}}{\partial t} + \rho_{(\vec{x},t)} \cdot \vec{v}_{(\vec{x},t)} \cdot (\nabla E_{(\vec{x},t)}) + \\
+\frac{1}{2} \cdot v^2_{(\vec{x},t)} \cdot \frac{\partial \rho_{(\vec{x},t)}}{\partial t} + \frac{1}{2} \cdot v^2_{(\vec{x},t)} \cdot \nabla(\rho_{(\vec{x},t)}) \cdot \vec{v}_{(\vec{x},t)} + \frac{1}{2} \cdot v^2_{(\vec{x},t)} \cdot \rho_{(\vec{x},t)} \cdot (\nabla \vec{v}_{(\vec{x},t)}) + \\
+\rho_{(\vec{x},t)} \cdot \frac{1}{2} \cdot \frac{\partial v^2_{(\vec{x},t)}}{\partial t} + \rho_{(\vec{x},t)} \cdot \vec{v}_{(\vec{x},t)} \cdot (\nabla \frac{1}{2} \cdot v^2_{(\vec{x},t)}) = \\
= -\nabla(P_{(\vec{x},t)} \cdot \vec{v}_{(\vec{x},t)}) - \rho_{(\vec{x},t)} \cdot \nabla \Phi_{(\vec{x},t)} \cdot \vec{v}_{(\vec{x},t)}
\end{aligned}$$

$$\begin{aligned}
e_{(\vec{x},t)} \cdot \frac{\partial \rho_{(\vec{x},t)}}{\partial t} + e_{(\vec{x},t)} \cdot (\nabla \rho_{(\vec{x},t)}) \cdot \vec{v}_{(\vec{x},t)} + e_{(\vec{x},t)} \cdot \rho_{(\vec{x},t)} \cdot (\nabla \vec{v}_{(\vec{x},t)}) + \\
+\rho_{(\vec{x},t)} \cdot \frac{\partial e_{(\vec{x},t)}}{\partial t} + \rho_{(\vec{x},t)} \cdot \vec{v}_{(\vec{x},t)} \cdot (\nabla e_{(\vec{x},t)}) + \\
= -\nabla(P_{(\vec{x},t)} \cdot \vec{v}_{(\vec{x},t)}) - \rho_{(\vec{x},t)} \cdot \nabla \Phi_{(\vec{x},t)} \cdot \vec{v}_{(\vec{x},t)}
\end{aligned}$$

$$\frac{\partial(\rho_{(\vec{x},t)} \cdot e_{(\vec{x},t)})}{\partial t} + \nabla(\rho_{(\vec{x},t)} \cdot \vec{v}_{(\vec{x},t)} \cdot e_{(\vec{x},t)}) = -\nabla(P_{(\vec{x},t)} \cdot \vec{v}_{(\vec{x},t)}) - \rho_{(\vec{x},t)} \cdot \nabla \Phi_{(\vec{x},t)} \cdot \vec{v}_{(\vec{x},t)} \quad \text{(A.3)}$$

Appendix B: Stellar-halo-mass relation fit parameters by Moster et al. 2013

The fit by Moster et al. 2013 [MNW13] is given by

$$M_{star\,(M)} = 2N \cdot M \cdot \left[\left(\frac{M}{M_1} \right)^{-\beta} + \left(\frac{M}{M_1} \right)^{\gamma} \right]^{-1} \tag{A.4}$$

with the following parameters:

$$\begin{aligned} M_1 &= 10^{11.59} \\ N &= 0.0351 \\ \beta &= 1.376 \\ \gamma &= 0.608 \end{aligned} \tag{A.5}$$

Appendix C: Halo 2 central galaxy morphology for the case of the four stellar feedback models

Images of the central galaxy for the four tested stellar feedback models described in Section 5.

SF default model

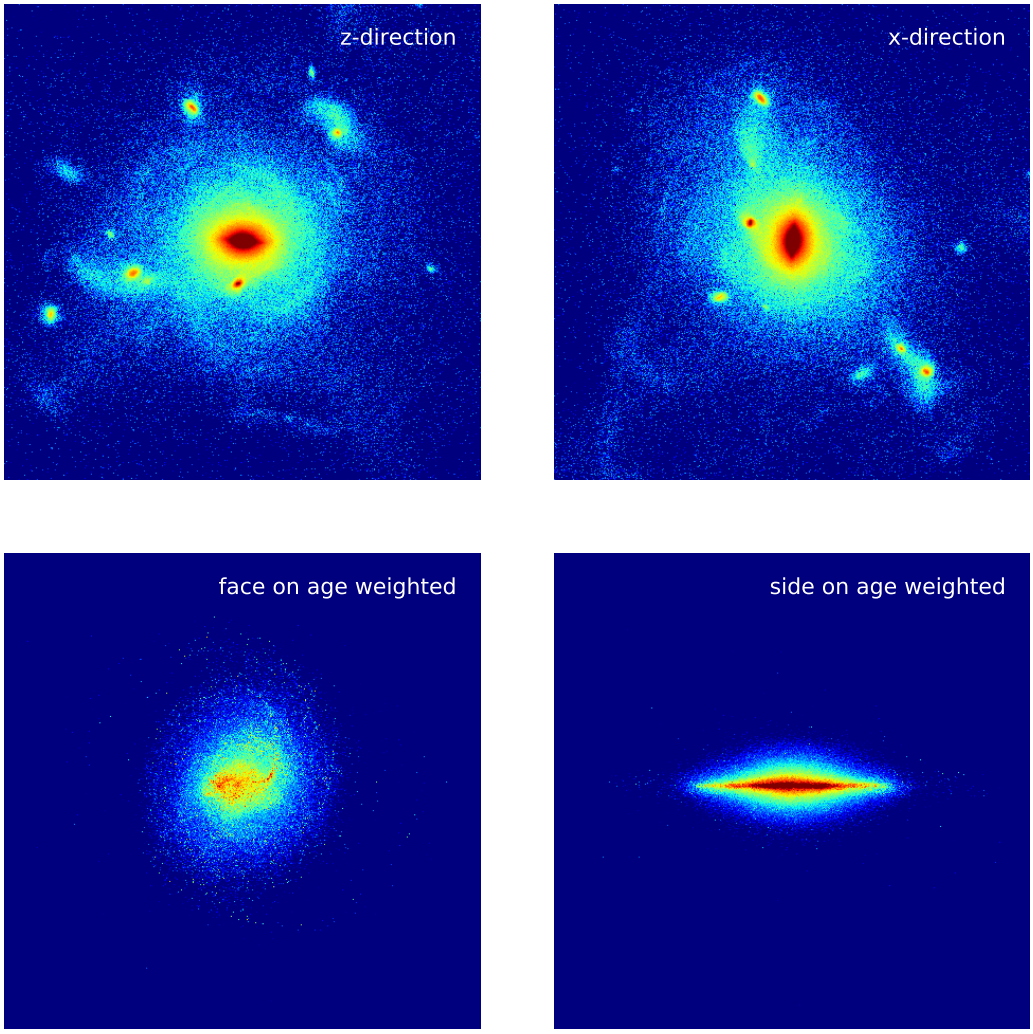

Figure A.1: **Galaxy maps for the SF default model. The image sizes are 830 kpc for the upper two images and 83 kpc for the lower two images. The colour scale is arbitrary.**

SF model 1

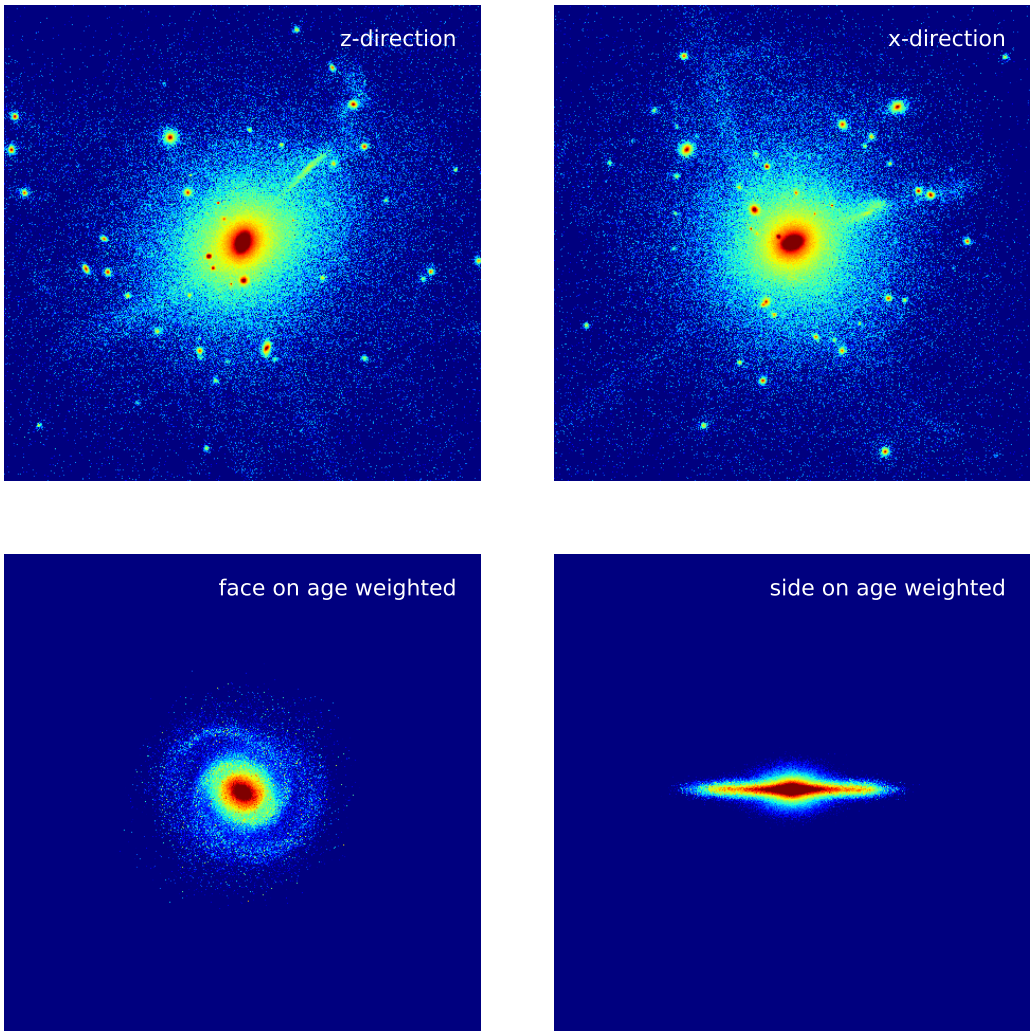

Figure A.2: **Galaxy maps for the SF model 1. The image sizes are 830 kpc for the upper two images and 83 kpc for the lower two images. The colour scale is arbitrary.**

SF model 2

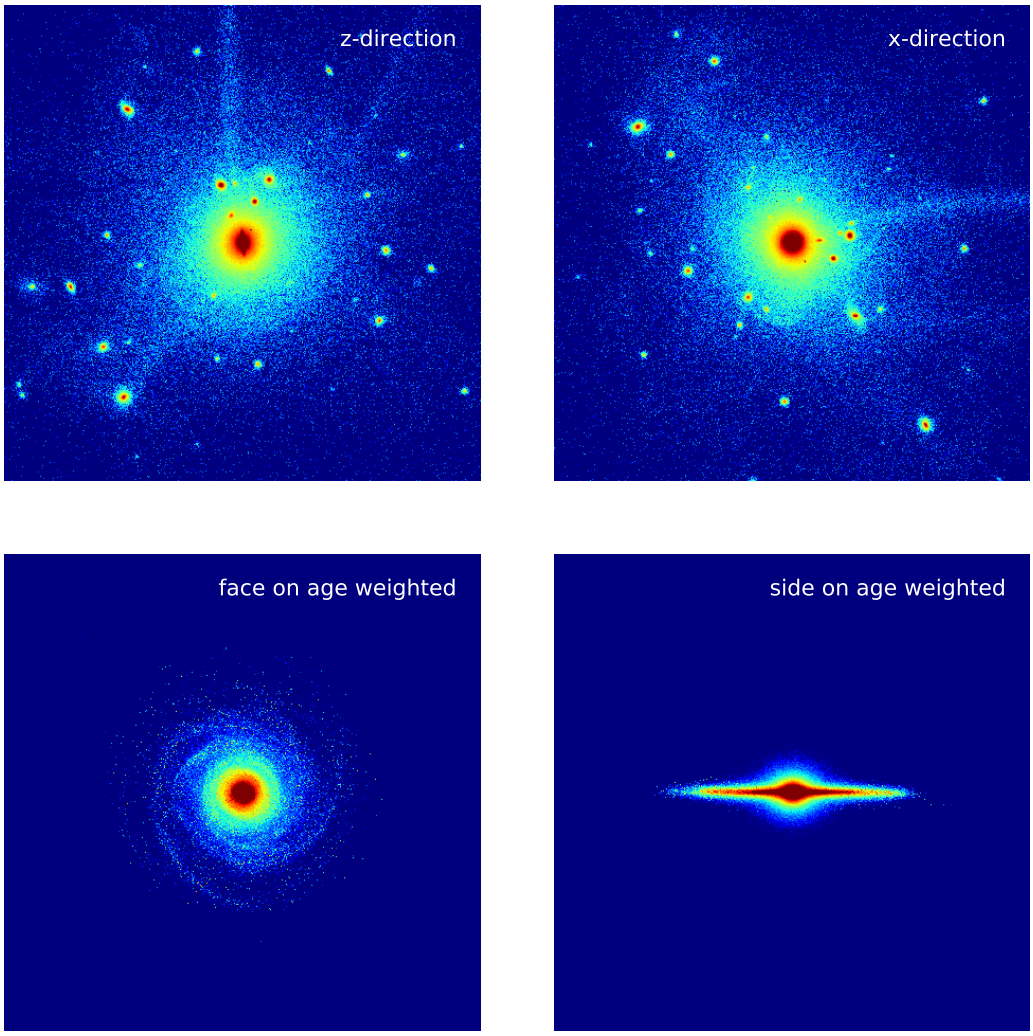

Figure A.3: **Galaxy maps for the SF model 2. The image sizes are 830 kpc for the upper two images and 83 kpc for the lower two images. The colour scale is arbitrary.**

SF model 3

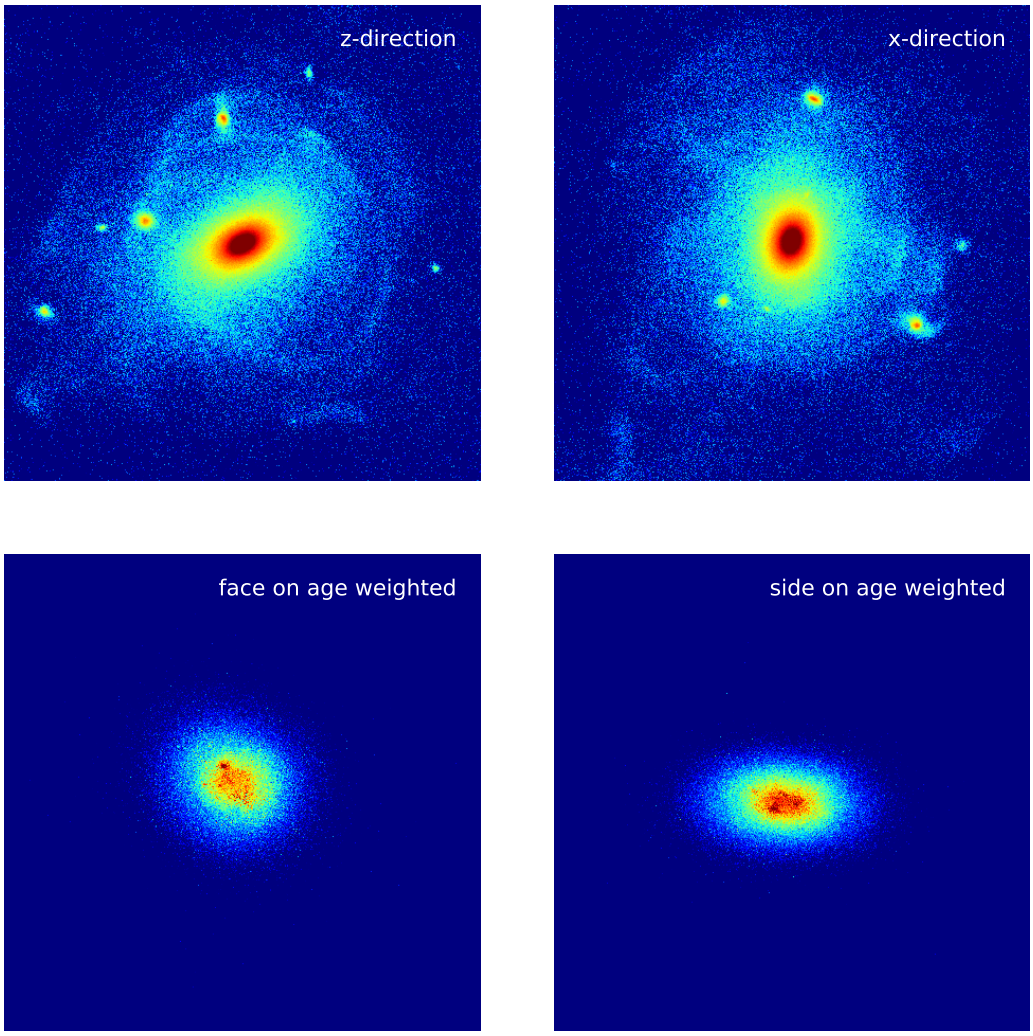

Figure A.4: **Galaxy maps for the SF model 3. The image sizes are 830 kpc for the upper two images and 83 kpc for the lower two images. The colour scale is arbitrary.**